Miniaturized Tunnel Magnetoresistance Sensors for Novel Applications of Atomic Force Microscopy

A Dissertation by

Ali Tavassolizadeh

Submitted in Partial Fulfillment of
the Requirements for the Degree of
Doctor of Philosophy

Faculty of Engineering
Christian-Albrechts-Universität zu Kiel

2015

Declaration

I hereby declare that I wrote this dissertation by myself and to the best of my knowledge and belief, used none but the indicated sources. I also declare that this dissertation has never been submitted for any degree to any university or institute. Moreover, I declare that this dissertation has been prepared subject to the Rules of Good Scientific Practice of the German Research Foundation.

Ali Tavassolizadeh
Christian-Albrechts-Universität zu Kiel

Date: ..... Signature: .....

Reviewers:

Prof. Dr.-Ing. Eckhard Quandt
Prof. Dr. Jeffrey McCord
Prof. Dr. Christine Selhuber-Unkel
Date for the oral exam: 29.01.2016

To My Lovely Family

Acronyms

AAF artificial antiferromagnet

AF antiferromagnetic

AFM atomic force microscopy

AM-AFM amplitude-modulated AFM

BE bottom electrode

BOA bond-orientation anisotropy

BOE buffered oxide etching

CMA cubic magnetic anisotropy

DNA deoxyribonucleic acid

DOS density of states

EB exchange bias

e-beam electron-beam

FD curve force-distance curve

FDTS $1H$, $1H$, $2H$, $2H$-perfluorodecyltrichlorosilane

FIB focused ion beam

FM ferromagnetic

FM-AFM frequency-modulated AFM

GMR giant magnetoresistance

HDD hard disk drives

IBE ion beam etching

ICP inductively coupled plasma

IEC interlayer exchange coupling

IPA isopropyl alcohol

IR infrared

LLG Landau-Lifshitz-Gilbert

LJ Lennard-Jones

MDD minimum detectable deflection

MDF minimum detectable force

MEMS microelectromechanical systems

MTJ magnetic tunnel junction

MR magnetoresistance

NC-AFM non-contact AFM

NM non-magnetic

NMP n-methyl-2-pyrrolidone

OOMMF object oriented micromagnetic framework

PCB printed-circuit board

PI proportion-integration

PMMA Poly(methyl methacrylate)

POA pair-ordering anisotropy

PSD power spectral density

PSV pseudo spin valve

RA resistance-area product

RIE reactive ion etching

RKKY Ruderman-Kittel-Kasuya-Yosida

RMS root mean square

RT room temperature

SAF synthetic antiferromagnet

SEM scanning electron microscopy

SIMS secondary ion mass spectrometry

SDSS sodium dihexyl sulfosuccinate

SDT spin-dependent tunneling

SPM scanning probe microscope

SW Stoner-Wohlfarth

TE top electrode

TMR tunnel magnetoresistance

UMA uniaxial magnetic anisotropy

vdW van der Waals

Abstract

Magnetostrictive tunnel magnetoresistance (TMR) sensors pose a bright perspective in micro- and nano-scale strain sensing technology due to their high strain sensitivity and compatibility with mass-production techniques. They can be exploited in the development of the self-sensing mechanism for atomic force microscopy (AFM) as they offer a simple and cost-effective detection system compared to the conventional optical read-out, especially in difficult environments such as in vacuum and in liquid. In contrast to other self-sensing techniques, TMR-based microcantilevers are advantageous to integrate the attributes of high bandwidth and miniaturization to achieve high resolution and high-speed AFM measurements. Such high-speed operation can have a revolutionary impact on high-speed imaging, nano-lithography, and nano-visualization of biological processes in various conditions.

The primary focus of this study is to understand TMR sensor responses to applied stress or strain in different magnetization configurations. Therefore, junctions based on the $Co_{40}Fe_{40}B_{20}/MgO/Co_{40}Fe_{40}B_{20}$ structure with nominal sizes of 100 µm^2, 289 µm^2, 729 µm^2, and 1369 µm^2 in squared, round, elliptical(1:3), and elliptical(1:10) shapes are investigated using a four-point bending apparatus. This range of junction sizes is chosen so that the junctions can be integrated to commercial AFM cantilevers. Mainly, changes caused by stress-induced anisotropy in $R(H)$ loops are studied to find out the optimum point for measuring tensile and compressive stress values. Having magnetization of the sense and reference layers of a TMR junction aligned at 45° toward the stress axis, the inverse impact by tensile and compressive stress on the tunnel resistance makes it possible to detect them both by a single sensor in presence of a bias field. This extends their applications to dynamic devices such as dynamic mode AFM. Measured strain loops $R(\varepsilon)$ at different bias fields reveal dependency of strain sensitivity, gauge factor, on the bias field. Below 0.2×10^{-3} strain, representative tensile and compressive strain loops for a round junction with a nominal diameter of 30.5 µm exhibit large gauge factors of $GF = 2150 \pm 30$ and $GF = 1750 \pm 35$ at -3.2 kA/m and +4 kA/m magnetic bias fields, respectively. However, no indication is visible regarding strain sensitivity dependence on the shapes and the sizes of the junctions fabricated in this study. Implemented shape anisotropy in the elliptical junctions is not suitable to replace the need of the bias field. Aiming for the same purpose, gauge factors of $GF \approx 400$ are measured by a round junction with 11.3 µm

nominal diameter at zero field. This can be beneficial for the development of a simple and compact detection system. Experimental results are supported by micromagnetic simulations using object oriented micromagnetic framework (OOMMF), developed by the *National Institute of Standards and Technology*, and energy minimization based on the Stoner-Wohlfarth (SW) model.

This work also includes a new technique providing a rough estimation of saturation magnetostriction of the sense layer in patterned TMR junctions. This allows to characterize the influence of the reference layer and the arrangement of MTJ layers after the fabrication process. Effective saturation magnetostriction of the sense layer is measured from a variation of stress-induced anisotropy fields, which are deduced from measured hard-axis $R(H)$ loops under compressive stress or strain, as a function of applied strain. The deviation originated from patterning effects and influenced magnetization of the reference layer is addressed by simulations using the SW model. Interestingly, the same range of effective saturation magnetostriction, nearly as in the literature, is measured for the $Co_{40}Fe_{40}B_{20}$ sense layer of different junction sizes.

The magnetostrictive TMR junctions with high strain sensitivity are successfully integrated to AFM microcantilevers in a complicated but well-established fabrication process. The deflection can be easily detected as resistance changes in a magnetostrictive TMR sensor. Self-sensing TMR cantilevers exhibit deflection sensitivity of about $3.9 \times 10^{-6}/\text{Å}$ which is better than piezoelectric and piezoresistive sensors. The deflection sensitivity depends on the bias field direction with respect to the reference layer magnetization. While modifying the field direction in a dynamic oscillation, the maximum strain sensitivity occurs for $H_{bias} = 60\,\text{Oe}$ at $\theta_{H_{bias}} = 105°$. These self-sensing cantilevers can be an alternative for replacing the conventional optical read-out as they are successfully used to record typical force-distance curves and AFM topography imaging in contact and dynamic modes. Growing tips with radius curvatures of $r_t = 15 - 30\,\text{nm}$ on AFM cantilevers, minimum detectable deflection as height and phase contrast are achieved by imaging atomic-step edges of Au(111) terraces and self-assembled monolayers of $1H$, $1H$, $2H$, $2H$- perfluorodecyltrichlorosilane (FDTS) in amplitude-modulated AFM and frequency-modulated AFM modes.

Contents

Chapter 1

Introduction

Strain sensing technology has evolved through demands in fields of characterization techniques, infrastructure and automobile health monitoring, utilizing piezoelectric[1] and piezoresistive[2] materials. Within the last decade ongoing research on strain sensing has pursued two different paths in terms of strain levels. In one aspect, they are focused on strain sensitivity only for large scales of deformations, aiming for high-strain sensing devices such as nanostructures embedded in stretchable polymer thin films[3–5]. Possible applications of these devices include future displays[6,7], robotics[8], and wearable strain sensors for human motion monitoring[9,10]. In other way, concerning nano- and microscale strain measurements studies are contributed to faster, more miniaturized, and more integrated devices. They are beneficial for applications that demand high strain sensitivity in small strain scales (below 0.2×10^{-3}) including force sensors, pressure sensors, and microcantilever technology[1,2].

Magnetostrictive TMR sensors with CoFeB/MgO/CoFeB junctions are a promising alternative to piezoresistive and piezoelectric strain sensors because of their high sensitivity and miniaturization possibilities. The magnetostrictive TMR sensors are basically magnetic tunnel junctions (MTJ)s with a magnetostrictive sense layer. The magnetization of the sense layer is free to rotate under mechanical stress or strain. Consequently, while the ferromagnetic reference layer is magnetically pinned, the magnetization configuration of the two layers alters upon the applied stress. The resulting change of the tunnel resistance, due to its angular dependence $R(\alpha)$ in MTJs[11], can be quantitatively related to the applied stress.

The aim of this research work is to fabricate and to characterize self-sensing AFM cantilevers based on the magnetostrictive TMR sensors, as depicted in Fig. 1.1, and to compare their performance with the conventional optical read-out. Integration of the TMR sensors into the AFM cantilevers brings simplifications in AFM measurements, particularly in difficult environments such as vacuum and liquid. For instance, it avoids delicate alignment of optical components in the optical read-out. In addition, the constraint on cantilever dimensions that applies for the optical read-out is avoided. This allows a variety of cantilever sizes and shapes. Accordingly, reducing the cantilever size allows a simultaneous increase in bandwidth and flexibility.

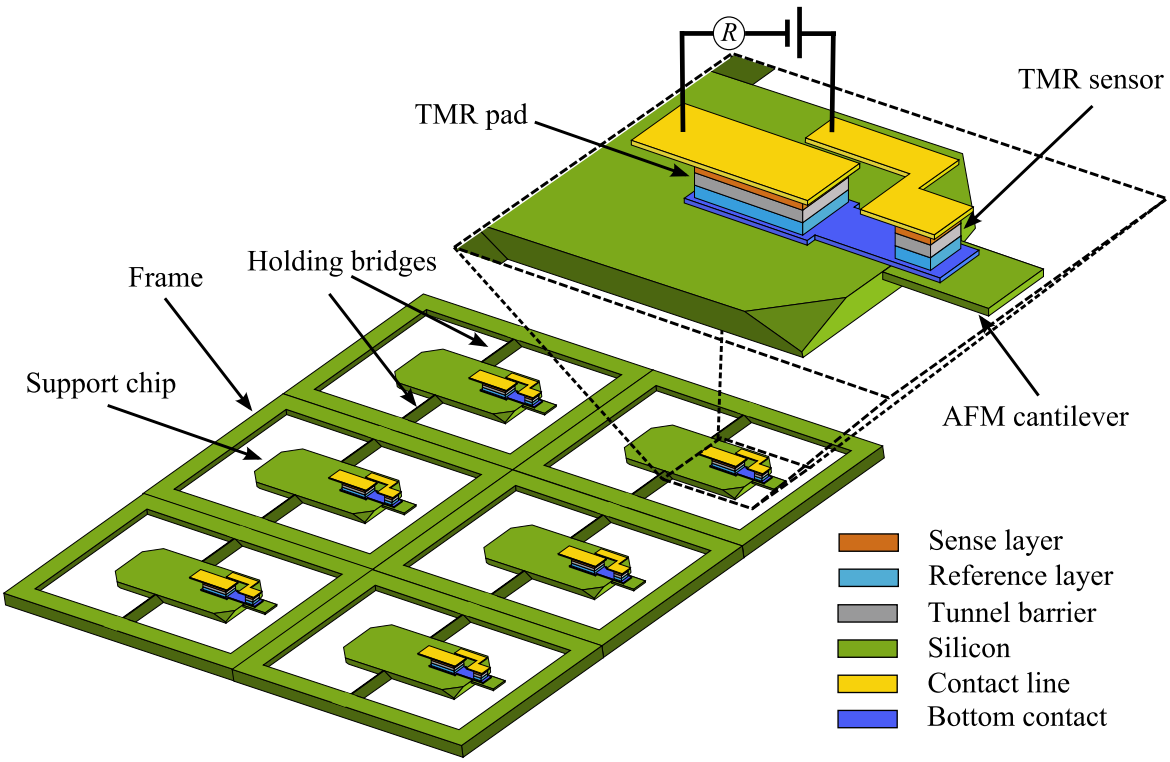

Figure 1.1: *Schematic of the self-sensing AFM cantilevers based on the magnetostrictive TMR sensors. Changes in the tunnel resistance are monitored to detect the beam deflection.*

As a primary focus, TMR sensors are studied to obtain sufficient insights regarding their strain sensing mechanism. TMR sensors with nominal sizes of 100 µm^2, 289 µm^2, 729 µm^2, and 1369 µm^2 in squared, round, elliptical(1:3), and elliptical(1:10) shapes are fabricated on 3 mm × 25 mm-sized Si cantilevers. Concerning the integration of these junctions into AFM cantilevers, this range of junction size matches standard dimensions of commercial AFM cantilevers. As described in chapter 6, the response of the TMR sensors to applied strain is investigated while monitoring changes in $R(H)$ loops using a four-point bending apparatus. Different configurations of physical quantities are considered. This leads to better understanding of magnetization reversal of the sense layer and allows to figure out optimum parameters required for high strain sensitivity. Strain loops $R(\varepsilon)$ measured for every junction at different bias fields under tensile and compressive stress provide values for the strain sensitivity, defined as the gauge factor measured under strain values up to 0.2×10^{-3}. This also allows to find out the strain sensitivity dependence on the bias field. Concerning the shapes of junctions, the round-shaped junctions are expected to demonstrate higher sensitivity because the absence of edges causes less restrictions, compared to the squared junctions, on coherent rotation of the magnetization of the sense layer. On the other hand, shape anisotropy imposed via the elliptical shapes is implemented to replace the need of the bias field required to keep the strain sensitivity at maximum level. In all strain sensors here, magnetization of the sense and reference layers is aligned at a $\pi/4$ angle toward the stress axis by field annealing. This allows detection of both tensile and

compressive stresses. In addition, theoretically, the strain effect on the TMR sensors is simulated by using the object oriented micromagnetic framework (OOMMF)[12] and the Stoner-Wohlfarth (SW) model. At the end of chapter 6, a technique is proposed to roughly estimate saturation magnetostriction of the sense layer in patterned MTJs. This method considers present structuring effects and possible interlayer couplings. Applications of the TMR sensors with high strain sensitivity in AFM measurements are represented in chapter 7. It is shown that the TMR strain sensors can be successfully integrated to AFM microcantilevers in a well-established fabrication process in single-chip and wafer scales. The TMR self-sensing microcantilevers are analyzed in terms of deflection sensitivity, minimum detectable deflection (MDD), and topography imaging in the contact mode and in the dynamic mode with amplitude-modulated AFM (AM-AFM) and frequency-modulated AFM (FM-AFM) feedback loops. In general, performance of the TMR self-sensing microcantilevers is compared with the conventional optical read-out.

1.1 State-of-the-art

Integration of self-sensing techniques into microcantilevers offers the possibility to eliminate the conventional optical read-out in atomic force microscopy (AFM)[13–15]. This avoids delicate alignment of a laser onto the backside of a cantilever and a photodiode, simplifying AFM measurements particularly in difficult environments such as vacuum and liquid conditions. The optical read-out is typically used in ambient environments for almost all AFM applications with high resolution[16]. However, self-sensing tuning forks with manually attached tips are preferred more for specific environments and at low temperatures[17–19]. Using integrated mass-fabricated sensors, different sizes and geometries of cantilevers can be created since there is no severe constraint on cantilever dimensions as for the optical read-out. This allows to improve the scanning speed limit in AFM via their high bandwidth of integrated sensors[20]. Possible applications of such feature include high-speed imaging, nano-visualization of processes, and lithography in biology and materials science[21,22]. Another approach for a fast operation with high throughput is to employ an array of multiple self-sensing cantilevers scanning simultaneously[23–30], as shown in Fig. 1.2. In comparison, the conventional optical read-out with a laser and an array of photodiodes[31,32] becomes too complex and expensive for parallel-probe high-throughput operations.

The piezoelectric[1] and piezoresistive[2] effects are commonly used as integrated methods in AFM measurements. In principle, the piezoelectric deflection sensing is based on charge formation upon application of stress in piezoelectric films, such as ZnO[14,33–35], $Pb(Zr,Ti)O_3$[36,37], and AlN[38], deposited on cantilevers. As a result, an electric voltage, which can be quantified to measure the cantilever deflection, is generated. Using the converse effect, piezoelectric films are also able to provide actuation in parallel to sensing operations[37], ideal for dynamic scanning. As the other important integrated method, the piezoresistive self-sensing approach was first proposed by Tortonese et al.[13] and was successfully employed in an AFM setup. The piezoresistive effect is defined as changes in electrical resistance as a function of applied mechanical stress

without generating any potential as for the piezoelectric effect. The effect in piezore-

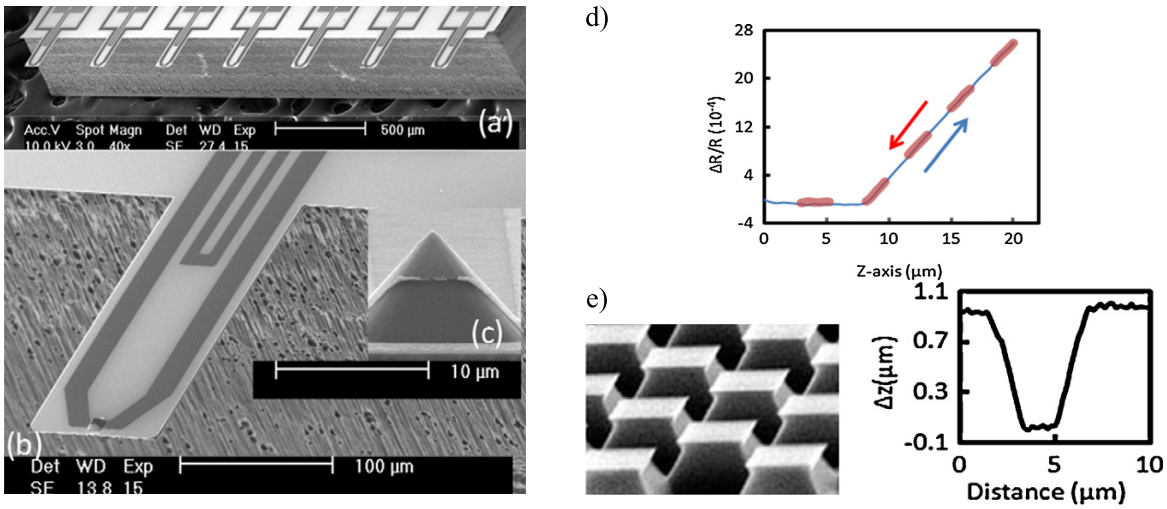

Figure 1.2: a) *Scanning electron microscopy (SEM) images of an array of probes with 5 - 10 nm ultrathin gold film sensors on silicon substrates for a high-throughput scanning probe microscope (SPM) with a scanning speed of 5 µm/s.* ***b)*** *Individual cantilevers include two resistors, one over the tip serving as a localized heater/thermal sensor and a second closer to the base serving as a resistor for the deflection sensing.* ***c)*** *SEM close-up of the tip.* ***d)*** *Force-distance curve (FD curve) of a probe exhibiting deflection sensitivity of 2×10^{-8} 1/Å, measured on a hard substrate such as glass.* ***e)*** *Left: SEM image of 10 µm pitch square grating with 1 µm height. Right: A 10 µm line scan. Reproduced with permission from Ref. 30 © 2012 Elsevier.*

sistive metals only depends on geometry changes, whereas in Si-based piezoresistive materials it is also related to their resistivity changes. Therefore, gauge factors up to 5 and 200 can be obtained by metallic- [39] and Si-based [2] piezoresistive strain gauges, respectively. In n-type Si, applying strain imposes shift into the lowest conduction band energies (valleys). Such shift leads to redistribution of the carriers between the valleys which have significantly different mobilities and effective masses of the carriers [2]. On the contrary, piezoresistive effects in p-type Si have not been fully understood because of the complex valence band structure. Nevertheless, p-type piezoresistors are usually preferred for cantilever technology because they possess higher piezoresistive coefficients than n-type piezoresistors [40]. While deflection sensitivity, as a relative change in electrical resistance divided by the cantilever deflection, is compared [30,41–46], the maximum deflection sensitivity of 2.4×10^{-7} 1/Å, reported so far, is achieved by doped Si cantilevers [41]. However, metallic films are advantageous in terms of the simplified fabrication and the capability of scaling down to smaller dimensions while maintaining the same sensitivity [45]. Piezoresistive and piezoelectric elements have been widely used in self-sensing based AFM for material characterization [47–49], imaging in fluid [50], and data storage applications [51,52]. However, their required material dimensions to realize high output signals restrict the optimal mechanical characteristics as well as the operational bandwidth. Moreover, their integration into a microcantilever can affect mechanical properties of the cantilever and impose undesired stress in the cantilever [53].

Additionally, their inherent noise limits the resolution for nano-scale imaging[53,54].

As an alternative to the piezoelectric and piezoresistive effects, the mechanism of magnetoresistance (MR) changes due to the inverse magnetostriction was introduced into AFM cantilevers by Mamin et al.[55–57]. Differently, Sahoo et al.[53] employed an MR sensor for topography measurements by monitoring changes in position of a micromagnet on an oscillating cantilever, as shown in Fig. 1.3. Such sensors are also used as magnetic probes for scanning magnetoresistance microscopy[58].

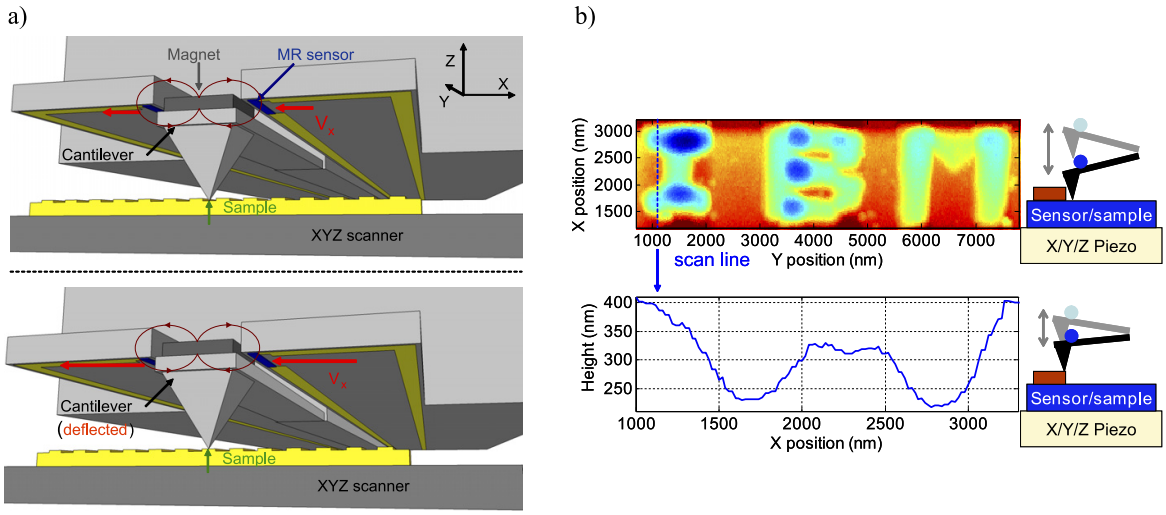

Figure 1.3: a) *Schematic of an SPM based on the MR sensors. Basically the cantilever displacement is translated into a relative motion between a micromagnet on the tip of the cantilever and the MR sensors.* ***b)*** *Top: constant-height, tapping-mode image obtained using the MR-SPM. Bottom: scan line across one amplitude profile. Reproduced with permission from Ref. 53 © 2011 Institute of Physics Publishing.*

Gauge factors in MR-based strain sensors have been significantly improved using giant magnetoresistance (GMR) and tunnel magnetoresistance (TMR) sensors with various multilayer structures. The earliest GMR strain sensors[55,59,60] showed a gauge factor on the order of 150 in spite of further improvement by replacing NiFe with a high magnetostrictive $Co_{50}Fe_{50}$ layer[61]. The significant enhancement in the gauge factor to the order of 300 to 600 has been achieved by TMR structures with crystalline $Co_{50}Fe_{50}$[62] and amorphous $(Fe_{90}Co_{10})_{78}Si_{12}B_{10}$[63] layers. Recently, employing CoFeB/MgO/CoFeB magnetic tunnel junctions (MTJ)s, which offer very large TMR effect amplitudes up to 600 %[64] as well as compatibility with mass-manufacturing techniques, resulted in a very large gauge factor up to 840[65]. Such high gauge factors can lead to improvement of the deflection sensitivity in the self-sensing cantilevers. In contrast to other integrated sensors, the TMR strain sensors offer higher gauge factors and more chance for miniaturization[66]. This allows reducing size of the cantilever and tuning its flexibility. In combination with their capability for high bandwidth operations[53], the TMR self-sensing microcantilevers have potential for higher resolution and faster measurements. Hence, they are considered as promising candidates for high-throughput AFM operations[67,68]. Note that these strain sensors require an external bias magnetic field during operation to set their strain sensitivity at maximum. This

is recognized as their technical drawback in terms of a simple and compact measuring setup. Therefore, it is necessary to study magnetization reversal of the sense layer in $R(H)$ loops with different configurations of magnetic systems in order to find out optimum conditions for high strain sensitivity at zero magnetic bias field.

Chapter 2

Basics

2.1 TMR Effect

According to quantum-mechanical physics, if a bias voltage is applied between two conducting electrodes separated by a thin insulating barrier ranging from few angstroms to few nanometers the electrons can tunnel through the barrier. The probability of tunneling through the barrier is given by the transmission coefficient (τ)[69]:

$$\tau = \exp\left\{-2\omega\sqrt{2m_e e\phi}\,/\hbar\right\}, \tag{2.1}$$

ω: Barrier width
ϕ: Barrier height
$\hbar$: Planck's constant
m_e: Effective mass of carrier
e: Elementary charge.

In magnetic tunnel junctions (MTJs), the two electrodes are ferromagnetic (FM) materials and the tunneling current or resistance depends on the relative magnetization configuration of these two electrodes. The tunnel resistance reaches the lowest R_p and the highest magnitude R_{ap} in parallel and antiparallel configurations, respectively. Such a jump in the tunnel resistance from the parallel to antiparallel orientation (Fig. 2.1) is the so-called TMR effect, that can be obtained by varying an external magnetic field. Having the two ferromagnetic layers with naturally different coercivity fields (hard/soft MTJs), the antiparallel configuration can be set at fields $H_1 < H < H_2$. Alternatively, one layer (the reference or pinned layer) can be magnetically stabilized by exchange biasing which shifts the hysteresis loop away from zero field (see section 2.3.1). The other layer is called sense layer.

In 1975 Jullière proposed a simple model[70], in which spin-dependent tunneling (SDT) is described as the origin for the TMR effect. The SDT effect, discovered earlier

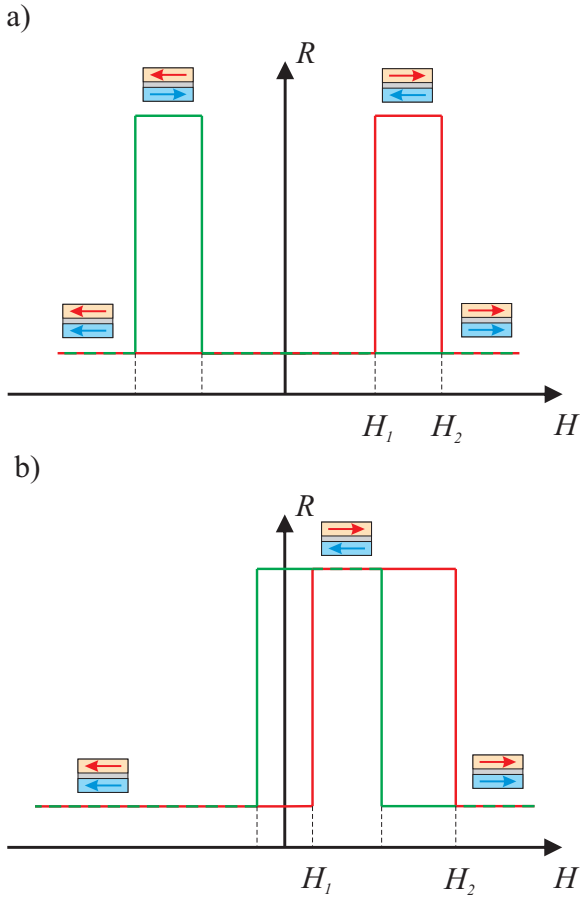

Figure 2.1: *Schematic of a typical TMR loop for MTJ structures with* ***a)*** *a magnetically hard and* ***b)*** *an exchange-biased reference layer. Small sketches of the MTJ element show the magnetization configuration with respect to the external field.* H_1 *and* H_2 *represent coercive fields of the soft (red arrow) or free and hard (blue arrow) or stabilized layers, respectively.*

by Meservey and Tedrow[71,72], is expressed by the imbalance between the tunneling current of the spin-up and -down electrons. This describes the fact that the tunneling probability of an electron through the barrier depends on its Fermi wave function[73]. The Fermi level is the highest occupied energy level, from which the electrons can tunnel through the barrier. In ferromagnetic materials the energy shift in the electronic bands at the Fermi level, due to Zeeman splitting caused by the internal magnetic field[74], implies different Fermi wave functions for the spin-up and -down electrons. In other word, the tunneling probability depends on the spin of the electrons[75].

There are two assumptions constituting the core of Jullière's model. First, the spin state of the electrons does not change during tunneling. It extends to that the tunneling current is carried by two independent spin-up and -down channels (two-current model) and the electrons originated from the first ferromagnetic layer are accepted by the unfilled states of the same spin orientation (see Fig. 2.2). Second, the tunneling conductance G for each spin is proportional to the product of the tunneling density of states (DOS) of the two ferromagnetic electrodes. Thereby, the tunneling

current for the parallel and antiparallel configurations depending on the number of the filled and unfilled states of the electrodes can be expressed as:

$$\begin{aligned} G_p &\propto \frac{1}{R_p} \propto D_1^{\uparrow}(E_F)D_2^{\uparrow}(E_F) + D_1^{\downarrow}(E_F)D_2^{\downarrow}(E_F) \\ G_{ap} &\propto \frac{1}{R_{ap}} \propto D_1^{\uparrow}(E_F)D_2^{\downarrow}(E_F) + D_1^{\downarrow}(E_F)D_2^{\uparrow}(E_F), \end{aligned} \tag{2.2}$$

where $D_{1,2}^{\uparrow}$ and $D_{1,2}^{\downarrow}$ are the DOS of the spin-up and -down electrons for the ferromagnetic electrodes 1 and 2 at the Fermi energy E_F. Accordingly, the TMR effect is quantified in terms of the spin polarization of the two ferromagnets P_1 and P_2:

$$TMR \equiv \frac{G_p - G_{ap}}{G_{ap}} = \frac{R_{ap} - R_p}{R_p} = \frac{2P_1P_2}{1 - P_1P_2}. \tag{2.3}$$

Here, the spin polarization of the ferromagnetic electrodes is considered to be equal to the spin polarization of the DOS at the Fermi level[76]:

$$P_{1,2} = \frac{D_{1,2}^{\uparrow}(E_F) - D_{1,2}^{\downarrow}(E_F)}{D_{1,2}^{\uparrow}(E_F) + D_{1,2}^{\downarrow}(E_F)}. \tag{2.4}$$

Note that there are different definitions for the TMR effect given in the literature[77]. Figure 2.2 shows a simplified DOS of an MTJ when the magnetization directions of the two ferromagnetic metals are parallel and antiparallel to each other. The DOS of each electron spin in the ferromagnetic electrode is shifted against the other because of the exchange splitting caused by the internal magnetic field.

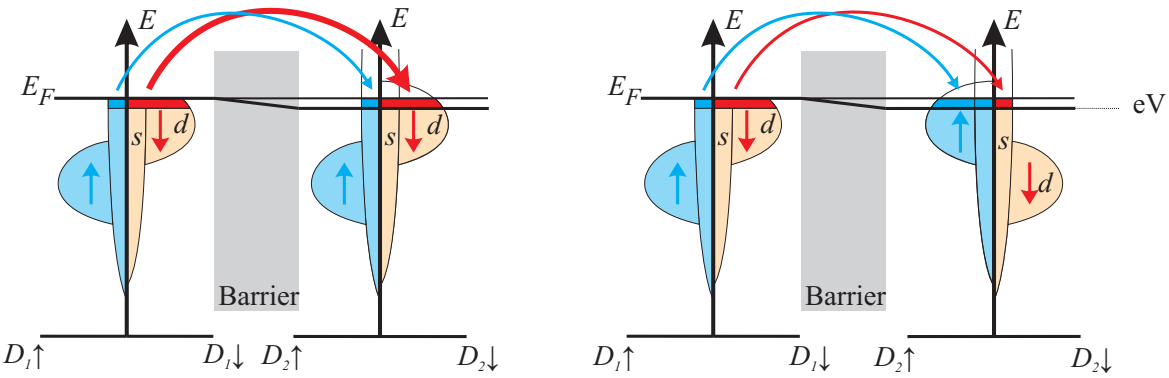

Figure 2.2: *Schematic illustration of DOS of the two ferromagnetic layers in the parallel (left) and antiparallel (right) configurations with a bias voltage V_{bias} applied across the junction. The spin splitting causes an unequal number of states for spin-up and spin-down electrons at E_F and as a result different contribution (curved arrows) to the tunneling current. Up and down expressions actually refer to magnetic moments of the electrons and not their spins. In the spin-up channel, a large number of filled states in the first electrode and unoccupied states in the second electrode at E_F lead to a large current, low resistance, in the parallel configuration. Reproduced with permission from Ref. 78, © 2003 WILEY-VCH.*

Simply considering that the tunneling conductance depends only on the DOS at the Fermi level led to inconsistency between the measured and predicted values of the spin polarization. For 3d ferromagnetic metals, at least Co and Ni, the spin polarization occurs to be negative since they hold a dominant contribution of the spin-down electrons at the Fermi energy. This disagrees with the positive spin polarization, which are experimentally measured, showing efficient tunneling of the spin-up channel[75]. Later, Stearns[79] resolved this inconsistency and demonstrated that the tunneling probability is associated with the effective mass for different bands assuming that the most dispersive bands provide almost all the tunneling current. According to his arguments, the localized d electrons with a large effective mass decay rapidly, whereas the dispersive s-like electrons decay slowly[75]. Following the early improvements, Slonczewski[80] implemented an additional factor related to the barrier in his more accurate theoretical interpretation of the TMR effect. He pointed out that the spin polarization of the tunneling current is not an intrinsic property of the two ferromagnets, and it depends on the structural and electronic characteristics of the electrodes, the tunnel barrier, and the electrode/barrier interfaces. Therefore, the effective spin polarization, based on Fermi wave vector of dispersive bands k and constant decay of wave function, determined as a function of the potential barrier U by $\kappa = \sqrt{(2m_e/\hbar^2)(U - E_F)}$, is given as[80]:

$$P = \frac{k^{\uparrow} - k^{\downarrow}}{k^{\uparrow} + k^{\downarrow}} \frac{\kappa^2 - k^{\uparrow}k^{\downarrow}}{\kappa^2 + k^{\uparrow}k^{\downarrow}}, \tag{2.5}$$

Using crystalline MgO layers, the theoretical calculations predicted huge TMR effect amplitudes of up to 1000 % for Fe(001)/MgO(001)/Fe(001) junctions[81,82]. Such high values are attributed to the variable tunneling probabilities of the Bloch states with different orbital symmetries. According to Bloch's theorem Bloch states or Bloch waves are the solution for Schrödinger equation, which defines the energy eigenstates of an electron in a crystal[83]. Considering the nature of the states present in both electrodes and the barrier, Butler described in a physical model[81] that the symmetry of both the propagating states in the electrodes and the evanescent states in the barrier material are extremely important to determining the tunneling conductance. As shown in Fig. 2.3, in Fe(001) the majority channel has three states with Δ_1, Δ_5, and $\Delta_{2'}$ symmetries, whereas in the minority channel the majority Δ_1 symmetry is replaced by the minority Δ_2 symmetry. Among the present tunneling states, the Δ_1 states have the slowest decay due to the effective coupling at either interfaces to the evanescent states with the Δ_1 symmetry in MgO. This is regarded as coherent tunneling. Additionally, the Δ_1 (spd hybridized states) band is fully spin-polarized at the Fermi level, whereas the other states reduce the net spin polarization[76]. Thus, having thicker tunnel barriers, the Δ_1 tunneling current dominant in the parallel configuration leads to the high spin polarization of the tunneling current. On the other hand, the Δ_1 decay faces total reflection in the antiparallel configuration since there is no Δ_1 propagating states in the minority channel on the right Fe electrode (Fig. 2.3 b)). Therefore, a high TMR amplitude is expected from epitaxial MTJs with a crystalline MgO(001) barrier.

2.2 Magnetic Tunnel Junctions

By fabricating magnetic tunnel junctions (MTJs) with smooth and pinhole-free Al_2O_3 layers, Moodera and Miyazaki obtained TMR effect amplitudes as high as 18 % at room temperature (RT)[84] that triggered the great interest in this field. Extensive studies on discovering electrodes with higher spin polarization and improving the quality of the barrier gave a steady rise to the TMR effect amplitude over the following decade. Currently, the largest TMR effect amplitude of 70 % for MTJs with an amorphous layer is obtained by Wang et al.[85] using $CoFeB/Al_2O_3/CoFeB$ junctions. Following theoretical predictions on epitaxially grown magnetic tunnel junc-

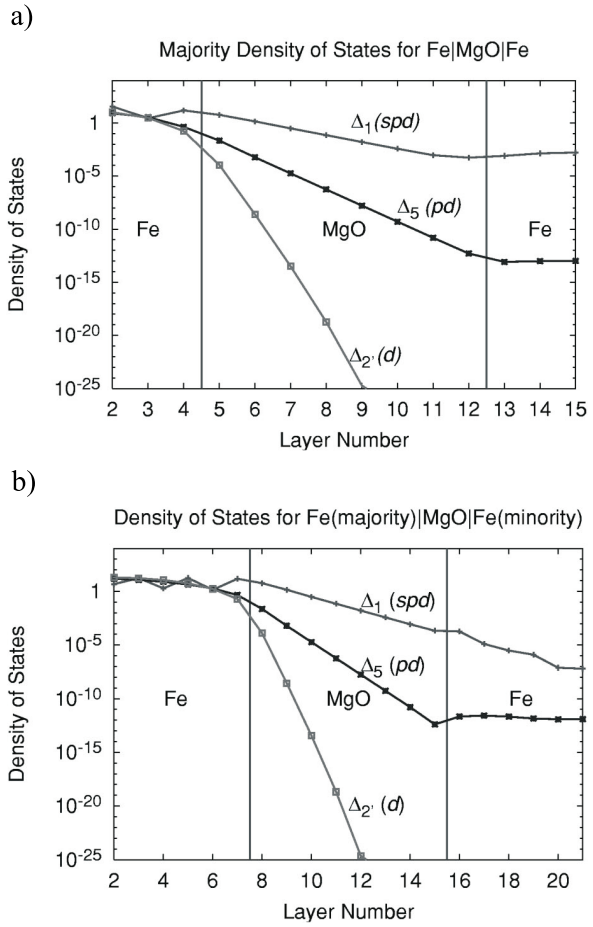

Figure 2.3: *Tunneling DOS of all symmetries for $k_{||} = 0$.* ***a)*** *In the parallel configuration the Δ_1 symmetry has the slowest decay rate, contributing the most to the tunneling current.* ***b)*** *Missing states with the Δ_1 symmetry in the second electrode in the antiparallel configuration lead to their exponential decay in the second electrode. Reproduced with permission from Ref. 81, © 2001 American Physical Society.*

tion (MTJ)s with crystalline MgO barriers[81] the second breakthrough occurred in 2004. Parkin et al.[86] and Yuasa et al.[87] fabricated, in two independent investigations, highly (001)-oriented Fe/MgO/Fe junctions and CoFe/MgO/CoFe junctions but using a molecular beam epitaxy technique and a conventional sputtering deposition technique. They obtained TMR effect amplitudes more than 180 % and 220 % at RT.

Motivated by these two works, even higher TMR effect amplitudes above 604 % has been achieved at RT for single-barrier MTJs of pseudo spin valves (PSVs) consisting of an MgO barrier and CoFeB electrodes[64].

For practical applications, Fe/MgO/Fe MTJs require additional pinning layers (see section 2.6) bringing difficulties to preserve the essential epitaxial growth. This problem was solved by developing CoFeB/MgO/CoFeB MTJs using sputtering deposition[88]. The two as-deposited CoFeB layers have an amorphous structure. The MgO barrier layer grown on the amorphous CoFeB can readily obtain a (001)-oriented texture. Post-deposition annealing at temperatures around 360 °C induces the epitaxial crystallization of the two electrodes as well as smooth interfaces, hence the CoFeB/MgO/CoFeB MTJs exhibit very large TMR effect amplitudes. Due to the amorphous nature of the deposited CoFeB layers, the CoFeB/MgO/CoFeB MTJs can be grown on any underlayer. It should be noted that the CoFeB layer adjacent to an MgO interface has a bcc(001) structure, indicating that the MgO barrier acts as a template[89]. Because at the CoFeB/MgO interface the crystallization temperature is reduced due to a drop of the B content, which clearly promotes the crystallization[90]. Despite several reported investigations by different techniques[90–100], there is still a clear disagreement on the tendency of the diffused B after annealing. Annealing at high temperature leads to complete crystallization of the CoFeB layers, improvement of the MgO barrier, and sharper interfaces[64,101–104], however at temperature above 450 °C the TMR effect amplitude starts to drop (Fig. 2.4 a)) probably due to Mn[102,105], Ru[102], and Ta diffusion[64]. Moreover, as given in Fig. 2.4 b) and c) the TMR effect amplitude critically depends on the thickness and composition of the electrodes[64,106–109] which influence the crystallization process by affecting the B diffusion and altering the interface energy at the CoFeB/MgO interfaces[110], respectively. That could finally cause partial crystallization and differences in the lattice mismatch.

2.2.1 Angular Dependence of TMR

MTJs are generally discussed by an abrupt resistance change between the two extreme magnetization configurations, so-called collinear configurations, i.e. when the two electrodes align either parallel or antiparallel. Nevertheless, few number of studies have given attention to investigate the possible non-collinear configurations in terms of the tunnel resistance or the tunnel conductance. Such configurations can be realized by an externally applied field, stress-induced anisotropy, and shape anisotropy, when one of the two layers adjacent to the barrier is softer. Each non-collinear configuration corresponds to different angles between the magnetization of the two electrodes, resulting in different tunnel resistance (see Fig. 2.5). In fact, knowing angular dependence of the tunnel resistance would be beneficial for applications operating in their non-collinear configurations or based on a coherent change in relative orientation of the two electrodes. It also allows to tune the outcome signal sensitivity, linearity, and reversibility[11]. Slonczewski[80] reported the first relation for low transmission range of the TMR effect, wherein he concluded linear dependence of the conductance on the

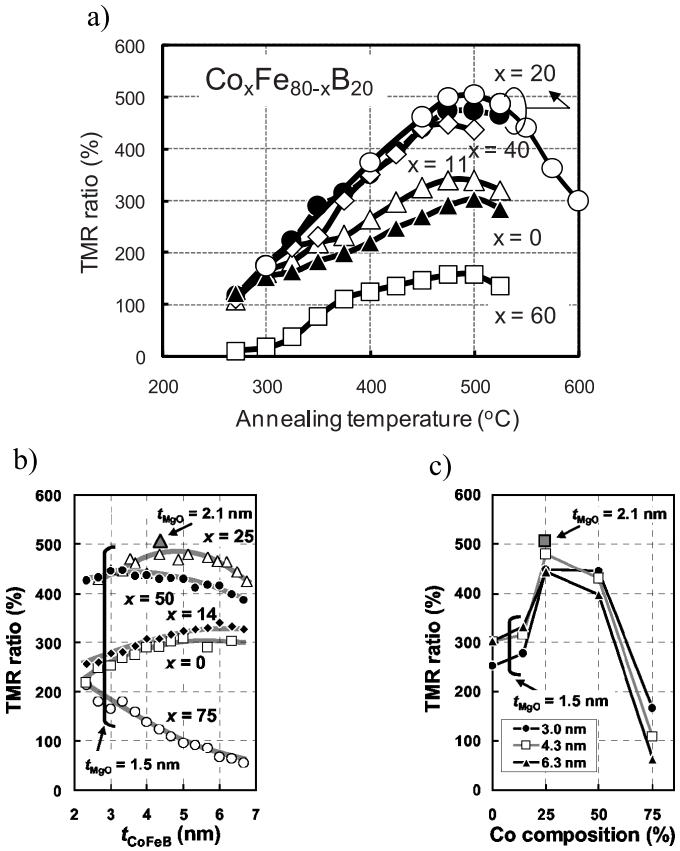

Figure 2.4: *TMR effect amplitude as a function of* ***a)*** *annealing temperature for pseudo spin valve (PSV) MTJs, having $Co_xFe_{80-x}B_{20}$ electrodes with $x = 0\,\%$ - $60\,\%$ and t_{CoFeB} =4.3 nm. The MgO thickness is 1.5 nm except for the open circles with t_{MgO} =2.1 nm,* ***b)*** *the thickness of the CoFeB electrodes for various Co compositions, and* ***c)*** *Co compositions for various CoFeB thicknesses. All MTJs have a 1.5 nm MgO barrier except for that plotted by a gray triangle in panel b) and a gray rectangle in panel c) which has a 2.1 nm MgO barrier. Panel* ***a)*** *reproduced with permission from Ref. 64 © 2008 American Institute of Physics Publishing . Panel* ***b)*** *and* ***c)*** *reproduced with permission from Ref. 106 © 2007 American Institute of Physics Publishing.*

cosine of the angle α between the magnetization of the two electrodes[80]:

$$G = G_{\perp}(1 + P_1 P_2\, cos(\alpha)). \tag{2.6}$$

Here, $G_{\perp}$ denotes the conductance in the perpendicular configuration. This expression is experimentally verified by Jaffrès et al.[11] for $Co/Al_2O_3/Co$ junctions resulting in a more complex form of the resistance expressed as[11]:

$$R(\alpha) = \frac{R_{\perp}}{1 + \frac{TMR_{Jaffres}}{2} cos(\alpha)}, \tag{2.7}$$

where amplitude of magnetoresistance is defined as:

$$TMR_{Jaffres} \equiv 2\frac{G_p - G_{ap}}{G_p + G_{ap}} = 2\frac{R_{ap} - R_p}{R_p + R_{ap}} = 2P_1P_2. \tag{2.8}$$

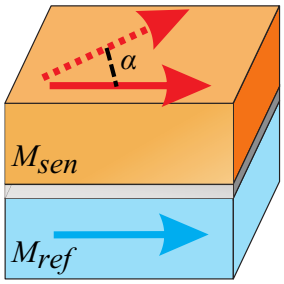

Figure 2.5: *Non-collinear configurations in an MTJ which is defined by the angle $\alpha = \theta_{sen} - \theta_{ref}$ between the magnetization of the sense (M_{sen}) and the reference layer (M_{ref}).*

This is different from generally referred angular dependence of the resistance, considering its linear relation to $cos(\alpha)$ found for $CoFe/Al_2O_3/Co$ junctions[84]. A more general formalism is proposed by Montaigne et al.[111] without any approximation, being valid for all transmission regimes.

2.3 Magnetic Coupling in MTJs

From a device perspective a simple MTJ structure with two FM layers separated by an insulator layer is not suitable for applications. But it can be tuned to create optimum operational conditions by adding several films into the layer structures. Here, we discuss three important concepts which can influence properties of MTJs according to requirements by typical applications.

2.3.1 Exchange Bias

A unidirectional type of magnetic anisotropy was observed by Meiklejohn and Bean[112] in 1956 in Co particles coated by its native oxide CoO which was then reproduced in thin film devices[113]. The origin of this phenomenon is the interfacial interaction between a FM layer and an antiferromagnetic (AF) layer spin systems. It causes a loop shift in the hysteresis loop of the FM layer in the field axis, the so-called the exchange bias, by the exchange bias field H_{EB}. Larger coercivity fields and a rather wide hysteresis loop come also along with such unidirectional anisotropy. As aforementioned before (see Fig. 2.1 b)), a well-defined switching of the magnetization configuration in an MTJ at low magnetic fields can be obtained by exchange biasing one of the FM layers, whereas the magnetization of the other FM layer is left free to rotate.

Figure 2.6 shows the mechanism of which the exchange bias is induced by a field annealing process. Annealing the FM/AF interface at a temperature T above the Néel temperature T_N of the AF layer and below the Curie temperature T_C of the FM layer ($T_N < T < T_C$) with a high positive magnetic field present, the moments in the FM

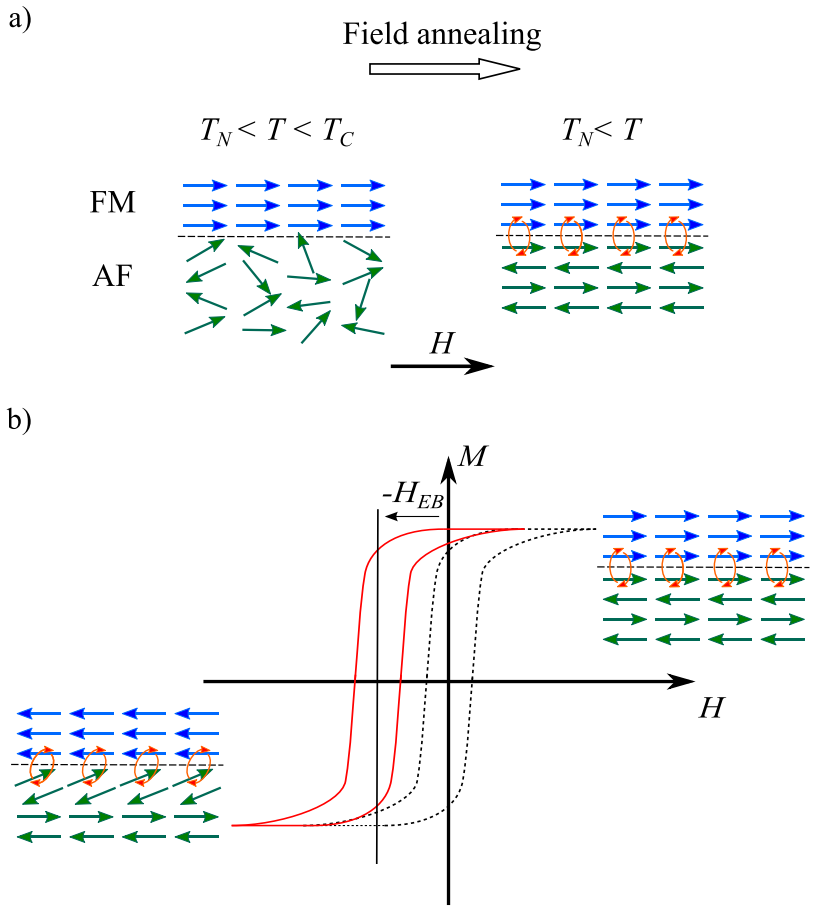

Figure 2.6: a) *Schematic of the field annealing process leading to the exchange bias effect H_{EB} at the FM (blue arrows)/AF(green arrows) interface. The orange arrows represent the exchange couplings between the neighboring moments.* ***b)*** *The exchange bias appears as a loop shift in the hysteresis loop of the FM layer. The reversed alignment to the original orientation is resisted by the AF moments at the interface.*

layer are aligned with the external field, whereas there is no magnetic order in the AF layer. Cooling down the temperature to T_N in the presence of the magnetic field, in a phenomenological model the neighboring moments of the AF layer at the interface align parallel to their neighbors in the FM layer due to the exchange interactions. The moments direction in the sublattices alternates from one sublattice to the next. At zero magnetic field, the magnetization of the FM layer is parallel to the direction of the annealing field. When a field applied in the opposite direction, the moments in the AF layer remain unchanged because of its high magnetocrystalline anisotropy below its blocking temperature. Therefore, the neighboring AF moments tend to pin the adjacent FM ones, resulting in the magnetization reversal of the FM layer at larger coercive fields. The magnetic moments in the AF layer do not adopt their original orientations and enhance the restoration of the direction of the annealing field once the field is applied to its original direction. As a result the switching occurs at a smaller field. This indicates that the FM moments have only one single stable configuration, i.e. the exchange bias constitutes a unidirectional anisotropy.

Considering a loop shift -H_{EB} as the interaction strength on the FM layer with M_s being the magnetization saturation, an energy density E_{EB} term can be defined as[114,115]:

$$E_{EB} = -\mu_0 H_{EB} M_s \cos(\beta). \tag{2.9}$$

β is the angle between the magnetization of the FM layer and the direction of the annealing field.

Apart from the ideal uncompensated surface of the AF layer, i.e. all surface moments point in the same direction, one should also include roughness and grain size effects as well as non-collinear spin configurations because any deviation from the ideal situation leads to conflicting interactions[78]. In MTJs applications, MnIr or PtMn is usually used as the AF layer. A promising antiferromagnet should result in a (111)-oriented fcc structure in an artificial antiferromagnet (AAF) (see Fig. 2.13). This supports the formation of an MgO(001) barrier with a 4-fold in-plane crystallographic symmetry on CoFeB layers, which is required for high TMR effect amplitudes[76]. Exchange bias by an MnIr layer, used in this study, depends on its crystal orientation and film thickness. For instance H_{EB} can reach to more than 80 Oe for a (111)-oriented MnIr film of 10 nm thickness[116].

2.3.2 Interlayer Exchange Coupling

Interlayer exchange coupling (IEC) between two FM layers across a non-magnetic (NM) spacer was first observed in a Fe/Cr/Fe(001) multilayer structure by Grünberg et al.[117] in 1986. The interest in the IEC was triggered after discoveries of its oscillatory behavior for various structures[118] and for GMR sensors[119,120]. The coupling between the two layers oscillates between FM and AF alignments with a variation in the thickness of the spacer layer. As shown in Fig. 2.7 for $Ni_{80}Co_{20}$/Ru/$Ni_{80}Co_{20}$ multilayers, with increasing the spacing the strength of the coupling reduces so that the energy difference between the FM and the AF alignments of the layers becomes smaller. Parkin et al.[121] described the oscillating behavior based on Ruderman-Kittel-Kasuya-Yosida (RKKY) interaction between magnetic impurities in a non-magnetic host. One interface or impurity sets an oscillatory polarization in the non-magnetic spacer due to a sharp cut-off from completely filled to completely unfilled states at the Fermi energy leaving an oscillatory spin density. Then, the second interface is coupled to the first as a function of the thickness of the spacing[122]. In addition, the band structure in the spacer layer, which is correlated to its crystallinity, is detrimental to the coupling strength. For instance, in CoFe/Ru/CoFeB trilayers replacing the crystalline CoFe layer as the bottom layer with an amorphous CoFeB layer leads to a weak exchange coupling owing to disordered orientation of the grains in the Ru spacer layer[123].

In MTJs, the AF coupled CoFe/Ru/CoFeB trilayers (synthetic antiferromagnet (SAF)[85]) are usually used to pin the reference layer (CoFeB) indirectly to a natural AF layer. Such trilayers are also called the artificial antiferromagnet (AAF)[124].

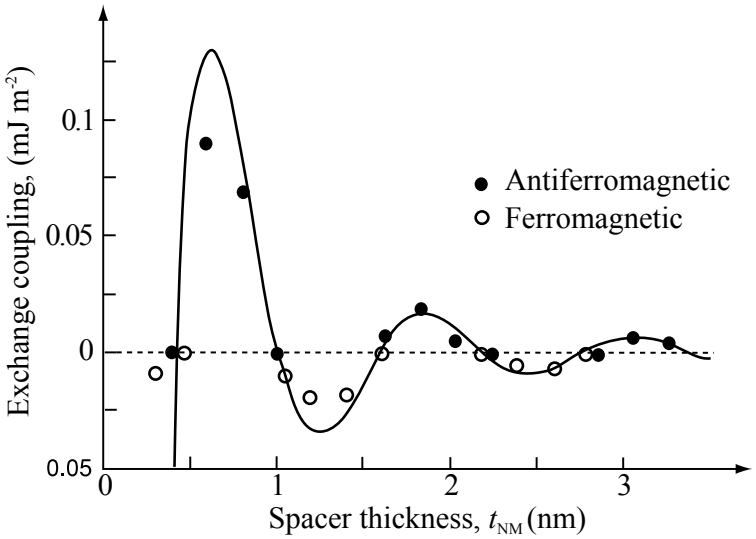

Figure 2.7: *Oscillating exchange coupling in $Ni_{80}Co_{20}/Ru/Ni_{80}Co_{20}$ trilayers. According to the thickness of the Ru layer, the alignment can be parallel (FM) or antiparallel (AF). The exchange coupling strength reduces for thicker Ru layers. The solid line corresponds to a fit to the data of an RKKY form. Reproduced with permission from Ref. 121 © 1991 American Physical Society.*

2.3.3 Néel Coupling

Néel in 1962 pointed out a type of coupling between two FM layers spaced by a NM layer[125]. The magnetization reversal of the sense electrode in an MTJ can be strongly affected by such coupling. In the so-called Néel coupling correlated dipoles are formed at either side of the NM layer due to the interface roughness and the discontinuities, i.e. mountains and valleys of waviness at the interfaces, as shown in Fig. 2.8. This is also known as the orange-peel coupling. The dipoles form in one side of the NM layer opposite to the other canceling each other out. This arrangement encourages a parallel alignment in an MTJ. The original Néel model, assuming infinite thickness of the FM

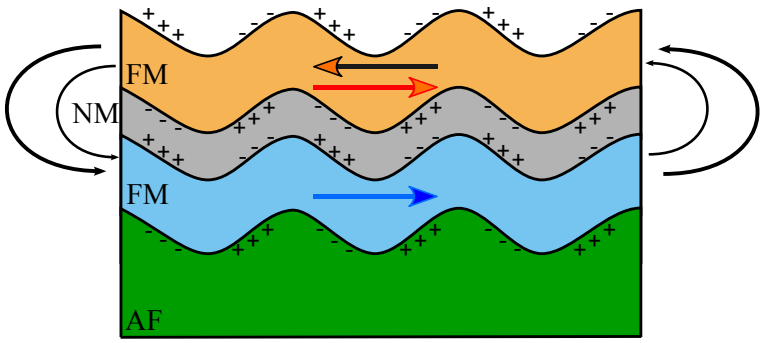

Figure 2.8: *The Néel coupling effect between the reference layer, which is pinned by an antiferromagnetic (AF) layer (green), and the sense layer (orange) encourages the parallel magnetization configuration. It competes stray field couplings (curved arrows at the sides) which favor the antiparallel configuration. The poles formed due to the interface roughness are shown by + and − sign.*

layers, has been extended to thin films by Kools et al.[126]. He considered magnetic poles created at the outer surfaces of the magnetic layers result in an antiferromagnetic interaction. For MTJs, which have a FM/NM/FM system, with a correlated waviness with an amplitude h_{NC} and a wavelength λ_{NC}, the Néel coupling energy density is given by[126]

$$E_{NC} = \frac{\mu_0 \pi^2 h_{NC}^2}{\sqrt{2}\lambda_{NC} t_{sen}} M_{sen} M_{ref} \cdot exp\left(-\frac{2\pi\sqrt{2}t_{NM}}{\lambda_{NC}}\right) \cdot \left[1 - exp\left(-\frac{2\pi\sqrt{2}t_{sen}}{\lambda_{NC}}\right)\right] \cdot \left[1 - exp\left(-\frac{2\pi\sqrt{2}t_{ref}}{\lambda_{NC}}\right)\right]. \tag{2.10}$$

Here, M_{sen}, M_{ref} stand for the saturation magnetization of the the sense and reference layers. t_{sen}, t_{ref}, and t_{NM} denote thickness of the sense layer, the reference layer, and the NM layer, respectively. The Néel coupling leads to a unidirectional anisotropy K_{NC} pointing at the angle θ_{NC} (see Fig. 2.16). The loop shift in the magnetization reversal of the sense layer H_{NC} can be calculated by

$$H_{NC} = \frac{-E_{NC}}{\mu_0 M_{sen} \cos(\theta_{NC} - \theta_{sen})}. \tag{2.11}$$

In MTJs, K_{NC} is parallel to the magnetization of the reference layer ($\theta_{NC} = \theta_{ref}$); therefore, one can re-write $\alpha = \theta_{NC} - \theta_{sen}$. The Néel coupling counteracts the stray field coupling, which favors the antiparallel magnetization orientation, across the sides of patterned junctions. In an MTJ device, the results appear as a field shift H_{sh} in minor TMR loops stabilizing either the parallel or the antiparallel configuration (see Eq. 2.22). Furthermore, it influences the magnetic configurations in the magnetization reversal.

2.4 Magnetostriction

Magnetostriction can be described as dimensional changes of a substance in response to a change of its magnetization. In 1842, this effect was discovered by Joule[127], who showed an anisotropic change in length of Fe and Ni specimens exposed to an external field. It is called Joule or anisotropic magnetostriction. Figure 2.9 shows the effect in terms of four domains starting from a demagnetized state. Upon application of an external magnetic field, the [100] domain expands as the other domains contract by the mechanism of domain wall motion. Consequently, the length of the specimen changes from L to $L + \Delta L$ where $\lambda_s = \Delta L/L$ defines the saturation magnetostriction in the [100] direction. Domain walls are categorized as 180° or non-180° walls according to their angles against the saturation magnetization. Since the magnetization reversal of domains with a 180° wall occurs through a specific region, domain wall motion does not contribute to any dimensional changes.

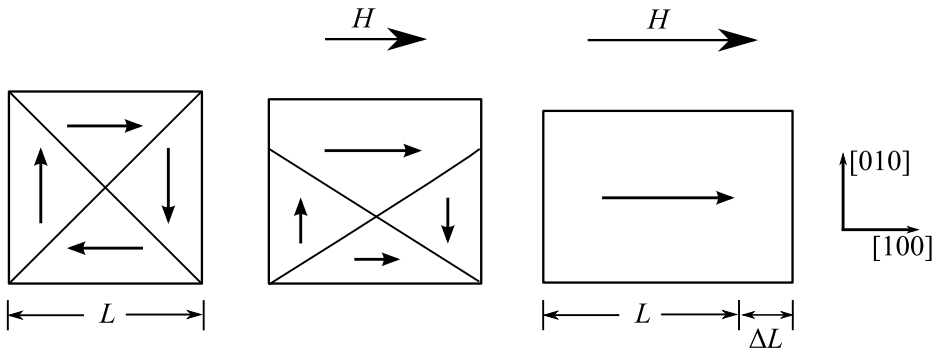

Figure 2.9: *Magnetostriction along the [100] direction in presence of a magnetic field. The specimen with four domains is in a demagnetized state at zero field. The [100] domain grows with the mechanism of domain wall motion resulting in a dimensional change. Reproduced with permission from Ref. 128 © 2009 WILEY.*

Such dimensional changes depend on the magnetic field and the measurement direction. Figure 2.10 depicts field dependence of the anisotropic magnetostriction in an isotropic material. It is customary to measure the magnetostriction from a demagnetized state in which the domains are magnetized uniformly over all possible directions. Dimensional changes can be measured parallel ($\varepsilon_{\parallel}$) and perpendicular ($\varepsilon_{\perp}$) to the applied magnetic field. Saturation magnetostriction $\lambda_s = \Delta L/L$ represents changes of dimensions in the material which is magnetized from a demagnetized state to its saturation[129]. With $(\Delta L/L)_{\parallel} < 0$ and $(\Delta L/L)_{\parallel} > 0$, materials can be negatively and positively magnetostrictive, leading to a reduction and an extension in dimensions, respectively.

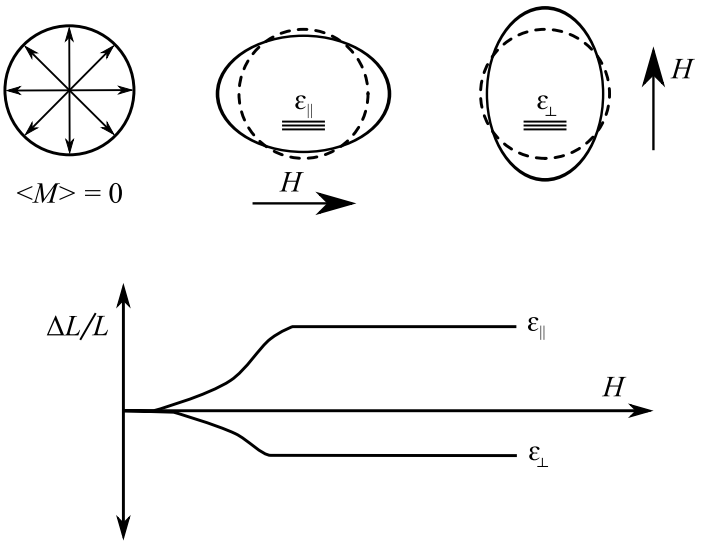

Figure 2.10: *Anisotropic magnetostriction as an external magnetic field is applied parallel and perpendicular to the measurement direction. The direction of the strain measurement is indicated by the three parallel lines. Reproduced with permission from Ref. 60 © 2000 WILEY.*

The calculation of λ_s in a crystalline structure depends on principal easy axes. For

example, for polycrystalline Fe with the cubic structure it can be measured by[69]

$$\lambda_s = \frac{2}{5}\lambda_{100} + \frac{3}{5}\lambda_{111}, \tag{2.12}$$

where two main values λ_{100} and λ_{111} are the saturation magnetostriction along [100] and [111] directions.

The inverse effect is also of great importance in use of these materials as stress or strain sensors. Applying stress to a material can impose changes in its magnetization direction. This phenomenon is called the inverse magnetostriction or the Villari effect[130]. For positive magnetostrictive materials, tensile (compressive) stress imposes a stress-induced anisotropy parallel (perpendicular) to the stress axis. If the easy axis is already along the induced anisotropy axis, applying stress only stabilizes further the axis by giving rise to its coercive fields.

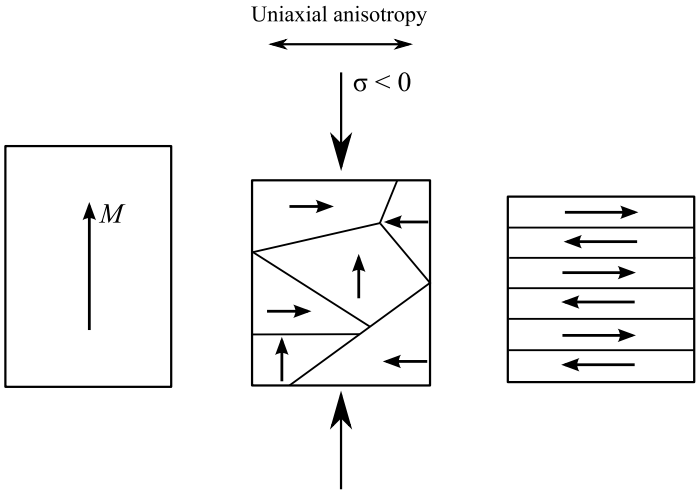

Figure 2.11: *Schematic of a positive magnetostrictive material under compressive stress. Increasing the stress results in formation of domains with their magnetization perpendicular to the stress axis. Domains tend to point into two possible directions due to the uniaxial character by the stress-induced anisotropy.*

Among the magnetostrictive materials, rare-earth-based thin films exhibit the largest magnetostriction, obtained by Tb-Dy-Fe films, up to 1000 ppm[131]. Recently, $Fe_{100-x}Ga_x$ alloys triggered new research interest owing to their high magnetostriction properties as well as their good mechanical properties[132]. Clark et al. reported $3/2\lambda_{100}$ up to 400 ppm by $Fe_{81.3}Ga_{18.7}$ films under very low fields[133]. Among existing highly magnetostrictive materials, CoFeB or CoFeB/CoFeBSi films are preferred as the sense layer for the magnetostrictive TMR sensors (see section 2.6) since they also offer high TMR effect amplitudes[65]. Among all compositions, the highest $\lambda_s = 120$ ppm was measured for as-deposited $Co_{43}Fe_{43}B_{14}$ films[134]. In fact, CoFe films should be taken into account instead for magnetostriction properties because after the field annealing process the amorphous CoFeB films crystallize into the CoFe films with a bcc structure due to the B diffusion (see section 2.2). Exploring the magnetostriction as a function of the composition shows that the magnetostriction reaches $\lambda_s = 75$ ppm in the vicinity of equiatomic compositions for as-deposited $Co_{50}Fe_{50}$ films[135,136]. The field annealing

process enhances the magnetostriction to 90 ppm at the same composition[136]. A more detailed study of the influence of a crystalline structure on the magnetostriction was performed by Hunter et al.[137]. They reported a maximum magnetostriction of 67 ± 5 ppm for $Co_{44}Fe_{56}$, whereas the other maximum value of 84 ± 5 ppm is for $Co_{73}Fe_{27}$. Slow cooling and quenching after annealing at 800 °C enhanced the maximum magnetostriction to 156 ± 7 ppm and 260 ± 10 ppm, respectively, for $Co_{66}Fe_{34}$. The influence of the annealing temperature on magnetostriction characteristics of CoFe films has been studied by Nakajima et al.[138]. However, annealing at very high temperatures above 450 °C is not applicable for CoFeB/MgO/CoFeB junctions (see section 2.2).

For small strain, the magnetoelastic energy density can be expressed as

$$E_\sigma = K_\sigma \sin^2(\psi) \tag{2.13}$$

in terms of uniaxial stress-induced anisotropy K_σ, which is scaling with the applied strain ε and given by $K_\sigma = \frac{3}{2}\lambda_s\sigma$ with $\sigma = Y\varepsilon$. In MTJs (see Fig. 2.16), angle ψ denotes the angle between the magnetization of the sense layer (θ_{sen}) and the stress-induced anisotropy axis (θ_σ). Using the same effect on the sense layer in MTJs one can detect small strain values in microcantilevers during AFM measurements.

2.4.1 Measurement of Saturation Magnetostriction Using Stress-induced Anisotropy Fields

Magnetostriction of ultra thin films are mostly studied as a multilayer which consists of a stack of the ultra thin film deposited repeatedly. Ali and Watts[135] described a simple technique to measure magnetostriction of the ultra thin films as a single layer deposited onto rigid substrates. The technique is based on applying stress and monitoring the stress-induced anisotropy field. The saturation magnetostriction can be calculated from a variation of the stress-induced anisotropy field as the applied stress varies using

$$\lambda_s = \frac{\mu_0 M_s}{3}\frac{\Delta H_k}{\Delta\varepsilon Y} \tag{2.14}$$

expression[128] with $\sigma = Y\varepsilon$.

2.5 CoFeB Thin Films

CoFeB thin films are used here as the sense and reference layers in MTJs multilayer structure. They are lately of great technological and fundamental importance because of their potential in rapidly developing spintronics applications. They are routinely used in multilayer structures as magnetic electrodes for TMR devices in sensor applications[139], magnetic random access memories[140], hard disk drives (HDD) read heads[141], current-induced magnetization switching[142]. The functionality of such devices requires soft magnetic properties with in-plane uniaxial magnetic anisotropy (UMA). There

have been extensive studies to understand anisotropy of CoFeB thin films with regard to film compositions, deposition parameters, and different underlayers. This allows to tune the coercivity and to tailor the present UMA depending on the envisaged applications.

The structural origin of their uniaxial anisotropy is described focusing on micro mechanism by two models; bond-orientation anisotropy (BOA)[143,144] and pair-ordering anisotropy (POA)[145]. The BOA mode postulates a medium- to long-range microstructural anisotropy as more near neighbors appear in the plane of the film compared to the perpendicular orientation[146,147]. On the contrary, POA considers the chemical ordering of near-neighbor atoms. It postulates that the source of the UMA is the difference in the number of like and unlike nearest neighbor distances of the atoms for the in-plane and out-of-plane directions, assuming a randomly oriented coordination polyhedral[145].

During film deposition in-plane UMA can be achieved provided that the azimuthal symmetry is broken, typically achieved by an in-plane applied magnetic field[148] or oblique geometry deposition[149]. Otherwise, one can expect that random local magnetic anisotropy occurs due to short-range ordering in amorphous ferromagnetic films. In absence of such symmetry breaking, interface interactions or internal film stress are debated as the origin for the UMA. In case of amorphous CoFeB thin films deposited on a GaAs (001) substrate, Hindmarch et al.[145] proposed interface interactions as the origin of symmetry breaking resulting in the bond-orientation at the interface. Then, this will propagate to the volume of the amorphous film. Unlike the GaAs film as a substrate, an MgO layer possesses a rather small spin-orbit interaction. Therefore, it is more likely that other causes, associated with interfacial structure between MgO and CoFeB films, account for the enhancement of the UMA in CoFeB layers[150]. Another possible origin can be long-range stress observed in a CoFeB layer deposited on a Si/SiO_2 substrate, giving rise to magnetic anisotropy via magnetoelastic coupling[151].

As-deposited CoFeB films grown on an MgO barrier can also be fabricated to exhibit the UMA in any arbitrary direction by field annealing. The crystallization of the as-deposited amorphous $Co_{80-x}Fe_xB_{20}$ layers starts at temperatures around 300 °C depending on their interfaces above and below, which leads to the overall increase in coercivity. It preferentially crystallizes at the interfaces depending on adjacent layers and is attributed to the out-diffusion of the B content. Note that different adjacent layers to the electrodes impose different crystallization mechanisms and crystalline structures in the CoFeB layers after annealing[89,92,101]. Lavrijsen et al.[152] reported such coercivity dependence in terms of the correlation between magnetic exchange length and grain size. This develops the opportunity to tailor the coercivity by annealing parameters, as shown in Fig. 2.12. Keeping the thickness below 20 nm and the annealing temperature less than 370 °C lead to formation of grains with sizes smaller than the exchange length. An averaging of the magnetic crystalline anisotropy allows easy domain wall motions or domain nucleation. This ensures soft magnetic properties suitable for a sharp switching magnetization process.

After the field annealing process of an amorphous CoFeB layer, a CoFe film with a bcc-like crystal structure exhibiting magnetocrystalline anisotropy with a cubic

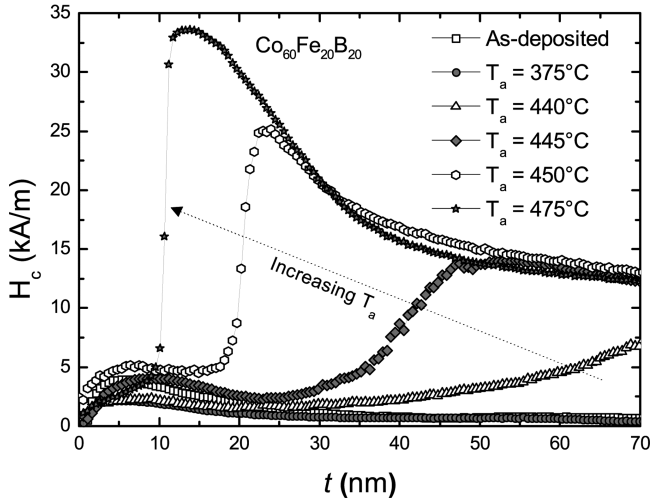

Figure 2.12: *Coercivity versus thickness of $Co_{60}Fe_{20}B_{20}$ layers for different annealing temperatures. Reproduced with permission from Ref. 152 © 2011 American Institute of Physics Publishing.*

symmetry is formed[89]. However, since in-plane magnetization is preferred by shape anisotropy, a fourfold in-plane cubic magnetic anisotropy (CMA) is expected. However, Kuschel et al.[153] found out that the resulting easy axes for $Co_{50}Fe_{50}$ do not have the same strength due to possibly present UMA, caused by the aforementioned origins. One CMA easy axis parallel to UMA (called more easy axis) is energetically favored with respect to the second CMA easy axis (called less easy axis).

2.6 Magnetostrictive TMR Junctions

Recently, employing CoFeB/MgO/CoFeB MTJs resulted in a very large gauge factor up to 840[65]. In comparison to GMR and AlO_x-based TMR sensors, high MR amplitudes by the $Co_{40}Fe_{40}B_{20}$/MgO/$Co_{40}Fe_{40}B_{20}$ structure (see section 2.2) and high magnetostrictive properties of the $Co_{40}Fe_{40}B_{20}$ layer (see section 2.4) as the sense layer are regarded as the origins for such a significant achievement in the strain sensitivity.

As shown in Fig. 2.13, the magnetostrictive TMR sensors are basically MTJs with a magnetostrictive sense layer (CoFeB), which is free to rotate under mechanical strain or stress. The ferromagnetic reference layer (CoFeB) is magnetically pinned to a natural AF (MnIr) in an artificial antiferromagnet (AAF) sandwich (AF (MnIr)/FM (CoFe)/NM(Ru)/FM (CoFeB))[154]. Exchange biasing (see section 2.3.1) provides a unidirectional anisotropy to the CoFe layer and the CoFe layer itself is antiferromagnetically coupled with the CoFeB layer via the IEC (see section 2.3.2) through the thin Ru layer.

Due to the inverse magnetostriction, the relative magnetization configuration of the sense and reference layers alters upon stress application. The resulting change of the tunnel resistance, owing to its angular dependence $R(\alpha)$ (see section 2.2.1) in MTJs[11],

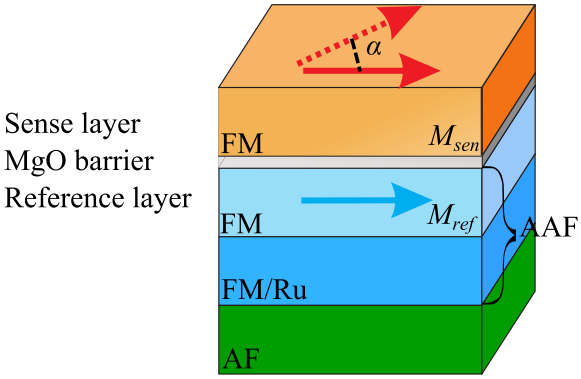

Figure 2.13: *Magnetostrictive TMR stack includes an MTJ with a reference layer pinned in an exchange-biased artificial antiferromagnet (AAF) (AF/FM/Ru/FM). Due to the inverse magnetostriction, the sense layer magnetization M_{sen} can rotate with respect to the magnetization of the reference layer M_{ref} upon stress application. The angle α is the angle between the two magnetization.*

can be quantitatively related to the applied stress (see Eq. 2.7).

Mostly, the initial magnetic anisotropy of the sense layer, i.e. the initial easy axis ($E.A.$) induced by field annealing, is aligned along or perpendicular to the axis of applied stress in order to monitor compressive or tensile stress, respectively (Fig. 2.14).

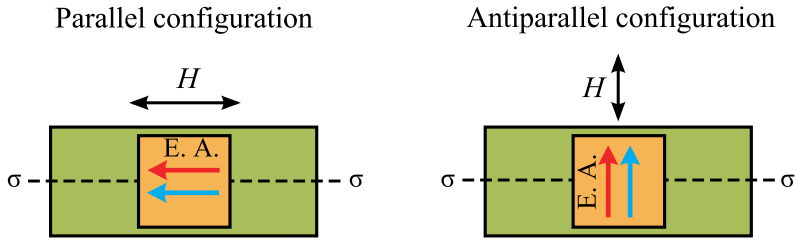

Figure 2.14: *Two different configurations where the easy axis E.A. (red arrow) induced by field annealing is parallel or perpendicular to the stress axis and an external magnetic field. The blue arrow represents the pinned magnetization of the reference layer M_{ref}.*

In the parallel configuration tensile stress gives additional anisotropy parallel to the stress axis resulting in an increase in coercive fields as well as in squareness in a minor TMR loop (see Fig. 2.15 a)). On the contrary, compressive stress imposes an additional easy axis (anisotropy) perpendicular to the stress axis, which encourages a gradual switching between the parallel and antiparallel configurations for larger stress values (Fig. 2.15 b)). In case of compressive stress, applying stress leads to a variation of resistance change ΔR, which strongly depends on the magnetic field. This suggests that one can get the maximum response to the applied stress by setting a magnetic bias field with maximum ΔR. In other words, the sensitivity of a magnetostrictive TMR sensor to applied stress reaches the highest possible level in presence of an optimum magnetic bias field. Opposite responses occur in the perpendicular configuration in terms of tensile and compressive stress. In all configurations the external field is applied parallel to the initial easy axis.

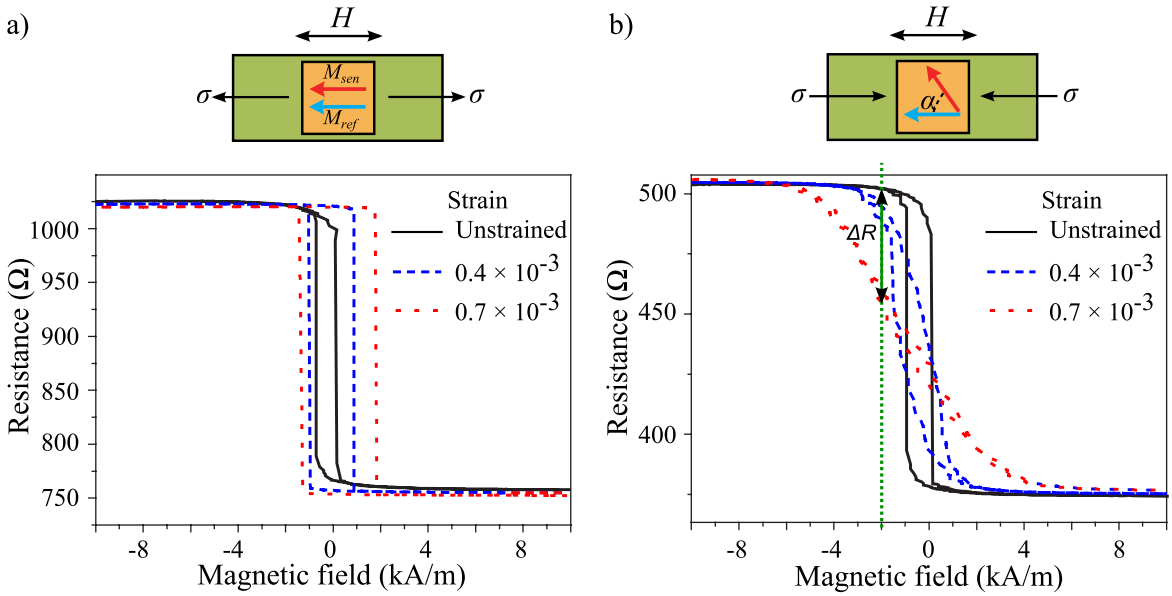

Figure 2.15: *TMR loop measurements of a junction under different stress (strain) amounts. In the parallel configuration,* ***a)*** *tensile stress stabilizes the TMR loop, which appears as larger switching fields by additional anisotropy along the initial E.A. (see Fig. 2.14) of the sense layer. On the contrary,* ***b)*** *compressive stress causes rotation of M_{sen} for small magnetic fields and the loop approaches a hard-axis switching behavior for larger stress values. This leads to field dependence of the resistance change ΔR within a loop of a strained junction. Reproduced with permission from Ref. 155 © 2004 Elsevier.*

2.7 Micromagnetism

In order to describe magnetic behavior of a ferromagnet, it is necessary to take into account local and non-local energy terms. The domain structure of ferromagnets is a result of minimizing total energy in consideration of microstructures, solving a formula based on the Landau-Lifshitz-Gilbert (LLG) equation. Considering single-domain behavior, the Stoner-Wohlfarth (SW) model is usually used to explain the magnetic behavior of a ferromagnet in presence of external physical quantities, depicted in Fig. 2.16. Below different energy terms are briefly described.

Exchange Energy

The exchange interaction is responsible for the spontaneous ordering of neighboring atomic magnetic moments. In ferromagnetic materials strong spin interactions between the nearest neighbors leads to a net magnetization. The exchange energy between two neighboring atoms with spins S_i and S_j can be expressed as[128]:

$$e_{ex} = -2J_{ij}S_i \cdot S_j, \tag{2.15}$$

where J_{ij} is the exchange constant, called also the exchange integral, between atomic spins. In continuum picture of the total volume (V) the exchange energy density of a

material as the sum of all pairs of nearest couplings is[69]

$$E_{ex} = \frac{1}{V} A \int_V \left(\vec{M}(\vec{r})/M_s\right)^2 d^3r \tag{2.16}$$

with $A = \frac{4JS^2}{a}$ being the exchange stiffness where a is the lattice constant for the bcc structure. Another key material parameter in micromagnetism, which defines the shortest scale on which the magnetization can be twisted, is the exchange length l_{ex} [156]:

$$l_{ex} = \sqrt{\frac{2A}{\mu_0 {M_s}^2}}. \tag{2.17}$$

A typical value of l_{ex} is about 3 nm for Co and Fe[69].

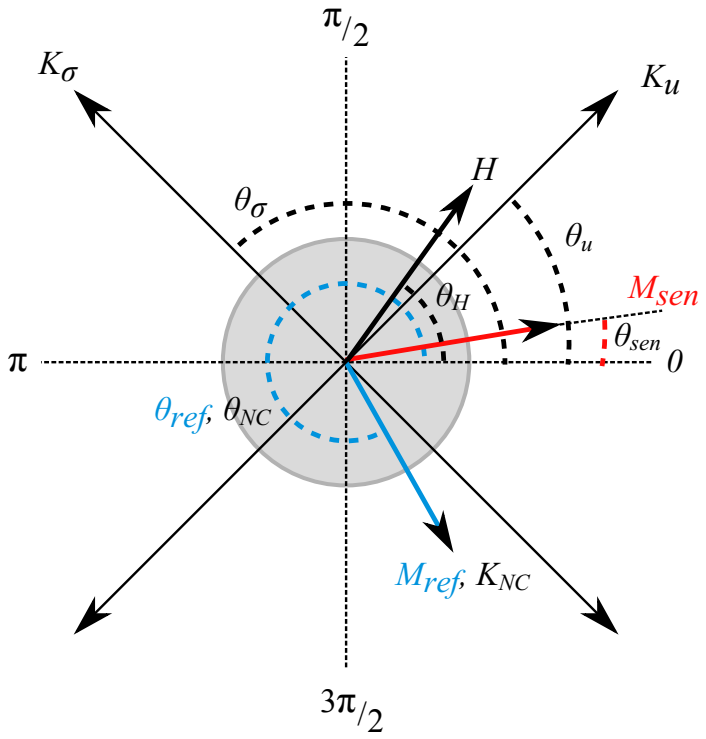

Figure 2.16: *Physical quantities in the Stoner-Wohlfarth model, which are present in a TMR junction. Single-sided and double-sided arrows stand for unidirectional and uniaxial anisotropies, respectively.*

Demagnetizing Energy

The demagnetizing energy density E_d is attributed to interactions of the magnetization and the demagnetizing field $\vec{H}_d$, which can be expressed as:

$$E_d = -\frac{1}{2V} \int_V \vec{H}_d \cdot \vec{M}\, dV. \tag{2.18}$$

The demagnetizing field, which arises from shape anisotropy, is created by the magnetization of the sample:

$$\vec{H}_d = N_d \cdot \vec{M}, \tag{2.19}$$

where N_d is the demagnetizing tensor which is determined by the shape of the sample. N_d can be calculated for different shapes of samples[128].

Magnetocrystalline Energy

In a crystalline ferromagnetic structure two types of couplings have to be taken into account; the spin-spin coupling and the spin-orbit coupling. The spin-spin coupling acts to keep the neighboring spins parallel or antiparallel. Even though it is very strong, it does not depend on the orientation of the spins with regard to the crystal lattice. Therefore, it can not have a contribution to the magnetocrystalline anisotropy. In comparison, the orientations of the orbits are strongly coupled to the lattice, which cannot be reoriented even by large magnetic fields. Therefore, due to the interaction between the spins and the orbits, there is resistance against an external magnetic field or other attempts which intend to reorient the spin axis. In other words, in ferromagnetic crystals the magnetization aligns along certain preferred crystallographic directions. They are called easy axes since they are the easiest to reach the saturation magnetization by applying an external field. This justifies the spin-orbit coupling as the main origin for the magnetocrystalline anisotropy[128]. The magnetocrystalline anisotropy energy is the energy required to overcome the spin-orbit coupling and to reorient the magnetization. The energy density can be expressed as a special case for a uniaxial anisotropy:

$$E_u = \frac{1}{V}\int_V K_u \sin^2(\theta_u - \theta)\, dV = K_u \sin^2(\theta_u - \theta_{sen}). \tag{2.20}$$

Here, K_u stands for the uniaxial magnetocrystalline anisotropy along the angle θ_u as shown in Fig. 2.16. θ_{sen} denotes the orientation of the sense layer magnetization. The energy is minimum when the magnetization points along the easy direction. The energy difference between the states magnetized along easy and hard directions is called the magnetocrystalline anisotropy energy[157]. As mentioned before in section 2.5, another uniaxial anisotropy is present due to the absence of the azimuthal symmetry. Here, we consider K_u as the compromise of the uniaxial magnetic anisotropy (UMA) and the magnetocrystalline anisotropy, which appears as a uniaxial anisotropy even in the bcc-structure CoFeB films after annealing.

Zeeman Energy

The Zeeman energy density E_z due to the magnetization orientation in an external magnetic field is

$$E_z = \frac{-1}{V}\int_V \vec{H} \cdot \vec{M}\, dV = -\mu_0 H M_{sen} \cos(\theta_H - \theta_{sen}), \tag{2.21}$$

where θ_H defines the orientation of the magnetic field (see Fig. 2.16). This energy term is minimized when the magnetization is fully aligned along the applied field.

Néel energy

As mentioned earlier (see section 2.3.3), possible roughness in TMR layers results in the Néel coupling between the sense and reference layers. It leads to a unidirectional anisotropy contribution favoring the parallel configuration in MTJs. The Néel coupling appears as a field shift H_{sh} in a TMR loop, from which the Néel energy density can be calculated by

$$E_{NC} = \frac{-1}{V} \int_V \vec{H}_{NC} \cdot \vec{M}\, dV = -\mu_0 H_{sh} M_{sen} \cos(\theta_{NC} - \theta_{sen}). \tag{2.22}$$

The angle θ_{NC} defines the Néel coupling unidirectional anisotropy, which is parallel to the reference layer magnetization θ_{ref}.

Stress-induced Anisotropy Energy

Due to the inverse magnetostriction effect, applying uniaxial stress σ will induce a uniaxial anisotropy K_σ, defined as $K_\sigma = \frac{3}{2}\lambda_s Y \varepsilon$. Such anisotropy is parallel and perpendicular to the stress axis θ_σ in case of tensile and compressive stress, respectively. For positive magnetostrictive materials under small strain values, the stress-induced anisotropy (see section 2.4) energy density can be expressed as

$$E_\sigma = \frac{1}{V} \int_V K_\sigma \sin^2(\theta_\sigma - \theta)\, dV = \frac{3}{2} \lambda_s Y \varepsilon \sin^2(\theta_\sigma - \theta_{sen}). \tag{2.23}$$

2.8 Landau-Lifshitz-Gilbert Equation

The Landau-Lifshitz-Gilbert (LLG) equation[156] is

$$\frac{d\vec{M}}{dt} = -\frac{\gamma_0}{1+{\alpha_0}^2} \cdot \left[\vec{M} \times \vec{H}_{eff}\right] - \frac{\gamma_0}{M_s} \cdot \frac{\alpha_0}{1+{\alpha_0}^2} \cdot \left[\vec{M} \times \left[\vec{M} \times \vec{H}_{eff}\right]\right] \tag{2.24}$$

frequently used to describe the magnetization dynamics $\vec{M}(r,t)$ and the domain structures. γ_0, α_0, and $\vec{H}_{eff}$ stand for the electron gyromagnetic ratio, the Gilbert damping factor, and the effective magnetic field, respectively. $\vec{H}_{eff}$ consists of all present interactions acting on the individual cells. The interactions also depend on the magnetization of the other cells. The effective field is the negative derivative of the total energy E with respect to the magnetization[156]:

$$\vec{H}_{eff} = -\frac{1}{\mu_0 M_s} \frac{\partial E}{\partial \vec{M}(r)} \tag{2.25}$$

For the problems discussed here the total energy density E_{total} is the sum of all present energy terms in a magnetic system:

$$E_{total} = E_{ex} + E_u + E_z + E_d + E_\sigma. \tag{2.26}$$

In principle, micromagnetic simulations using object oriented micromagnetic framework (OOMMF) solve the LLG equation for each cell of a two- or three-dimensional grid[12].

2.9 Stoner-Wohlfarth Model

To describe the functional mechanism of a TMR strain sensor even in the absence of a magnetic field, it is necessary to understand magnetic behavior of the sense layer in a minor TMR loop of a junction exposed to stress. This also helps to determine optimum conditions in which TMR sensors reveal their highest strain sensitivity. For simplification in order to simulate complex and large samples, the rotation of the sense layer magnetization M_{sen} is assumed to maintain single-domain behavior in the magnetization reversal, and effects due to domain formation are neglected. A modified SW model, as an energy model, calculates the magnetic state of the sense layer by minimizing its total energy. Here, the SW model is a modified model since the stress and the Néel coupling terms are additionally included. The total energy density $E(\theta_{sen})$ of the sense layer, with magnetization oriented at the angle θ_{sen} in polar coordinates (see Fig. 2.16), in TMR stacks can be written as a sum of several energy terms:

$$E(\theta_{sen}) = E_u(\theta_u) + E_z(\theta_H) + E_{NC}(\theta_{NC}) + E_\sigma(\theta_\sigma), \tag{2.27}$$

where E_u, E_z, E_{NC}, and E_σ denote the uniaxial magnetocrystalline anisotropy energy density, the Zeeman energy density, the Néel energy density, and the stress-induced anisotropy energy density, respectively. In-plane shape anisotropy is assumed to be negligible for junctions which are either circular or large in dimensions in case of squared junctions.

2.10 Atomic Force Microscopy

Atomic force microscopy (AFM) is a widely used technique to measure interacting forces and to image surface topography in nano-scale studies. In a typical AFM configuration, there is a tip with a radius curvature of 10-20 nm, attached to a micromachined cantilever, interacting with the atoms on the surface of the sample. Then, the interaction is detected as it causes deflection to the cantilever.

In order to understand the AFM operating principles, it is necessary to interpret the interacting forces between the tip and the sample. These forces are experimentally available by measuring the so-called force-distance curve (FD curve). While the tip is approaching toward the sample, the tip experiences variable amounts of forces, as

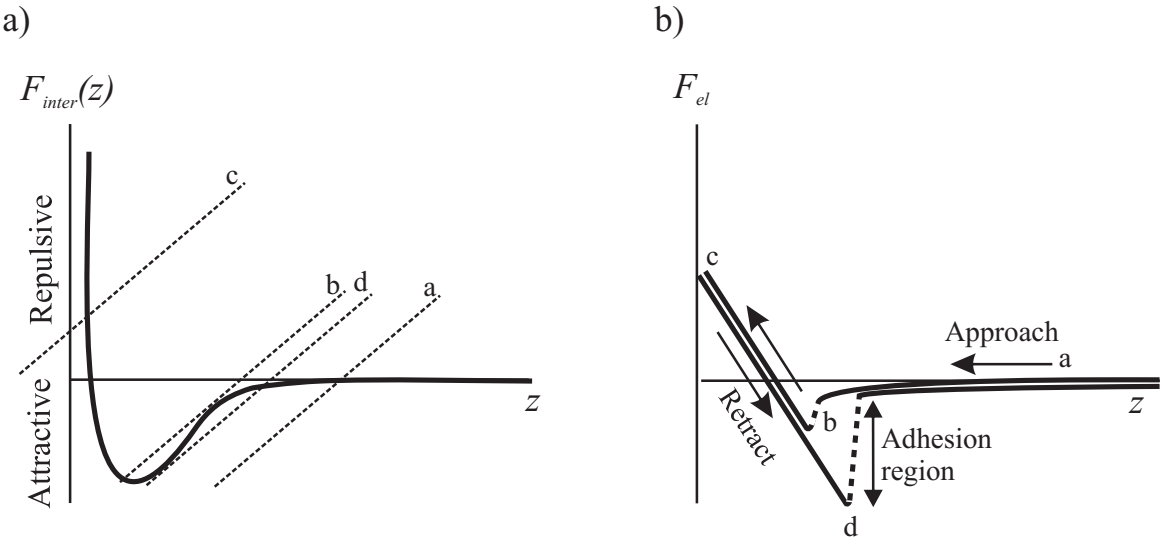

Figure 2.17: a) *Typical tip-sample interacting force versus tip-sample distance ($F_{inter}(z)$) curve. The lines a-d stand for the elastic force of the cantilever F_{el} as a function of the distance. At each distance the cantilever bends until the elastic force and the tip-sample force are equal in an equilibrium state, which is the intersection of the F_{el} line and the $F_{inter}(z)$ curve.* ***b)*** *Schematic of a force-distance curve. At the distance a, the tip is far from the surface. Further, the attractive forces bend the cantilever until it jumps into the surface (the dashed segment of the approach path). The force becomes repulsive as the cantilever is moved more toward the surface (the distance c). On the retracting path at the distance d, the jump-off takes place when the adhesion force is overcome (the dashed segment of the retract path). Reproduced with permission from Ref. 158 © 1999 Elsevier.*

shown in Fig. 2.17 a). The forces vary from attractive to repulsive forces[19], given in Table 2.1, depending on the tip-sample distance z.

By approaching the tip close to the surface and retracting it, the interaction of the tip and the sample leads to a bending of the cantilever so that the two exerted forces, the interacting force $F_{inter}\,(z)$ and the elastic force F_{el} caused by the deflection, are in an equilibrium state. Hence, the interacting force can be estimated from the deflection for the cantilever with a known spring constant by considering the Hooke's law:

$$F_{el} = k_z \delta_{el}, \tag{2.28}$$

where k_z and δ_{el} represent the cantilever stiffness and the cantilever deflection, respectively. As depicted in Fig. 2.17, a typical FD curve can be deduced from intersecting points of the elastic force lines a-d and the interacting force curve. At close distances, due to the high gradient in the force field, the cantilever becomes unstable by varying the tip-sample distance between the lines b and d (the dashed segments in Fig. 2.17 b)). Hence, a mechanical hysteresis occurs, which can be deliberately diminished for cantilevers with higher stiffness[19].

AFM operations are generally divided into two modes, the contact mode and the dynamic mode. The contact mode simply involves measuring the static deflection of

Table 2.1: *Some of the tip-sample interacting forces.*
* *Repulsive forces can be extracted from the second part (z^{-12}) of Lennard-Jones (LJ) potential V_{LJ} with r_0 and ϵ_0 being the equilibrium distance, at which the force is zero, and the depth of the potential well*[83]*, respectively. However, it must be modified depending on the shape of the tip*[19]*.*
** *The vdW force is given for a spherical tip with radius r_t and a flat surface. A_H is the Hamaker constant*[159]*.*
*** *The basis of the capillary force is the vdW forces among the water molecules and atoms at the tip and on the sample. Θ is the contact angle and Φ is the angle of the meniscus. γ_s stands for the surface tension.*
**** *ε_0 is the permittivity of free space.*

Interacting force	Origin	Formula
Repulsive	Pauli exclusion; overlap of electronic wave functions of two atoms	$V_{LJ} = -4\epsilon_0 \left(\frac{r_0^6}{z^6} - \frac{r_0^{12}}{z^{12}}\right)$ *, Ref. 160
Van der Waals	induced electric dipoles in neutral atoms and molecules	$F_{vdW} = -\frac{A_H r_t}{6z^2}$ **, Ref. 161
Capillary	water molecules absorbed on the surface in ambient conditions	$F_{cap} = \frac{4\pi r_t \gamma_s \cos\Theta}{1+z/[r_t(1-\cos\Phi)]}$ ***, Ref. 162
Electrostatic	Coulomb's law; a charged or conductive tip and sample with potential difference U	$F_{elec} = -\pi\varepsilon_0 \frac{r_t U^2}{z}$ ****, Ref. 19

the cantilever while the cantilever is scanned in the x-y plane at a certain set-point in the repulsive regime. By changing the z-position of the sample to maintain a constant tip-sample force, the topography can be reconstructed. As such, the contact mode is operated in the repulsive regime. On the other hand, the dynamic mode is operated as the cantilever vibrates in the non-contact region, where weak attractive and repulsive forces govern the tip-sample interactions. While approaching the cantilever with a driven frequency f_d close to its resonance frequency f_0 toward the sample, harmonic oscillator of the cantilever and the oscillation frequency is distorted due to the tip-sample interaction. Also, the phase and the amplitude of the oscillation respond differently. Motion of such cantilever $z(t)$ can be approximated by considering a 1-dimensional point mass m attached at a spring[19]:

$$m\ddot{z}(t) + k_z z(t) + \frac{m\omega_0}{Q}\dot{z}(t) = F_{inter} + A_d \cos(\omega_d t). \tag{2.29}$$

Here, A_d and ω_d are the oscillating amplitude and the angular frequency, respectively, driven by an external actuator. Q is the quality factor of the cantilever and $\omega_0 = 2\pi f_0$ is the angular resonance frequency of the cantilever. In far distance from the sample, equation 2.29 defines driven harmonic oscillator with damping, as the interaction can be neglected. The general solution for this model including a steady-state solution

(first term) and transient one (second term) is[163]

$$z(t) = A\cos(\omega t - \varphi) + Be^{-\xi t}\cos(\omega_r t + \phi), \tag{2.30}$$

with ω_r and φ being the resonance angular frequency of the cantilever influenced by the damping effect and the phase difference between the driving force and the cantilever motion, respectively. While the transient term decays exponentially with a time constant $1/\xi = 2Q/\omega_0$, the steady-state motion becomes dominant. $z(t)$ will exhibit sinusoidal behavior with an amplitude of A and a phase φ depending on the driving frequency f_d[19]:

$$A = \frac{A_d}{\sqrt{\left(1 - \frac{f_d^2}{f_0^2}\right)^2 + \left(\frac{1}{Q_0}\frac{f_d}{f_0}\right)^2}} \tag{2.31}$$

$$\tan\varphi = \frac{1}{Q_0}\frac{\frac{f_d}{f_0}}{1 - \frac{f_d^2}{f_0^2}}. \tag{2.32}$$

Since all three frequency, amplitude, and phase respond to the tip-sample interaction, interpretation of the dynamic mode is complicated. This can be solved by setting feedback loops which keep the internal parameters fixed by modification of the external variables. As the simplest and the most common method, the driving frequency is fixed at a pre-defined value f_d while the driving amplitude is kept constant by a feedback loop. This is called amplitude-modulated AFM (AM-AFM) mode. In the amplitude modulation, distortion of harmonic oscillator merges as changes in the amplitude and the phase. The amplitude is used as a feedback loop for topography imaging and the phase signal is recorded as a dissipation signal[19]. In case of more sensitive phase signal the phase and the resonance frequency can be utilized as a feedback signal. In frequency-modulated AFM (FM-AFM) mode, the cantilever is always oscillated at its resonance frequency. This is achieved by feeding back the oscillation signal of the cantilever into the piezo element. The detected signal is phase-shifted 90° and is used for excitation of the cantilever. This adjusts the driving frequency to the resonance frequency of the cantilever influenced by the tip-sample interaction. The topography feedback loop is adjusting the sample position in the frequency modulation to match a certain frequency offset from the resonance frequency[68].

Optical beam deflection is a conventional read-out system for AFM measurements, It typically consists of a laser diode with a beam focused at the tip of a cantilever, and the reflected beam is aligned to the center of a four-segment photodiode (Fig. 2.18). The intensity difference of the two top and the two bottom segments indicates vertical deflection while lateral deflection is extracted from the intensity difference between the two pairs of segments on the right and the left[162].

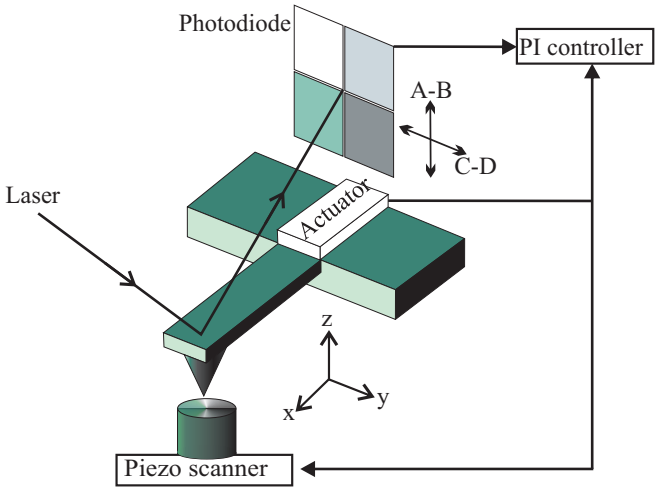

Figure 2.18: *Schematic of an optical beam deflection read-out system. Bending of the cantilever changes the laser intensity in segments at the photodiode, which is fed to a proportion-integration (PI) controller as signals to modify tip-sample distance via an actuator. A scanner is used for in-plane movement. Reproduced with permission from Ref. 162 © 2004 Springer.*

Table 2.2 compares a couple of detection techniques for measuring cantilever deflection in AFM in terms of the noise level[164–167]. The optical beam deflection provides a

Table 2.2: *Comparison of detection techniques for cantilever deflection in AFM in terms of deflection noise at different oscillation frequencies. Deflection noise values are generally obtained by multiplying the measured voltage noise with the deflection sensitivity.*

Detection method	Frequency (kHz)	Noise (fm/$\sqrt{\text{Hz}}$)
GMR sensor	1000	80 (Ref. 53)
Quartz tuning fork	33	170 (Ref. 168)
	33	35 (Ref. 169)
Interferometer	1000	1 (Ref. 170)
	274	2 (Ref. 171)
	4.5	2 (Ref. 172)
Optical beam deflection	800-1660	5.7-7.3 (Ref. 164)
	303-435	56-56 (Ref. 165)
	10000	4.7 (Ref. 166)
	20000	4.5 (Ref. 167)

very low deflection noise of 4.5 fm/$\sqrt{\text{Hz}}$, even at 20 MHz frequency, suitable for high speed AFM applications. However, the experimental setup becomes more expensive and more complex for high resolution measurement in sealed vacuum[173] or at low temperature[174]. The same applies to the interferometric techniques[170–172]. On the

contrary, the tuning forks with a low noise level[168,169] can be cost-effective, but they are not compatible with mass-production processes. Unfortunately, there was no value on the noise level with the same unit in the literature for integrated piezoelectric and piezoresistive microcantilevers, which are commercially available for AFM applications. GMR sensors, which show $80\,\mathrm{fm}/\sqrt{\mathrm{Hz}}$ noise, was used to detect the movement of a micromagnet placed at the tip of the cantilever (Fig. 1.3). Even though the detecting sensor was not completely integrated to the cantilever, the results approve the capability of MR sensors at high operating bandwidth with a low deflection noise value. This value can be further improved using TMR sensors.

Therefore, in favor of replacing the optical read-out, the magnetostrictive TMR sensors should be studied in terms of parameters related to sensitivity and noise levels. Those parameters include cantilever dimensions, the magnetostrictive sense layer, the magnetic configuration of the MTJ (see section 2.6), and the resistance-area product of the MTJ. Thus, the definition of the sensitivity for AFM applications and possible noises are briefly explained in the next two sections.

2.10.1 Sensitivity

The deflection δ_{el} of one-sided clamped cantilevers induced by a vertical point force F can be expressed as[175]

$$\delta_{el}(x) = \frac{6\,F\,L\,x^2\,(1 - x/3\,L)}{Y\,w\,t^3}, \tag{2.33}$$

where Y is the Young′s modulus, w is the cantilever width, L is the cantilever length, t is the cantilever thickness, and x is the distance from the base. Depending on the cantilever stiffness $k_z = Y\,w\,t^3/4L^3$, such deflection corresponds to longitudinal stress σ , varying across the length and the thickness of the cantilever:

$$\sigma(x) = \frac{6\,F\,(L - x)}{w\,t^2}, \tag{2.34}$$

as it has the maximum value at the base and zero value at the neutral axis of the cantilever. Therefore, deflection TMR sensors are located at the fixed end of the cantilever (see Fig. 4.16 b)). Due to the inverse magnetostriction and the angular dependence of the tunnel resistance, deflection-induced stress results in the resistance change of the deflection sensor. The sensitivity of the read-out sensor is usually determined by their deflection sensitivity, which is basically the output voltage signal V_{out} from the Wheatstone bridge (see section 7.1) generated by 1 Å cantilever deflection. Since this value can be arbitrarily large by varying the gain of the amplifier, in the TMR read-out system, the relative tunnel resistance change dR/R as a function of the vertical deflection δ_{el} is considered as the deflection sensitivity:

$$S_\delta = \frac{\Delta V_{out}}{\delta_{el}} \equiv \frac{(dR/R)}{\delta_{el}} \equiv \frac{\delta\sigma}{\delta_{el}}. \tag{2.35}$$

Generally speaking, due to the proportionality of longitudinal stress to the fractional resistance change, the deflection sensitivity is maximized by designing a cantilever with

higher stiffness. Thus, it causes larger stress for a specific amount of deflection. In addition to the deflection sensitivity, force sensitivity can be calculated by simply dividing the deflection sensitivity to the cantilever stiffness:

$$S_F = \frac{\Delta V_{out}}{\delta F} \equiv \frac{(dR/R)}{\delta F} \equiv \frac{\delta\sigma}{k_z \delta_{el}}. \tag{2.36}$$

Inversely, force sensitivity can be improved by making the cantilever long, thin and narrow. In the next section, possible present noises in MTJ-based sensors are briefly explained.

2.10.2 Noise

Electrical noises can be attributed to different origins such as defects motion, magnetic domain or spin fluctuations, charge carriers crossing an energy barrier, electronic traps, current redistribution in electronic materials[73]. These sources will give rise to frequency-independent noises including thermal and shot noises, and also frequency-dependent noises including $1/f$ and random telegraph noises. The thermal noise[176,177], also known as the Johnson and Nyquist noise, appears in all resistors due to thermal fluctuations of the carriers in the resistor. It yields a power spectral density (PSD) as follows:

$$S_v^{thermal}\left[V^2/Hz\right] = 4k_B T R. \tag{2.37}$$

Here, $k_B T$ is the thermal energy, and R is the resistance value of the device. The shot noise[178–180] is associated to the movement of the current crossing an energy barrier. It is considered as fluctuations of the current flow around a mean level arising as a consequence of discrete nature of the electrical charges. The PSD of the shot noise is expressed by

$$S_v^{shot}\left[V^2/Hz\right] = 2\,e\,I\,R_d^2, \tag{2.38}$$

where e, I, and R_d represent the electron electrical charge, the flowing current, and the differential resistance, respectively. In MTJs, the tunnel barrier as a discontinuity between the two conducting ferromagnetic layers gives rise to the shot noise[181].

The $1/f$ noise designates fluctuations of a physical variable like resistance with a PSD following a $1/f$ law. The resistance fluctuations can be extracted from voltage fluctuations by applying a current. The applied current reveals the fluctuations above the white noise rather than creating them[73]. The $1/f$ noise given by the Hooge equation[182] is

$$S_v^{1/f} = \frac{\gamma\, V^2}{A\, f}. \tag{2.39}$$

Here, γ is the Hooge parameter, and A stands for the area of an MTJ replacing the number of carriers, which denoted by N_c in the original equation. In MTJs, the Hooge

parameter generally increases by larger resistance-area products (RAs), smaller TMR effect amplitudes, and lower bias voltages[183–186].

The $1/f$ noise has a magnetic component and an electronic component[179,187]. The magnetic component can be attributed to thermal magnetization fluctuations in the ferromagnetic layers that couple to the resistance via the spin-dependent tunneling effect[188]. Besides, the electronic component can be ascribed to fluctuations of the tunnel barrier height[188] due to charge trapping at defects in the tunnel barrier and at the interfaces. As discussed in section 2.2, crystallization of CoFeB/MgO/CoFeB multilayers leads to smooth and sharp interfaces. This results in less defects and dislocations which mitigates the electronic $1/f$ noise in MTJs[189].

The random telegraphic noise is related to fluctuations of the sense layer magnetization even in submicron scale MTJs[188,190]. Magnetic metastability emerges as domain wall hopping between pinning sites or thermally activated fluctuations in the magnetization of the sense layer[191]. Scola et al.[192] pointed out that a proper annealing process can reduce the random telegraphic noise by improving the stability of the magnetic domains in the sense layer.

Some of the approaches mentioned above for eliminating the noises require compromises in sensor design. These methods will require further studies to find compromised parameters of the thickness of the sense layer, the thickness of the MgO layer, the area of MTJs, and the annealing procedure in order to minimize the noises.

In contrast to piezoresistive and piezoelectric sensors[38], the deflection sensitivity, the noise, and the signal-to-noise ratio of TMR-based self-sensing cantilevers are not theoretically simulated yet. Therefore, it is still unclear how to improve the sensitivity, minimum detectable deflection (MDD), and minimum detectable force (MDF) simultaneously by design optimization. First, the resistance change under stress needs to be taken into account. It depends on magnetostrictive properties of the sense layer, the TMR effect amplitude, the magnetic configuration of MTJs (see section 2.6), and the resistance-area product of MTJs. Second, the origin of noise in MTJs, as mentioned above, and in electronic components should be recognized. Third, cantilever dimensions and tip quality are also associated to stress levels exerted to the sensor as well as imposed deflection. Hence, such calculation and design optimization are beyond the scope the present study. Here, the primary focus is to realize strain-sensitive TMR sensors and operating TMR self-sensing AFM cantilevers, for which the deflection sensitivity and the MDD are defined experimentally by the slope of FD curves and the minimum measurable height, respectively. Noise measurement is not performed in this study since integration of optimum tips, in terms of sharpness and stiffness, and optimum electronics for TMR sensor read-outs are ongoing tasks.

2.11 Anisotropic Si Etching in KOH Solution

Anisotropic wet etching in aqueous potassium hydroxide (KOH) solutions remains the most popularly used processing technique in Si technology with a broad range of

microelectromechanical systems (MEMS) applications. Such devices require smooth surfaces and precisely repeatable fabrication conditions. The roughness strongly depends on the crystallographic orientation and principal planes. The (100)-oriented planes showed the smoothest etched surface among all the orientations[193,194].

For better understanding, there have been studies over years on anisotropic etching in order to suppress fundamental problems such as formation of pyramidal hillocks and round pits on etched surfaces, which are critical to mechanical, optical, and surface properties. Formation of the pyramids have been associated to a number of origins based on a common mechanism in which some materials are stabilized on the surface, which can act as micromasks obstructing chemical reaction. Hydrogen bubbles formed on the surface during a detachment process[195,196], polymerized residues[197], SiO_2 precipitates[198,199], re-deposition of reaction products[198], semipermeable silicate particles[200], and impurities in the solution[195,196,201–203] are suggested for pseudo-masking during etching in the literature. In case of round pits, the surface morphology is built up with these features, which is generally attributed to the hydrogen bubbles due to their similar geometries. However, Gosálvez and Nieminen presented that these surface inhomogeneities are the result of the anisotropy of the etching process between pit nucleation and step propagation[204].

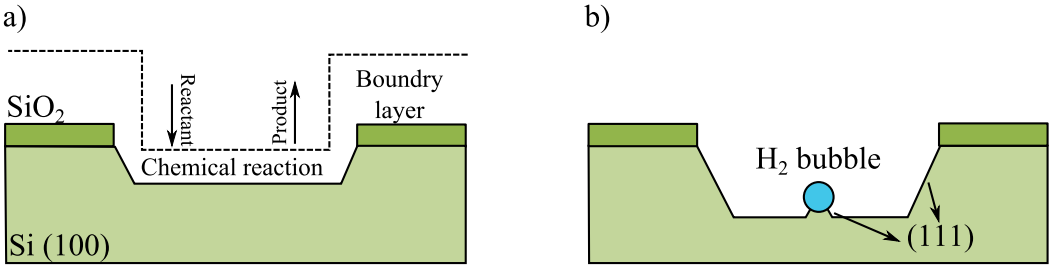

Figure 2.19: *Schematic of* ***a)*** *etching mechanism through the reaction boundary layer and* ***b)*** *the pseudo-masking by H_2 bubbles (or other materials), leading to pyramidal features with (111)-oriented sidewalls at a 54.74° angle relative to the (100) surface. Reproduced with permission from Ref. 205 © 2005 Elsevier.*

Reduction of surface roughness by suppressing these morphological features can begin with increase of the KOH concentration of lower than 40 wt%[194,201,206], decrease of the temperature[205], and reduction of impurities[207]. Note that increase of the etchant above 40 wt%, unlike increase of the temperature, affects the etching rates of different crystallographic planes and selectivity of (111) and (100) planes[194]. For further surface improvement mechanical agitation like magnetic stirring can accelerate the diffusion of etchant and products (Fig. 2.19) and decrease the duration of the bubbles on the surface[205,206]. Table 2.3 gives a list of published studies on the improvement of the surface quality by means of the mechanical agitation and some additives.

Using ultrasonic agitation instead allows uniform etching conditions as well, especially for wafer-scale etching[195,205,206,213]. Raising the agitation frequency to megasonic waves not only reduces significantly the size of the H_2 bubbles which remain attached to the surface but also is suitable for fabrication of very fine microstructures such as membranes and microcantilevers, which can be easily damaged using the other me-

Table 2.3: *Published roughness values of the substrate surface etched in KOH solutions using different techniques for the improvement of the surface quality. Note that a proper conclusion from this table requires consideration of different etch depth and roughness measuring devices. Roughness values are given as either R_a (average) or R_{RMS} (root mean square).*
** p-type Si with a hard-mask patterned by reactive ion etching (RIE) and then exposed to a buffered oxide etching (BOE) solution.*
*** isopropyl alcohol (IPA)*
**** sodium dihexyl sulfosuccinate (SDSS)*

Substrate	KOH	Temperature (°C)	Additive	Agitation	Etch depth (µm)	Measurement /area	Roughness (nm)
Si	34 wt%	70	—	—	51	...	R_a= 11 [193]
Si*	30 wt%	80-100	—	Stirrer	20-60	Profilometer	R_a= 25-28 [205]
Si*	30 wt%	80-100	—	Ultrasonic	20-60	Profilometer	R_a= 9-7.5 [208]
Si*	30 wt%	...	—	Megasonic	37	AFM, 49 µm^2	R_{RMS}= 1.7 [209,210]
Si*	30 wt%	66	—	Megasonic	70	Profilometer	R_a= 70 [210]
Si*	5 M	85	Ethylene glycerol, 1 M	Stirrer	20	AFM, 1 µm^2	R_{RMS}= 0.867 [211]
Si*	18 M	40-80	IPA**, saturated	Stirrer	50	AFM, 100 µm^2	R_{RMS}= 3-9 [211]
Si*	30 wt%	80-100	SDSS***, 0.02 wt%	Stirrer	20-100	Profilometer	R_a= 7.5-15 [208]
Si*	40 wt%	85	SDSS, 0.02 wt%	—	22	AFM, 0.014 mm^2	R_a= 7.5-15 [206]
Si*	40 wt%	80	Sb_2O_3, 5 mmol	—	300	AFM, 900 µm^2	R_{RMS}= 2 [212]

chanical agitation techniques[208–210]. Furthermore, various additives such as different alcohols[196,211,214,215], oxidizing agents[195], different surfactants[203,205,206,208], and polymeric oxides[212] are added to the solution, which modifies the properties of the etchant. As a result, the bubbles will have difficulty to adhere to the etched surface because of improved wetability. Among these candidates listed in Table 2.3, using a megasonic module and adding Sb_2O_3 result in a very smooth surface. The surface roughness remains constant after deep etching, whereas with other techniques it increases by the etching time.

Compensating Structures

MEMS devices after deep etching in KOH suffer from underetching at convex corners due to formation of high-index planes, which have high etching rates. To tackle this difficulty, additional compensating structures are implemented at convex corners delaying the etching process. There are different shapes recommended for these compensating structures[216], which vary in dimensions depending on the etch depth. Figure 2.20 shows the performance of two different compensating structures. The one in Fig. 2.20 a) with folding strips seems to be not sufficient in dimension so that underechting occurs at the convex corner. However, the squared-shaped compensating structure, shown in Fig. 2.20 b), successfully protected the convex corner.

Furthermore, some additives like IPA can change the etching anisotropy and reduce

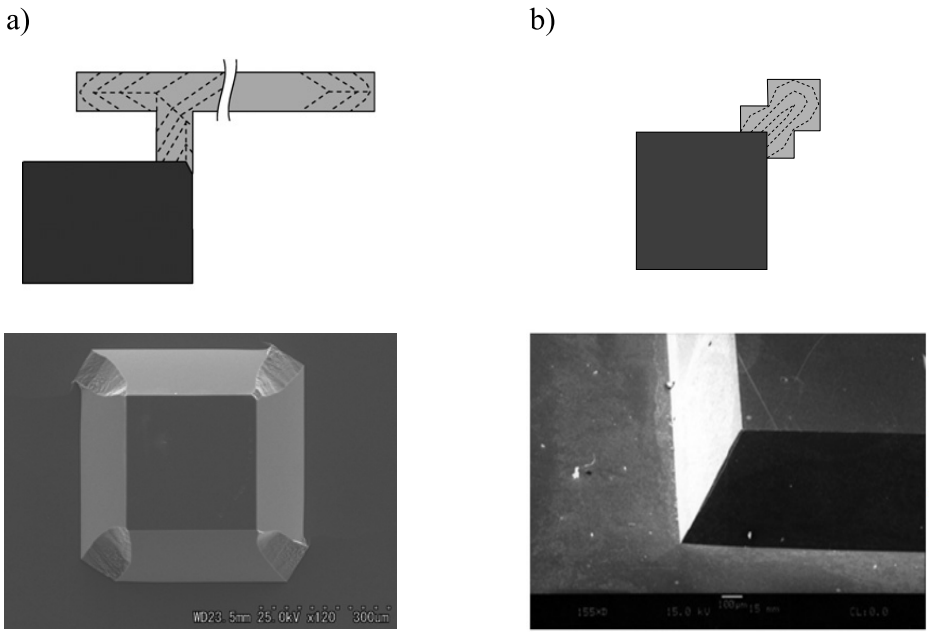

Figure 2.20: *Schematic of two compensating structures with* ***a)*** *squared-shaped corners and* ***b)*** $\langle 110 \rangle$*-oriented folding strips. Dashed outlines depict successive etched shape patterns. SEM images show the performance of the compensating structures. In the panel a) the underetching at the convex corners takes place because either the dimension or the shape of the compensating structure is wrongly implemented. Panels reproduced with permission from:* ***a)*** *Ref. 216 © 2007 Institute of Physics Publishing;* ***b)*** *Ref. 217 © 2006 Elsevier.*

the convex corners underetching by changing the surface tension[215,218].

Chapter 3

Experimental Techniques and Parameters

This chapter includes description of techniques employed for fabrication and characterization during the sample preparation in the next chapter. Figure 3.1 shows patterning of the magnetostrictive TMR sensors and integrating them to microcantilevers in four steps, which will be explained in detail in chapter 4. The techniques, used in every step, are listed in the figure caption. These techniques as well as characterization techniques, including scanning electron microscopy (SEM), optical microscopy, profilometer, and atomic force microscopy (AFM), are described in this chapter.

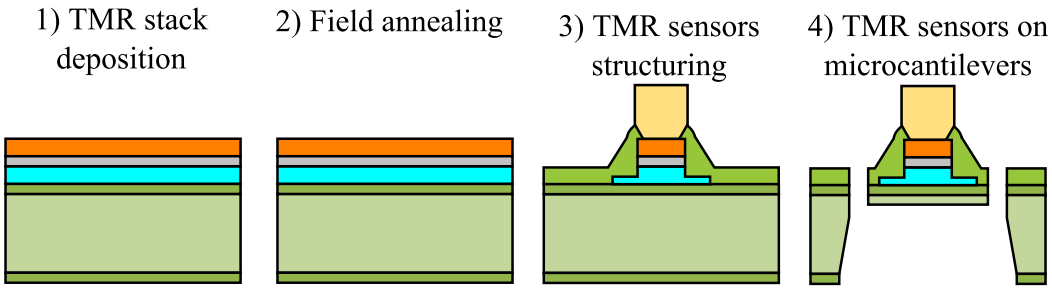

Figure 3.1: *Patterning of TMR sensors in four steps: 1) TMR stack deposition: sputter deposition, 2) Field annealing: field annealing process, 3) Patterning of TMR sensors: lithography, ion beam etching (IBE), and sputter deposition, 4) Integration of TMR sensors to microcantilever: lithography, reactive ion etching (RIE), anisotropic KOH etching, sputter deposition, and beam-assisted deposition.*

Here, the techniques are not explained in detail, but rather technical specifications, limitations, and advantages of the techniques. Moreover, it is explicitly stated in which part and for what purposes these techniques are used. Exceptionally, field annealing process and inductively coupled plasma (ICP)-reactive ion etching (RIE) of Si are thoroughly discussed since they were developed within the framework of this study. Note that anisotropic KOH etching is thoroughly described in chapter 5. The results of this chapter are used in the sample preparation in chapter 4.

3.1 Deposition Methods

Sputtering

Magnetic tunnel junctions (MTJs) with CoFeB electrodes and MgO as the tunnel barrier were deposited on Si substrates using a Leybold Systems CLAB 600 Cluster-Tool sputtering system. There are four 4″ DC, one 4″ RF, used for MgO deposition, one 3″ DC, and one 2″ DC sputter sources. MTJs have the following multilayer structure (from bottom to top): Ta (5) / Ru (30) / Ta (10) / Ru (5) / MnIr (12) / CoFe (3) / Ru (0.9) / CoFeB (3) / MgO (1.8) / CoFeB (3) / Ta (5) / Ru (5). The numbers in parentheses indicate the layer thickness in nm. The $Co_{40}Fe_{40}B_{20}$ (3 nm) layer, which is known for high magnetostrictive coefficient[134], serves as the sense layer. The reference layer CoFeB with the same composition is magnetically stabilized via MnIr (12 nm)/CoFe (3 nm)/Ru (0.9 nm) layers, forming an exchange-biased artificial antiferromagnet[154]. The deposition of the stack by magnetron sputtering at a base pressure of 2×10^{-7} mbar was carried out in the group of Prof. Günter Reiss at *Bielefeld University*. Table 3.1 gives sputtering parameters for the deposition of the MTJ stack.

Table 3.1: *Sputter-deposition parameters for Cr, Au, and SiO_x thin films and layers in the MTJ stack.*

Target/size (inch)	Gas/flow (sccm)	DC power (W)	RF power (W)	Pressure (mbar)	Deposition rate ($^{nm}/_{s}$)
Au/8	Ar/25	200	–	6E-3	1.1
Cr/8	Ar/25	200	–	4E-3	0.55
SiO_x/8	O_2/20, Ar/18	–	800	4E-3	0.39
MgO/4	Ar/20	–	115	2.37E-2	0.014
MnIr/4	Ar/20	115	–	1.3E-3	0.49
Ru/4	Ar/20	115	–	1.3E-3	0.32
Ta/3	Ar/20	65	–	1.3E-3	0.19
CoFe/4	Ar/20	115	–	1.3E-3	0.29
CoFeB/4	Ar/20	115	–	1.3E-3	0.2

To deposit a Cr/Au bilayer as top electrodes (TE)s for MTJs (see Fig. 4.5 c)) and reflective coatings for the AFM cantilevers (see section 4.3) a Von Ardenne CS 730 S magnetron sputter depositing cluster tool is used. It has two sputtering chambers, each can be equipped with two 4″ and two 8″ sputter targets, and one etching chamber. This device is also employed for reactive sputtering deposition of insulating SiO_x layers, which will be used in the fabrication of the TMR junctions (see Fig. 4.5 b)). A cooling step (O_2 20 sccm/Ar 20 sccm at a pressure of 2E-2 mbar) is also included for 20 s between every 10 s sputtering period. This keeps the wafer temperature below 80 °C

measured on the wafer surface by a thermostrip and prevents photoresists to become highly resistant during lift-off processes. Sputtering parameters are given in Table 3.1 for the deposition of the three thin films.

Beam-assisted Deposition

A Helios Nanolab 600 dual-beam SEM/FIB system from FEI is used for Pt deposition employing a chemical vapor deposition technique in the presence of an ion or electron beam. This technique allows tip growth at the head of the AFM cantilevers (see Fig. 4.19). Tips can be grown with few nm- to few µm-sized heights and with a typical radius curvature of 20 nm. An easily obtainable variety of tip heights required for different measurements indicates the versatility of this technique. Other possible mass-production methods for the tip growth on the AFM cantilevers can make the fabrication of the TMR-based AFM cantilevers very complex. Different cross sections can be given as scan areas for ion and electron beams. A gas including Pt precursor (trimethyl Pt; $C_9H_{16}Pt$) flows out of a gas injecting needle. The precursor is dissociated by high-energy Ga^+ ions or electrons as it adsorbs to a Si surface. The dissociation of the precursor due to its interaction with ions or electrons results in Pt deposition. The resultant volatile products are pumped away[219].

3.2 Field Annealing Process

Field annealing is a common technique applied to MgO-based MTJs. It leads to crystallization of the CoFeB layers, texture improvement of the MgO barrier, and smoother interfaces, resulting in high TMR effect amplitudes (see section 2.2). Another important effect is that the applied field aligns the magnetization of the sense layer and pins the reference layer magnetization by setting up the exchange bias (EB) in FM/AF multilayers (see section 2.3.1). It is crucial to perform the process in an environment like vacuum to avoid oxidation, which degrade the TMR effect, of the layers. For this purpose, a field annealing chamber suitable for 4″ Si wafers and smaller samples was constructed at *Kiel University*.

As shown in Fig. 3.2, the field annealing chamber comprises of the following components:

- Cross vacuum chamber (constructed by Kurt J. Lesker manufacturer): CF flanges on front/back and top/bottom are 6.75″ and 6″ in the outer diameter. The chamber is made of stainless steel with 1.03 relative magnetic permeability, which is the most widely used for high vacuum applications. Feedthroughs for the electrical power (up to 500 V and 10 A), the thermocouple (Type K), and the air inlet/outlet (1/4″ Swagelok fitting) were implemented to a blinded CF flange on the back via welding in our workshop at the *Faculty of Engineering*. The front side is for mounting samples and the chamber is connected to a vacuum pump

from bottom. On top a flange equipped with a viewport is used to measure the temperature on samples surfaces by an infrared (IR) camera.

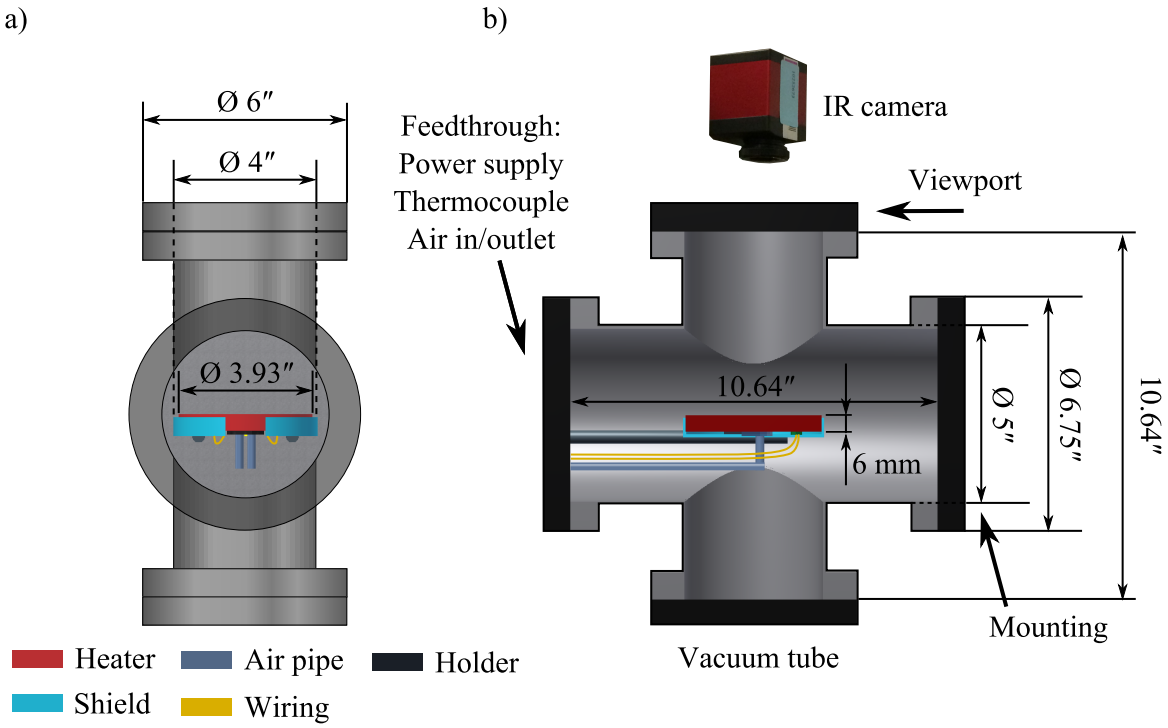

Figure 3.2: *Schematic of* ***a)*** *the frontview and* ***b)*** *the cross-sectional sideview of the field annealing chamber. A detailed technical drawing of the heating element is depicted in Fig. Appendix-D.1.*

- Heating element (a customized product from Bach Resistor Ceramics GmbH): a heater (diameter: 100 mm, thickness: 6 mm) made of silicon nitride, which can be heated up to 450 °C, with integrated ceramic heating conductors. For supplying power Ni wires are brazed to the heater by ceramic pads. The maximum temperature is limited by the temperature resistance of the brazing materials.
- Cooling module: cooling channels are brazed into the heater for cooling with compressed air. These channels are vacuum tight so that it can be operated as active cooling while keeping vacuum outside of the heater (for more details see Fig. Appendix-D.1). Compressed dry air or nitrogen can be applied at a pressure up to 6 bar and with flow rates up to 20 l/min.
- Heating control: the heating rate is tuned into a power supply and controlled by an Euroterm via monitoring a thermocouple close to the surface of the heating element.
- Thermocouple: a home-built thermocouple type K (Ni-NiCr) is placed inside a hole from the backside, which reaches up to 1 mm below the upper surface. This temperature, T_s, is used as an input for the Euroterm in the heating control unit.
- Holder and shield: there is a stainless shield attached to the backside flange by two bars.

- Infrared camera (PIR uc180; purchased from InfraTec GmbH): the camera, which is imaging samples on the heater surface through the viewport of the top flange, is tightly fixed on top of the chamber. The camera lens should stay parallel to the viewport. The IR camera spectral ranges from 7.5 µm to 13 µm offering a wide temperature range from −20 °C to 850 °C. The viewport (purchased from Torr Scientific Ltd) is ZnSe Zero Length (diameter: 63 mm) coated with anti-reflective coating (AR 10.6). It offers above 90 % transmission for almost the whole operating wavelength range of the IR camera (see Fig. Appendix-D.2). It also allows bake-out to a maximum temperature of 120 °C.

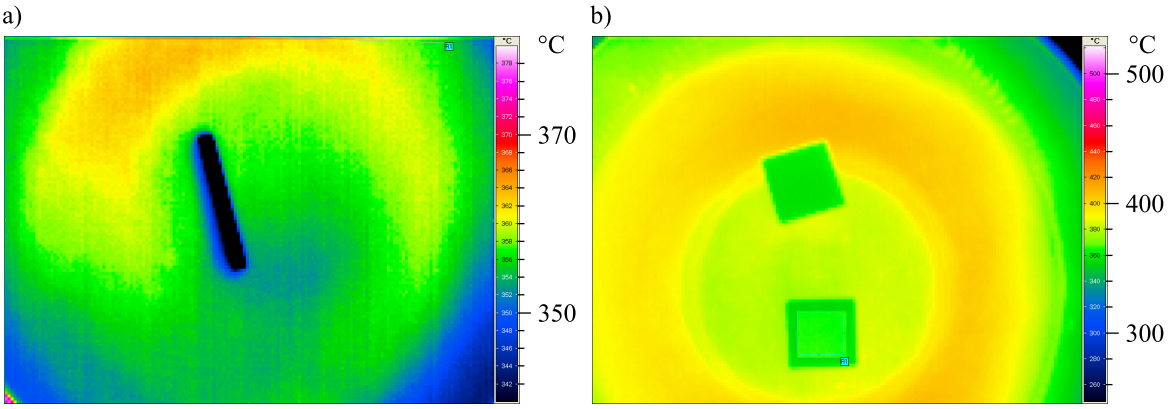

Figure 3.3: *Images taken by the IR camera through the ZnSe viewport at 450 °C set temperature. The measured temperatures are corrected by a software with regard to the transmission (above 90%) of the viewport.* ***a)*** *Temperature distribution for a 4″ Si wafer, which is covered by the black coating, shows maximum 364 °C with a temperature span of about 10 °C. A rectangular Si piece was laid on the wafer for better focusing of the camera.* ***b)*** *For both Si pieces (1 cm × 1 cm) roughly the same maximum temperature of 368 °C is measured. Note that the surroundings are the heater surface where no coating is introduced.*

- Electromagnet (Bruker ER072): magnetic fields up to 159.2 kA/m (2000 Oe).
- Vacuum pump: a vacuum up to 2×10^{-6} mbar can be obtained. The vacuum drops to 1×10^{-5} mbar at 450 °C set temperature. Annealing in vacuum will prevent the film oxidation, which can degrade their quality in terms of TMR effect amplitudes, in the MTJ stack.

As there is always a temperature offset between measuring points, T_s, by the thermocouple and a sample in vacuum, temperature is measured on the sample surface, T_m, by the IR camera for accurate calibration. Such accuracy is required since achievement of high TMR effect amplitudes strongly depends on the annealing temperature (see section 2.2). The calibration was carried out for a Si wafer (Fig. 3.3 a)) and Si-wafer pieces (Fig. 3.3 b)), on which black coatings with emissivity close to 1 were sprayed. Transmission, reduced by the viewport, was taken into account for the whole wafer and one of the two pieces. In case of the wafer, the temperature span is less than 10 °C at 450 °C set temperature inside a circle with 3 in diameter. In other word, the temperature variation on the wafer is only 3% caused by the heat loss through the cooling

lines. In case of the pieces placed 1 cm away from each other they show approximately the same maximum temperature of 368 °C (see Fig. 3.3 caption).

To find out the temperature offset between the thermocouple and the sample at different set temperatures, IR measurements should be done for every temperature set at the Eurotherm. Figure 3.4 shows that the offset becomes higher by increasing the set temperature.

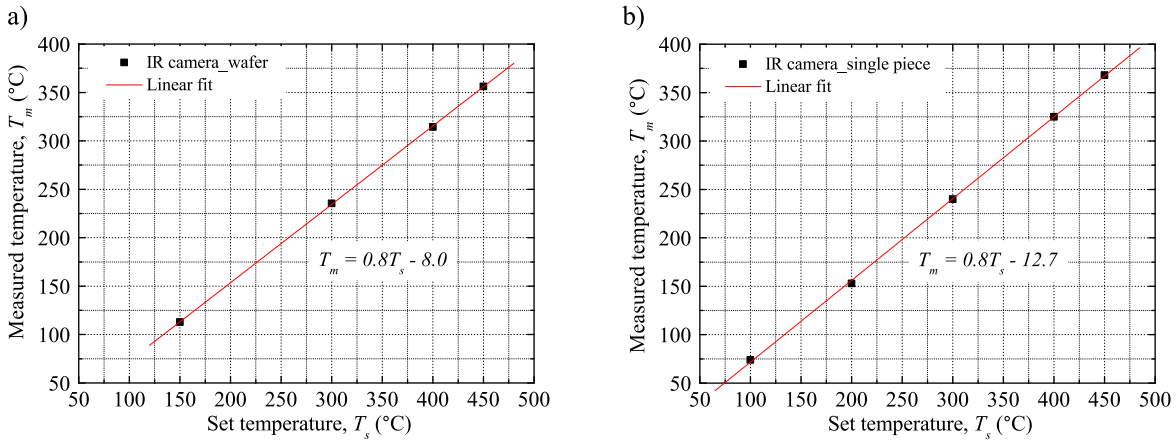

Figure 3.4: *Temperature calibration performed by the IR camera for* ***a)*** *a 4″ Si wafer on the heater, and* ***b)*** *a single piece in the center of the heater. As the temperature of the thermocouple T_s is set at higher values, the offset temperature will increase with respect to the surface temperature T_m of the explored specimens.*

3.3 Optical and Electron-beam Lithography

To fabricate the TMR junctions, the photoresist AZ 6612 (positive), AZ 6632 (positive), and AZ 5214e (image reversal) are deposited on 4″ Si wafers and Si-wafer pieces by a OPTIspin ST22 spin coating from SSE Sister Semiconductor Equipment GmbH. The UV exposure to the spin-coated resists is carried out using a SÜSS MicroTec Mask Aligner MA-6/BA-6. The resolution of the device is experimentally proven to be around 700 nm. This machine is also capable of backside alignment, which allows structuring on either sides of wafers according to the other side. For strain gauges used to investigate mechanical hysteresis (See section Appendix-E.1) AR-N 7520.17 electron-beam (e-beam) resist (negative) from Allresist GmbH is applied to Si-wafer pieces. This resist allows pattering of smaller features (30 nm) with much lower dose-dependency of the structure width[220]. The resist is scanned according to input drawings by an e-beam using an integrated advanced SEM/FIB nanolithography system from Raith GmbH.

3.4 Dry Etching

Ion Beam Etching

Following the optical and e-beam lithography, the patterned photoresist structures are transferred into metallic layers by an IBE system of Ionfab300plus from Oxford Instrument. This technique is physical and not-selective suitable for patterning of the MTJ stack. Wet etching of different materials in the stack can be problematic and chemical solutions attack the materials selectively. The chamber has a base pressure of 1×10^{-7} mbar and an Ar pressure of 1×10^{-4} mbar during etching. Ar ions generated in a plasma chamber by an RF generator (1000 W and 13.56 MHz) are extracted into an etching chamber through accelerating grids. The device is equipped by a secondary ion mass spectrometry (SIMS) which analyzes the removed materials from the surface of the sample by passing them through energy filters. This is very helpful to stop an etching process precisely at a desired layer (see a SIMS profile in Fig. 4.7). The stage can be rotated at 8 rpm to conduct a uniform etching process.

Regarding IBE of the stack, it is critical to avoid re-deposition at sides of the junctions. This causes parallel current paths and shorting the tunnel barrier. Such concern is generally fulfilled by having a neutralizer which supplies electrons to the ion beam (Ar^+). In addition, a low ion beam current (70 mA), which results in a low etching rate, is used to avoid surface damages and the stage is angled at 30° to the normal incidence of ions. The stage is also rotated in order to obtain homogenous etching all over samples[221].

Reactive Ion Etching

To etch Si and SiO_2 substrates with vertical profiles (see Fig. 4.16) an ICP-RIE SI500 device from SENTECH Instruments GmbH is used. The etcher has a plasma source with a 1200 W RF power supply (13.56 MHz) and an automatic matching network, and offers substrate electrodes for wafers with a diameter of up to 6″. Its planar triple spiral antenna produces an inductive high-density and low-energy plasma including reactive species, ions, and electrons at a low operation pressure. An additional bias source controls the ion bombardment energy. Therefore, the ion density and the ion kinetic energy are tuned independently. This avoids damage of small features within deep RIE processes, which require a high etching rate. Parameters for SiO_2 etching are given in Table 3.2.

In contrast to SiO_2, Si is etched in a sequence of parameterized steps. Recipes for Si dry etching are usually a modified version of the Bosch process, which allows much higher aspect ratios, being obtained by very high etch rate selectivity[222]. Table 3.3 shows a range of Si etch process conditions. The table indicates process conditions which were performed to establish reasonable etch sidewall profiles. All etching recipes include three main steps and some an additional evacuation step. The process starts with passivation (Fig. 3.5), whereby C_4F_8 is dissociated into CF_2 forming a Teflon-like

Table 3.2: *Processing parameters for the reactive ion etching of SiO_2 (Etching rate: 230 nm/min).*

Parameter	
ICP power	800 W
Bias (RF) power	120 W
CHF_3 flow	50 sccm
Temperature	RT

polymer ($(CF_2)_n$) on the surface[223]. As a result, bottoms and sidewalls of features on the surface are covered by the polymer films. Then, the polymer films are removed only at the bottom of the features during a so-called depassivation step in presence of a large bias voltage which enhances etching directionality. Therefore, the sidewalls are still protected during the etching step, within which the surface is exposed to SF_6 gas. In some recipes at the end of each cycle, an additional step is implemented to evacuate the chamber from the etching radicals and the by-products. This step also leads to very effective stabilized plasma in the passivation step of the next cycle.

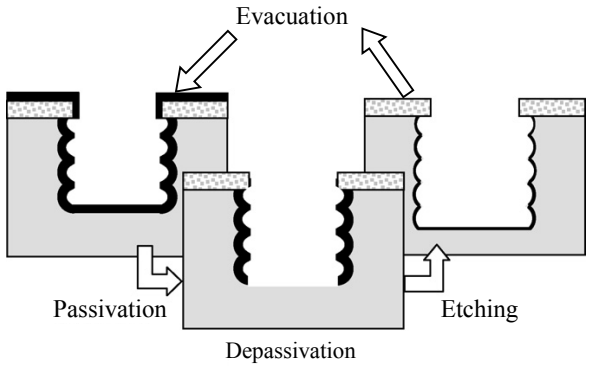

Figure 3.5: *Schematic viewgraph of a modified Bosch process. Each scallop indicates one etching cycle, in which sidewalls are protected by polymeric coatings (solid black) deposited during the passivation step. Reproduced with permission from Ref. 224 © 2008 Elsevier.*

In ICP systems, the matching circuit is usually operated automatically, whereby one load and one tuning capacitors vary accordingly in order to minimize the reflected power and to keep the plasma stable. The values for the capacitors strongly depend on several parameters which define the load impedance, like the gas composition, the chamber pressure, the electrode size, the power density, and possible magnetic confinement[225]. Therefore, in this study different values were chosen for each step since the pressure and the gas alter in every step. Such optimization should be regularly carried out since the chamber condition varies over time. Figure 3.6 displays how the optimized values of the capacitors improve sidewall profiles. Stable plasma results in successful wall protection, which promotes vertical sidewalls and suppressed underetching. Note that the parameters, which are notified on SEM images in this section,

Table 3.3: *Processing parameters of Si etch recipes by RIE. The matching box is tuned except for the process 1. The process 5 is the optimum recipe, which will be used for fabrication of the AFM cantilevers in this study.*

Process	Passivation					Depassivation				
	Gas/Flow (sccm)	Pressure (Pa)	Source (W)	Bias (W)	Time (s)	Gas/Flow (sccm)	Pressure (Pa)	Source (W)	Bias (W)	Time (s)
1	C_4F_8/50	1.5	700	9	8	O_2/50, N_2/199	3	700	16	3
2	C_4F_8/50	1.5	700	9	8	O_2/50, N_2/199	3	700	16	3
3	C_4F_8/50	1.5	600	9	8	O_2/50, N_2/199	3	700	14	3
4	C_4F_8/50	1.5	600	9	8	O_2/50, N_2/199	3	700	14	3
5	C_4F_8/50	1.5	700	9	8	O_2/50, N_2/199	3	700	14	3
6	C_4F_8/50	1.5	700	9	8	O_2/50, N_2/199	3	700	16	3
7	C_4F_8/50	1.5	700	9	8	O_2/50, N_2/199	3	700	20	3

Process	Evacuation			Etching				
	Gas/Flow (sccm)	Pressure (Pa)	Time (s)	Gas/Flow (sccm)	Pressure (Pa)	Source (W)	Bias (W)	Time (s)
1		—		SF_6/259	3	1000	15	14
2		—		SF_6/259	3	1000	15	14
3		—		SF_6/259	3	1000	15	14
4	C_4F_8/100	3	10	SF_6/259	3	1000	15	14
5	C_4F_8/100	3	10	SF_6/259	3	1000	15	14
6	C_4F_8/100	3	10	SF_6/259	3	1000	15	14
7	C_4F_8/100	3	10	SF_6/259	3	1000	15	14

indicate differences of their etching recipe with the optimum recipe, the process 5, in Table 3.3.

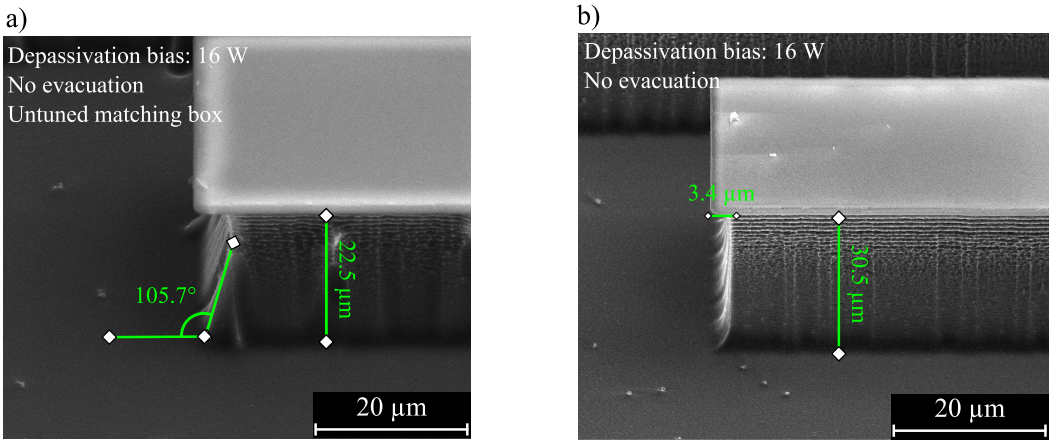

Figure 3.6: *SEM images of sidewall profiles etched by* ***a)*** *the process 1 and* ***b)*** *the process 2 after 40 cycles. Both samples were etched using the same recipe except the values of the load and tuning capacitors were only optimized for the process 2. Optimized parameters are referred to parameters at which zero reflected power and stable plasma are obtained.*

The evacuation step, which occurs between every etching and passivation steps, provides a smooth transition without abrupt peaks in the reflected power. Simultaneously, the etching radicals and the by-products are evacuated from the chamber. This allows stable palsma and uniform polymerization during the passivation step. Figure 3.7 shows the influence of the evacuation step by comparing performance of the processes 3 and 4. It is clear that the underetching reduces by half and the sidewall profiles become much more vertical by adding the evacuation step.

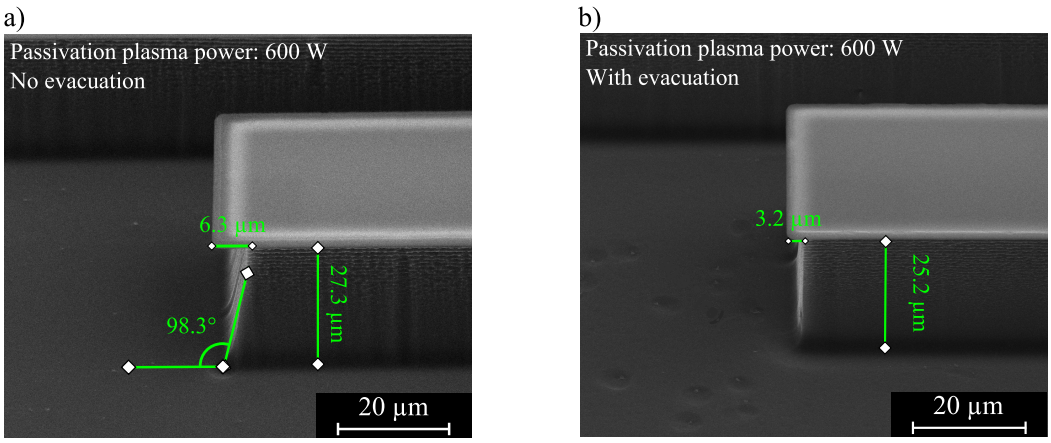

Figure 3.7: *SEM images of sidewall profiles etched by* ***a)*** *the process 3 and* ***b)*** *the process 4 after 40 cycles. The evacuation step between the passivation and the etching steps leads to smaller underetching and more vertical sidewalls.*

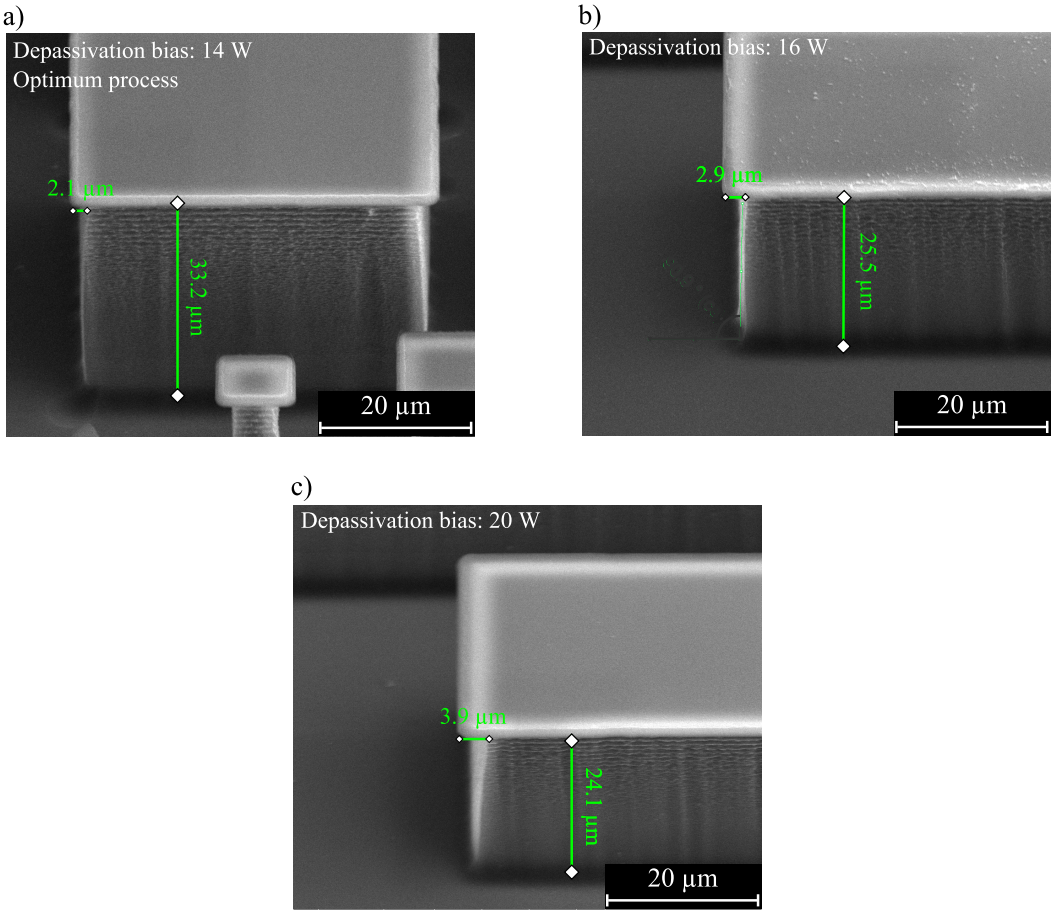

Figure 3.8: *SEM images of sidewall profiles of samples etched by* ***a)*** *the process 5 (etching rate: 0.3 µm/cycle),* ***b)*** *the process 6, and* ***c)*** *the process 7 after 40 cycles. Higher bias power may attack the passivation on the sidewalls and promote the lateral etching. The process 5 is the optimum process since it offers underetching of 2.1 µm, the smallest among the processes in Table 3.3.*

Figure 3.8 shows the influence of bias power of the etching step on the underetching. Applying bias power promotes the removal of the polymer film at the bottom of the trench (see Fig. 3.5), and consequently improves the aspect ratio. However, a very high bias power imposes a negative impact by attacking the passivation on the sidewalls and enhancing lateral etching. Comparison of the process 5 in Fig. 3.8 a), and the process 4 in Fig. 3.7 b) indicates that increase of the plasma power in the passivation step from 600 W to 700 W can enhance the protection of the sidewalls and reduce the underetching up to about 1 µm.

The optimum recipe, the process 5, is advantageous to offer a stable and uniform etching condition on a 4″ Si wafer. It offers 2.1 µm underetching at etch depth of 33 µm with an etching rate of 0.3 µm/cycle. SEM images of sidewall profiles at an etch depth of approximately 23 µm, shown in section Appendix-A.1, clearly demonstrate a uniform etching condition and etching depth over a 4″ Si wafer.

3.5 Scanning Electron Microscopy

The Helios Nanolab 600 dual-beam SEM/FIB device also offers high resolution SEM images with acceleration voltage up to 30 kV. In this work, the SEM is used to visualize conditions of TMR junctions in terms of their shapes, roughness of edges, performance of wet anisotropic etching by KOH, dimensions of the AFM cantilevers and the grown tips, etching profiles of features defined by dry etching, and location of the junctions on the AFM cantilevers.

3.6 Optical Microscopy

In addition to SEM investigations, the performance of UV-lithography processes and MEMS techniques are inspected by an ECLIPSE L200 optical microscopy from Nikon. Light in the middle of the visible spectrum with a wavelength of 500 nm can resolve features down to approximately 300 nm[226]. Si etch depth above 100 µm, etched by KOH, is also calculated by measuring width of slanted {111}-oriented planes, considering the anisotropic etching and the angle between the Si{111} and the Si{100} planes.

3.7 Profilometer

Si and SiO_2 etch depth up to 100 µm developed by wet and dry etching techniques are measured by a XP-2 Stylus profilometer from Ambios Technology. The device offers 1.5 Å and 15 Å vertical resolutions for 100 µm and 400 µm vertical ranges, respectively. The lateral resolution is about 100 nm[227]. The profilometer is also used to measure the sputter-deposition rate for different types of thin films (see Table 3.1). Another

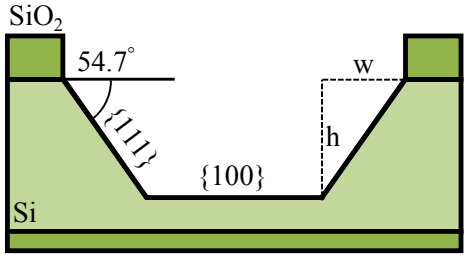

Figure 3.9: *Schematic of planes orientation during the anisotropic etching by KOH. The etch depth h can be calculated by $h = w \cdot tan(54.7^{\circ})$ with w being the width of the slanted Si{111} planes.*

usage of this device is to evaluate lithography processes, in addition to the inspections performed by the light microscopy.

3.8 Atomic Force Microscopy

An AFM with an Autoprobe CP-Research model from THERMO MICROSCOPE instruments with a APSC-0100 model large area scanner is used to measure topography of Si surfaces etched in KOH solutions. The scanner offers maximum lateral and vertical scan ranges of 100 µm and 7.5 µm with maximum resolution of 0.25 Å and 0.025 Å, respectively. The aim is to improve surface roughness applying different modifications to the KOH solutions. To determine the roughness, a few 10 µm × 10 µm areas are scanned by commercial Si_3N_4 cantilevers from Nanosensors with a nominal spring constant of 0.1-0.6 N/m. The cantilevers are integrated to pyramidal tips with a height range of 2.5 µm to 8 µm and a nominal tip radius of 20 nm. After the recorded image is treated by flatten auto, the root mean square (RMS) of the roughness is calculated by a software from ProScan Data Acquisition. Note that another AFM setup described in section 7.1 is used to investigate performance of the TMR self-sensing cantilevers.

Chapter 4

Sample Preparation

This chapter is focused on sample preparation procedures for the chapters 5, 6, and 7. In the first section, different etching parameters of KOH solutions are described with regard to the improvement of the etched Si surfaces and to the convex corner of the support chips (chapter 5). In the second section, the optimized fabrication flow for the magnetostrictive TMR sensors onto 3 mm × 25 mm cantilevers is explained step by step (chapter 6). Finally, it is shown that the TMR sensors can be successfully integrated to the AFM microcantilevers by a complicated but a certainly established fabrication process (chapter 7).

4.1 Si Anisotropic Etching

Surface roughness investigations were carried out on 4″ Si(100) wafers (purchased from Si-Mat Silicon Materials, Germany), single-sided polished and coated by a thermally grown SiO_2 layer (1.5 µm). To address our concerns about the reflectivity of the TMR-based AFM cantilevers, discussed in chapter 7, surface treatment of the TMR cantilevers, prior to the anisotropic etching in a KOH solution, was duplicated. The SiO_2 layer is structured via RIE using the same lithography mask as for dry etching of the backside oxide layer during the fabrication of the AFM cantilevers (see Fig. 4.13). For Si etching at the opened areas, a KOH 40 wt% solution is chosen to lower the number of morphological features[194,201,206] on the etched surface. Consequently, it leads to a better surface quality in comparison with other KOH concentrations. In order to enhance the surface quality further, several techniques were applied, as listed below:

- Exposing the opened Si areas, which appear in the SiO_2 layer after the RIE process, to an ammonium fluoride solution (purchased from Sigma-Aldrich), known as the buffered oxide etching (BOE) solution, for 1.5 min prior to Si etching.
- Temperature increase of the etching solution from 80 °C to 100 °C.
- Replacing magnetic stirring by ultrasonic agitation (400 kHz) with 250 W and

500 W power. The temperature of the solution is set to 60 °C due to a technical limitation of the ultrasonic transducer (purchased from SONOSYS Ultraschallsysteme GmbH).

- Adding SDSS 0.02 wt% (purchased from Cytec Industries Inc.) and Sb_2O_3 8×10^{-5} M and 33×10^{-5} M (purchased from Sigma-Aldrich) to the solution to avoid the need of the mechanical agitation.

Figure 4.1 shows a simple design of compensating structures introduced by Fan and Zhang[217]. Here, two compensating structures with small (a_1=200 µm, a_2=300 µm) and big (a_1=267 µm, a_2=533 µm) dimensions are applied at the corners of the support chips of the AFM cantilevers (see Fig. 4.13). The dimensions of these structures depend on the desired etch depth and additive materials[215,218].

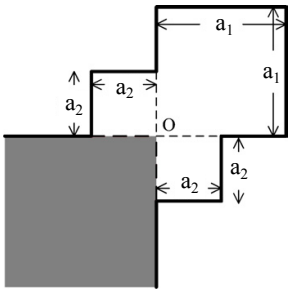

Figure 4.1: *Simple design of the compensating structure applied to a convex corner (gray). Reproduced with permission from Ref. 217 © 2006 Institute of Physics Publishing.*

4.2 Magnetostrictive TMR Sensors

The magnetic tunnel junction (MTJ) stacks were deposited on 4″ Si (525 ± 25 µm)/SiO_2 (1.5 µm) wafers, purchased from Si-Mat Silicon Materials, by Dr. Karsten Rott at *Bielefeld University*. The stack has the following multilayer structure (from bottom to top): Ta (5) / Ru (30) / Ta (10) / Ru (5) / MnIr (12) / CoFe (3) / Ru (0.9) / CoFeB (3) / MgO (1.8) / CoFeB (3) / Ta (5) / Ru (5). The numbers in parentheses indicate the layer thickness in nm.

The field annealing of the as-deposited stacks is carried out at about 360 °C for 1 h in a vacuum of 1×10^{-6} mbar under a magnetic field of 159.2 kA/m (2 kOe) (see section 3.2). Figure 4.2 depicts the direction of the applied field with respect to geometry of the junctions. The field direction defines the orientation of the induced magnetocrystalline anisotropy K_u.

As explained in section 2.6, aligning M_{sen} and M_{ref} along or perpendicular to the stress axis gives the opportunity to detect either tensile or compressive stress. Figure 4.3 demonstrates another configuration, in which the magnetocrystalline anisotropy and the unidirectional anisotropies in the layers (see section 2.6) are aligned at a 45° angle against the stress axis. In this configuration, both compressive and tensile stresses

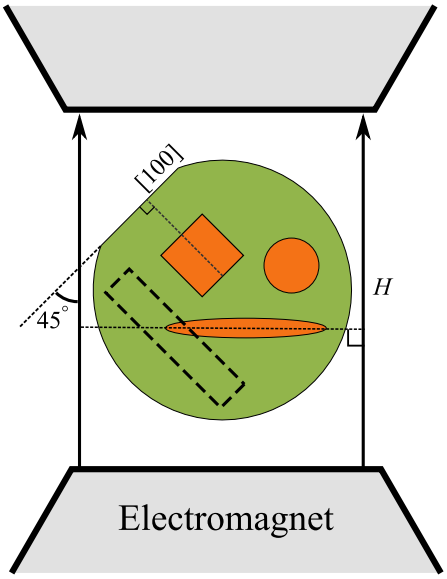

Figure 4.2: *Schematic of a wafer (green circle) mounted on the heating element between the poles of the electromagnet for the field annealing. The angle between the field direction and the [100]-flat of the wafer is 45°. The orange figures show positioning of the junctions, which will be patterned later, with round, squared, and elliptical shapes. The size of the junctions are exaggerated here. The dashed rectangle specifies the cantilever geometry. The orientation of the magnetization of the reference layer M_{ref} is set with respect to the long length of the cantilever, the stress axis, by the direction of the magnetic field H (see Fig. 4.3).*

cause changes in the angle α, and consequently the tunnel resistance. This extends the applications further to detection of both tensile and compressive uniaxial stresses by a single sensor[228].

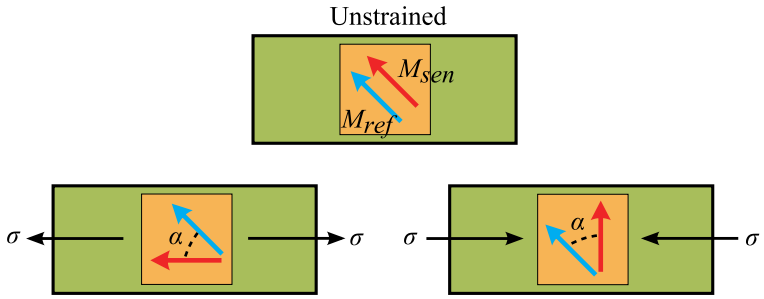

Figure 4.3: *Simple demonstration for detecting tensile and compressive stress by a single TMR sensor, in which the magnetization of the electrodes, M_{ref} and M_{sen}, are aligned at 45° with respect to the stress axis. Such alignment can be induced by the direction of the magnetic field during the field annealing process.*

On the contrary, for magnetostriction measurement of the sense layer (see section 6.6), the magnetic field is applied perpendicular to the [100]-flat of the wafer during the field annealing process. This defines the induced magnetocrystalline anisotropy K_u

perpendicular to the length of the cantilevers. As demonstrated in Fig. 4.4, M_{sen} and M_{ref} stay parallel at zero bias field in unstrained condition due to the Nèel coupling.

Figure 4.4: *The magnetocrystalline anisotropy K_u, M_{sen} and M_{ref} are set perpendicular to the length of the cantilevers during the field annealing for measuring magnetostriction of the sense layer (see section 6.6).*

As depicted in Fig. 4.5, the TMR junctions are structured using a sequence of MEMS techniques. This is achieved in three major steps of lithography: 1) bottom

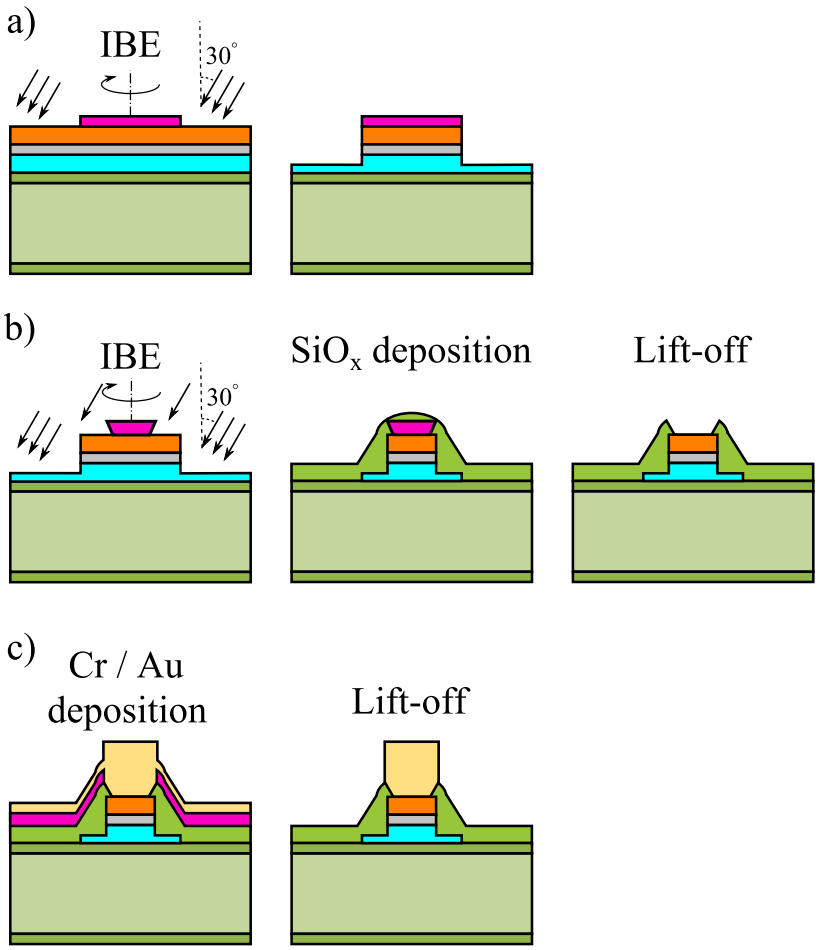

Figure 4.5: *MEMS fabrication flow of TMR junctions in three major steps. Layers of a junction are shown in three colors: layers above the tunnel barrier (orange), the barrier (gray), layers below the barrier (blue).* ***a)*** *Bottom electrode (BE): UV-lithography with a positive resist (violet) and ion beam etching (IBE),* ***b)*** *TMR junctions: UV-lithography with an image reversal resist (undercut profiles at sidewalls), IBE, SiO_x deposition (green), and lift-off, and* ***c)*** *top electrode (TE): UV-lithography with an image reversal resist, Cr/Au deposition (yellow), and lift-off.*

Table 4.1: *Nominal dimensions and shapes of the junctions. D, S, SA, and LA stand for the diameter, the side, the short axis, and the long axis, respectively.*

Area (µm^2)	Circle	Square	Ellipse(1:3)		Ellipse(1:10)	
	D (µm)	S (µm)	SA (µm)	LA (µm)	SA (µm)	LA (µm)
100	11.3	10	6.5	19.6	3.6	35.7
289	19.2	17	11.1	33.2	6.1	60.7
729	30.5	27	17.6	52.8	9.6	96.4
1369	41.8	37	24.1	72.33	13.2	132.1

electrode (BE): to access the junctions electrically from below, 2) TMR junctions, 3) top electrode (TE). The TE and the BE are connected through contact lines, which are separated from the junctions. Table 4.1 gives details about nominal shapes and dimensions of the junctions.

The outline (blue area) shown in Fig. 4.6 is defined as the BE using standard optical lithography, followed by an IBE step (see section 3.4). This provides a common BE for all the junctions, which can be accessed from two sides (green rectangles) after the whole process is completed. Then, a patterned positive photoresist AZ 6632, special for dry etching, is used as a protective layer during the IBE process. Table 4.2 gives the details of the lithography process.

Table 4.2: *Processing parameters for the bottom electrode (BE) UV-lithography.* **purchased from MicroChemicals GmbH*

Processing step	Material/Parameter
Adhesion promoter	HMDS[1]/100 °C
Spin coating	AZ 6632*/4000 rpm, 30 s
UV-exposure	Hard contact, 11.8 s
Soft bake	110 °C, 50 s
Development	AZ 726 MIF*, 50 s
Hard bake	125 °C, 50 s

Prior to actual etching, a Ta layer deposited on a 6″ Si wafer is etched for 15 min to improve the base pressure of the etching chamber via the gettering effect. The beam current of 350 mA is set at high level to have a thicker deposited Ta layer on the inner walls of the chamber. Afterward, in purpose of defining the BE, the TMR stack outside of the blue region (zone 1) is etched in a 1.2×10^{-7} mbar base pressure. The etching is deliberately stopped once the signal of the most bottom Ru layer rises in the etching

[1] Abbreviation for 1,1,1,3,3,3-hexamethyldisilazane, this is used to improve adhesion of a Si wafer to resists, especially positive resists. Annealing is required to remove the surface water [229].

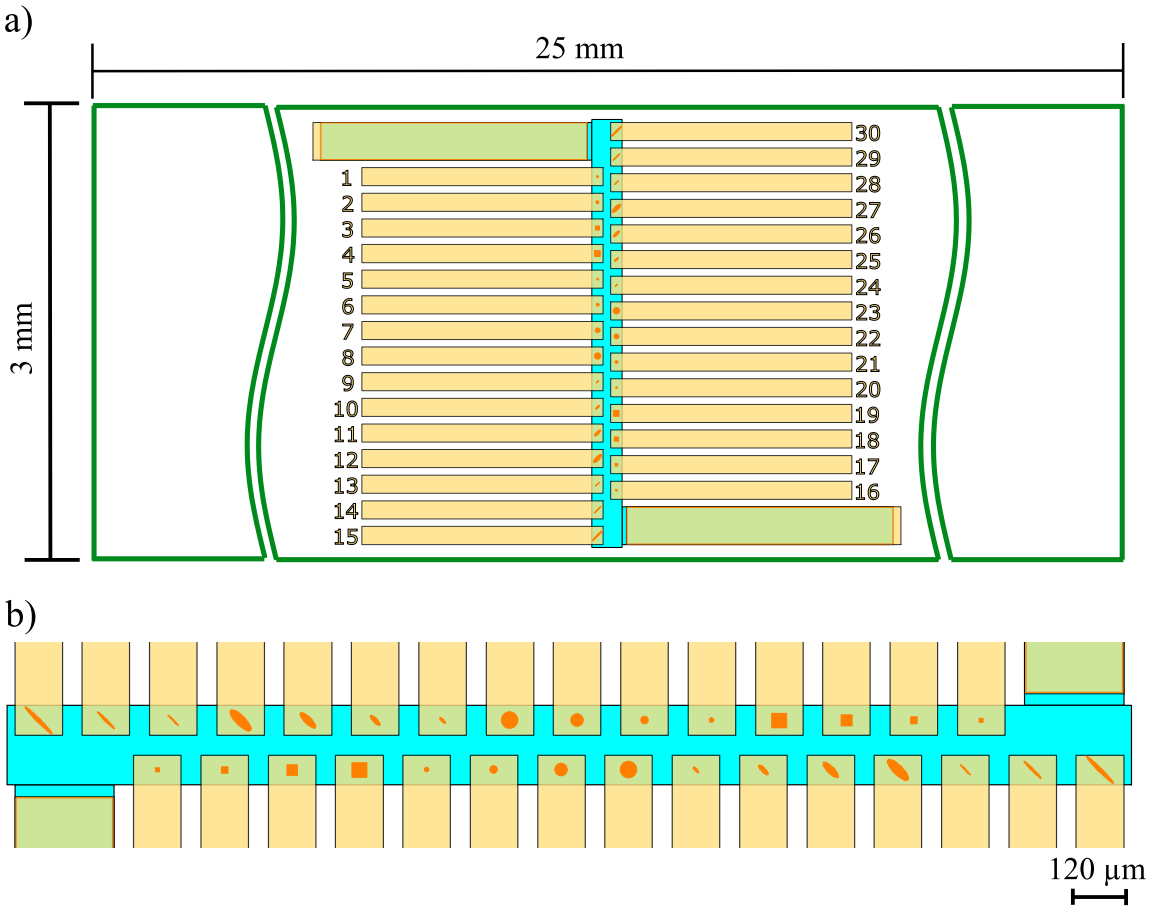

Figure 4.6: *Three masks are required to accomplish three major fabrication steps: bottom electrode (BE) (blue), TMR junctions (orange), and top electrode (TE) (yellow) (see Fig. 4.5).* ***a)*** *Mask drawings for a 3 mm × 25 mm Si cantilever (green outline). Using 5″×5″ Chromium masks (see Fig. Appendix-B.2), 73 cantilevers are fabricated from a TMR stack deposited wafer. The green colors of two rectangles indicate the overlap of three mask in that area. This gives an electrical access to the junctions from below.* ***b)*** *A zoomed-in view, rotated by 90°, of 30 junctions on a cantilever.*

depth profile of the SIMS, as shown in Fig. 4.7. This supposedly guarantees a metallic layer being in the surrounding while the MgO layer is being etched during pattering of the junctions in the next step. This avoids charging on the surface and consequently the re-deposition of etched materials[230]. Other conditions such as rotation of the stage, a 30° tilt of the stage, and the neutralizer are present during the etching (see section 3.4). Then, the residual resist is stripped off by n-methyl-2-pyrrolidone (NMP) at 60 °C in the ultrasonic bath with a frequency of 400 kHz. Typical time in the ultrasonic bath is set to 30 min and resist stripping is inspected by the optical microscopy. If necessary, a longer period and higher temperature are applied.

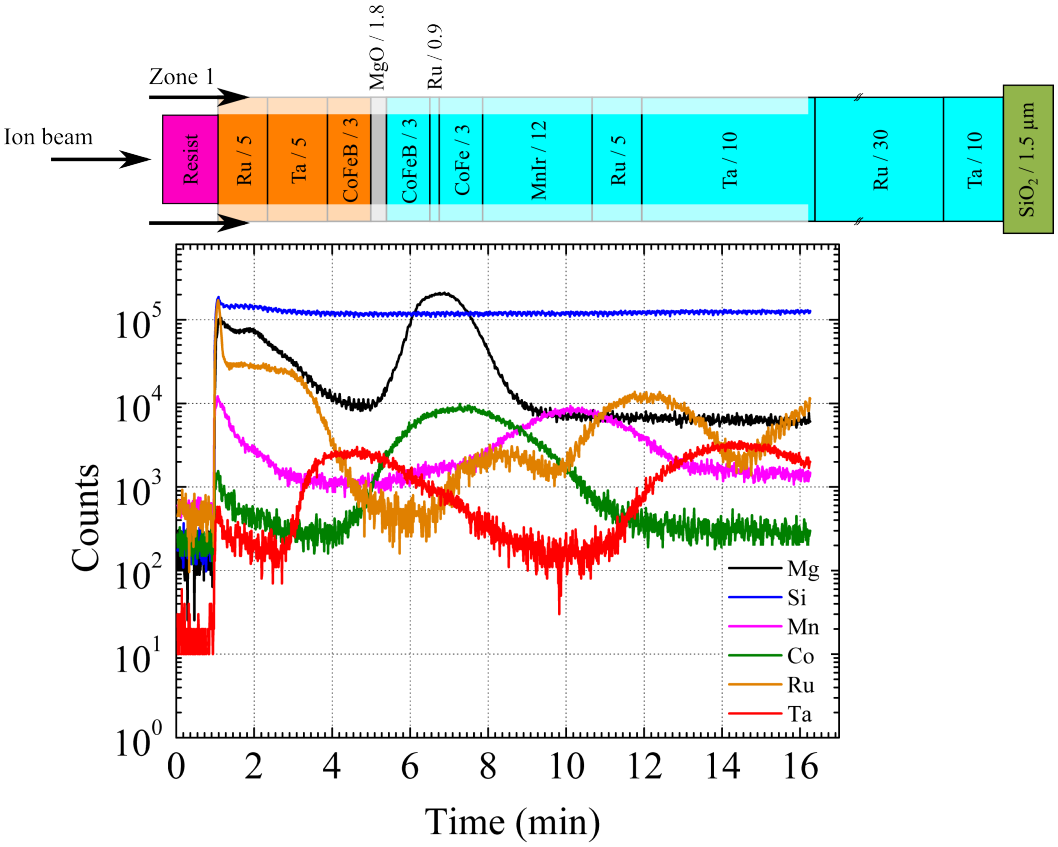

Figure 4.7: *SIMS etching depth profile (first). The jumps at the beginning indicate the opening of the shutter in about a minute after the SIMS detector is turned on. The profile starts with high Ru counts until the MgO maximum is reached after 6 min. The two separate CoFeB layers and the CoFe layer appear as a broad peak, which can be recognized by the rise of the MgO and Ru signals. A schematic on top approximately relates to the etching time, assuming that a layer is completely etched away, when counts of an element from the next layer start to rise.*

Patterning of the TMR junctions starts with image reversal lithography, as shown in Fig. 4.5 b). The processing parameters are summarized in Table 4.3. The undercut profile of the image reversal resist assists the lift-off process after the SiO_x deposition.

Table 4.3: *Processing parameters for the TMR junctions UV-lithography.*
* *purchased from MicroChemicals GmbH*

Processing step	Material/Parameter
Adhesion promoter	HMDS/100 °C
Spin coating	AZ 5214 e*/4000 rpm, 30 s
Soft bake	110 °C, 50 s
UV-exposure	Vacuum, 2.1 s
Reversal bake	120 °C, 2 min
UV-exposure	Flood, 9 s
Development	AZ 726 MIF*, 50 s
Hard bake	125 °C, 50 s

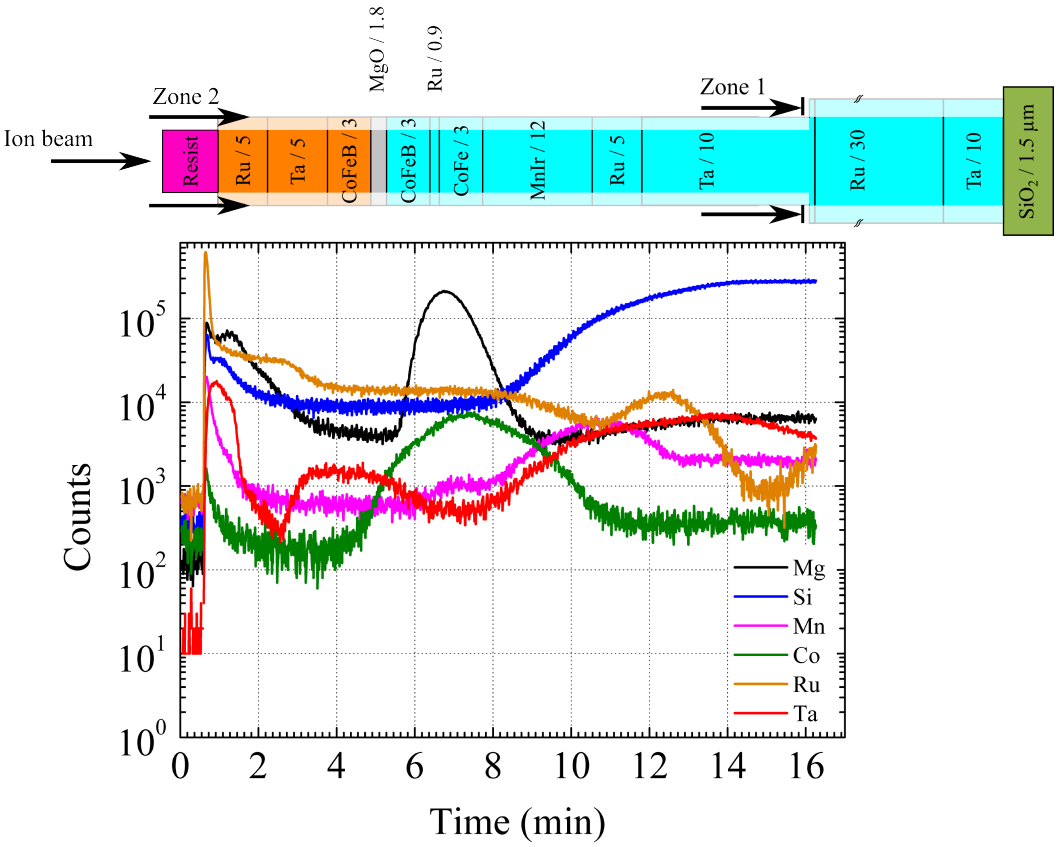

Figure 4.8: *SIMS etching depth profile (second). All the signals appear at nearly the same time except Ta and Ru ones owing to signals from the residual metallic layers from the BE structuring step (zone 1). For instance, it leads to a longer Ru peak at the beginning. The Si peak rising at 2 min after the MgO maximum indicates that the possible charging and the re-deposition at the sides of the barrier are prevented. At the end a thick (Ta 5 nm/Ru 30 nm) bottom electrode, zone 2, is left, which leads to low electrical resistance in contact lines. Such resistance is considered as series resistance, which might influence TMR effect amplitudes in case of junctions with a low RA. Numbers indicate layers thickness in nm.*

After the gettering process by the Ta etching, the junctions plus two large rectangular pads are structured on the BEs (blue elements) by another IBE process. During etching the thin layer left intentionally from last step (zone 1) is removed completely, which is noticeable as a Si peak in the SIMS depth profile shown in Fig. 4.8. The last Ru layer being etched in the surroundings (zone 1) as the MgO layer is reached in the etching depth (zone 2) prevents the surface charging.

Immediately, the wafer is transferred to the sputtering chamber for depositing a 150 nm thick SiO_x layer (see section 3.1). It prevents any physical contact between the top and bottom contact lines so that the electrical current path is through the barrier. Prior to the actual SiO_x deposition, free sputtering is performed for 20 min to clean up the Si target.

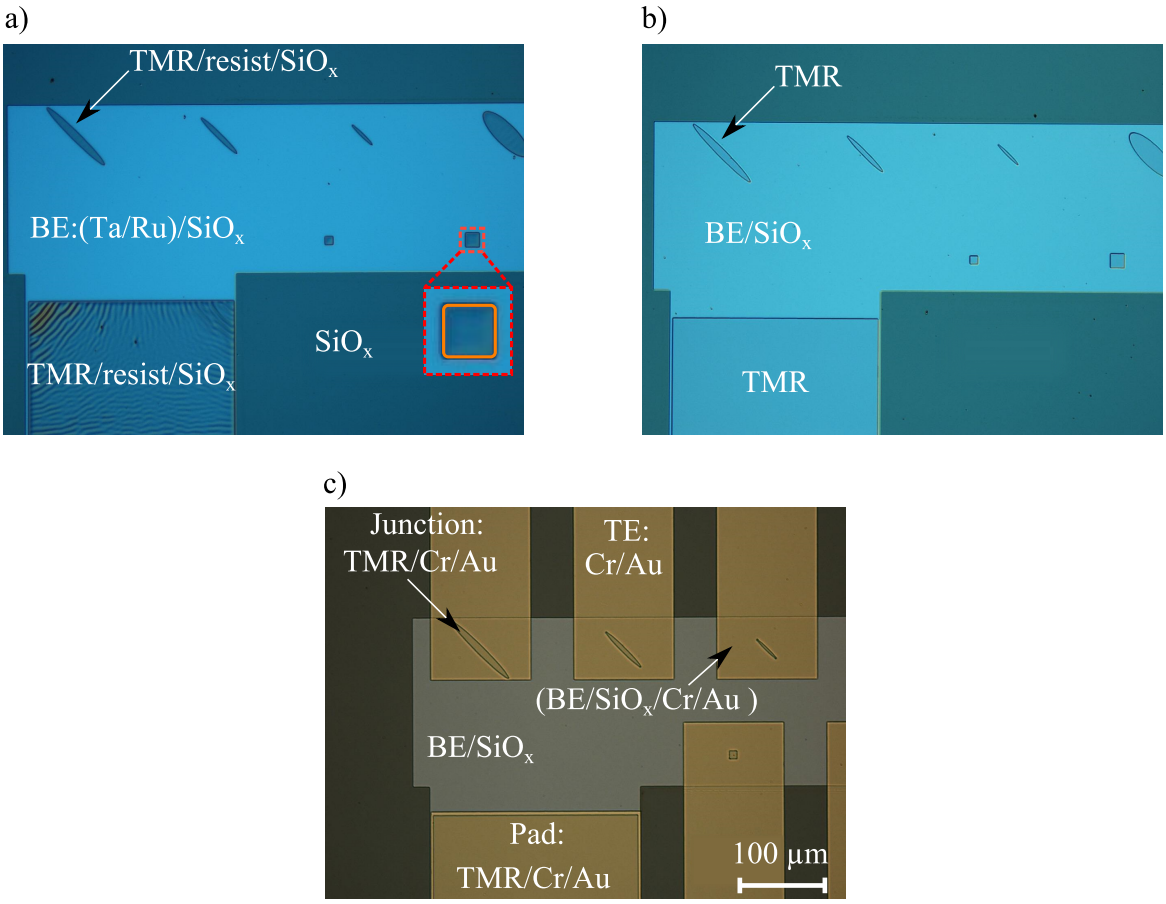

Figure 4.9: *Optical microscopy images after* ***a)*** *the SiO_x deposition,* ***b)*** *the first lift-off in NMP, and* ***c)*** *the Cr/Au deposition and then the second lift-off. Wrinkles due to the film stress in the resist disappear, which is an indication for the end of the first lift-off. The orange outline shows round corners of the squared junction.*

Stress induced due to SiO_x deposition wrinkles the resist which is patterned in the last lithography. This can be taken as a reference for the first lift-off being successful. Figure 4.9 a) taken by the optical microscope vividly shows that the wrinkles disappear by removal of both the resist and the oxide layer above (see Fig. 4.5 b)). In order to realize the openings, the wafer is kept in a 75 °C hot NMP inside the ultrasonic

bath (40 kHz). The openings include the TMR junctions (orange) and the two large TMR pads (two green rectangles) providing an electrical access to the junctions from bottom.

In order to electrically access the junctions from top without any damage, extended TE contact lines (yellow rectangles) are necessary. At regions where the TE contact lines overlap the common BE, the quality of the SiO_x layer plays a critical role to protect the junctions from any short circuits. As shown in Fig. 4.6, every junction has a separate TE. Performing a UV-lithgraphy process with AZ 5214 e resist (see Table 4.3) followed by the Cr (20 nm) / Au (130 nm) deposition, the contact lines are defined by the second lift-off process inside the ultrasonic bath. Note that since the lithography is less critical in this step in terms of the resolved feature size, the hard contact exposure mode is chosen.

Figure 4.10 shows deviation of junction dimensions from the nominal values listed in Table 4.1. The standard deviation is calculated for the junctions placed in a concentric circle with a diameter of 1″ on the wafer. The junctions, which will be used for the strain sensitivity characterization in chapter 6, are chosen from this region. Investigating junction dimensions by SEM, for all sizes and shapes the mean area value is slightly less than the nominal one. This can be attributed to the IBE process leading to early removal of thin resist layers at the edges, and as a result to the area reduction. The standard deviation of the side, the diameter, and the axis in the squared, round, and elliptical junctions depends slightly on the junction size and shape, but stays below 350 nm (4 %). The standard deviation of the junction area increases for lager junctions to a value close to 25 µm². The nominal dimensions and areas will be corrected by the mean values with the standard deviation in chapter 6.

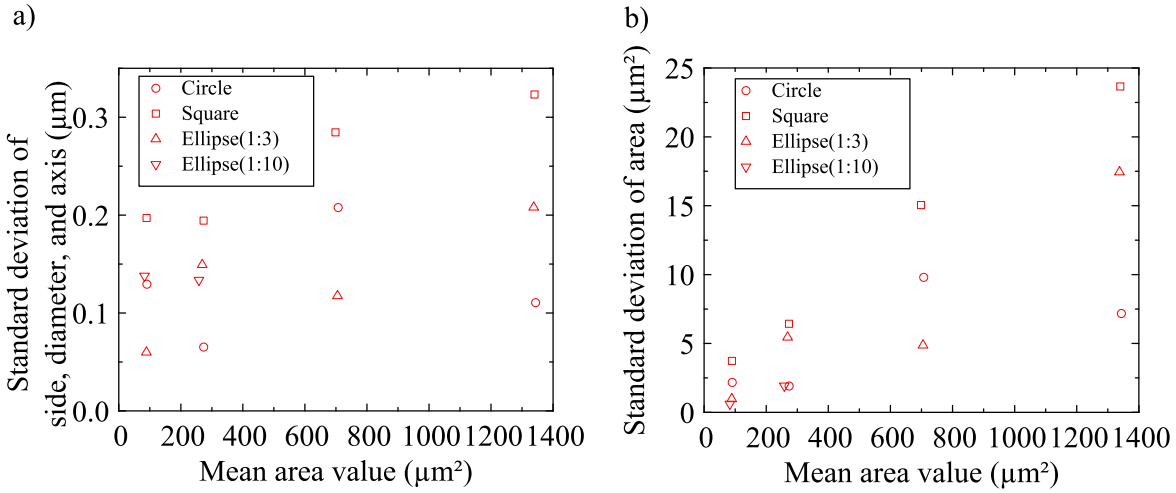

Figure 4.10: *Standard deviation of junction dimensions from the nominal values given in Table 4.1. For a specific junction and shape dimensions of three junctions placed in a concentric circle with a diameter of 1″ on the wafer are investigated using SEM. The standard deviation of the side, the diameter, and the axis in the squared, round, and elliptical junctions stays below 350 nm(4 %). The standard deviation of the junction area reaches 25 µm² for the largest junction. Values for Ellipse(1:10) with a nominal area of 729 µm² are missing because of damages by the dicing trench.*

At the end the wafer is diced into seventy three 3 mm × 25 mm-sized cantilevers. A 160 µm wide dicing path between the cantilevers is included in the mask design so that the saw trench will not affect the junctions at the outermost sides. For strain measurement, every junction is wire bonded from an exclusive top and a common bottom contact lines (see Fig. 4.11). But as for TMR characterization precise needles are sufficient to apply the bias voltage.

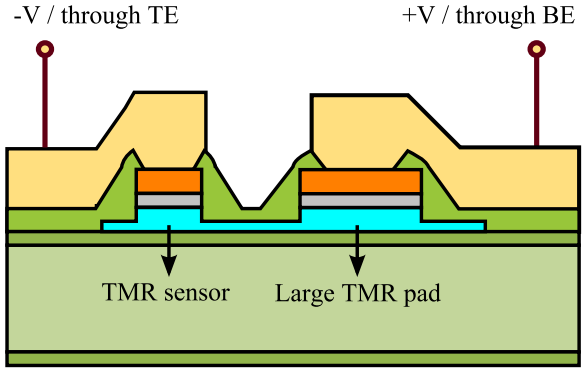

Figure 4.11: *The TMR junctions are contacted at the bottom through the large TMR pads and the common BE. Due to their large size, these pads reveal a very low electrical resistance as well as negligible TMR effect amplitudes in serial measurements.*

4.3 Self-sensing Microcantilevers

Considering high strain sensitivity of the TMR junctions, presented in chapter 6, the same multilayer structure is deposited on the front side of 4″ Si (300 ± 2 µm) wafers, purchased from Si-Mat Silicon Materials, by Dr. Karsten Rott at *Bielefeld University*. The substrate is covered on front with a 2 µm-thick and on back with a 100 nm-thick thermally grown silicon dioxide layer. They respectively serve as a hard mask for KOH etching and as an insulating substrate for the TMR junctions. Spring constants and resonance frequencies in the range of commercial cantilevers are intended to achieve a reasonable variation of cantilever flexibility and stability.

The self-sensing TMR cantilevers are fabricated in four major steps (Fig. 4.12): 1) dry etching: structuring the backside SiO_2 layer, 2) patterning of the TMR junctions on the front side of the wafer, explained thoroughly in section 4.2, 3) wet etching: etching down the Si wafer from the back side, 4) dry etching: release of the cantilevers. In Table 4.4 the details of the squared TMR junctions and the AFM cantilevers are given.

The fabrication process starts with transferring windows or openings into the backside SiO_2 layer (Fig. 4.12 a)), the hard mask, for the later anisotropic KOH etching of Si. Green areas in Fig. 4.13 are covered by AZ 6632 photoresist as parameters in Table 4.2 are applied. The windows dimensions on the mask have been precisely calculated so that it leads to openings after approximately 290 µm Si etching and enough

Table 4.4: *Nominal parameters for the TMR self-sensing microcantilevers. Young's modulus of 169 GPa is considered for spring constant calculation (see section 2.10.1) since the length of the cantilevers is along the [110] direction. The resonance frequency is defined as:* $f = 0.162\sqrt{\frac{Y}{\rho}} \cdot \frac{t}{L^2}$ [231] *with* $\rho = 2330\,kg/m^3$ *being the Si density.*

No.	Length, L (µm)	Width, w (µm)	Thickness, t (µm)	Spring constant (N/m)	TMR size (µm^2)	Resonance frequency (kHz)
1	700	20	10 ± 2	1.3 - 4.3	10×10	22.5-33.8
2	650	20	10 ± 2	1.6 - 5.3	10×10	26.1-39.2
3	600	20	10 ± 2	2 - 6.8	10×10	30.7-38.3
4	700	30	10 ± 2	1.9 - 6.4	17×17	22.5-28.2
5	650	30	10 ± 2	2.4 - 8	17×17	26.1-32.7
6	400	40	10 ± 2	13.5 - 45.6	27×27	69-86.2
7	370	40	10 ± 2	17.1 - 57.7	27×27	80.6-100.8
8	350	40	10 ± 2	20.2 - 68.1	27×27	90.1-112.6
9	300	40	10 ± 2	32 - 108.2	27×27	122.6-153.3
10	350	50	10 ± 2	25.2 - 85.1	37×37	90.1-112.6

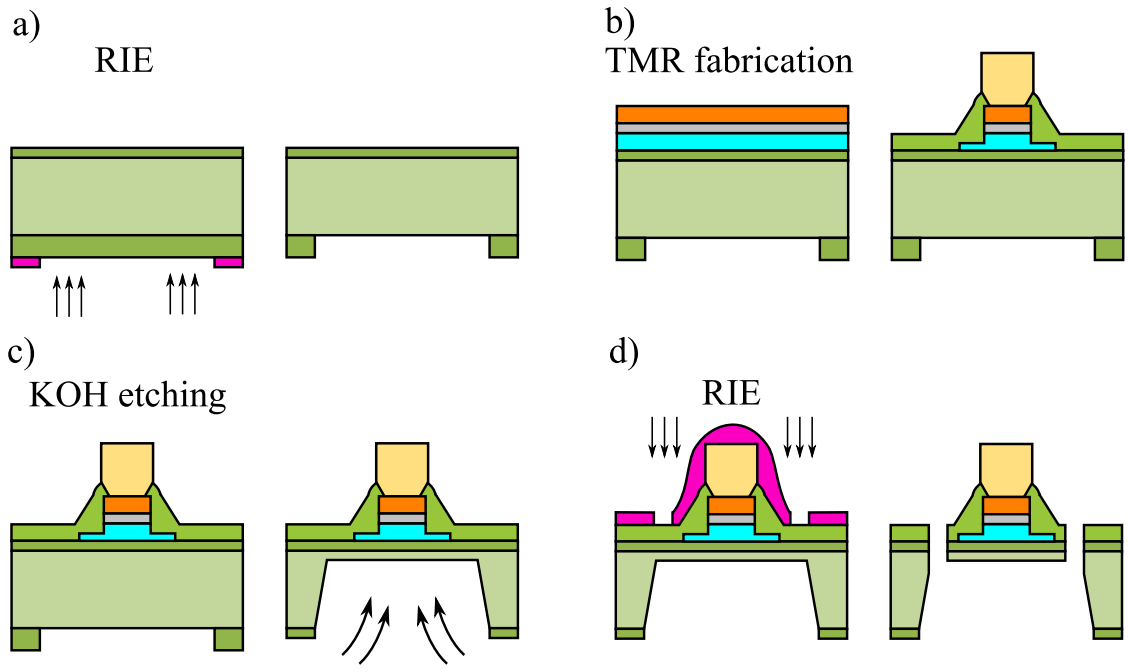

Figure 4.12: *MEMS fabrication flow of the self-sensing TMR microcantilevers.* ***a)*** *Structuring the backside SiO_2 layer: UV-lithography with a positive resist (violet) and reactive ion etching (RIE),* ***b)*** *the fabrication of TMR junctions (see details in Fig. 4.5),* ***c)*** *etching down the Si wafer in a KOH bath, and* ***d)*** *release of the cantilevers: UV-lithography with a positive resist and RIE.*

space to detach the microcantilevers without any damages to the cantilevers. The SiO_2 layer in the outer regions is removed using RIE for 545 s (etch depth $\approx$ 2100 nm). Etching parameters are given in Table 3.2. Meanwhile, the front side of the wafer should be coated by a photoresist to protect it from possible scratches and contamination.

The structuring of the hard mask is preferably carried out before the stack deposition. Then, the residual resist is stripped off by Aceton or NMP at RT or at 75 °C in the ultrasonic bath with 40 kHz.

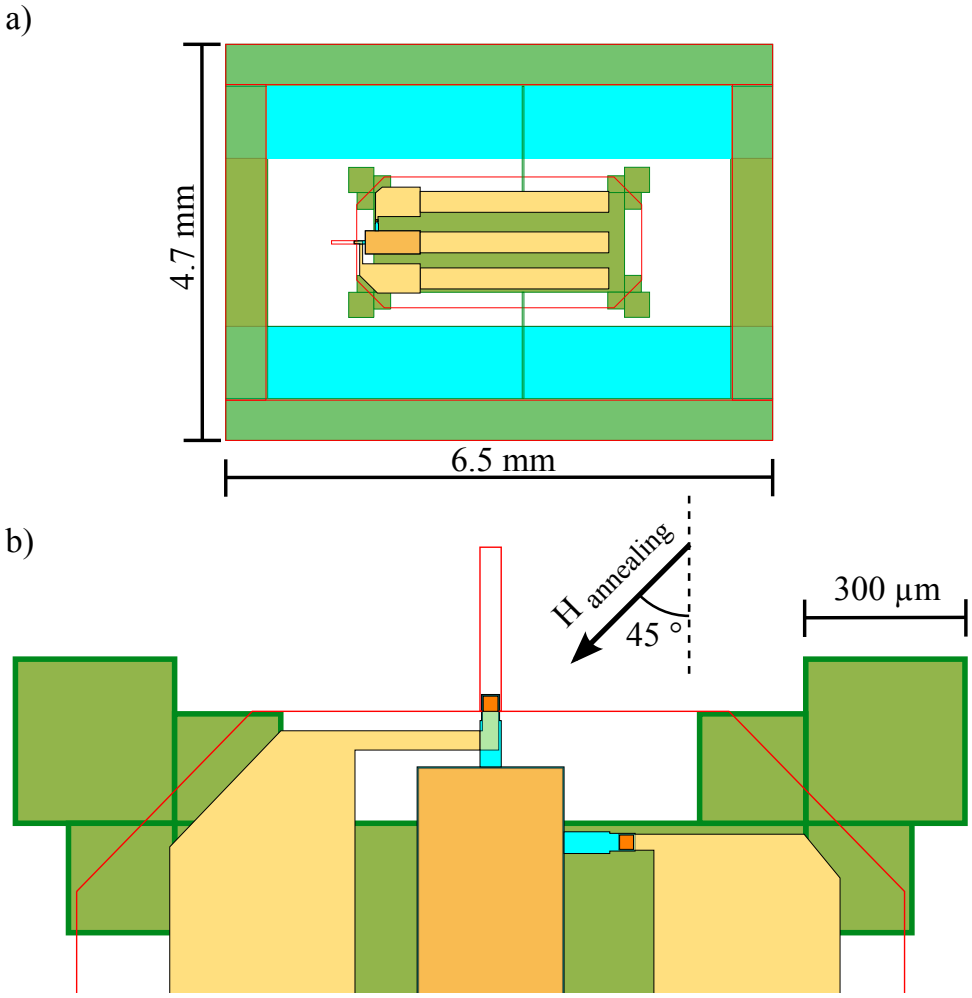

Figure 4.13: *Five masks are required to accomplish fabrication steps: dry etching of the backside SiO_2 layer (green), bottom electrode (BE) (blue), TMR junctions (orange), top electrode (TE) (yellow), and the release of the cantilevers from the front side (red).* ***a)*** *Drawings of a single unit including a cantilever integrated to a bulky support chip, which is attached to a rectangular frame by two narrow bridges. Using 5″×5″ Cr masks (see Fig. Appendix-C.2), 128 units, self-sensing cantilevers, can be fabricated from a 4″ TMR-stack-deposited wafer.* ***b)*** *A zoomed-in view of a single unit. There are two junctions designed; one on the cantilever as the deflection sensor and the other on the chip as the reference sensor. The two junctions have separate TEs while sharing a common BE (in the middle). The green squares serve the compensating structures during KOH etching. The arrow shows the orientation of the applied field during the field annealing conducted before the stack patterning.*

After the TMR stack deposition, the wafer is annealed at about 360 °C for 1 h in a vacuum of 1×10^{-6} mbar under a magnetic field of 159.2 kA/m (2 kOe) (see section 3.2). As marked in Fig. 4.13 b), the annealing field is applied at a 45° angle against the

length of the cantilever or the stress axis, which is the same as for samples for the four-point bending measurements. Afterward, the fabrication is proceeded by definition of the BE according to the alignment marks of the patterned SiO_2 layer on the back using backside alignment lithography. The two large blue strips (see Fig. 4.13 a)) are deliberately included to improve the signals in SIMS spectrum. Other than this, structuring of the TMR junctions is the same as explained in section 4.2. Two TMR junctions are patterned on an AFM cantilever and its support chip. One is placed at the fixed end of the cantilever, which serves as a deflection sensor experiencing maximal stress during bending. The second is located on the chip and only incorporated as a reference sensor for optional differential measurements. To build up a common BE a large rectangular TMR pad is added on the support chip. As shown by optical microscopy images in Figure 4.14, the corners of squared junctions are rounded. This is regarded as optical lithography limitation. The round corners in structured resists are transferred to the junctions after IBE. Figure 4.15 a) shows the look of the front side after finishing the TMR fabrication.

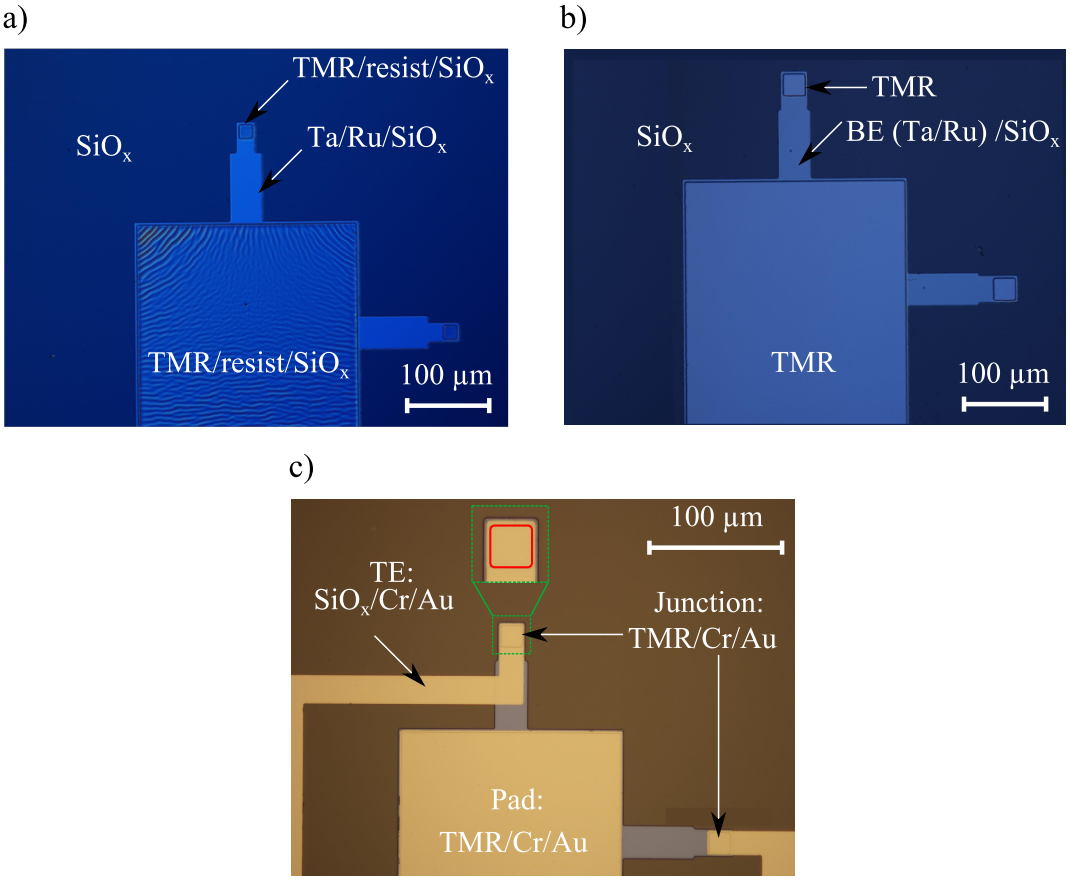

Figure 4.14: *Optical microscopy images after* ***a)*** *the SiO_x deposition: film stress forms wrinkles in the resist,* ***b)*** *the first lift-off by NMP: the top of the two TMR junctions and the pad become open , and* ***c)*** *the Cr/Au deposition and then the second lift-off. Orange outline depicts round corners of the nominally squared junction.*

Prior to Si etching in a KOH bath, the residual oxide from the areas opened by RIE in the first step and the native oxide layer are effectively removed by the ammonium

fluoride solution (see Table 5.1). The backside of the wafer is exposed to ammonium fluoride for 1.5 min while the front side is protected by a hard-baked layer of AZ 1518 resist purchased from MicroChemicals GmbH. Then, the wafer is mounted inside a wafer holder made entirely from PEEK (purchased from Advanced Micromachining Tools), which is designed for a single-side time based etching process. Etching of the Si wafer for about 4 h and 35 min in a KOH-40 wt% solution at 80 °C results in a membrane with a thickness below 15 µm (see Fig. 4.12 c)). As discussed in chapter 5, to improve the surface quality antimony oxide (Sb_2O_3), see details in Table 5.1, can be added to the KOH solution. Note that the 2 µm SiO_2 layer reduces in thickness, but still remains as the hard mask after approximately 290 µm Si etching.

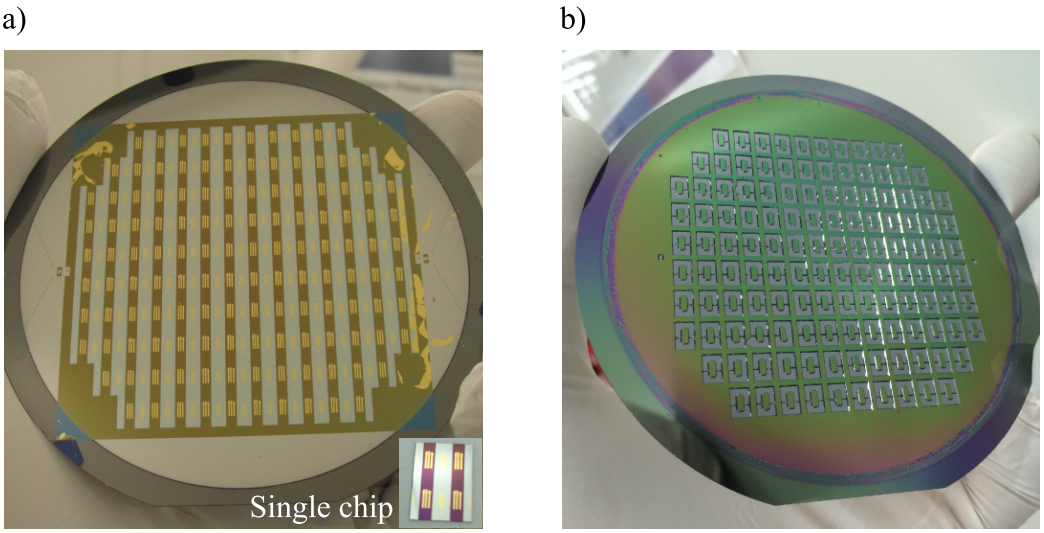

Figure 4.15: *Images taken by a digital camera of* ***a)*** *the front side after the TMR fabrication in the wafer and single-chip scales and* ***b)*** *the back side after etching in the KOH solution.*

In order to terminate accurately Si etching in KOH bathes at a certain cavity depth or a certain membrane thickness by the optical microscopy technique (see section 2.11), the small thickness tolerance in an order batch of 25 wafer is demanded. This prevents contamination into KOH bathes, bending due to mechanical stress, and complex etch stop processes, which are commonly observed for conventional etch stop techniques such as boron-doped Si layers, photoelectrochemical etching, photoinduced anodization, and thin insoluble films[229]. Here, the wafers are double-sided polished with Total Thickness Variations of about 1.2 µm. This leads to uniformity of finished membrane thickness all over processed wafers, and consequently appears as a uniform thickness distribution of finally produced cantilevers as demonstrated in Fig. Appendix-A.2. The cavity depth is measured by the optical microscopy about 10 min before reaching the final thickness.

To release the cantilevers, another UV-lithography specified by the red outline in Fig. 4.13 and Fig. 4.16 a) is performed on the front side of the wafer. A thicker AZ 6632 resist layer is applied under 2000 rpm rotating speed (see Table 4.2). Since the chuck vacuum is strong enough to damage the thin cavities, the actual wafer is mounted on

another wafer during processing of this step. Later, the SiO_2 layer (100 nm) and the thin Si layer ($\approx$ 15 µm) is etched (Fig. 4.12 d)) by CHF_3 gas for 45 s (see Table 3.2) and consecutive application of SF_6 gas (see Table 3.3). The etching continues until the release of the cantilevers is accomplished.

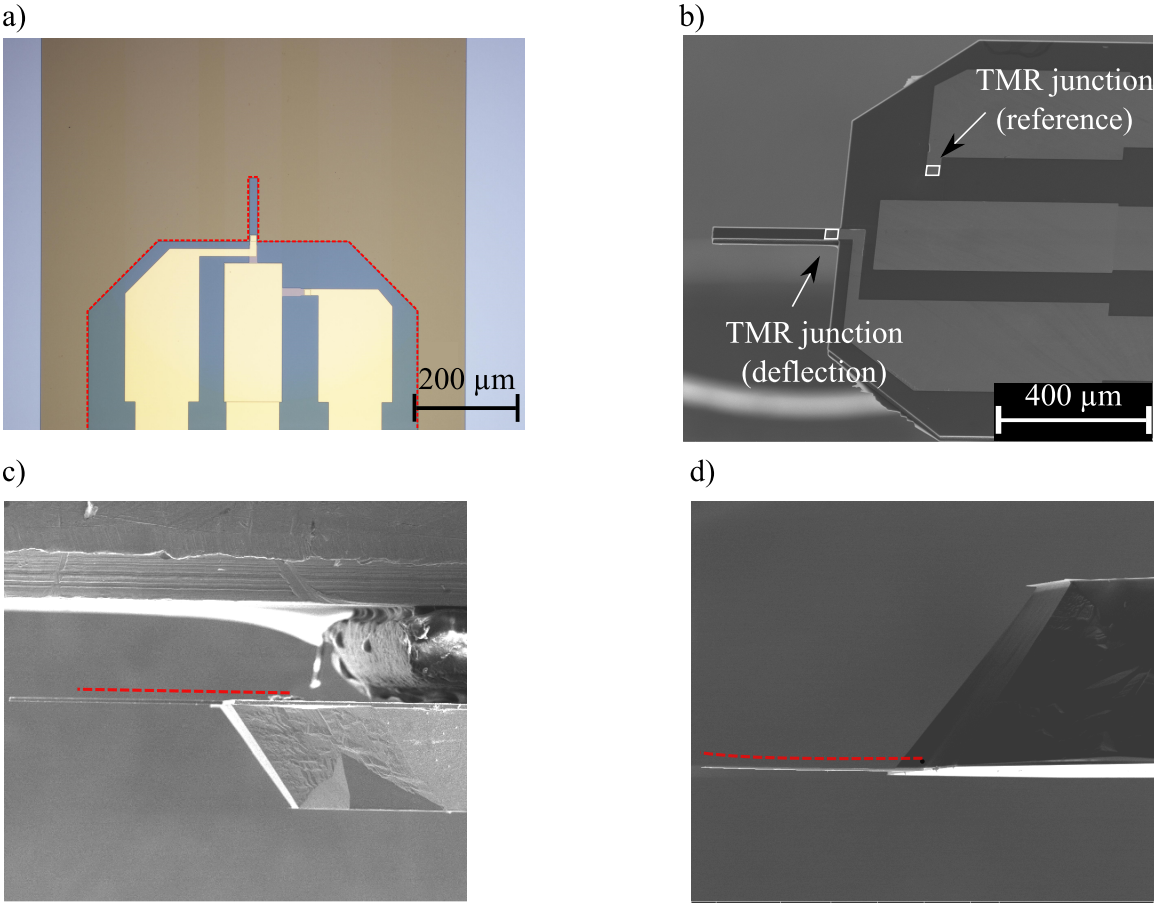

Figure 4.16: a) *Optical microscope image after the UV-lithography step for the release of the cantilevers and SEM images of* ***b)*** *two TMR junctions on a cantilever and its support chip,* ***c)*** *a straight cantilever with $t \approx 11\,\mu m$, and* ***d)*** *a bent cantilever with $t \approx 4\,\mu m$ (the support chip is flipped compared to the image in panel c)). A small cantilever thickness is detrimental to the bending amount at the end of the fabrication process.*

As depicted in Fig. 4.16 c), cantilevers with a thickness in the range of 10 µm stay straight, which was the purpose of employing this type of wafers and not silicon-on-insulator wafers. Because such pre-bending can change the initial orientation of M_{sen} by additional stress-induced anisotropy varying the optimum configuration of the physical quantities required for high strain sensitivity. Nevertheless, reducing down the thickness to about 4 µm leads to downward bending of the cantilevers (Fig. 4.16 d)). This bending is associated with interfacial stress formed during wafer production at the Si/SiO_2 interface. The wafers, used here, have unequal SiO_2 layers on either sides, 2 µm on one side and 100 nm on the other side. The Si supplier firstly grew a 2 µm-thick SiO_2 layer on both sides, followed by stripping the oxide layer on one

side. Then, growth of a 100 nm-thick oxide layer is carried out on the same side. Consequently, mechanical stress is formed at the Si/SiO_2 interface. Notice that the cantilevers bending is not related to the integration of the TMR sensors on the AFM cantilevers since their sizes are limited compared to the length of the cantilevers.

It is crucial to place the deflection TMR sensors entirely on the cantilevers, as depicted in Fig. 4.17 a). This allows to transfer completely strain of a bent cantilever to its TMR deflection sensor during AFM measurements. The Si underetching during the RIE step must be under control otherwise the junctions will not be completely placed on bulky cantilevers. Figure 4.17 b) demonstrates a partly free standing junction on a cantilever. This can lead to pre-stress and an initial change in stress distribution of the sense layer, affecting the strain sensitivity of the junction.

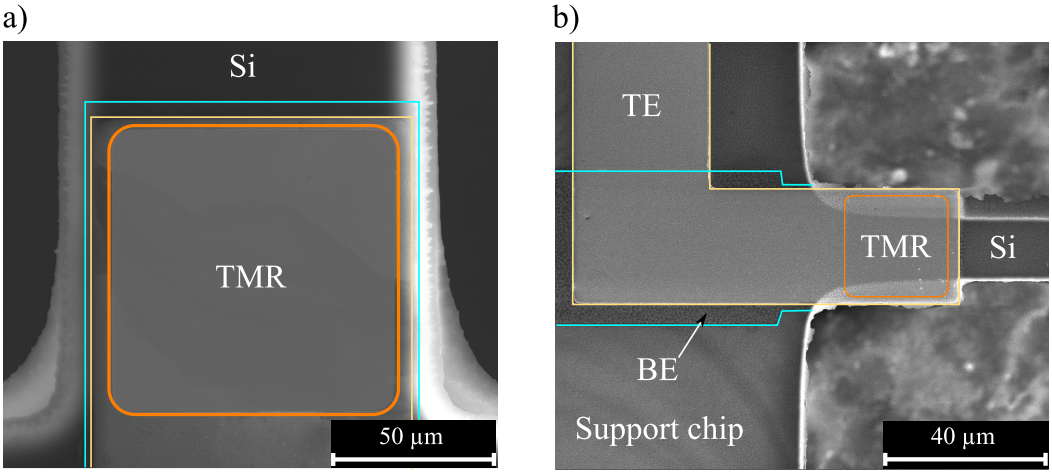

Figure 4.17: *SEM images of a TMR deflection sensor on an AFM cantilever. The TMR junction, the BE, and the TE are marked by orange, blue, and yellow lines, respectively.* ***a)*** *The junction is placed entirely on the cantilever, thereby imposed strain in the cantilever will be completely delivered to the junction.* ***b)*** *The junction is partly free standing due to the Si underetching. Moreover, the part of the BE on the cantilever is broken. Consequently, the sense layer of the junction will be exposed partially to the imposed strain, which affects the junction response and its strain sensitivity.*

Finally, the back sides of the cantilevers are coated by the Cr (20 nm)/Au (130 nm) films, which improve the reflectivity of the etched surfaces and signals for the optical deflection read-out system. Then, the resist on the top side is stripped off by NMP inside the ultrasonic bath (400 kHz) at 60 °C. Such transducer with high frequency is required to remove smaller contaminants and residual resist without breaking fine structures such as membranes and microcantilevers [208–210]. This resist, which is applied to the surface for the cantilevers release, covers all the junctions and contact lines and should be removed after the deposition of the reflective coatings to avoid electronic shortcuts.

Such fabrication process can be performed in both wafer and single-chip scales. Figure 4.18 shows the outcome after the release of the cantilevers. Every chips, for

which an individual holder is required for the wet etching step, include only four TMR self-sensing cantilevers. In comparison, the fabrication in the wafer scale allows to produce a large number of the TMR self-sensing cantilevers with high strain sensitivity and desired mechanical properties. Nevertheless, this number, on one hand, is limited by the quality of the deposited TMR stacks explained in section 6.2. On the other hand, non-uniform plasma during the cantilever release leads to a variation of etching rates over the wafers, and as a result some cantilevers remain unreleased, specially in the outer regions (see Fig. 4.18). Longer etching is not recommended since the Si underetching in the central regions can deteriorate the performance of the TMR sensors.

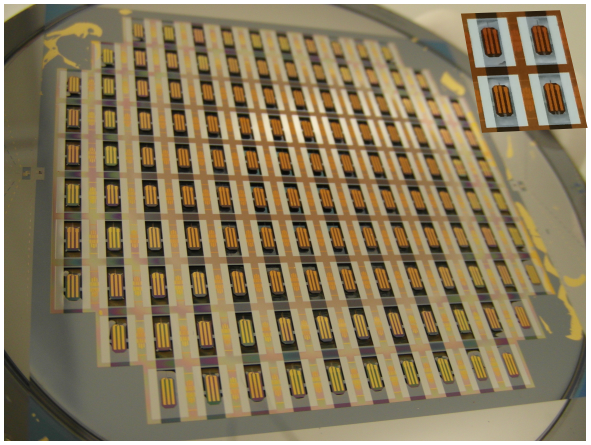

Figure 4.18: *Images taken from the front side by a digital camera after the cantilevers release in the wafer and single-chip scales. In the outer sides some cantilevers are not released completely for this wafer.*

In order to improve the lateral resolution, tips, made of Pt, are grown on the cantilevers by a combination of focused ion beam and electron beam deposition (see section 3.1). This technique offers a maskless process to integrate the tips to the cantilevers at the very last step without any modification on the fabrication process of the TMR self-sensing cantilevers.

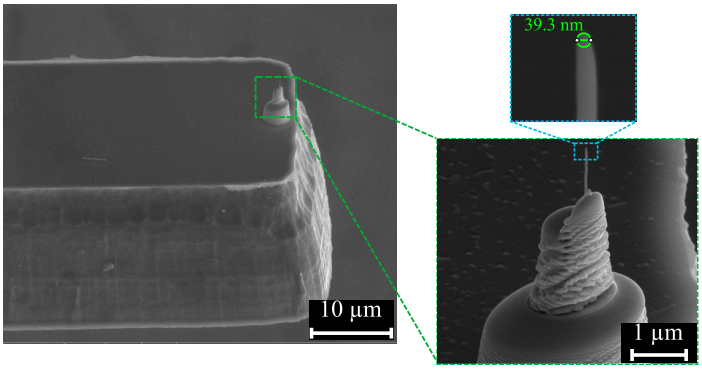

Figure 4.19: *SEM images of a tip with 20 nm radius curvature. The tips are grown on the front side of the cantilevers.*

As shown in Fig. 4.19 by SEM images, every tip includes a two-parts base and a

needle. The base parts are 5 µm and 12 µm in diameter and overall 4 µm - 5 µm in height. The needles depending on the deposition time and the current amount have a radius curvature of 15 nm to 30 nm and variable heights of 200 nm to 1.2 µm.

Chapter 5

Surface Quality of Silicon after Anisotropic Etching

This chapter mainly deals with the optimization of etching parameters in the KOH solution, which are described in the section 4.1, with regard to the improvement of the etched Si surfaces. From technical point of view, smooth etched surfaces serve better reflectivity required for the TMR-based self-sensing AFM cantilevers since the optical read-out system will be used as a comparison in parallel to the TMR sensors read-out (see section 7.1). This becomes crucial if the AFM cantilevers are narrower with respect to the size of the laser spot. Having narrow cantilevers lowers the intensity of the reflected laser to the photodiode in the optical read-out (see Fig. 2.18). On the other hand, rough etched surfaces affect mechanical properties of thin AFM cantilevers. From the earlier works (see Table 2.3), it is shown that temperature, ultrasonic agitation, and additives i.e. sodium dihexyl sulfosuccinate (SDSS) and Sb_2O_3 have strong impacts on the surface roughness. However, the initial roughness of Si substrates, the measuring method, and its parameters differ in every study. This makes the comparison difficult. Therefore, the influence of these techniques is investigated by means of the AFM described in section 3.8. As a technical achievement, optimum parameters for the Si wet etching are beneficial to the fabrication of the AFM cantilevers (see Fig. 4.15). Finally, two compensating structures are introduced to obtain desired shapes and dimensions of microstructures after the anisotropic Si etching. They are implemented to the support chips of the AFM cantilevers in order to secure the cantilevers from the underetching at the convex corners (see Fig. 4.13).

5.1 Surface Roughness

Roughness measurements of the etched surfaces are performed by the AFM explained in section 3.8 in the contact mode. The average of RMS roughness at three scanned areas represents the measured roughness of the etched surface for every etching condition. Different etching conditions are explained in section 4.1.

The surface roughness values corresponding to different etching circumstances are listed in Table 5.1. Comparing these values to the published results given in Table 2.3 is difficult since the measuring devices, size of the scanned areas, the etched depth, and the type of representative roughness (average or RMS) might differ. Therefore, it is easier to compare the results here to each other.

Table 5.1: *Roughness (RMS) values of the surface etched by KOH 40 wt% solutions using different techniques for the improvement of the surface quality. The measurements are performed by the AFM on three different scan areas of 40 µm × 40 µm. The average value is given in the list. A prior buffered oxide etching (BOE) step is carried out for all samples except the sample 1. For a fair comparison the etched depth for the samples 1 to 9 is intended to be around 60 µm. Compared to the other techniques, by adding Sb_2O_3 the low roughness remains constant after deep etching down to 270 µm.*

Sample	Temperature (°C)	Additive	Agitation	Etch depth (µm)	R_{RMS} (nm)
1	80	—	Stirrer	62	38
2	80	—	Stirrer	62	22
3	100	—	Stirrer	82	17
4	60	—	Ultrasonic, 500 W	54	18
5	60	—	Ultrasonic, 250 W	43	25
6	100	SDSS, 0.02 wt%	—	57	14
7	100	SDSS, 0.02 wt%	Stirrer	58	16
8	80	SDSS, 0.02 wt%	Ultrasonic, 500 W	54	16
9	80	Sb_2O_3, 8×10^{-5} M	—	60	8
10	80	Sb_2O_3, 33×10^{-5} M	—	270	8

Applying a buffered oxide etching (BOE) step prior to the wet etching reduces the surface roughness to 22 nm (sample 2). The opened areas after the RIE process are exposed to the ammonium fluoride solution. This leads to removal of the native oxide layer and the residual oxides, which promotes the pseudo-masking (see Fig. 2.19). This helps to get rid of morphological features, which deteriorate the surface quality.

Si etching at 100 °C improves the surface condition further (sample 3), which conflicts with the earlier study[205]. Gosálvez and Nieminen pointed out in their theoretical study that higher temperatures result in a large number of pits on the surface[204]. Regardless, increasing the temperature requires more caution concerning safety and attention for the KOH concentration because of water evaporation. Also, note that one needs a thicker hard mask for deep etching since the etching rate of SiO_2 increases for higher temperatures as well.

Using the ultrasonic agitation even at 60 °C is as effective as the magnetic stirring at 80 °C. Furthermore, higher power (higher intensity) of the transducer reduces the roughness to 18 nm. The measured value is still much higher than 1.7 nm reported by Park et al.[209], for which a megasonic transducer is used. According to a technical

report[232], increasing the transducer frequency from 400 kHz to 1 MHz enhances the cavitation phenomenon and consequently reduces the minimum size of particles or the H_2 bubbles removed from the surface from 1 µm to 100 nm, leading to smoother etched surfaces. As a drawback, keeping the temperature constant can be problematic and requires additional components such as a circulation pump and a circulation bath[210] since the transducer must not be exposed to the KOH solution.

As observed in the sample 6, adding SDSS up to 0.02 wt% to the KOH solution has a better impact on the surface roughness compared to the mechanical agitation. This is more protective for etching of very fine structures such as membranes and microstructures. Yang et al.[205,208] and Canavese et al.[206] reported that the SDSS surfactant alters the wetting ability so that the H_2 bubbles have difficulty to adhere to the etched surface. This lowers the possibility for the pseudo-masking yielding a better surface quality and a higher etching rate. Such effect can be promoted at higher temperatures. The difference between the obtained and the published roughness (see Table 2.3) is probably associated to the measuring conditions and different SDSS suppliers. Figure 5.1 shows the surface topography of the etched surface including the shallow pits expected from the surface etched by the KOH solution without any additives. Adding antimony oxide (sample 9: 8×10^{-5} M and sample 10: 33×10^{-5} M)

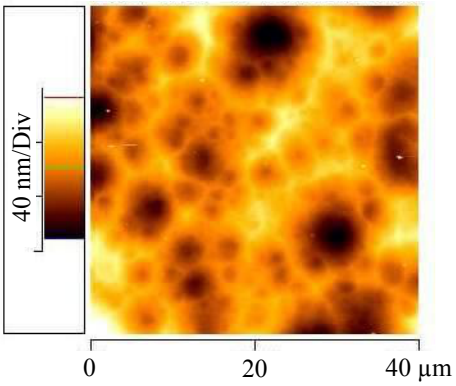

Figure 5.1: *AFM topography image of the Si surface etched (sample 7) by a KOH 40 wt% solution with SDSS 0.02 wt% as a surfactant at 80°C. Even though this additive successfully reduces the surface roughness to R_{RMS} = 16 nm at 58 µm etch depth, still shallow pits appear on the surface.*

as an additive in the etching solution reduces the surface roughness to 8 nm. As shown in Fig. 5.2, such low surface roughness remains constant even after Si deep etching, whereas in other techniques the roughness rises by the etch depth. Sb atoms modify typical redox reactions of the Si etching mechanism in the KOH solution, in which the etched surface is covered with water-rich and -poor silicates giving rise to the pseudo-masking and the surface roughness[212]. Sb atoms cause formation of a black film immediately on the etched surface. The film gets thicker over time and starts to peel off the surface as flakes. Although the H_2 bubbles are present inside the solution, the surface becomes very smooth and free of the shallow pits (see Fig. 5.2).

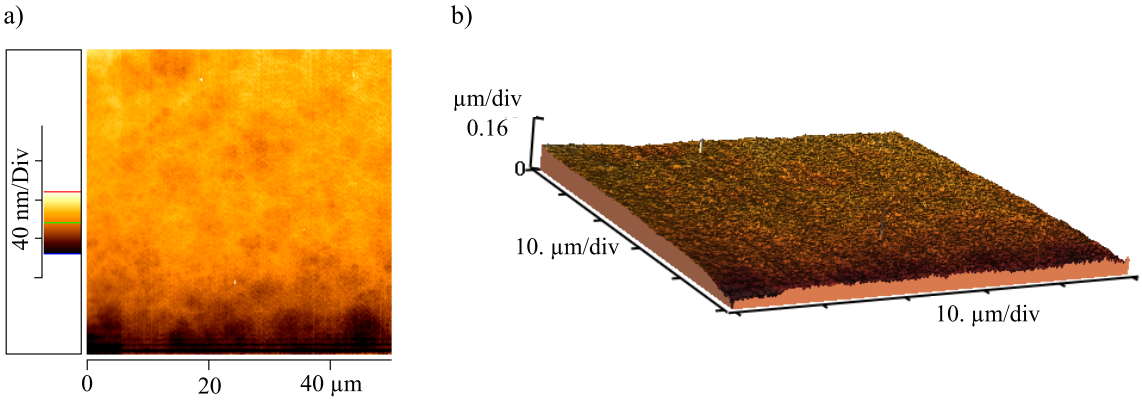

Figure 5.2: *AFM topography images of the Si surface etched by KOH 40 wt% $+Sb_2O_3$ 33×10^{-5} M at 80 °C. The measurement is carried out at an etch depth of 270 µm. The surface shows no evidence of typical shallow pits, leading to a sufficient surface quality (R_{RMS} = 8 nm). This offers better reflectivity of the laser beam in the optical read-out system and better mechanical properties of thin AFM cantilevers.*

5.2 Compensating Structures

Figure 5.3 shows performance of the small and big compensating structures (see Fig. 4.1) inside the KOH solution (40 wt%, 80 °C, 33×10^{-5} M Sb_2O_3) after 4 h and 30 min. Adding Sb_2O_3 and the etching duration meet criteria discussed in the section 4.3 for the fabrication of the AFM cantilevers, leading to better reflectivity and a narrower thickness range of the cantilevers. In case of the small structure, formation of high-index crystallographic planes ({411}, {311}) with high etching rates still results in the underetching at the convex corners (Fig. 5.3 a)).

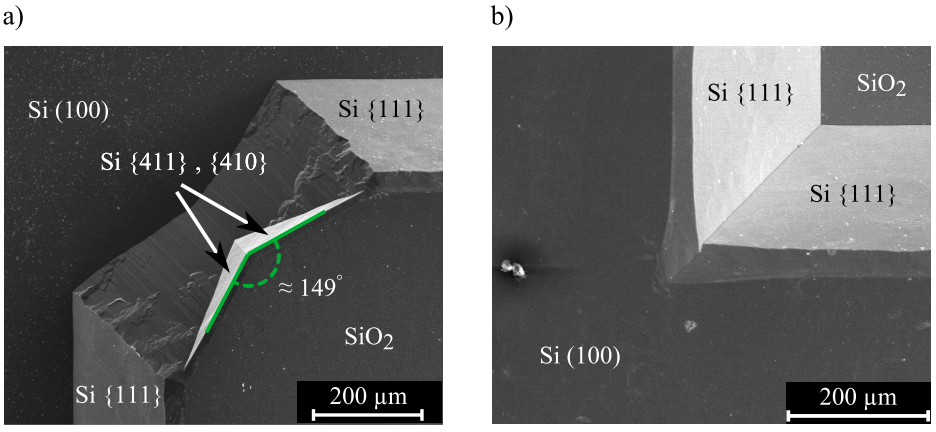

Figure 5.3: *SEM photographs of the compensating structures, which are represented in Fig. 4.1, after 4 h and 30 min wet etching (KOH 40 wt%, 80 °C, magnetic stirrer, 33×10^{-5} M Sb_2O_3). **a)** With the small structure (a_1 = 300 µm, a_2 = 200 µm) some underetching still occurs. From the angle between slanted planes at the corner, one can estimate that they are either {411} or {410} planes. **b)** The big structure (a_1 = 533 µm, a_2 = 267 µm) protects the convex corner to keep the original shape.*

The compensation etching process for the big structure is shown in Fig. 5.4. In comparison, the corner remains fairly perfect without any underetching after the bigger compensating structure is etched away (Fig. 5.3 b)). However, the small structure is preferred because the edges of the support chips appear very clean and with no residual Si attached to the end of the AFM cantilevers after their release using the RIE process (see Fig. 4.16).

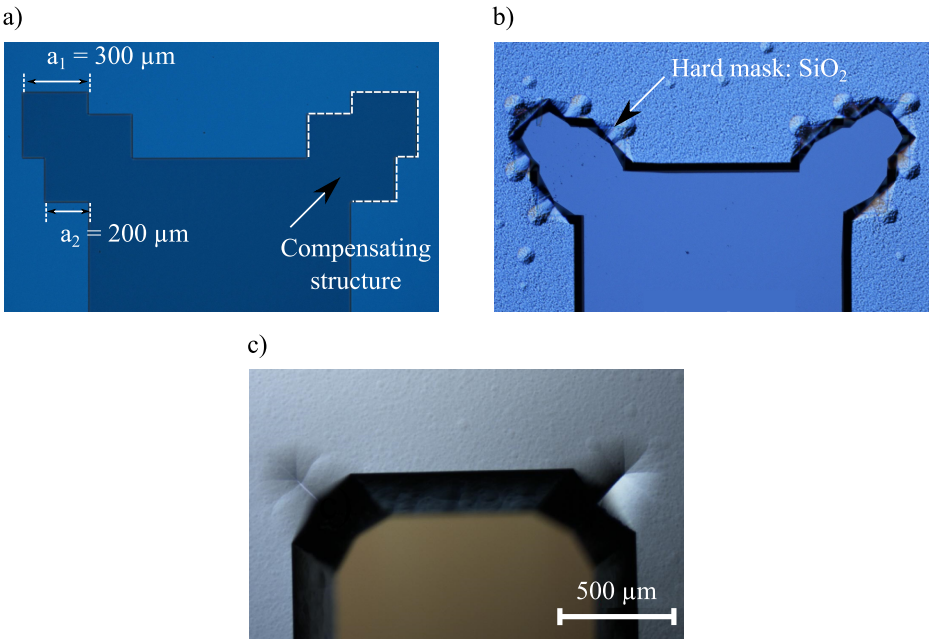

Figure 5.4: *Optical microscopy photographs of the compensation etching process, see Fig. 4.1, after* ***a)*** *structuring of the backside SiO_2 using the RIE process,* ***b)*** *1 h wet etching (KOH 40 wt%, 80 °C, magnetic stirrer): etching under the hard mask and irregular bumps due to the pseudo-masking probably by trapped H_2 bubbles,* ***c)*** *4 h and 30 min wet etching (additive: 33×10^{-5} M Sb_2O_3): the additive does not influence the etching rates, but clearly improves the surface quality (no bumps). The hard mask (SiO_2) becomes thinner and smaller over the etching process until it vanishes eventually.*

Using Sb_2O_3 in the etching solution will not change the etching anisotropy[212], thereby the compensating structures will have the same finish condition in term of consumption.

5.3 Conclusions

In summary, different conditions of anisotropic Si etching in the KOH solutions are investigated in order to improve the surface quality of the etched surfaces. This enhances the reflectivity of the etched surface, which is beneficial for optical MEMS devices. Moreover, thin microstructures such as AFM cantilevers and membranes with very low surface roughness exhibit more mechanical strength.

As a treatment before the KOH etching, the buffered oxide etching step prevents the morphological features due to the pseudo-masking by the SiO_2 residual. This already results in a better surface quality. The etching at 100 °C also reduces the surface roughness compared to the etching at 80 °C. The ultrasonic agitation with 400 kHz frequency at 60 °C is as effective as the magnetic stirring at 80 °C on the improvement of the surface quality via detachment of the H_2 bubbles from the surface. However, reducing the ultrasonic power to 250 W leads to higher surface roughness. Also, the influences of SDSS and Sb_2O_3 as additives are studied because the mechanical agitation can damage fine microstructures like membranes. The surface etched by the KOH solution with 0.02 wt% SDSS has the same surface roughness as the surface etched using the mechanical agitation. The SDSS additive reduces the H_2 bubbles adhesion to the surface by reducing the wetting ability. Additional mechanical agitation does not enhance the performance of the SDSS additive. Compared to the other techniques, adding Sb_2O_3 reveals the most effective impact on the surface quality as it reduces the roughness to 8 nm. More importantly, such low roughness remains constant even after the Si deep anisotropic etching up to 270 µm, whereas in the other techniques the surface roughness increases by the etch depth. Finally, two compensating structures are introduced. They are beneficial to obtain desired shapes and dimensions of microstructures.

As a technical achievement, the optimum parameters for the KOH etching as well as the compensating structures is used in the fabrication of the AFM cantilevers (see section 4.3).

Chapter 6

Strain Sensitivity of Magnetostrictive TMR Sensors

Here, the main content is focused on the effect of size and shape on performance of the magnetostrictive TMR sensors. TMR sensors with nominal sizes of $100\,\mu m^2$, $289\,\mu m^2$, $729\,\mu m^2$, and $1369\,\mu m^2$ in squared, round, elliptical(1:3), and elliptical(1:10) shapes are patterned onto $3\,mm \times 25\,mm$ cantilevers (see section 4.2). The standard deviation of junction dimensions from the nominal values is given in Fig. 4.10. This range of junction size is chosen so that the junctions can be integrated to commercial AFM cantilevers. The round junctions are expected to show higher sensitivity compared to the squared ones since there is no corner, which avoids domains confinement in the sense layer. Thus, it can serve easier rotation of M_{sen} under strain due to the inverse magnetostriction effect. On the other hand, shape anisotropy in the elliptical junctions is intended to compensate energetically the need of the bias field for keeping the strain sensitivity at maximum (see section 2.6). Note that K_u is aligned at a $\pi/4$ angle toward the stress axis by the field annealing, which allows detection of both tensile and compressive stresses.

In addition, it includes description of a TMR and strain measurement setup as well as simulations configurations using the Stoner-Wohlfarth (SW) model and the object oriented micromagnetic framework (OOMMF) software. Then, after TMR characterization the junctions are exposed to different stress or strain quantities whereby the strain effect on resistance versus field ($R(H)$) loops are monitored as $H \perp K_u$. A representative macrospin model provides details about the rotation of M_{sen} of a strained junction in the $R(H)$ loops. Afterward, the strain sensitivity of such junctions are determined and discussed by measuring strain loops ($R(\varepsilon)$). Finally, the round TMR junctions sensitive to strain at zero bias field are introduced. This helps to eliminate the requirement of the bias field. The experimental observation on the $R(H)$ loops and the strain loops is modeled using the energy minimization based on the Stoner-Wohlfarth (SW) model.

The last part highlights a technique which allows to nearly measure the satura-

tion magnetostriction of the sense layer of patterned MTJs. This method considers present structuring effects since the measurement can be performed after a complete fabrication process. Patterning process can affect magnetic behavior of the sense layer by changing the edge conditions, such as edge roughness[233,234] and edge tilts[235–237], imposed during the IBE step. Furthermore, present layers in the multilayer structure can induce surface roughness and additional magnetic couplings (see section 2.3) to the sense layer. The surface roughness[238–240] and the external couplings[241] can play critical roles in magnetic properties.

6.1 Experimental and Simulation Configurations

6.1.1 TMR and Strain Sensitivity Measurement Setup

Prior to any investigation of the strain influence on MTJs, standard resistance versus field ($R(H)$) loops, minor and major loops, are measured while the external field is applied parallel to the induced magnetocrystalline anisotropy ($H \parallel K_u$). It provides details about the extreme resistance values, R_p and R_{ap}, the TMR effect amplitude, and the field shift H_{sh} due to the Néel coupling. H_{sh} contributes to the Néel energy in the SW model. For measurements, the junctions on the cantilevers, which are placed between a Bruker electromagnet (a B-EC1 power supply and a B-E10f magnet), are contacted to a Keithley 2400 source meter via two Au-plated Be-Cu positionable needles. Then, while sweeping the magnetic field gradually by a sweep of 0.4 kA/m (5 Oe), the current flow is acquired under a constant voltage drop of 10 mV sourced to the junction. The current flow varies in the range of 1 to 100 µA, depending on the size and the location of the junction on the wafer. At the end a TestPoint program, which controls the TMR setup, converts the current to the resistance values and plots them versus the applied external field.

In order to study the influence of mechanically applied uniaxial stress to the magnetostrictive TMR junctions, a four-point bending apparatus is used based on a so-called pusher block[59,63]. Homogenous straining is imposed to the cantilever by the inner pieces (made of macor, purchased from MCI GmbH, and constructed at *Kiel University*) with two contact points, which are driven by a 850G linear actuator using a ESP300 motion controller (manufactured by Newport), whereas outer Al pieces with other two contact points are fixed. Figure 6.1 shows the corresponding configuration. The cantilever is placed between the four mechanical contact points. Depending on which direction the ceramic part moves toward the cantilever, compressive or tensile stress can be introduced to the cantilever.

The apparatus is mounted inside the electromagnet from the TMR setup where the relative orientation of the external field and the axis of the applied stress can be configured manually. This allows the $R(H)$ loops measurement under desired applied stress for any configuration of the stress axis, the external field, and the induced magnetocrystalline anisotropy of the sense layer (see section 6.1.2).

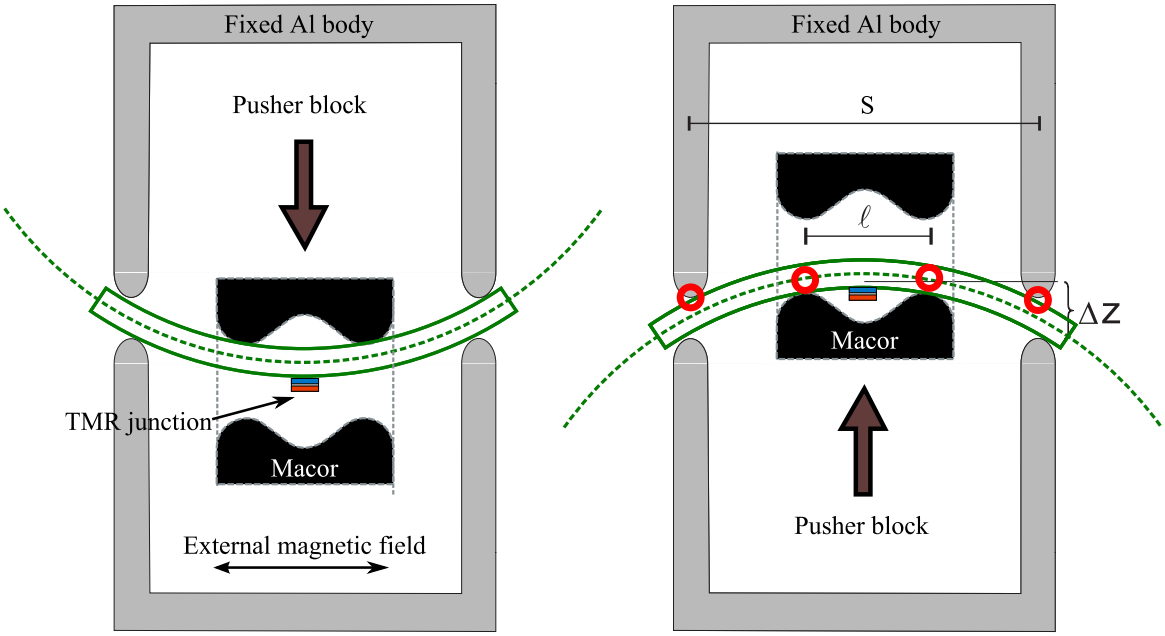

Figure 6.1: *Schematic of the four-point bending apparatus. The displacement of the pusher block Δz moves the ceramic (Macor) pieces and imposes tensile (left) and compressive (right) stress into the TMR junction. The red circles depict the equidistant contact points ($S = 3l$). Note that the mechanical components can be rotated inside the electromagnet. This allows free adjustments of the junction and the cantilever with respect to the external magnetic field (see Fig. 6.2).*

As mentioned in Fig. 4.3, in this study the induced magnetocrystalline anisotropy is aligned at a 45° angle against the stress axis or along the length of the cantilevers. Figure 6.2 depicts the configuration of physical quantities required for understanding of the magnetostrictive TMR sensors. For strain measurements, unlike the standard loops, the external field is perpendicular to the magnetocrystalline anisotropy ($H \perp K_u$). As the external field is applied along the hard axis of the sense layer, measured $R(H)$ loops are called hard-axis TMR loops in this context. The hard-axis $R(H)$ loops are measured for every junction under 0 to 0.76×10^{-3} strain values in order to figure out at what bias fields the maximum resistance change (ΔR) occurs. Readers should notice that the orientation of the elliptical junctions is parallel to the field axis. The shape anisotropy of these junctions is intended for replacing the need of the bias field, which is necessary to set the sensors to high strain sensitivity[65]. Moreover, strain can be continuously ramped up to about 1×10^{-3} (continuous displacement of the pusher block up to 120 µm) while recording the junction resistance at a bias magnetic field. The bias field is selected so that the highest strain sensitivity is expected to occur. This gives a so-called strain loop ($R(\varepsilon)$), from which one can deduce the strain sensitivity of measured junctions. The strain is imposed by the applied stress, originating from the cantilever bending.

Each cantilever is mounted on a printed-circuit board (PCB) and each time three junctions are wire bonded to connect to the source meter. Since the junctions are small and patterned in the center of the cantilevers while applying mechanical stress

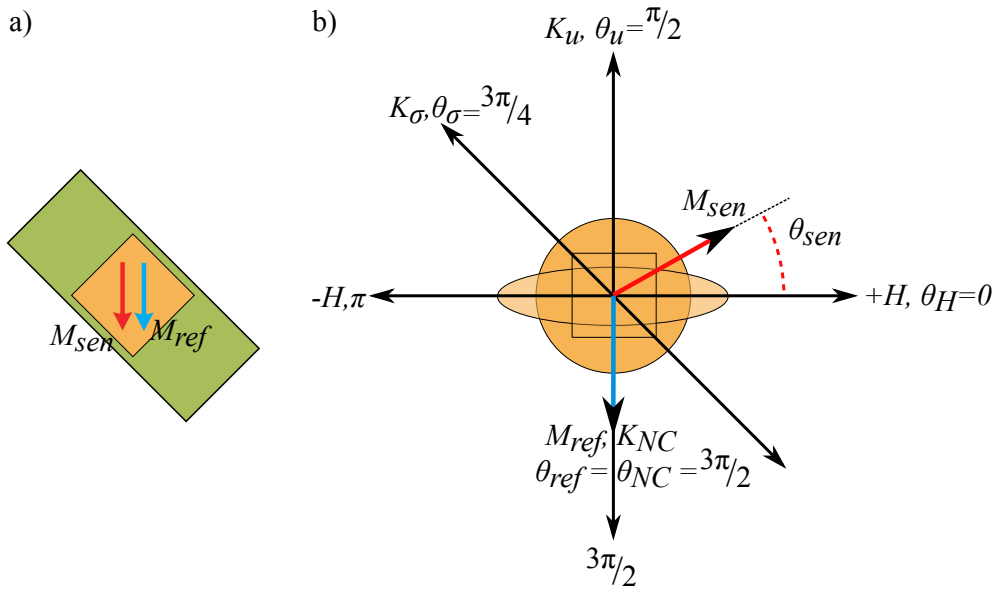

Figure 6.2: ***a)*** *45° alignment of the induced magnetocrystalline anisotropy of the reference and sense layers with respect to the cantilever length. M_{sen} and M_{ref} of unstrained junctions stay parallel at zero field due to the Néel coupling.* ***b)*** *Configuration of physical quantities with respect to the induced magnetocrystalline anisotropy K_u and the stress axis. The uniaxial stress-induced anisotropy K_σ shown here is for tensile stress, whereas in case of compressive stress K_σ resides at $\theta_\sigma = \pi/4$.*

the magnetic field and the applied stress are assumed to be in-plane and homogenous. The imposed strain depending on the displacement of the pusher block is calculated by[242]

$$\varepsilon = \frac{9t}{2S^2}(\Delta z + t/2) \approx 7.64 \times 10^{-3}\Delta z. \tag{6.1}$$

Here, $t = 550\,\mu m$, $S = 18\,mm$, and Δz in µm are the thickness of the cantilever, the distance between the two outer mechanical contact points, and the displacement of the pusher block. The applied strain to the junction varies from 0 to about 0.76×10^{-3} over a 100 µm displacement in the pusher block. For Si⟨110⟩ crystalline directions, as for the long side of the cantilever, the Young's modulus is 169 GPa. Thus, the applied stress ranges from 0 to about 128 MPa assuming the validity of Hooke's law in small strain ranges.

In measured strain loops a certain amount of magnetic hysteresis is overlaid with some mechanical hysteresis from the measuring setup. This is noticed by a plateau of the measured resistance, around the turning point, as the pusher block retracts. The mechanical hysteresis is estimated by piezoresistive strain gauges (see details in Appendix-E.2) and is subtracted as an offset from measured strain loops of the TMR junctions.

Measurement of saturation magnetostriction is carried out using the four-point bending apparatus. Changes in the $R(H)$ loops of the round junctions are studied under a variation of compressive strain. The magnetocrystalline anisotropy K_u, M_{sen},

and M_{ref} are aligned perpendicular to the length of the cantilevers during the field annealing (see Fig. 4.4). Figure 6.3 schematically depicts the measurement configuration. After a simple mathematical calculation based on the method proposed by Ali and Watts[135] (see section 2.4.1), an effective value for the saturation magnetostriction of a patterned $Co_{40}Fe_{40}B_{20}$ sense layer is deduced.

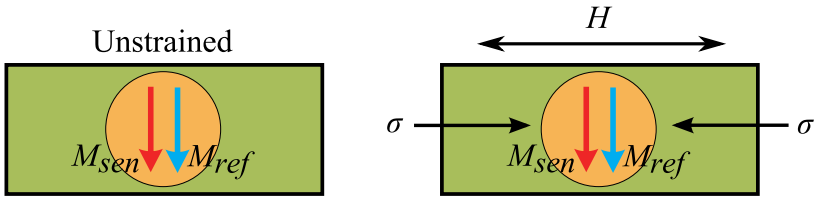

Figure 6.3: *Magnetostriction measurement configuration, in which the external field and the stress axes are perpendicular to K_u.*

The physical quantities illustrated in Fig. 6.2 might face slight misalignment, which can be examined by measuring the $R(H)$ loops as an external magnetic field is swept perpendicular to the induced K_u. A deviation of few degrees is intentionally introduced into the angle between H and K_u ($\angle(H, K_u)$) by rotating the TMR junction on the cantilever. This provides a good approximation for actual misalignment during the strain measurements. Figure 6.4 shows the $R(H)$ loops for a round junction of $30 \pm 0.2\,\mu m$ in diameter for different values of $\angle(H, K_u)$. From experimental experiences such misalignment can be diminished maximum up to $\pm 2\,°$. The origin of the misalignment is probably a construction misalignment in the measuring setup or a deviation in the alignment during the field annealing process, where the unidirectional anisotropy of the exchange-biased reference layer is defined.

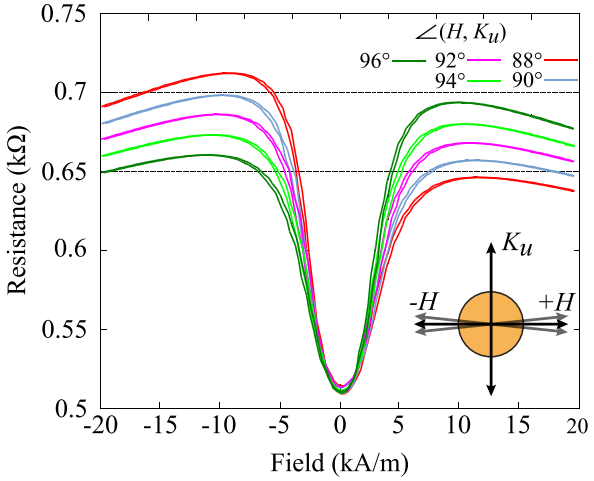

Figure 6.4: *Measured $R(H)$ loops for a round junction with a diameter of $30 \pm 0.2\,\mu m$ under a slight variation of $\angle(H, K_u)$. This reveals a good approximation regarding the misalignment of the physical quantities in Fig. 6.2 during the strain measurements.*

Furthermore, other error sources such as the external magnetic field, the measured resistance, and the displacement of the pusher block (applied) might influence the

investigation of the strain sensitivity. Figure 6.5 a) shows magnetic field offset of 10% between fields set by a Gauss meter FM 3000 from Projekt Elektronik, which is placed at the side of the electromagnet, and fields measured by a FW Bell Gauss meter 6010 at the center, which is nearly the position of the TMR junctions on the cantilevers during the measurement. The Gauss meter FM 3000 is placed at the side of the electromagnet because the central space is occupied by the four-point bending apparatus. In order to estimate the resistance error, the resistance in the parallel state of four junctions are measured 10 times, as every time the needles are retracted and contacted again. As shown in Fig. 6.5 b), the standard deviation in the range of few ohms can be neglected because of the relatively large resistance values. Considering the mean area value and the standard deviation of the junction area represented in Fig. 4.10 and the standard deviation of the resistance, the standard deviation of RA stays below 1.5 %.

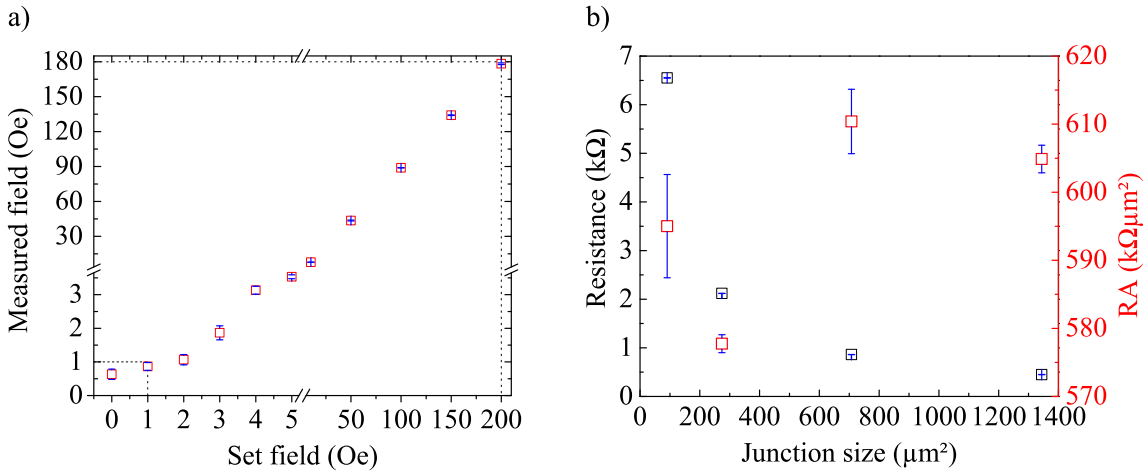

Figure 6.5: a) *Field offset between fields set at the side and measured at the center of the electromagnet. The offset is about 10%. For the strain measurement, the field to current ratio of the electromagnet is calibrated by a Gauss meter placed at the side of the electromagnet due to lack of space. The standard deviation of the measured field is less 1 Oe.* ***b)*** *Resistance error of four round junctions in the parallel state. For each junction the resistance is measured 10 times. The standard deviation of the resistance is only few ohms, which can be neglected. Taking the mean area values and the standard deviation of the area from Fig. 4.10, the calculated standard deviation of RA is below 1.5 %. The standard deviation of the resistance shown in panel b) leads to standard deviation less that 0.1 % for TMR effect amplitudes.*

The accuracy in displacement of the pusher block, which defines the error in the applied strain, is estimated to be less than 0.1% of the displacement[243].

6.1.2 Simulation Configurations

Stoner-Wohlfarth Model

Assuming single-domain behavior, calculations based on the Stoner-Wohlfarth (SW) model are performed to attain a basic understanding of M_{sen} behavior within the hard-

axis $R(H)$ loops in unstrained and strained states, and in the $R(\varepsilon)$ loops. The experimental measurement of magnetostriction of the sense layer is also simulated using the SW model. The junctions shape and size are not taken into account. Considering the parameters in Table 6.1, the total energy density $E(\theta_{sen})$ is determined by

$$\begin{aligned} E(\theta_{sen}) = K_u sin^2(\theta_u - \theta_{sen}) \quad & - \mu_0 H M_s cos(\theta_H - \theta_{sen}) - K_{NC} cos(\theta_{NC} - \theta_{sen}) \\ & + K_\sigma sin^2(\theta_\sigma - \theta_{sen}). \end{aligned} \tag{6.2}$$

Later in the text only the physical quantities and their orientations and not the equation are given for any calculation in order to avoid repetition. K_u is calculated from the relation $K_u = \mu_0 H_k M_s/2$ where $H_k = 4\,\mathrm{kA/m}$ (50 Oe) is the magnetic anisotropy field determined from fitting the hard-axis hysteresis curves[244]. This value is in agreement with the magnetic anisotropy reported for annealed CoFeB layers[245–248]. Note that the second CMA easy axis (see section 2.5) called the less easy axis is not taken into account for sake of simplicity. In order to calculate E_σ, the Young's modulus is assumed to be 169 GPa along Si⟨110⟩ directions. Considering a thin CoFeB layer, there is a minor effect on strain transmission from the Si substrate to the CoFeB layer, which is neglected in the SW model. Nevertheless, slightly different values of $1.6 \times 10^{12}\,\mathrm{dyn/cm^2}$ (160 GPa)[249,250] and 162 GPa[145] for CoFeB and 200 GPa[62] for CoFe are used in the literature[62,145,249] with no details about how the Young's modulus is determined. The Young's modulus depending on crystalline structures[250] and annealing temperatures[251] varies for thicker CoFeB layers.

Table 6.1: *Material parameters used for the SW model.*

Physical quantity	Value
Saturation magnetization (M_s)	$1030\,\mathrm{kA/m}$,Ref. 244
Induced anisotropy (K_u)	$2050\,\mathrm{J/m^3}$
Isotropic magnetostriction (λ_s)	30×10^{-6} , Ref. 252

The energy minimization is carried out for every H or ε using the MATLAB® software. This resolves the equilibrium states of M_{sen} (θ_{sen}), as H is swept or ε is ramped. Then, the equilibrium angle α values are calculated as $\alpha = \theta_{sen} - \theta_{ref}$ with θ_{ref} constantly being $3\pi/2$. Using equation 2.7 by Jaffrès et al.[11], $R(\alpha)$ is determined for every equilibrium state, which results in the $R(H)$ and the $R(\varepsilon)$ loops for H and ε being the variables, respectively. The parallel R_p and antiparallel resistance R_{ap} as well as the perpendicular resistance $R_\perp$ are determined experimentally (see Fig. 6.6).

Micromagnetic Simulation

Micromagnetic simulations are carried out using the OOMMF[12] in order to theoretically take into account domain formation by minimizing the total free energy of the magnetic system, numerically solving the LLG equation, described in section

2.7. Such simulations can also determine the reliability of the assumption regarding single-domain behavior of M_{sen}.

The simulation volume consists of a mono-layer of cubic discretization cells, having an edge length of 5 nm. This is on the order of the exchange length of CoFeB[253], giving a compromise between accuracy and computation time. For simplicity only the sense layer of a round junction with a diameter of 11.3 µm is taken into account. The simulation parameters are summarized in Table 6.2. K_u was calculated from the relation $K_u = \mu_0 H_k M_s/2$ where $H_k = 6.4\,\mathrm{kA/m}$ (80 Oe) is the magnetic anisotropy field determined from fitting the hard-axis hysteresis curves[244]. The magnetoelastic energy is assumed in terms of a uniaxial anisotropy K_σ with λ_s being the isotropic saturation magnetostriction and $Y = 200\,\mathrm{GPa}$ the Young's modulus[62].

Lateral junction dimensions are taken from bitmap files and a randomizing algorithm is used in order to introduce edge roughness of up to 30 nm, which is of the same order as previous reports using magnetic force microscopy images[254].

Table 6.2: *Material parameters used for the micromagnetic simulations.*

Physical quantity	Value
Saturation magnetization (M_s)	$1030\,^{\mathrm{kA}}/_{\mathrm{m}}$, Ref. 244
Induced anisotropy (K_u)	$3860\,^{\mathrm{J}}/_{\mathrm{m}^3}$
Isotropic magnetostriction (λ_s)	30×10^{-6} , Ref. 252
Exchange stiffness (A)	$6.5 \times 10^{-12}\,^{\mathrm{J}}/_{\mathrm{m}}$, Ref. 246

The induced magnetocrystalline anisotropy is modeled using a textured vector field, having its principal axis parallel to the applied magnetic field during the field annealing. Using the equation published by Jaffrès et al.[11], the calculation of the resulting junction resistance $R(\alpha)$ is done with the MATLAB® software, as the simulation cells of the sense layer are assumed to be parallel conduction channels as published recently[255]. For each cell, the magnetization angle with respect to the reference layer fixed magnetization is calculated by iterating over magnetization vector field files. Finally, this results in hard-axis $R(H)$ loops under different strain and magnetoelastic energy amounts. A simulated $R(H)$ loop of a round junction with a diameter of 11.3 µm under 1×10^{-3} strain is demonstrated in Fig. 6.12.

6.2 TMR Characteristics

Figure 6.6 shows representative minor and major loops of a round TMR junction with a diameter of $10.8 \pm 0.1\,\mu\mathrm{m}$. Within the minor loop only the magnetization of the sense layer (CoFeB, M_{sen}) switches at its switching fields (Fig. 6.6 a)). Therefore, an abrupt resistance change occurs between the parallel (R_p) and antiparallel states (R_{ap}). A TMR effect amplitude of 201% and a RA of $223\,\mathrm{k\Omega\mu m^2}$ can be calculated from the plot. In addition, the field shift (H_{sh}) of about 0.44 kA/m appears due to

the Néel coupling (see section 2.3.3). In the major loop, an extended field interval of −350 kA/m to 350 kA/m, as shown in Fig. 6.6 b), causes a change in the reference layer magnetization (CoFeB, M_{ref}). This appears as a gradual resistance change due to the unidirectional anisotropy by the pinning effect from the layer below (see section 2.6).

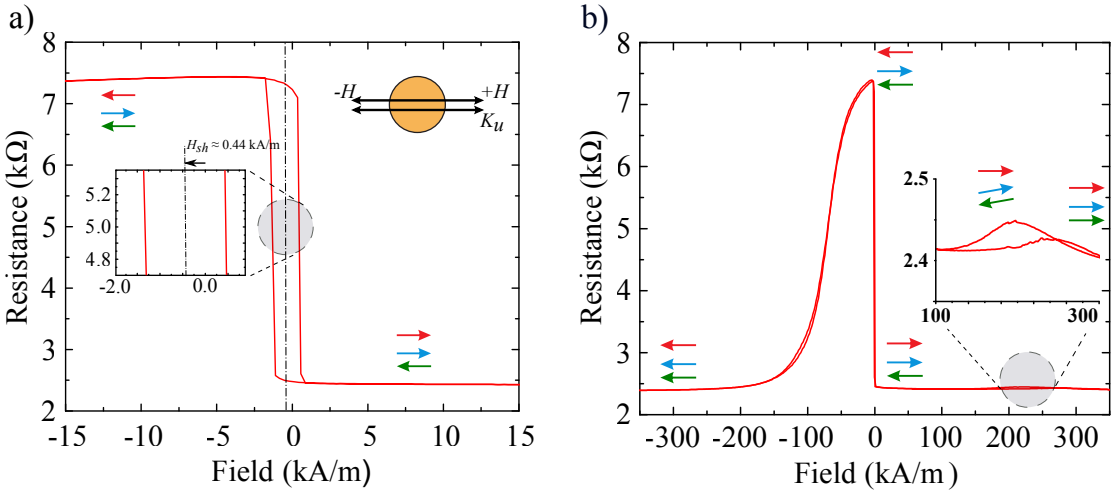

Figure 6.6: a) *Minor loop ($H \parallel Ku$) of a round-shaped junction ($D = 10.8 \pm 0.1\,\mu m$), where only M_{sen} (red arrow) changes as the magnetization of the reference layer (blue arrow) and the pinned (green arrow) layer remains unchanged. Inset on the left side: a field shift of $H_{sh} = 0.44$ KA/m in the loop due to the Néel coupling, which encourages the parallel state at zero field.* ***b)*** *An extended field interval leads to gradual rotation of M_{ref} within the negative field region. Inset on the right: the pinned layer (CoFe) is affected within the 100 kA/m to 300 kA/m magnetic field interval. This influences the reference layer magnetization appearing as a slight resistance increase.*

This plot offers information about the availability of the parallel and antiparallel states as well as the stability of the reference layer magnetization. Within $H \approx 100\,\text{kA/m} \cdots 300\,\text{kA/m}$ the CoFe layer adjacent to the MnIr layer interacts to the magnetic field, which is followed by the reference layer due to the AF interlayer coupling (see section 2.3.2). This effect, so-called scissoring effect [256], leads to a slight resistance increase. Outside of the mentioned magnetic interval IEC in (CoFe/Ru/CoFeB) is overcome by the applied field and the magnetization of the three ferromagnetic layers are aligned parallel.

Distribution of the TMR effect amplitude versus the RA obtained from the minor loops yields information with regard to the quality of deposition and structuring of the TMR junctions. Figure 6.7 shows the statistics of 30 junctions on a cantilever (see Fig. 4.6) from the central region of a wafer. Data points concentrated mostly in a narrow range at around 200% TMR effect amplitude and around 550 kΩμm^2 RA, independent of the shape and the size, indicate successful processing and acceptable homogeneity. The RAs are calculated by multiplying the measured resistance and the mean area value (see Fig. 4.10). The standard deviation of the RA is less than 1.5 %

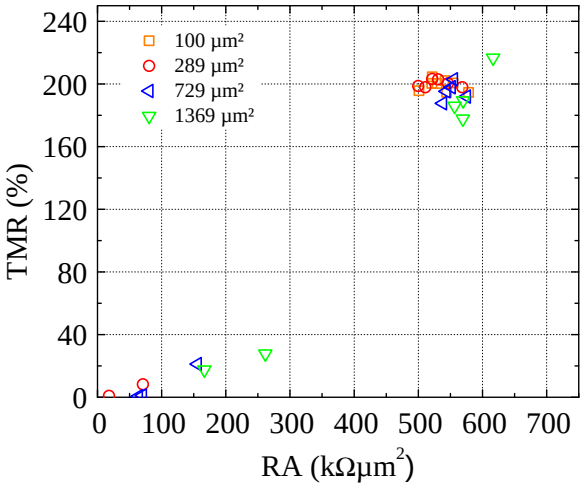

Figure 6.7: *Distribution of TMR effect amplitudes and Resistance-Area Products (RAs) of the junctions on a cantilever from the central region of a 4″ wafer. The narrow statistical range, independent of the shape and size, is an indication for the successful fabrication process. The RAs are calculated by multiplying the measured resistance and the mean area value given in Fig. 4.10. The standard deviation of the RA is less than 1.5 % with regard to the standard deviation of the resistance (see Fig. 6.5 b)) and the area (see Fig. 4.10 b)). A few failure occurs due to the parallel currents leading to low TMR effect amplitudes and low RAs.*

with regard to the standard deviation of the resistance (see Fig. 6.5 b)) and the area (see Fig. 4.10 b)).

Nevertheless, some junctions are faulty exhibiting low TMR effect amplitudes in combination with low RAs. It is attributed to parallel currents between the top and the bottom contacts. However, the faulty junctions mostly show the typical switching behavior between the parallel and antiparallel states in their minor loops. The parallel currents are explained to be related to defects in the SiO_x layer, where the top and bottom contact lines overlap, or the re-deposited materials at the sides of the junctions[257]. The latter is less likely because the re-deposition is obstructed using the neutralizer and the 30° tilt in the stage during the IBE step. The two junctions (729 µm^2) with nearly zero TMR effect amplitude are the junctions with the ellipse(1:10) shape. As in the mask design they are close to the dicing saw path, they are probably affected by the saw trench.

Note that the narrow distribution is obtained for the cantilevers inside a 2″ circular region at the center of the wafer[244]. The junctions inside exhibit TMR effect amplitudes around 170 %. However, the average RA changes over 50 kΩµm^2 from one cantilever to another (not displayed here). The variation emanates from the exponential dependence of the RA on the MgO thickness[87], as the deposition rate is different over the wafer. The RA difference is noticeable among the junctions, for which their results are shown in the next sections. As aforementioned in section 6.1.1, for the strain measurements the strain influence on the hard-axis $R(H)$ loops ($H \perp K_u$) is investigated to find out the maximum resistance change (ΔR). The hard-axis loop shown in Fig. 6.8 a) is measured for the same junction as for Fig. 6.6.

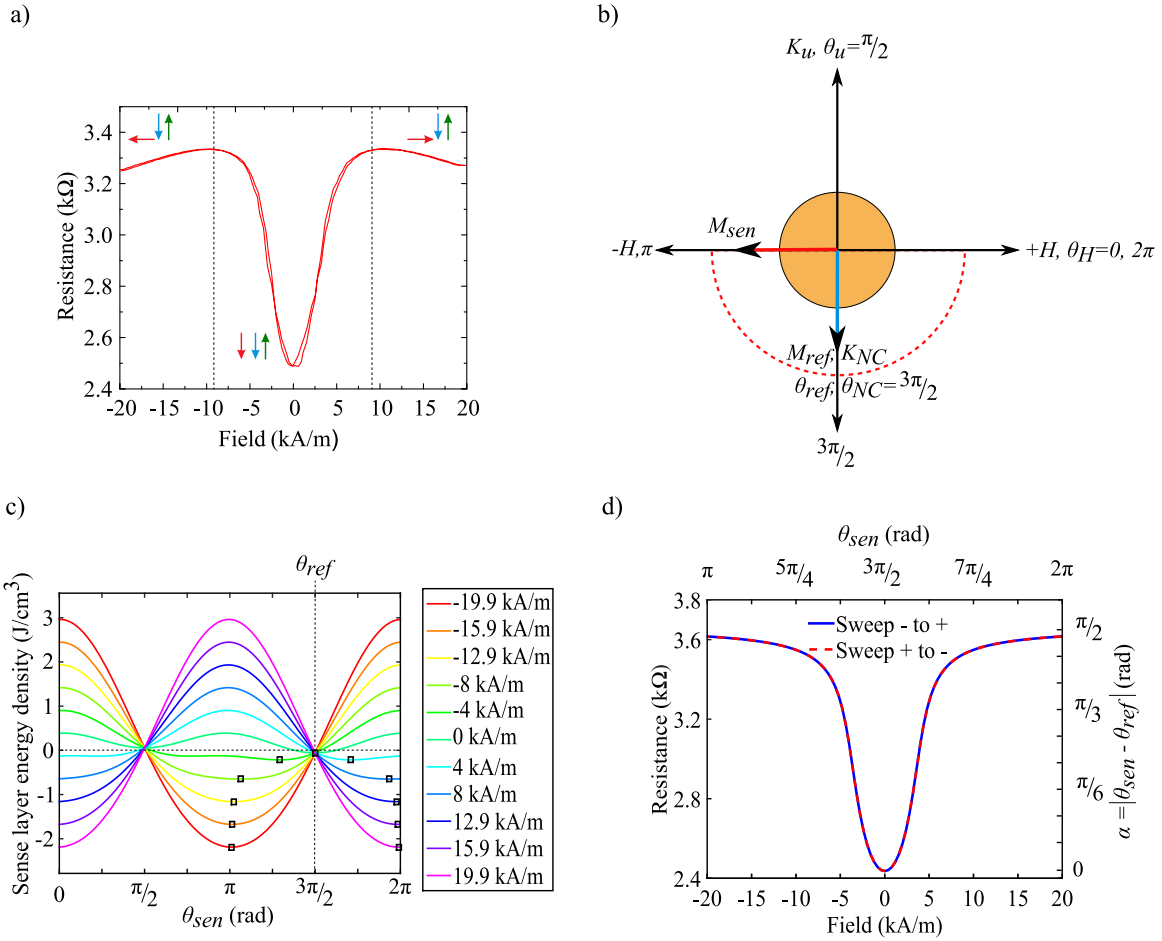

Figure 6.8: a) *Hard-axis $R(H)$ loop, $H \perp K_u$, of the same junction in Fig. 6.6. M_{sen} (red arrow) rotates through the parallel state. The blue and green arrows belong to M_{ref} ($\theta_{ref} = 3\pi/2$) and the magnetization of the pinned CoFe layer.* ***b)*** *Configuration of the physical quantities in the sense layer in addition to M_{ref}.* ***c)*** *Evolution of energy density profiles, which are calculated based on the SW model of the sense layer as a function of the external field. The squares represent the equilibrium orientation, the minimum energy, of M_{sen}, rotating from $\theta_{sen} = \pi$ to $\theta_{sen} = 2\pi$ through the parallel state ($\theta_{sen} = 3\pi/2$ at $H = 0$).* ***d)*** *Calculated hard-axis $R(H)$ loop using equation 2.7. The angle α at different field is calculated by $\alpha = \theta_{sen} - \theta_{ref}$ with θ_{sen} being the orientation of M_{sen} with the minimum energy and $\theta_{ref} = 3\pi/2$, which is assumed to remain unchanged.*

At $H = -19.9\,\mathrm{kA/m}$ (250 Oe) M_{sen} points to the left ($\theta_{sen} \approx \pi$), thereby the junction is nearly in the perpendicular state ($\alpha = \pi/2$, $R_\perp$). Decreasing the field, the resistance drops to 2.5 kΩ at $\theta_{sen} = 3\pi/2$, which is close to the measured R_p of the junction (see Fig. 6.6). This indicates M_{sen} and M_{ref} are aligned parallel at zero field[258]. As the field is increased to $H = +19.9\,\mathrm{kA/m}$ the junction resistance returns to $R_\perp$, as M_{sen} is pointing to the right ($\theta_{sen} = 2\pi$). The rotation of M_{sen} from $\theta_{sen} = \pi$ to $\theta_{sen} = 2\pi$ through the parallel state emanates from the Néel coupling energy. As shown in Fig. 6.8 b), the Néel coupling anisotropy K_{NC}, which is parallel to M_{ref}, is unidirectional.

In order to prove the experimental results, the energy minimization of the sense layer makes it possible to figure out the equilibrium orientation of M_{sen} in an MTJ. For calculation of the energy density of the sense layer in the magnetization reversal as in the hard-axis $R(H)$ loop, the Zeeman energy, the magnetocrystalline anisotropy energy, and the Néel coupling energy are considered with $\theta_u = \pi/2$, $\theta_H = \pi$, and $\theta_{NC} = 3\pi/2$ in equation 6.2.

Figure 6.8 c) represents the evolution of energy density profiles for the sense layer as the magnetic field is swept from -19.9 kA/m to +19.9 kA/m. It is clear that the minimum energy orientation rotates from $\theta_{sen} = \pi$ to and $\theta_{sen} = 2\pi$. In other word, the angle α between M_{sen} and M_{ref} varies from $\pi/2$ to 0, and then again to $\pi/2$, as the magnetization of the reference layer is assumed to remain unchanged ($\theta_{ref} = 3\pi/2$). Taking R_p =2.5 kΩ and R_{ap} =7.4 kΩ from Fig. 6.6 a), $R(\alpha)$ is calculated by equation 2.7. This results in a calculated $R(H)$ loop which simulates the experimentally obtained $R(H)$ loop. However, they differ at fields higher than $\pm 7.5\,\mathrm{kA/m}$ (94 Oe), where the resistance reduces in the experimental loop, as specified by vertical dashed lines in Fig. 6.8 a). This is attributed to the influence of the applied field on M_{ref}. As $H \perp M_{ref}$ a large torque is imposed into the magnetization of the reference layer. Accordingly, M_{ref} starts to rotate at $H > \pm 7.5\,\mathrm{kA/m}$ to be in a parallel state with respect to the applied field. This reduces the angle α and as a result the tunnel resistance.

In the next section, the strain effect on the hard-axis TMR loops is discussed.

6.3 Strain Effect on $R(H)$ Loops

In order to understand how applying strain affects $R(H)$ loops, energy density profiles of the sense layer, as demonstrated in Fig. 6.9, are calculated for different amounts of tensile strain at zero field. The total energy density is calculated using equation 6.2 as the magnetocrystalline anisotropy energy ($\theta_u = \pi/2$), the Néel coupling energy ($\theta_{NC} = 3\pi/2$), and the stress-induced anisotropy energy ($\theta_\sigma = 3\pi/4$) are taken into account.

In the unstrained state the minimum energy belongs to the direction of M_{ref} and energy reduction ($\frac{\delta E}{\delta \theta} < 0$) occurs within $\theta_{sen} = \pi$ to $3\pi/2$. This approves the rotation of M_{sen} through the parallel configuration due to the Néel coupling energy. On the other hand, application of stress contributes an additional energy term E_σ to the total

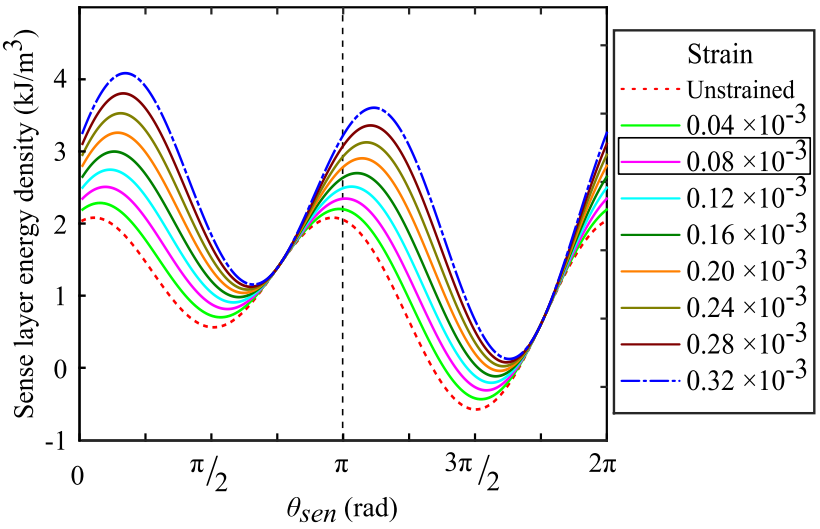

Figure 6.9: *Energy density profiles calculated based on the SW model of the sense layer for different amounts of tensile strain at zero field. The vertical dashed line represents the start point in a $R(H)$ loop ($\theta_{sen} = \pi$). The energy drop ($\frac{\delta E}{\delta \theta} < 0$) occurs from $\theta_{sen} = \pi$ to $3\pi/2$, in comparison to $\varepsilon > 0.08 \times 10^{-3}$ whereby the energy reduction takes place within $\theta_{sen} = \pi$ to $3\pi/4$ range. The energy drop determines the rotation tendency of M_{sen} in the hard-axis $R(H)$ loops (see Fig. 6.10).*

energy. According to the SW model, under a sufficient amount of strain $\varepsilon > 0.08 \times 10^{-3}$ the stress energy term exceeds the Néel energy ($580\,\mathrm{J/m^3}$ for $H_{sh} = 0.44\,\mathrm{kA/m}$). Consequently, in comparison to the unstrained state the field-induced magnetization reversal of M_{sen} is expected to occur clockwise over the closer direction of stress ($\theta_\sigma = 3\pi/4$ for tensile strain) as the sense layer energy drops ($\frac{\delta E}{\delta \theta} < 0$) within $\theta_{sen} = \pi$ to $3\pi/4$. Therefore, two rotation tendencies are considered for M_{sen} in Fig. 6.10 a).

Figure 6.10 b) demonstrates the successive changes of the measured hard-axis $R(H)$ loop imposed by different levels of uniaxial tensile strain. Note that the junction is the same as in Fig. 6.8 a). For $\varepsilon > 0.08 \times 10^{-3}$ the $R(H)$ loop looks differently because of the change in M_{sen} tendency in the rotation, as the Néel coupling is overcome due to further increase of the stress-induced anisotropy. Eventually, the effective anisotropy, which is influenced by both K_u and K_σ, introduces switching fields into the loop for strain values larger than a threshold of about 0.23×10^{-3}, at which an abrupt resistance change occurs. Modeling of $R(H)$ loops under tensile strain in Fig. 6.10 c) verifies a transition in the rotation of M_{sen} at $\varepsilon = 0.08 \times 10^{-3}$. The maximum resistance in the loops for $\varepsilon = 0.12 \times 10^{-3} \cdots 0.24 \times 10^{-3}$ reaches the maximum resistance R_{ap}, but as for the experimental $R(H)$ loops this takes place for $\varepsilon > 0.27 \times 10^{-3}$. This is very likely due to deviation from the homogenous magnetization. Such deviation occurs after the Néel coupling energy is overcome by the magnetoelastic energy ($\varepsilon > 0.08 \times 10^{-3}$) until a strong uniaxial stress-induced anisotropy is formed ($\varepsilon > 0.27 \times 10^{-3}$). There is no evidence of domain formation in the calculated loops since the calculation is carried out under the assumption of single-domain behavior.

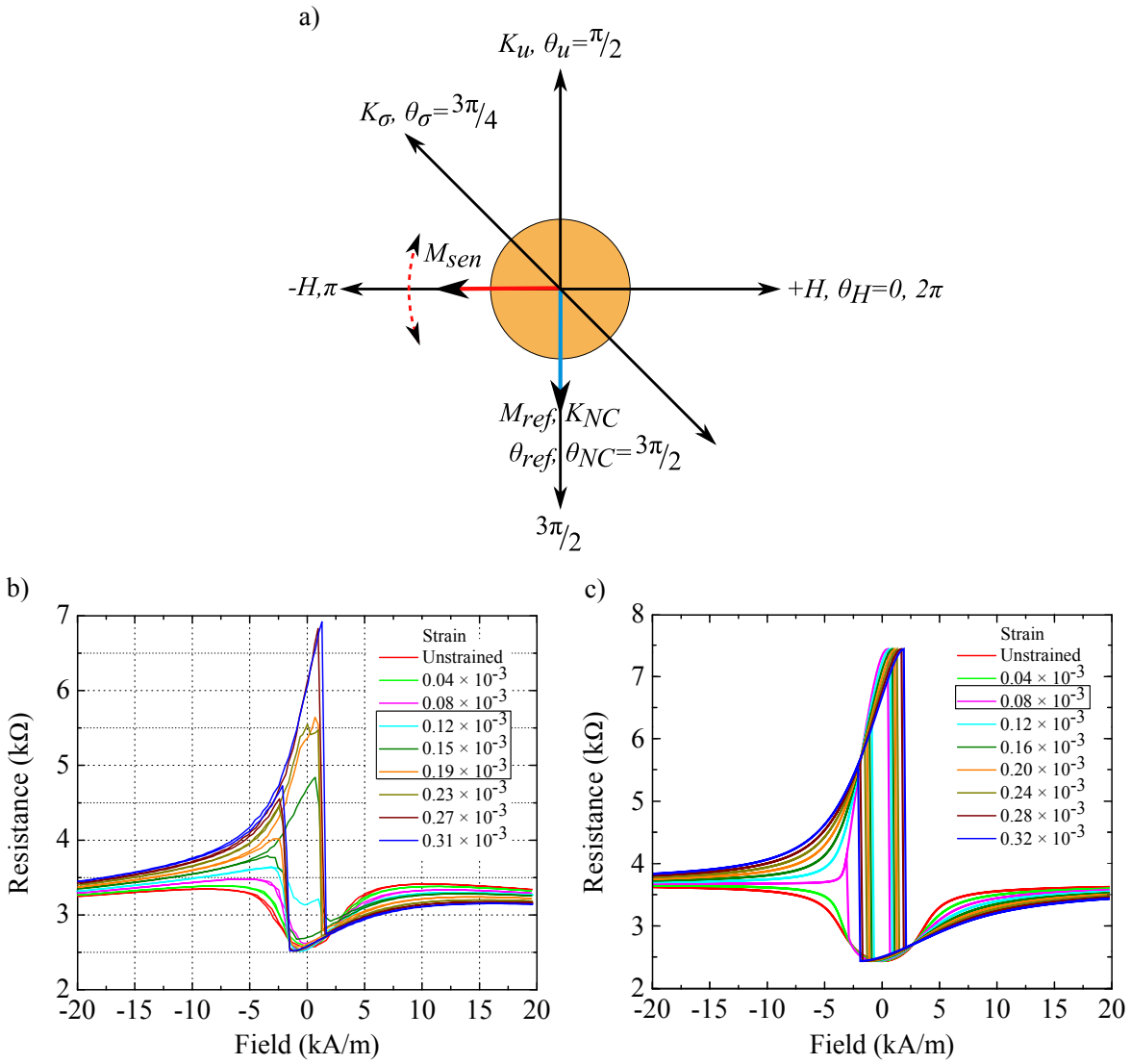

Figure 6.10: a) *Additional stress-induced anisotropy K_σ (tensile, $\theta_\sigma = 3\pi/4$) induced to the unstrained sense layer (see Fig. 6.8 b)). M_{sen} can rotate clockwise and anticlockwise, depending on the strain amount.* ***b)*** *Measured $R(H)$ loops imposed by different amounts of uniaxial tensile strain ($\theta = 3\pi/4$). The junction is the same as in Fig. 6.8 a). The stress-induced anisotropy, which overcomes the Néel coupling ($\varepsilon > 0.08 \times 10^{-3}$), alters the rotation mechanism of M_{sen}.* ***c)*** *Changes calculated by the SW model in the $R(H)$ loop, as in Fig. 6.8 d), under tensile strain.*

As shown in Fig. 6.11 a) for a round junction being 30 ± 0.2 µm in diameter, increasing the strain further up to 0.76×10^{-3} not only results in higher switching fields, but also a smaller asymmetry of the plot. Higher strain also increases the highest resistance measured in the field loops, which is nearly R_{ap} ($\theta_{sen} = \pi/2$). R_p ($\theta_{sen} = 3\pi/2$) is also reached within the minor loop, indicating a complete rotation of the M_{sen} (black curve). In case of compressive stress, the corresponding stress-induced anisotropy is perpendicular to the axis of the applied stress ($\theta_\sigma = \pi/4$). As a result, a similar but mirrored resistance versus field characteristic ($R(H)$) is observed (Fig. 6.11 b)).

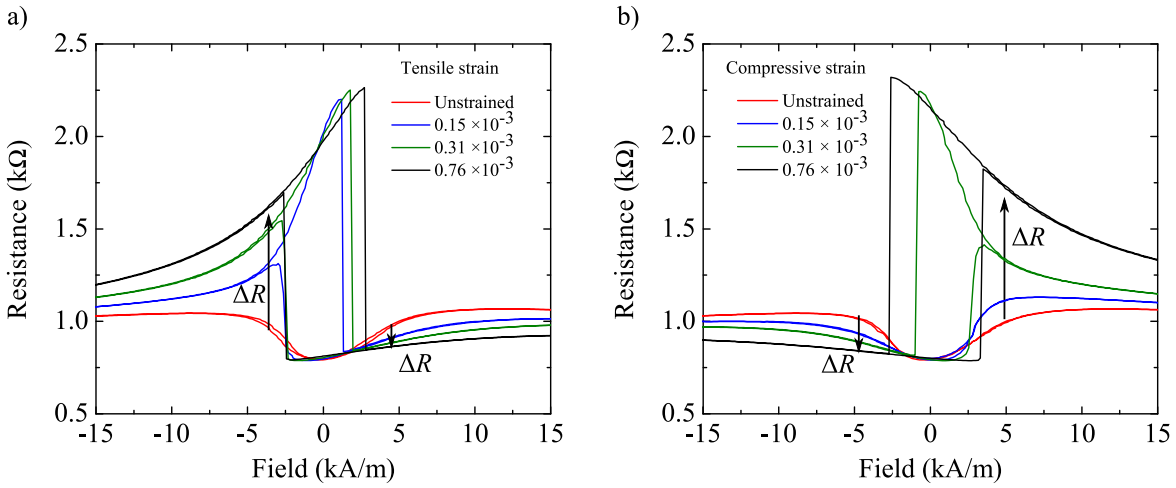

Figure 6.11: *Applying* ***a)*** *tensile (K_σ, $\theta_\sigma = 3\pi/4$) and* ***b)*** *compressive stress (K_σ, $\theta_\sigma = \pi/4$) impose deformation into the hard-axis TMR loop of a junction with $30 \pm 0.2\,\mu m$ diameter. The red plots represent the $R(H)$ loops in the unstrained state. Tensile strain leads to a large resistance increase ΔR at negative fields range (H >-3 kA/m (38 Oe)), whereas it emerges at positive fields (H >+4 kA/m (38 Oe)) for compressive strain. However, a small resistance decrease occurs at positive and negative fields for tensile and compressive strain, respectively.*

In terms of rotation mechanism of M_{sen}, a schematic illustration in Fig. 6.12 a) qualitatively demonstrates all steps in a macrospin model of a strained junction. Starting at high negative field values $-H_{max}$ the magnetization of the sense layer resides nearly perpendicular to the reference layer ($\alpha = \pi/2 + \delta$) turning toward the axis of stress because of the induced anisotropy by stress. Higher strain leads to larger deviation δ and larger resistance values, which are in agreement with experimental observations at $H = -19.9$ kA/m in Fig. 6.11 a). With approaching zero magnetic field M_{sen}, as a positive magnetostrictive material, lies first along the stress-induced axis and then, with increase of the external field in the positive direction it approaches the antiparallel configuration by reducing the magnetocrystalline anisotropy energy (step (1)). Therefore, the resistance rises gradually to a certain value somewhat below R_{ap}. As the positive switching field is reached, the magnetization flips into the other direction of the stress-induced axis causing a sharp drop in the resistance (step (2)). The configuration of the two layers becomes again nearly perpendicular with increasing the field toward the positive maximum field $+H_{max}$, slightly giving rise to the resistance (step (3)). With higher strain the resistance reduces at $+H_{max}$ (see Fig. 6.11 a)). As the field is decreased to negative values, going across the stress axis, both layers align parallel, which corresponds to the lowest resistance R_p (step (4)). The magnetization flips back toward the induced stress axis after the negative switching field (step (5)) and finally it returns to the start point of the model by further field increase (step (6)). An inverse macrospin model applies for compressive strain.

Furthermore, micromagnetic simulations approve the rotation macrospin model. Figure 6.12 b) shows the simulated field loop of a junction with a diameter of 11.3 µm under 1×10^{-3} tensile strain. In contrast to the measured loops (see Fig. 6.11), the

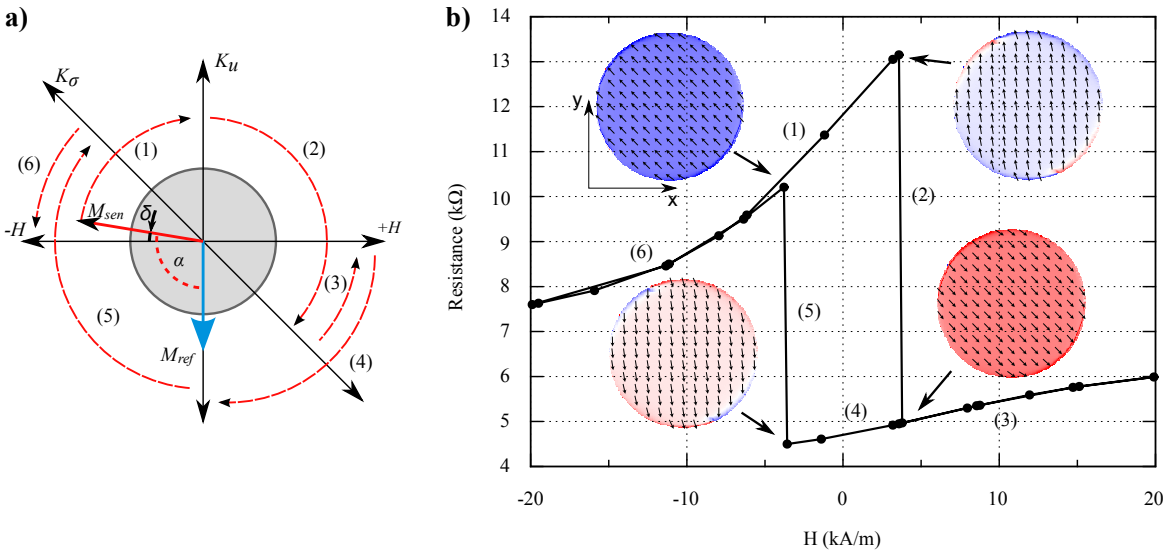

Figure 6.12: a) *A macrospin model of coherent rotation which describes qualitatively hard-axis $R(H)$ loops of a junction exposed to tensile strain, (1) field reduction and gradual rotation to the K_u axis ($\alpha = \pi$), the MTJ in the antiparallel state, (2) magnetization flip to the axis of stress ($\alpha = \pi/4$), (3) aligned roughly along $+H_{max}$ ($\alpha = \pi/2 - \delta$), (4) crossing zero field and reaching the parallel state ($\alpha = 0$), (5) switch to the other direction of the effective induced anisotropy ($\alpha = 3\pi/4$), and (6) return to the initial point.* ***b)*** *A micromagnetic simulated loop of a junction ($D = 11.3\,\mu m$) under 1×10^{-3} strain, which matches very well every step of the measured loops of the strained junctions. The magnetization configuration exhibits the domain flip at either switching fields, indicating valid coherent single-domain rotation. The arrows show the in-plane magnetization vectors.*

switching fields are symmetric because misalignment of the physical quantities (see Fig. 6.4) and the Néel coupling are not implemented in the simulation. Following almost single-domain behavior of M_{sen}, a coherent rotation in the center of the sense layer has been observed in the calculated magnetization configurations. Only a small fraction of the volume magnetization is confined to a non-uniform region propagating to about 100 nm from the edges, which follows the overall magnetization reversal with a small lag leading to the intermediate formation of canted magnetization. This approves the assumption of single-domain behavior of M_{sen} in the SW model to be nearly accurate.

The four magnetization configurations shown adjacent to the graph demonstrate the sudden flip of M_{sen} at the switching fields. At the positive switching field, M_{sen} flips from the antiparallel state to a direction with minimized energy, nearly along the stress axis (step (2)), whereas it flips from the parallel state to the other direction of the stress axis at the negative switching field (step (5)).

Concerning the strain effect on the hard-axis $R(H)$ loops depending on junctions shape, Figure 6.13 demonstrates representative measured loops for nominally 289 μm^2-sized junctions with the round, squared, elliptical(1:3), and elliptical(1:10) shapes. For simplicity, the $R(H)$ loops are shown only in unstrained and under 0.76×10^{-3} strain

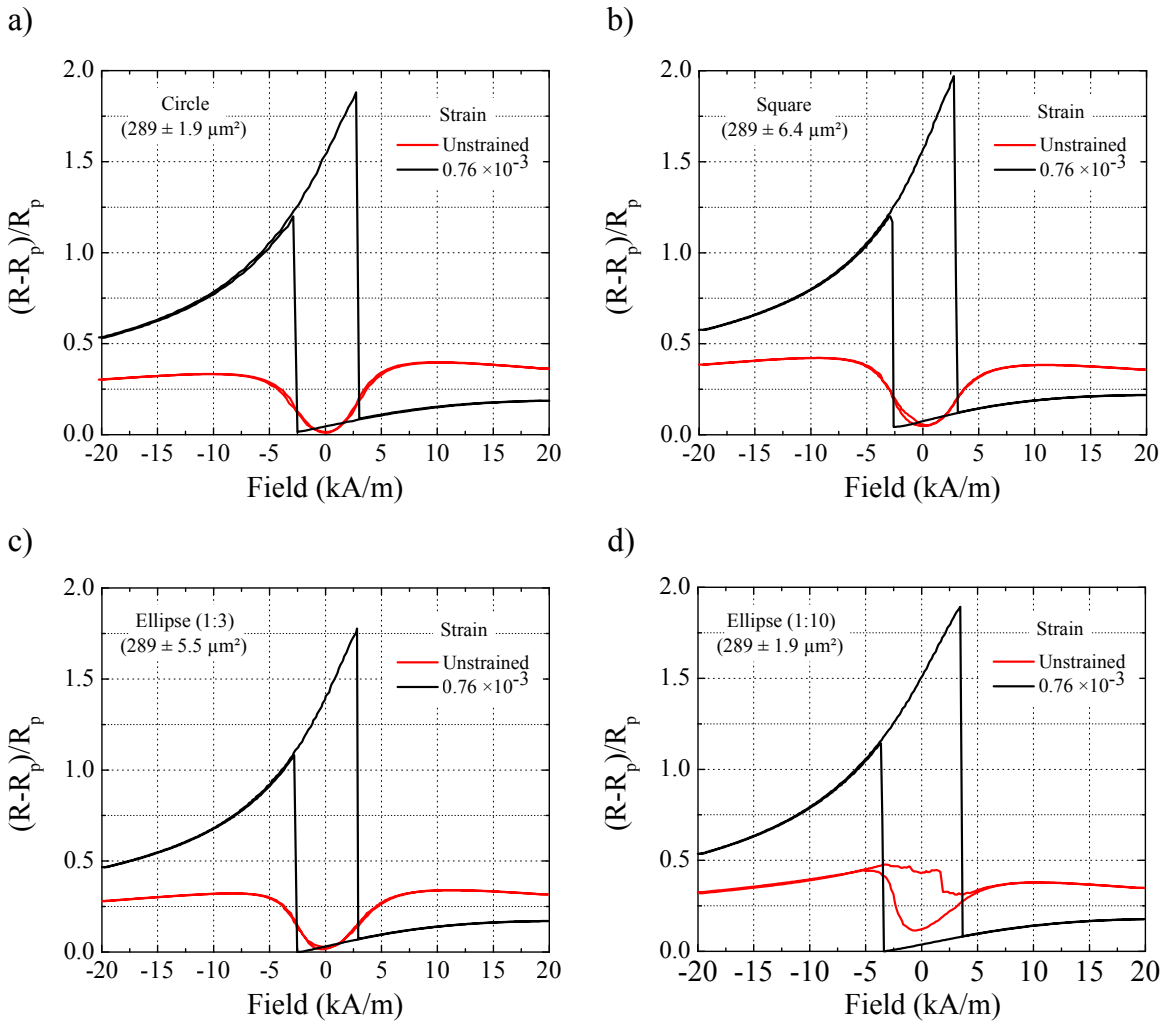

Figure 6.13: *Representative $R(H)$ ($(R - R_p)/R_p$ vs. H) loops which are experimentally measured for junctions with a nominal size of 289 µm in different shapes in unstrained and under 0.76×10^{-3} strain states. In case of the ellipse(1:10) the $R(H)$ loop exhibits an opening which indicates domain formation because of the shape anisotropy. The standard deviation of the junction area is represented in Fig. 4.10.*

states. Furthermore, $(R - R_p)/R_p$, which offers a straightforward comparison of the junctions from different spots on the wafer with various RAs, is used instead of R. The strain effect on the squared (Fig. 6.13 b)) and the elliptical(1:3) (Fig. 6.13 c)) junctions is the same as for the round junctions. This can be attributed to the round corners after the lithography of the squared junctions (see Fig. 4.9) and the ineffective shape anisotropy by the elliptical(1:3) junctions. Therefore, the macrospin (see Fig. 6.12 a)) is also a good approximation for these two shapes in this range of junction size. However, the elliptical(1:10) junction in unstrained state exhibits deviation from the typical rotation of M_{sen} through the parallel configuration (see Fig. 6.8). The opening, that appears at low fields, is probably associated with the stronger shape anisotropy, compared to the elliptical(1:3) junction. It is energetically unfavorable to align M_{sen} along the short axis due to a large stray field. As a result, the domain formation or the domain wall motion probably occurs close to zero magnetic field. Because of such

deviation, elliptical(1:10) junctions are not investigated with regard of the strain sensitivity in the next section even though the $R(H)$ loop of the junction under 0.76×10^{-3} strain is expected to nearly follow the macrospin model. Note that there is a minor asymmetry in the loops of the unstrained states for the round, squared, and elliptical(1:3) junctions. This can be attributed to the misalignment, discussed in Fig. 6.4, of the physical quantities.

As discussed in Fig. 6.13, the strain impact on the hard-axis $R(H)$ loops is the same for the squared, round, and elliptical(1:3)-shaped junctions. Therefore, it is sufficient to only show representative strain loops for the round junctions in the following sections.

6.4 Strain Sensitivity of TMR Sensors

To achieve high strain sensitivity, it is essential to determine the optimum magnetic bias field H_{bias} for the maximum ΔR. For all measured $R(H)$ loops, with the junction strained up to 0.76×10^{-3}, the large resistance increase ΔR occurs at negative fields ($H >$-3 kA/m), reaching the maximum near the switching fields (see Fig. 6.11 a)), for tensile stress. But as for positive fields ($H >$+3 kA/m) the resistance slightly decreases. The strain effect is mirrored for compressive stress (see Fig. 6.11 b)) since the uniaxial stress-induced anisotropy resides at $\theta = \pi/4$. Consequently, under compressive strain the large resistance increase and the small resistance decrease take place at positive and negative fields ($H > \pm 3$ kA/m), respectively. Representative strain loops $R(\varepsilon)$ for the same junction as in Fig. 6.11 at ± 3.2 kA/m (± 40 Oe) and ± 4 kA/m (± 50 Oe) bias fields are depicted in Fig. 6.14. The bias fields are chosen to be away from the switching fields at which domains become unstable leading to domain formation[62]. Following the minor loop without application of stress in Fig. 6.11, prior saturation and then gradual field reduction to the bias field leads to a slight tilt of M_{sen} toward M_{ref} due to the Néel coupling ($\alpha = \pi/2 - \beta$). This is thoroughly depicted in the measurement configurations in Fig. 6.14 a) and b). At -3.2 and -4 kA/m ($\theta_{sen} = \pi + \beta$), applying tensile strain results in rotation of M_{sen} as well as a resistance increase and eventually alignment along the stress axis. The strain loops exhibit two regimes with different rates of the resistance change. As of great importance for AFM applications, the first part up to 0.2×10^{-3} exhibits 42 % $\Delta R/R$ and a resultant gauge factor of $GF = 2150 \pm 30$ at -3.2 kA/m. At $H_{bias} = -4$ kA/m, $\Delta R/R$ and the gauge factor drop to 31 % and 1550 ± 25, indicating the strong field dependence of the strain sensitivity. In comparison, compressive strain leads to opposite rotation of M_{sen} causing resistance reduction. The gauge factor of 260 and 335 are measured at -3.2 kA/m and -4 kA/m, respectively. The inverse impact on the resistance by tensile and compressive stress gives the possibility to distinguish between both stresses even though the gauge factor for compressive stress at these bias fields is comparably low. Lower GF by compressive stress is because M_{sen} rotates by a smaller angle toward its energetically favored direction which is perpendicular to the stress axis ($\theta_\sigma = \pi/4$), as depicted in Fig. 6.14 a). Note that the small hysteresis present in the loops is attributed to magnetic hysteresis as the measured mechanical hysteresis of the four-point bending device is subtracted from the recorded data (details

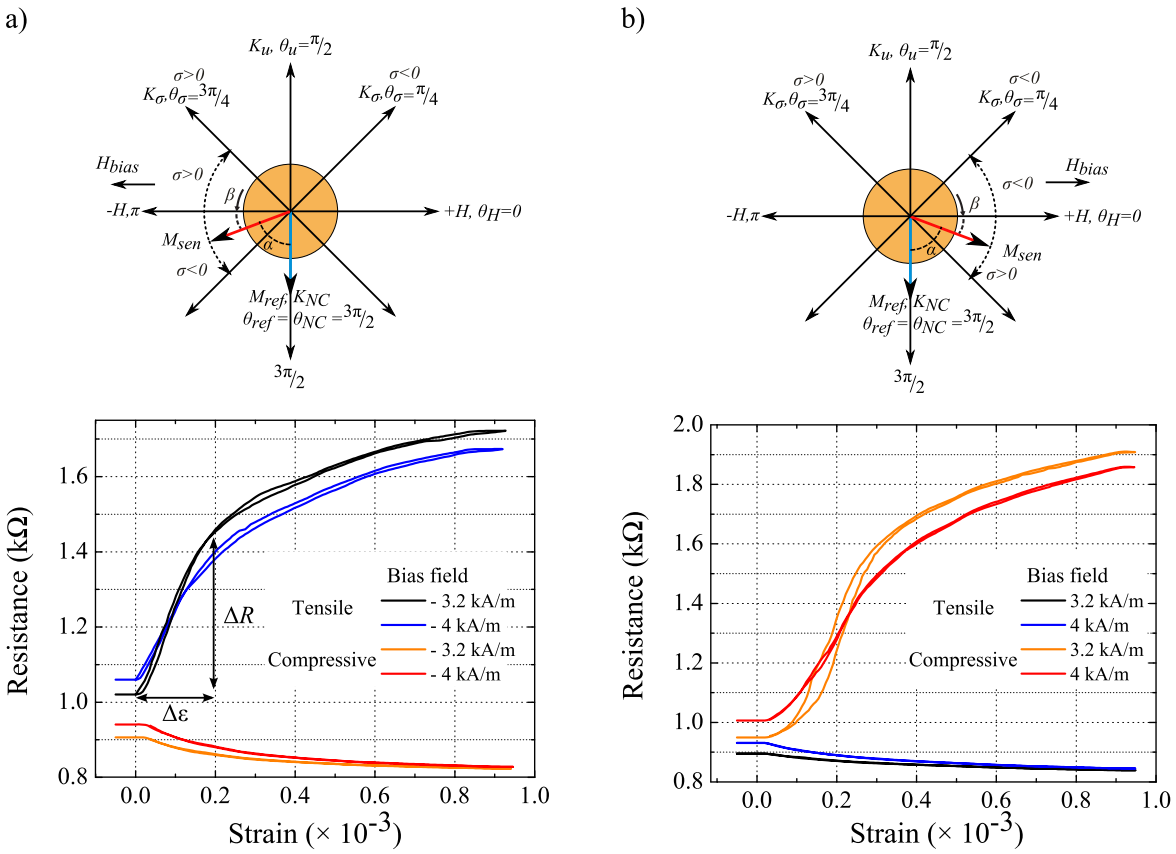

Figure 6.14: *Configuration of physical quantities and measured strain loops ($R(\varepsilon)$) under tensile and compressive stress. For tensile strain K_σ resides at $\theta_\sigma = 3\pi/4$, but as for compressive strain it is induced at $\theta_\sigma = \pi/4$. For calculation of gauge factors, defined as: $GF = (\Delta R/R)/\Delta\varepsilon$, only the part up to 0.2×10^{-3} is considered.* ***a)*** *At $-3.2\,kA/m$ ($-40\,Oe$) and $-4\,kA/m$ ($-50\,Oe$) bias fields tensile (compressive) stress increases (reduces) the angle α resulting in rise (drop) in the tunnel resistance. The gauge factor is 2150 ± 30 and 260 measured at $-3.2\,kA/m$ field under tensile and compressive stress, respectively.* ***b)*** *At positive fields the response is reversed with regard to the impact of compressive and tensile stress on the resistance. The junction exhibits gauge factors of 1750 ± 35 and 250 at $+4\,kA/m$ under compressive and tensile stress, respectively. The hysteresis in the compressive strain loop at $+3.2\,kA/m$ shows the boundary for the bias field. Bias fields should be outside of the switching fields in the $R(H)$ loops of the strained junctions (see Fig. 6.11).*

in Appendix E.1).

Conversely, at +3.2 and +4 kA/m bias fields M_{sen} ($\theta_{sen} = 2\pi - \beta$) can rotate more under compressive stress compared to tensile stress (Fig. 6.14 b)). Therefore, the junction reveals a very large $GF = 1750 \pm 35$ at +4 kA/m for compressive stress. Even though the gauge factor is also large at +3.2 kA/m, it causes a clear magnetic hysteresis. This is attributed to the bias field being between the switching fields in the $R(H)$ loops (see Fig. 6.11 b)). Under tensile stress, gauge factors of 150 and 250 are measured at +3.2 kA/m and +4 kA/m bias fields.

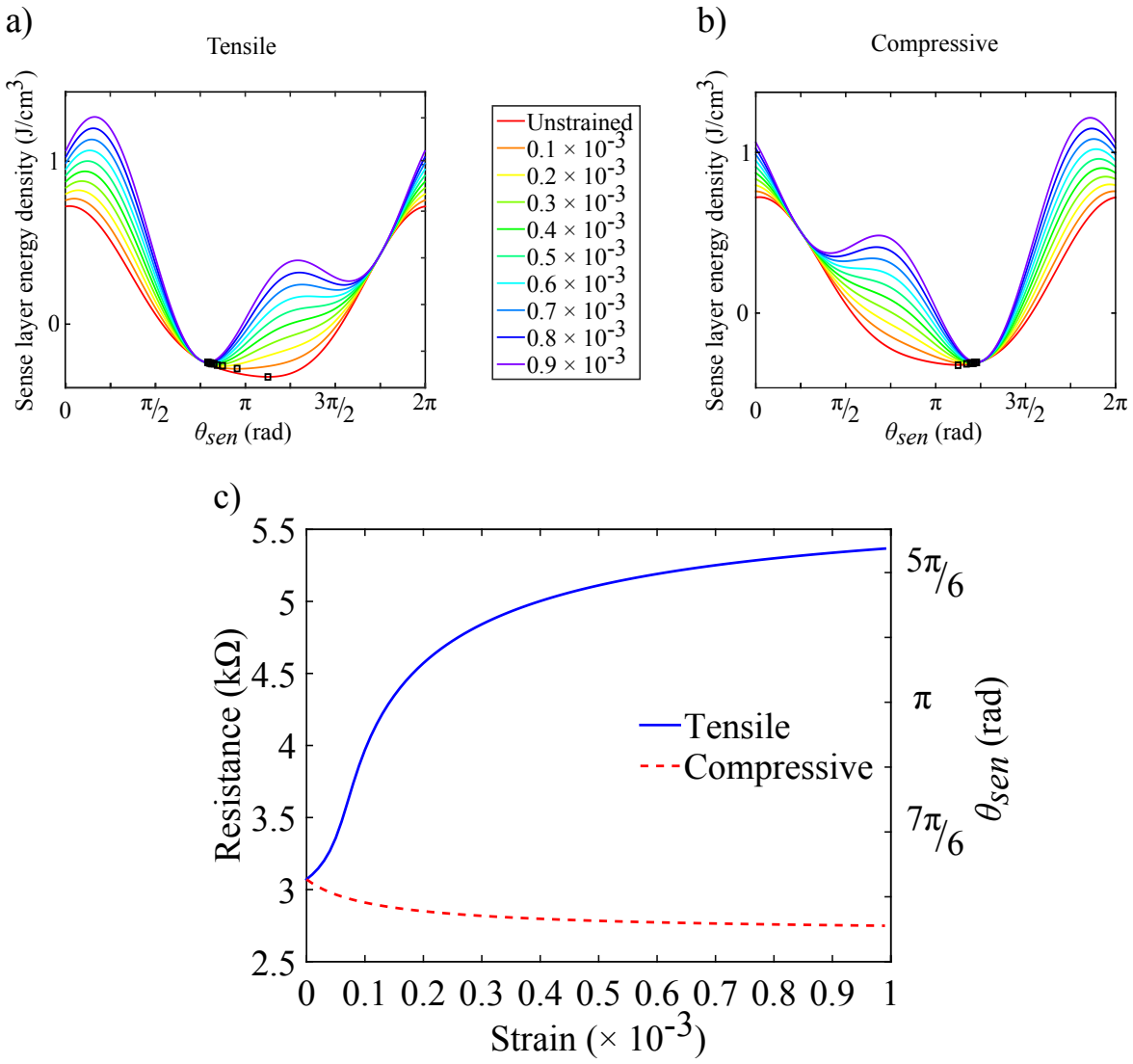

Figure 6.15: *Orientation of M_{sen}, squares at minimum points, in the energy density profiles of the sense layer at −3.2 kA/m (−40 Oe) under* ***a)*** *tensile and* ***b)*** *compressive stress.* ***c)*** *Calculated strain loops show the the same trend as the measured loops shown in Fig. 6.14 a). The right y-axis indicates the corresponding orientation of M_{sen}, extracted from the energy density profiles. Up to 0.2×10^{-3} strain, gauge factors of 2380 and 360 are calculated for the tensile and compressive strain loop, respectively.*

For better understanding, the strain loop at H_{bias} =−3.2 kA/m is simulated by the SW model under compressive and tensile stress. Considering the magnetocrystalline anisotropy energy ($\theta_u = \pi/2$), the Zeeman energy ($\theta_{H_{bias}} = \pi$), the Néel coupling energy ($\theta_{NC} = 3\pi/2$), and the stress-induced anisotropy energy ($\theta_\sigma = 3\pi/4$ or $\pi/4$), the total energy density of the sense layer can be calculated using equation 6.2. Here, the same configuration as for the measured strain loops for tensile ($\theta_\sigma = 3\pi/4$) and compressive ($\theta_\sigma = \pi/4$) stress is considered, as shown in Fig. 6.14 a). Figure 6.15 a) and b) represent evolution of energy density profiles in the sense layer. The minimum energy point in the unstrained state determines the initial orientation of M_{sen}, as $\theta_{sen} = \pi + \beta$ in Fig. 6.14. With H_{bias} =−3.2 kA/m and E_{NC} =580 J/m^3, β is about $3\pi/24$ (22.5°). M_{sen} rotates toward the stress-induced anisotropy axis under tensile ($\theta_\sigma = 3\pi/4$) and compressive ($\theta_\sigma = 5\pi/4$) stress. This meets the mechanism explained in Fig. 6.14 a). From the energy density profiles the orientation of M_{sen} is known at every stain level. As $\alpha = \theta_{sen} - \theta_{ref}$ with $\theta_{ref} = 3\pi/2$, one can plot the $R(\varepsilon)$ loop using equation 2.7 to calculate $R(\alpha)$. R_p =2.5 kΩ and R_{ap} =7.4 kΩ are the experimental values of the junction in Fig. 6.6.

The calculated strain loops have the same trend as the measured loops in Fig. 6.14. They are defined as two regimes with different rates for resistance change. Up to 0.2×10^{-3} strain, gauge factors of 2380 and 360 are calculated under tensile and compressive stress, which are in the range of the measured gauge factors.

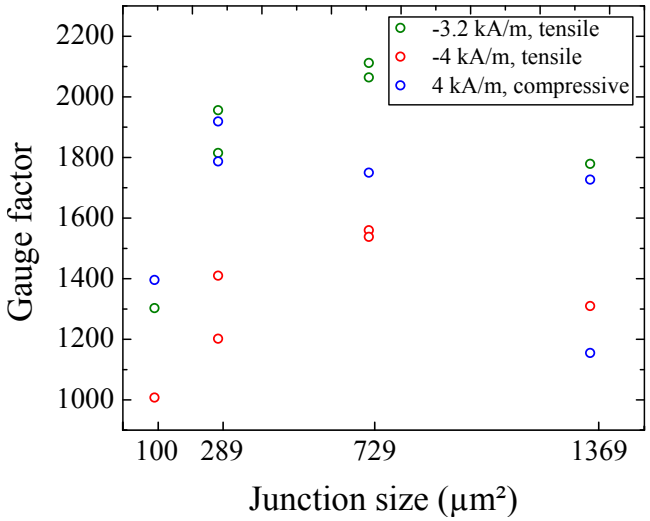

Figure 6.16: *Comparison of gauge factors of the round junctions with different sizes, measured from their strain loops at -3.2 kA/m and -4 kA/m bias fields for tensile stress and at 4 kA/m bias field for compressive stress. The mean area value given as the junction size has a standard deviation of about 2.5 % for the round junctions (see Fig. 4.10).*

Strain loop measurement is carried out on other junctions with all different sizes and shapes. Statistics in Fig. 6.16 show gauge factors measured for nine round junctions. The number of measured junctions is limited because of complex fabrication and a low number of produced junctions with the same TMR effect amplitude and RA range. For tensile stress gauge factors average at about 1800 and 1300 at −3.2 kA/m (−40 Oe)

and −4 kA/m (−50 Oe), respectively. This generalizes the field dependence of the strain sensitivity, observed in Fig. 6.14, for all sizes. In addition, no indication exists for junction size dependence of the strain sensitivity within the size scale used in this study. Variations of the strain sensitivity between the junctions with different sizes and between the junctions with the same size can be attributed to differences in TMR characteristics, properties of layers in the junctions, and patterning conditions such as the edge roughness. Note that the junctions which their gauge factors are shown in Fig. 6.16 belong to different locations on the wafer.

Figure 6.17 shows no indication for shape dependence of the strain sensitivity. This agrees with the observation of the strain impact on the $R(H)$ loops in Fig. 6.13. Considering all the shapes and sizes, for tensile stress gauge factors also average at about 1800 at −3.2 kA/m. This clearly shows that at this size range the strain sensitivity is the same for all the shapes except the ellipse(1:10). Furthermore, as observed in Fig. 6.13 self-biasing by the shape anisotropy of the elliptical junctions is not applicable to replace the need of the bias field.

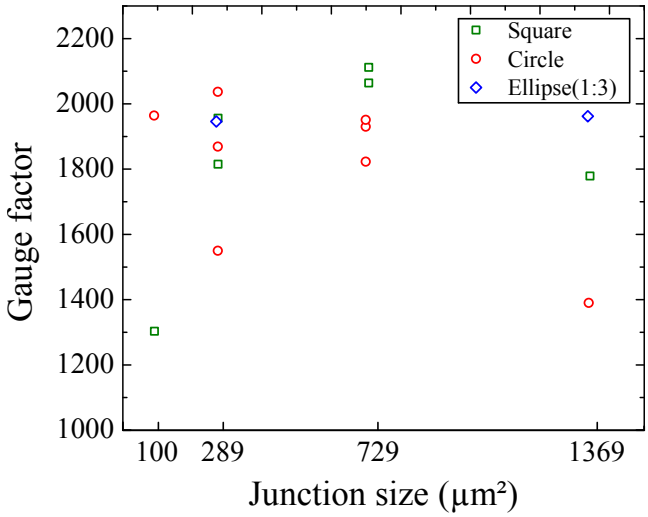

Figure 6.17: *Comparison of gauge factors of seventeen junctions with different shapes measured from their tensile strain loops at -3.2 kA/m bias field. The mean area value is given as the junction size, which has a standard deviation of about 2.5 %, 4.2 %, and 2 % for the round, squared, and elliptical(1:3) junctions, respectively (see Fig. 4.10).*

6.5 Strain Sensitivity at Zero Bias Field

Even though the self-biasing by the shape anisotropy implemented into the elliptical-shaped junctions is not successful so far, the early concept of the 45° alignment can be still beneficial for having TMR strain sensors at zero field. Figure 6.18 a) shows strain loops at zero bias field of a round junction, the same junction as in Fig. 6.6, with 10.8 ± 0.1 µm diameter. In comparison with the strain loops, which require a

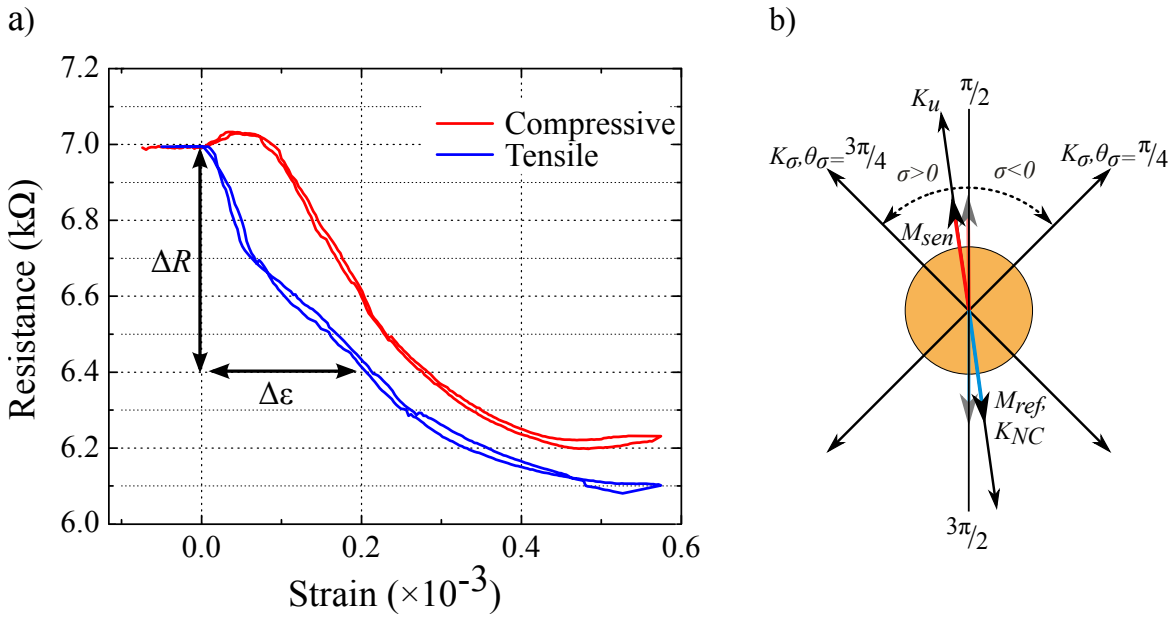

Figure 6.18: a) *Representative tensile and compressive strain loops for a round junction with* $10.8 \pm 0.1\,\mu m$ *diameter without bias field. According to the configuration in* ***b)*** *both rotations by tensile and compressive strain have a similar impact on the resistance and are not distinguishable. As strained up to* 0.2×10^{-3}*, the junction exhibits* 400 ± 7 *and* 435 ± 5 *under tensile and compressive stress, respectively. The bump in the compressive strain loop is associated with slight misalignment of* K_u *(*$\theta_{sen} > \pi/2$*) occurred during the field annealing process.*

magnetic bias field in the previous section, a saturation field is applied opposite to M_{ref}, nearly resulting in an initial antiparallel state ($\theta_{sen} \approx \pi/2$, $\alpha \approx \pi$) proven by the measured resistance value. However, K_u is still aligned at $\pi/4$ against the stress axis (see the configuration in Fig. 6.18 b)). This allows equal $\pi/4$ rotation of M_{sen} for tensile and compressive stress to be along or perpendicular to the stress axis. M_{sen} rotates toward the stress axis (K_σ, $\theta_\sigma = 3\pi/4$) under tensile stress, thereby the angle α as well as the tunnel resistance decreases. Despite that the compressive stress causes inverse rotation of M_{sen} toward K_σ axis ($\theta_\sigma = \pi/4$), it also leads to a reduction in the tunnel resistance. Therefore, the sensor is not able to distinguish the type of applied stress in this configuration. The measured strain loops reveal gauge factors of 400 ± 7 and 435 ± 5 under tensile and compressive stress. The bump in the compressive strain loop is attributed to the misalignment during the field annealing process (see Fig. 6.4). Such deviation can also occur due to misalignment of the field applied for the saturation of M_{sen} prior to the strain loop measurements. The initial orientation is slightly off K_u axis ($\theta_{sen} > \pi/2$). Therefore, applying compressive stress M_{sen} rotates toward the antiparallel state leading to the increase in the resistance at first and afterward to the resistance drop.

Strain loops are simulated by the SW model at zero bias field under compressive and tensile stress using equation 6.2. Considering the saturation magnetization at $\theta_{sen} = \pi/2$ and continuous strain strokes, the energy of the sense layer includes the magnetocrystalline anisotropy ($\theta_u = \pi/2$), the Néel coupling energy ($\theta_{NC} = 3\pi/2$),

and the stress-induced anisotropy energy ($\theta_\sigma = 3\pi/4$ or $\pi/4$).

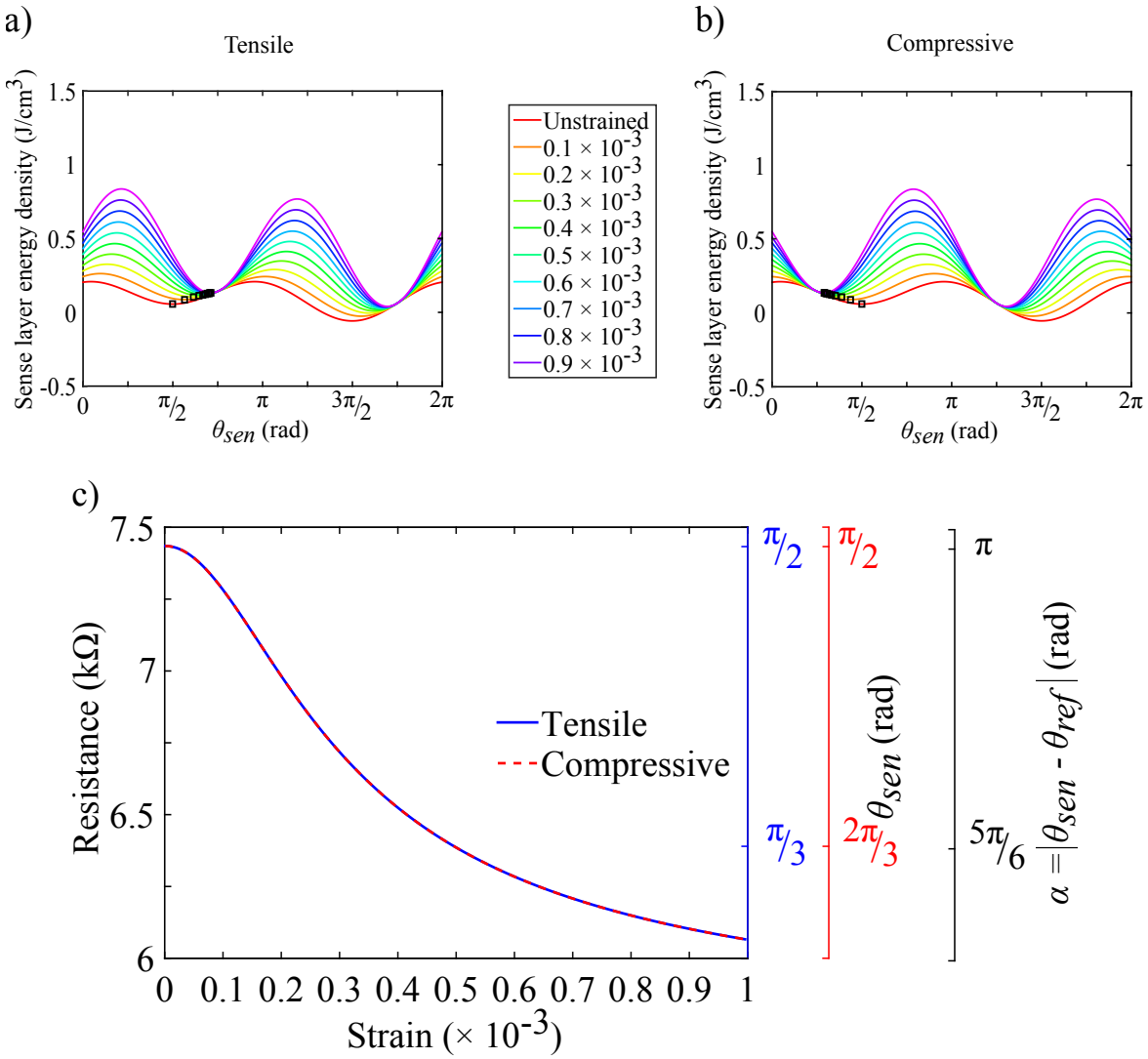

Figure 6.19: *Energy density profiles of the sense layer at zero bias field under* ***a)*** *tensile and* ***b)*** *compressive strain. Squares demonstrate rotational tendency of M_{sen} from the initial state, $\theta_{sen} = \pi/2$ after the prior saturation. M_{sen} rotates depending on strain type toward $\theta_\sigma = 3\pi/4$ or $\theta_\sigma = \pi/4$. However, both lead to the resistance decrease in* ***c)*** *calculated strain loops, exhibiting gauge factor of $GF = 305$ for $\varepsilon = 0.2 \times 10^{-3}$. Changes of θ_{sen} and α, which correspond the resistance in the strain loops, are specified as the vertical axes on the right.*

Figure 6.19 a) and b) shows evolution of energy density profiles under compressive and tensile strain. The initial orientation of M_{sen} is $\theta_{sen} = \pi/2$, $\alpha = \pi$ as in Fig. 6.18 b). Applying tensile and compressive strain, M_{sen} rotates toward the axis of K_σ at $\theta_\sigma = 3\pi/4$ and $\theta_\sigma = \pi/4$, respectively. The equilibrium orientation of M_{sen} is specified by squares in the energy density profiles. The minimum points close to $\theta_{sen} = \pi/2$ are taken because of applying the saturation field along the same direction in the experimental. As shown in Fig. 6.19 c), the calculated strain loops of both stresses cause a resistance reduction as the measured strain loops shown in 6.18 a). Within

0.2×10^{-3} compressive and tensile strain $GF = 305$, which is in the same range of the experimental results, is calculated

In order to clarify the slight increase in the measured compressive strain loop (see Fig. 6.18), a calculation based on the SW model shown in Fig. 6.19 is performed while introducing a 5° deviation into the initial orientation of M_{sen} ($\theta_{sen} = \pi/2 + \pi/18$). As depicted in Fig. 6.20, the 5° deviation causes a resistance difference of about 0.5% from the initial resistance and the maximum resistance until the antiparallel state is reached ($\theta_{sen} = \pi/2$). Since the same resistance difference is present in the measured compressive strain loop, one can presume that the deviation in the experimental is about 5°. Note that possible deviations from single-domain behavior by M_{sen} are not considered.

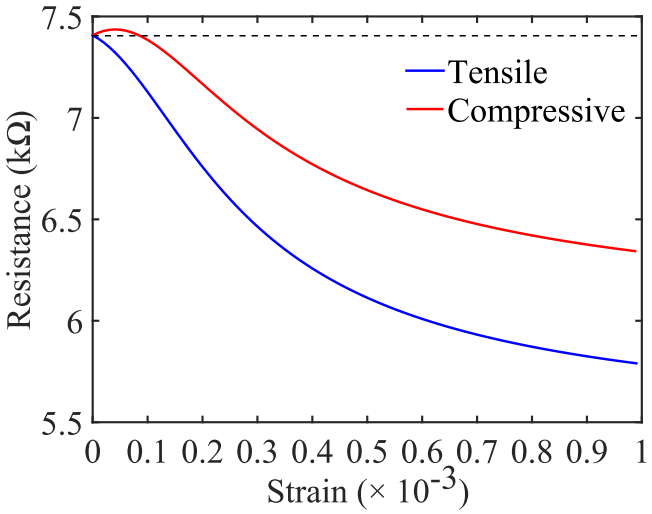

Figure 6.20: *Re-calculation of the strain loops in Fig. 6.19, while introducing a 5° deviation into the initial orientation of M_{sen}. This leads to a resistance increase of about 0.5% at the beginning of the compressive strain loop, as in the measured strain loop in Fig. 6.18.*

6.6 Magnetostriction of Sense Layers of Patterned MTJs

Figure 6.21 a) represents the influence of applied compressive strain on the $R(H)$ loops. In an unstrained condition, the magnetic configuration of the junction supposedly varies from the perpendicular to the parallel and again to the perpendicular state within the field loop (see details in Fig. 6.8). However, two deviations are visible. On one hand, the reduction in resistance at $H > \pm 7.5\,\mathrm{kA/m}$ indicates that the perpendicular configuration is not reached, as M_{ref} is affected by the magnetic field. On the other hand, the resistance at zero field is higher than $R_p = 0.3\,\mathrm{k\Omega}$. This can be attributed to the formation of canted magnetization at the edges of the sense layer (see Fig. 6.12).

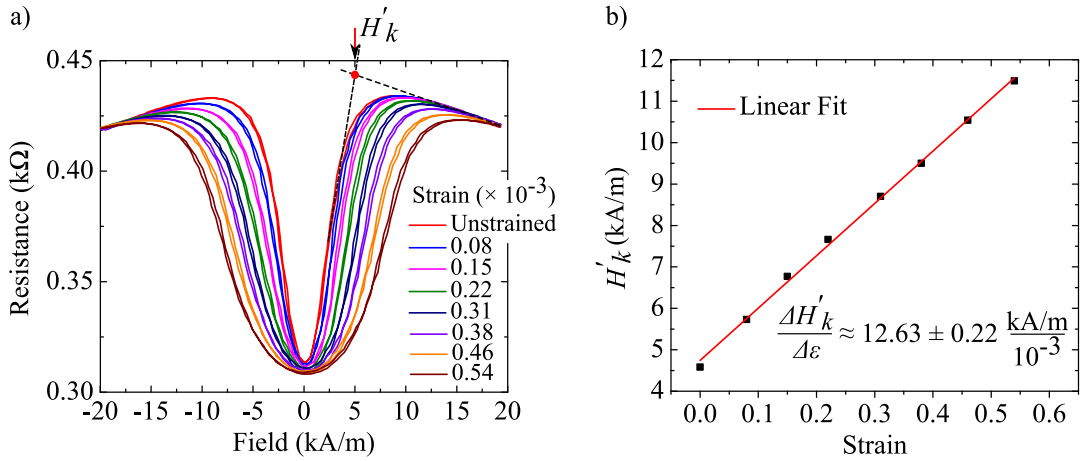

Figure 6.21: a) *$R(H)$ loops of a round junction with a diameter of $41.4 \pm 0.1\,\mu m$ under different levels of compressive strain. Higher strain causes stabilization of M_{sen} along its initial direction, leading to harder rotation of M_{sen} within the field loops. H'_k is a field at an intersection of a line drawn along the linear section of an $R(H)$ loop after its inflection point and the common tangent line at the maximum field. H'_k values can quantify the strain influence on the $R(H)$ loops.* ***b)*** *Variation of the effective anisotropy field H'_k measured from the $R(H)$ loops in panel a) as a function of applied compressive strain.*

Applying compressive stress stabilizes M_{sen} along its initial direction due to the uniaxial stress-induced anisotropy (K_σ) parallel to K_u. Consequently, for higher strain levels larger magnetic fields are required to rotate M_{sen}. In addition, the resistance at zero field becomes closer to $R_p = 0.3\,\text{k}\Omega$ (Fig. 6.21 a)), as the portion of the canted magnetization probably decreases under larger K_σ. It is also visible that M_{ref} is less affected at higher fields compared to the unstrained state, as M_{ref} is more stabilized due to larger K_σ.

Nevertheless, the assumption of single-domain behavior of the sense layer is still applicable at fields slightly away from zero field, as coherent rotation of M_{sen} probably occurs. No jumps and hysteresis in the $R(H)$ loops indicate no abrupt changes in M_{sen}. Applying strain leads to harder rotation of M_{sen}, and as a result changes in the slope of the linear part of the $R(H)$ loops in Fig. 6.21 a). Accordingly, changes in H'_k, instead of the anisotropy field H_k, as a function of the applied strain can be used in equation 2.14 to measure the effective saturation magnetostriction of the sense layer:

$$\lambda'_s = \frac{\mu_0 M_s}{3Y} \frac{\Delta H'_k}{\Delta \varepsilon}. \tag{6.3}$$

Figure 6.21 b) demonstrates the variation of H'_k measured from the $R(H)$ plots in Fig. 6.21 a). The variation is nearly linear as Ali and Watts reported for H_k versus ε characteristics[135]. The linearity is attributed to the stress-induced anisotropy, which scales linearly with applied stress or strain. Using equation 6.3, the patterned CoFeB film, as the sense layer in the MTJ, exhibits $\lambda'_s = 32.24 \pm 0.56\,\text{ppm}$.

In order to understand the deviations from single-domain behavior, $R(H)$ loops for continuous films shown in Fig. 6.22 a) are calculated using equation 2.7. $R_p = 0.3\,\mathrm{k\Omega}$ and $R_{ap} = 1.03\,\mathrm{k\Omega}$ used for the calculation are determined experimentally. The equilibrium orientation of M_{sen} as a function of H is deduced by the energy minimization in the SW model. The total energy includes the magnetocrystalline anisotropy ($\theta_u = \pi/2$), the Zeeman energy ($\theta_H = \pi$), the Néel coupling energy ($\theta_{NC} = 3\pi/2$), and the stress-induced anisotropy energy ($\theta_\sigma = \pi/2$).

The modeling parameters except $\lambda_s' = 32.24 \pm 0.56$ ppm are given in section 6.1.2.

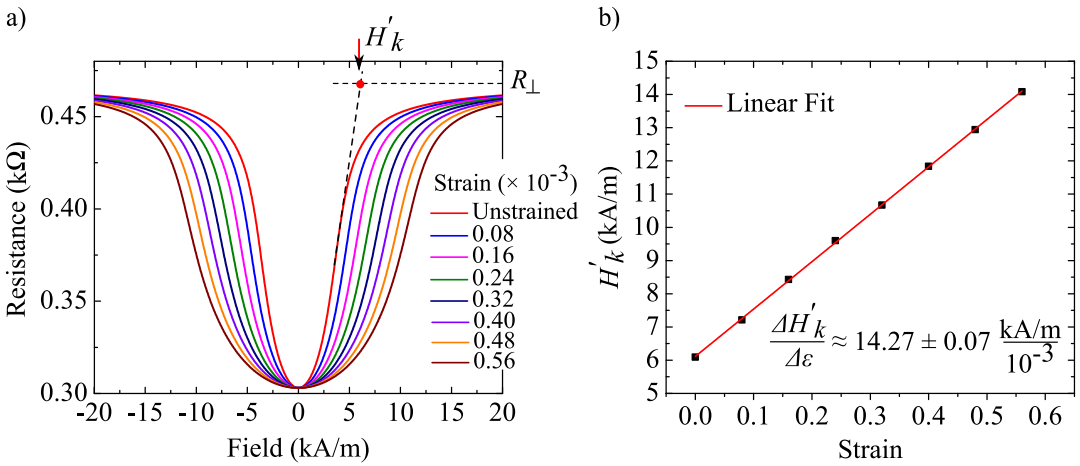

Figure 6.22: a) *Calculated $R(H)$ loops using the SW model incorporating with equation 2.7. Compressive stress stabilizes M_{sen}, leading to smaller slopes in the linear part of the $R(H)$ loops. H'_k is a field at an intersection of a line drawn along the linear section of an $R(H)$ loop after the inflection point and the saturation line at $R_\perp = 0.47 k\Omega$.* ***b)*** *Variation of H'_k as a function of applied compressive strain. The slope is different from the value obtained from the measured $R(H)$ loops in Fig. 6.21 b).*

As shown in Fig. 6.22 a) the resistance reaches R_p at zero field and no resistance reduction appears in the calculated $R(H)$ loops in comparison to the measured loops in Fig. 6.21 a). Figure 6.22 b) shows calculated H'_k as a function of applied strain, exhibiting a linear variation but with a different slope compared to the measured slope in Fig 6.21 b). Such difference can be attributed to the fact the tunnel resistance is not a direct measure of M_{sen}. Also, errors in graphical deduction of H'_k values should not be neglected.

From the calculated $R(H)$ loops in Fig. 6.22 a), one can first deduce $Cos(\alpha)$ versus field characteristics for all strain levels using equation 2.7. Then, $Sin(\alpha)$ as a function of field represented in Fig. 6.23 a) can be plotted, as $Sin(\alpha) = \sqrt{1 - Cos^2(\alpha)}$. $Sin(\alpha)$ basically simulates normalized magnetization of the sense layer in the field direction ($M_{sen,x}/M_{sen}$). As shown in Fig. 6.23 b), the H_k versus ε plot deduced from the calculated $M_{sen,x}/M_{sen}$ plots has a slope in the same range of the measured value obtained in Fig. 6.21 b). Extraction of $Sin(\alpha)$ or magnetization versus field from the measured $R(H)$ loops is unfortunately not possible due to the present deviations from single-domain behavior. Nevertheless, the proposed measuring technique is legitimate

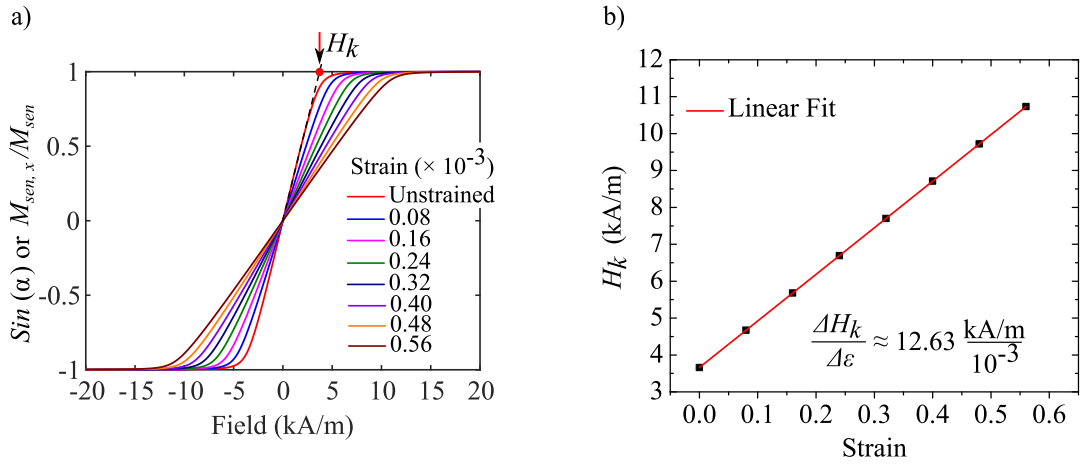

Figure 6.23: a) *Calculated $Sin(\alpha)$, $M_{sen,x}/M_{sen}$, plots as a function of applied field deduced from the $R(H)$ loops in Fig. 6.22 b). H_k is defined as an intersection of the saturation line and the slope of the tangent line of each plot at zero point. These curves considered as magnetization curves are not sharp lines, as for typical SW model plots. This is associated with the additional uniaxial stress-induced anisotropy and the additional unidirectional anisotropy due to the Nèel coupling.* ***b)*** *Variation of H_k as a function of applied compressive strain, exhibiting the same value obtained from measured $R(H)$ loops in Fig. 6.21 b).*

since the measured value is in agreement with saturation magnetostriction reported for thin CoFeB films by Wang et al.[85] and Barsukov et al.[259], whereas Lebendev et al. published $\lambda_s = 50 - 120$ ppm for different CoFeB compositions[134].

Influence of Junction Size

Table 6.3 gives effective saturation magnetostriction values measured for the sense layer in round junctions with different sizes.

Table 6.3: *Measured H_k' variation as a function of ε and λ_s' for the CoFeB sense layer of round junctions with different sizes.*

Junction diameter	10.8 ± 0.1 µm	18.7 ± 0.1 µm	30 ± 0.2 µm	41.4 ± 0.1 µm
$\frac{\Delta H_k'}{\Delta \varepsilon}\left[\frac{kA/m}{1\times 10^{-3}}\right]$	13.63 ± 0.1	14.18 ± 0.24	13.66 ± 0.25	12.63 ± 0.22
λ_s' [ppm]	34.8 ± 0.24	36.2 ± 0.61	34.86 ± 0.63	32.24 ± 0.56

The H_k' variation and λ_s' values are in the same range. However, smaller junctions lead to openings in $R(H)$ loops and enhance impacts of deviation from single-domain behavior on the measurement. In comparison, larger size can reduce the effect of the canted magnetization.

6.7 Conclusions

The stress-induced anisotropy effect on hard-axis $R(H)$ loops is investigated for the magnetostrictive TMR sensors with nominal sizes of $100\,\mu m^2$, $289\,\mu m^2$, $729\,\mu m^2$, and $1369\,\mu m^2$ in squared, round, elliptical(1:3), and elliptical(1:10) shapes. The external magnetic field and the stress axis are set at $\pi/2$ and $\pi/4$ angles, respectively, toward the induced magnetocrystalline anisotropy. Strain effect on the $R(H)$ loops is the same for all junctions except the elliptical(1:10) junctions. As approved theoretically by the SW model, applying strain alters the magnetization reversal of M_{sen} through M_{ref} in the unstrained state. For tensile strain above 0.27×10^{-3}, the switching fields appear as the abrupt changes of the tunnel resistance in the $R(H)$ loops. A macrospin model supported by the micromagnetic simulations is proposed describing details of the rotation mechanism of M_{sen} in the $R(H)$ loops of the junctions exposed to tensile stress. A certain agreement prevails in the experimental results and the representative model.

As the corresponding stress-induced anisotropy is perpendicular to the stress axis for compressive stress, mirrored $R(H)$ loops are observed compared to tensile stress. Tensile stress leads to a large resistance increase ΔR at negative fields ($H >$-3 kA/m), whereas it emerges at positive fields ($H >$+4 kA/m) for compressive stress. However, a small resistance decrease occurs at positive and negative fields for tensile and compressive strain, respectively. Considering the inverse impact by tensile and compressive stress on the tunnel resistance, a single sensor with a bias field detects both stresses. This extends their applications to dynamic devices such as dynamic mode AFM.

Representative experimentally measured tensile and compressive strain loops $R(\varepsilon)$ for a round junction with a diameter of $30 \pm 0.2\,\mu m$ at ± 3.2 kA/m and ± 4 kA/m bias fields reveal the strain sensitivity dependence on the bias field and the inverse impact by both stresses on the tunnel resistance. At -3.2 kA/m and -4 kA/m, the junction exhibits gauge factors of $GF = 2150 \pm 30$ and $GF = 1550 \pm 25$ for tensile strain, whereas for compressive strain the gauge factors of 260 and 335 are measured. Conversely, at +4 kA/m, a positive bias field, the junction shows $GF = 1750 \pm 35$ and $GF = 250$ for compressive and tensile strain, respectively. Using the energy minimization based on the SW model, the rotation of M_{sen} in the tensile and compressive strain loops are successfully simulated. The calculated strain loops exhibit nearly the same trends and gauge factors as the experimentally measured strain loops. In addition, the statistical measurements demonstrate that the strain sensitivity is independent of the junction shapes and sizes used in this study.

The shape anisotropy of elliptical junctions is not suitable for replacing the bias field probably because of its uniaxial character and the large sizes of the junctions. The shape anisotropy can lead to the domain formation at low magnetic fields. However, we represented a round junction with $10.8 \pm 0.1\,\mu m$ diameter which exhibits the gauge factors of 400 ± 7 and 435 ± 5 at zero bias field under tensile and compressive stress, respectively. For comparison, Si-based piezoresistive sensors in small strain ranges exhibit gauge factors of about 200. Therefore, the round junction TMR junctions provide a miniature detection system suitable for strain sensing applications limited

by the size of read-out systems. For instance optical read-out systems become complex, tiresome, and bulky for AFM imaging in liquid and vacuum environments.

Finally, a new technique is proposed to nearly measure the saturation magnetostriction of the sense layer of patterned MTJs. This allows to characterize the sense layer after the junctions are completely fabricated. Accordingly, strain sensitivity of MTJs can be tuned considering the patterning effects and presence of other layers in the junction. The effective saturation magnetostriction of the patterned $Co_{40}Fe_{40}B_{20}$ sense layer is deduced from the $R(H)$ loops, based on the method proposed by Ali and Watts[135]. The deviations in the $R(H)$ loops originated from the patterning effects and the affected M_{ref} are addressed by the simulation using the SW model. The variation of the effective anisotropy field H'_k, instead of the anisotropy field H_k, is used to measure the effective saturation magnetostriction λ'_s. Values with the same range in the literature are measured for the CoFeB sense layer of different junction sizes.

Chapter 7

Self-sensing AFM Cantilevers Based on TMR Sensors

In this chapter, AFM applications of the magnetostrctive TMR senors with high strain sensitivity are described. Integration of the TMR sensors to the AFM microcantilevers is thoroughly explained in section 4.3. Their performance is investigated via a home-built AFM in *Karlsruhe Institute of Technology*. The setup, which is briefly explained here, was constructed by Dr. Tobias Meier. These TMR self-sensing cantilevers are analyzed in terms of deflection sensitivity, minimum detectable deflection (MDD), and topography imaging in the contact and dynamic modes with AM-AFM and FM-AFM feedback loops. In the following sections, the quality of their results are compared with those obtained by the conventional optical read-out.

7.1 AFM Setup with TMR and Optical Read-outs

In order to characterize the TMR self-sensing microcantilevers for AFM applications, the cantilever deflection must be measured independently by means of the conventional optical read-out and the TMR sensors in parallel. For this purpose, a home-built AFM setup was constructed in *Karlsruhe Institute of Technology* by Dr. Tobias Meier[260]. In addition to optical and mechanical parts, two pairs of magnetic coils serve the required bias field to maintain the maximum strain sensitivity (see Fig. 6.14). Unlike commercial available instruments, all components are chosen deliberately to be non-magnetic as any stray field can distort the bias magnetic field and also affect magnetic properties of the TMR sensors. In order to achieve a large field of view in combination with high spatial resolution, a high resolution open-loop piezo scanner (5 µm×5 µm×5 µm) is nested on a large area closed-loop piezo scanner (800 µm×800 µm in x-y plane and 35 µm in z axis). The AFM is operated with a commercial ARC2-biPolar AFM controller by Asylum Research. The controller can directly drive open-loop piezo scanners, because of its integrated high voltage amplifier. For the closed-loop scanner this is also possible by an attached high voltage

amplifier and a closed-loop controller[260].

Figure 7.1 schematically shows the detection principle of the cantilever deflection. Upward and downward cantilever deflection, respectively, correspond to tensile and compressive stress imposed into the deflection sensors. As the same configuration in Fig. 6.14 a) is applied here, accordingly M_{sen} rotates and consequently the junction resistance changes.

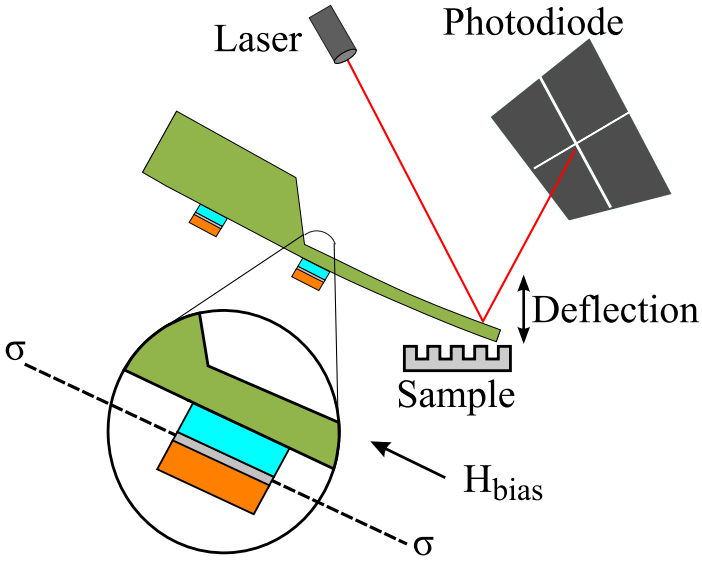

Figure 7.1: a) *Schematic of the optical read-out in parallel with a self-sensing microcantilever integrated with magnetostrictive TMR sensors. Upward and downward deflection impose tensile and compressive stress σ on the bottom side of the cantilever. This is detected by the resistance change of the deflection TMR sensor (see Fig. 4.16 b)). The TMR sensor on the support chip is not subjected to stress and can be used as a reference.*

As the measurements in chapter 6 a small bias voltage of 10 mV is applied to monitor the junction resistance during AFM measurements. Such small bias voltage leads to small tunneling currents in the µA range. In contrast to the electronics with long integration time in the four-point bending apparatus (see section 6.1.1), in the AFM very fast and precise read-out electronics are required to detect small resistance changes. Therefore, the deflection TMR sensor is electrically monitored in a Wheatstone bridge configuration with an attached high gain and bandwidth amplifier[260]. Using a bridge voltage of 20 mV, drop voltage of 10 mV, a variation of a few nanovolts occurs for small cantilever deflections and, correspondingly, small resistance variations. Therefore, the amplifier has to show a low intrinsic noise level. This requires as less components as possible (as every component adds intrinsic noise) and short wires between the TMR sensor, the bridge, and the amplifier as they act as antennas picking up RF-noise[260]. The cantilever is mounted on a PCB is wire-bonded to the integrated amplifier. Applying higher bias voltage to the bridge enhances the signal compared to the noise, however, this will reduce the TMR effect amplitude of the sensors[75,261,262] and, as a result their strain sensitivity. Therefore, bias voltage requires to be tuned for the optimum signal-to-noise ratio. Readers are referred to the Ph.D. dissertation by Dr. Tobias

Meier[260] for more details regarding the measuring parameters.

In the following sections the TMR read-out and the optical read-out are compared as this will highlight the capability of the TMR self-sensing microcantilevers for AFM applications. Here, AFM measurements include analysis of the deflection sensitivity in the contact and dynamic modes and contact and dynamic imaging on different substrates. At the end, the minimum detectable deflection (MDD) of the TMR sensors is discussed.

7.2 Deflection Sensitivity

Figure 7.2 displays the force-distance curve (FD curve) measured by the TMR and optical read-outs as the cantilever is approached and retracted toward the surface of a Poly(methyl methacrylate) (PMMA) line grating. A self-sensing cantilever with specification no. 10 given in Table 4.4 is used as the junction holds 121% TMR effect amplitude and 61 kΩμm^2 RA. A comparably large travel of the z-piezo (about 6 μm) is chosen in order to monitor the resistance change also for high strain levels in the TMR sensor. Approaching the cantilever causes upward bending (tensile strain) resulting in resistance increase. This is expected since the same configuration, except here $H_{bias} = 60$ Oe, is applied as for the tensile strain loop in Fig. 6.14 a). The different bias field is applied because higher sensitivity is observed at $H_{bias} = 60$ Oe in experimental AFM conditions.

For measurement of the relative resistance change of the TMR sensor by the Wheatstone bridge, the voltage between the midpoints is amplified by 60 dB and low-pass filtered with a cut-off frequency of 300 kHz. The minor hysteresis observed for the TMR sensor is probably caused by magnetic hysteresis since no mechanical hysteresis is present in the FD curve for the optical read-out. The deflection signal is roughly linear for the optical beam-deflection while the read-out of the TMR sensor ($\Delta R/R$) reveals a non-linear relation to the applied z-displacement. This change of sensitivity, the slope, of the FD curve of the TMR system originates from the angular dependency of the resistance on the angle α (see equation 2.7). Note that during imaging an AFM is typically operated with cantilever deflection below 100 nm and one can assume a roughly linear sensor response for such scales. From the curve in Fig. 7.2 the deflection sensitivity, as a relative change in the resistance divided by the cantilever deflection (see equation 2.35), is calculated. The value obtained near the equilibrium position of the cantilever, dashed line, is about $S_\delta = 3.9 \times 10^{-6}$ /Å. This value is at least one order of magnitude better than previously reported values for metallic-based[30,45] and semiconductor-based[41–44,46] piezoresistive sensors. The maximum deflection sensitivities of 2.5×10^{-7} /Å and 1×10^{-8} /Å, reported so far, belong to Si[41] and Au[45] microcantilevers, respectively.

As depicted in Fig. 7.3 for a TMR sensor with 27 μm × 27 μm nominal size, the deflection sensitivity can be also investigated in the dynamic mode as the cantilever oscillates at its resonance frequency. Oscillating upward and downward bending of the cantilever leads to stress alternation $\sigma(t)$ between tensile and compressive stress,

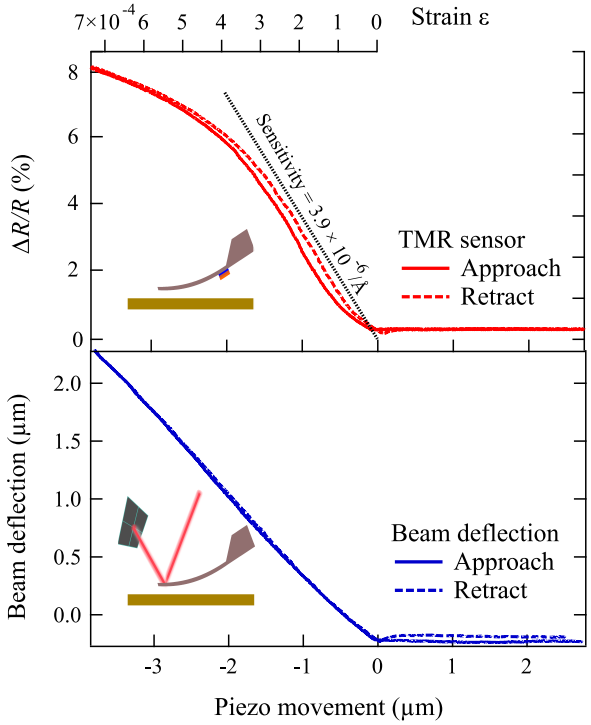

Figure 7.2: *Comparison of Force-Distance curves (FD curves) measured with the TMR sensor (top) and the optical beam deflection systems (bottom). The hysteresis between the approach and retraction curves for the TMR sensor is caused by magnetic hysteresis effects. The dashed line in the TMR curve represents a sensitivity of* $3.9 \times 10^{-6}/\text{Å}$*. The axis on top shows nominal strain acting on the TMR sensor. Having strain axis, defined as:* $\varepsilon = \frac{6lk}{wt^2Y}\delta_{el}$*, on top gives the chance to compare the FD curves with the strain loops. Applied strain is calculated at the center of the junction placed at the base of the cantilever.*

imposed to the deflection TMR sensor.

It was explained earlier that all physical quantities upon the sense layer in the TMR microcantilevers have the same configuration as in Fig. 6.14, thereby, high strain sensitivity as well as the inverse impact by tensile and compressive stress on the tunnel resistance is expected. Therefore, as the cantilever oscillates M_{sen} also oscillates at its initial orientation set by $H_{bias} = 60\,\text{Oe}$ (see Fig. 7.3 a)). Accordingly, the angle α varies ($\alpha(t)$), which appears as oscillation of the tunnel resistance as shown in Fig. 7.3 b). The beam deflection ($A(t)$) quantified by the optical read-out can be converted to strain imposed to the TMR sensor using the equation given in the caption of Fig. 7.2. Figure 7.3 c) shows the relative resistance change as a function of the applied strain for four chosen bias field directions with respect to M_{ref} ($\theta_{H_{bias}}$). The deflection sensitivity as the plot slope ($(\Delta R/R)/\varepsilon$) strongly depends on the field direction. The junction shows higher strain sensitivity for tensile strain, which agrees with the previous results of the four-point bending measurements represented in Fig. 6.14. In contrast to other field directions, for $\theta_{H_{bias}} = 135\,^\circ$ tensile (compressive) strain causes resistance increase (decease). As the bias field is misaligned, M_{sen} can pass the cantilever length, thereby, the junction responses inversely. Overall, these plots simulate the strain loops in

chapter 6. In order to realize the angular dependence of the deflection sensitivity, the cantilever oscillation is measured by the TMR read-out for $\theta_{H_{bias}}$ from 0° to 180° angles in a 5° step, as prior saturation of the sense layer magnetization is carried out. Figure 7.3 d) shows the normalized deflection sensitivity as a function of $\theta_{H_{bias}}$ in a logarithmic polar plot. The highest deflection sensitivity occurs at $\theta_{H_{bias}}$ = 105°-110° toward M_{ref}. For symmetry reasons, the behavior of the TMR sensor can be assumed to have the same sensitivity for negative $\theta_{H_{bias}}$, however, the signal from the TMR sensor is inverted with respect to the signal for positive $\theta_{H_{bias}}$.

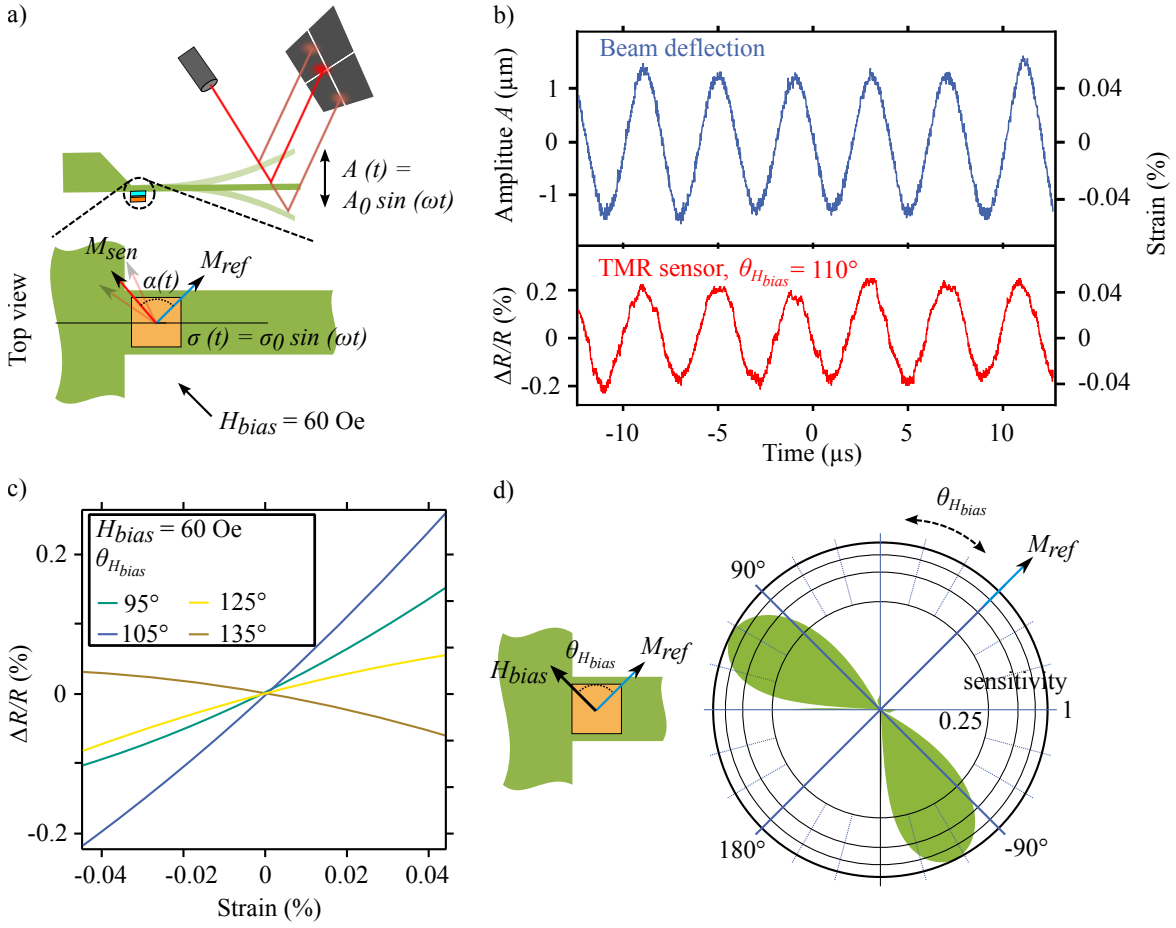

Figure 7.3: *Deflection sensitivity of a 27 µm × 27 µm-sized TMR sensor in the dynamic mode depending on the bias field direction*[260,263]*. $\theta_{H_{bias}}$ defines the field direction with respect to M_{ref}.* ***a)*** *The cantilever is oscillated at its resonance frequency while the oscillating amplitude $A(t)$ is monitored by the optical read-out. As upward and downward bending cause stress alternation between tensile stress (positive) and compressive stress (negative), the angle α between M_{sen} and M_{ref} accordingly varies during the oscillation.* ***b)*** *The increase and decrease in the tunnel resistance is correlated to the stress alternation, as the inverse impact of tensile and compressive stress is shown in Fig. 6.14.* ***c)*** *The relative change in the resistance $\Delta R/R$ as a function of the applied strain, imposed by the cantilever deflection, for four chosen $\theta_{H_{bias}}$.* ***d)*** *The normalized deflection sensitivity as a function of $\theta_{H_{bias}}$. Maximum sensitivity occurs at $\theta_{H_{bias}}$ = 105°-110° toward M_{ref}.*

The dependence of the deflection sensitivity can be explained by the angular dependence of the tunnel magnetoresistance, explained in section 2.2.1. Fig. 7.4 illustrates the tunnel resistance and the relative resistance change, calculated using equation 2.7, as a function of the angle α. R_p =86 Ω and R_{ap} =239 Ω are the experimental values of the junction in Fig. 7.3. The maximum rate of resistance change is calculated at $\alpha = 110°$, which is in agreement with the experimental observation in Fig. 7.3 d). Note that all the explanation regarding the TMR response presume single-domain behavior of the sense layer, which is a good approximation after the magnetization saturation as shown in chapter 6, and unchanged M_{ref}.

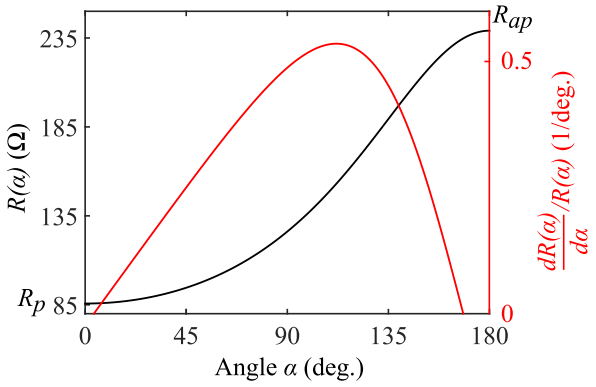

Figure 7.4: *The angular dependence of the tunnel resistance and the relative resistance change as a function of the angle α, calculated using equation 2.7. The maximum rate of the resistance change takes place in the same angle range for the measured maximum deflection sensitivity in Fig. 7.3 d). R_p =86 Ω and R_{ap} =239 Ω are experimentally measured from the minor loop of the junction.*

7.3 Topography Imaging

As the early fabricated cantilevers were tipless, one of the cantilever apexes is used for scanning surfaces[264]. For measurements shown in this section, the same self-sensing cantilever in Fig. 7.2 is used because of its high deflection sensitivity. Also, a bias field of 60 Oe is present at $\theta_{H_{bias}} = 90°$. Figure 7.5 represents contact mode images of a PMMA grating with the TMR and optical read-outs in the contact mode. For comparison of the images quality, the same position of the sample is scanned with both read-outs. After scanning with the feedback on the optical beam deflection setup, the TMR sensor read-out is directly fed into an analog-digital convertor of the AFM controller. The cantilever is 20 µm in thickness leading to very high loads and drag forces exerted to the sample. As PMMA is relatively soft, drag forces during the first scanning by the 50 µm-wide cantilever apex caused damages into the grating profiles. These damages reveal as kinks at the walls of the grating during the second scanning. Nevertheless, both images with the feedback on the optical beam deflection and the TMR sensor exhibit the same imaging quality.

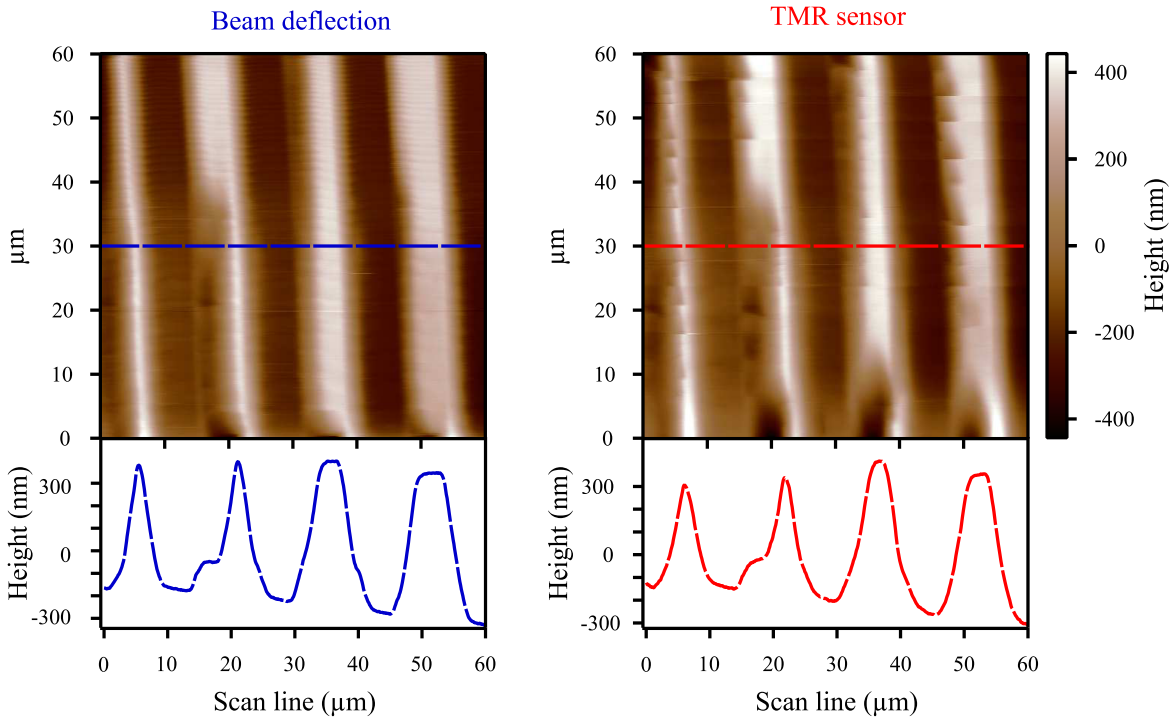

Figure 7.5: *Contact mode images of a PMMA grating with the feedback on the TMR sensor and the optical beam deflection system, edited with permission[260]. For both feedback systems, the same position of the sample is scanned with a tipless cantilever. During the first scan with the feedback on the beam deflection, drag forces from the cantilever apex caused damages on the sample profile as PMMA is relatively soft. The topography is modified during the first scan. However, in the subsequent image with the feedback on the TMR sensor those damages appear as kinks at the walls of the grating. Accordingly, differences can be noticed in the height profiles.*

As shown in Fig. 7.6, using the amplitude modulation, topography images of the same sample are recorded in the dynamic mode with the TMR sensor and the beam deflection read-outs. This helps to reduce the damages appeared in the contact mode imaging by the drag forces from the wide cantilever apex. The oscillation amplitudes, usually set in the AM-AFM mode, are in nanometer range, considerably smaller than the piezo movement for the FD curve presented in Fig. 7.2. Therefore, one can assume that the TMR sensor response to the cantilever deflection is linear as for the optical read-out. Consequently, both detection systems have nearly the same resonance curves shown on top in Fig. 7.6. They both reveal the same resonance frequency at f =123.5 kHz. The difference in the amplitude scales is associated with different voltage gains employed on the deflection raw signals in volts. Calculated quality factors from the resonance curves, $Q_{optical} = 190$ and $Q_{TMR} = 200$, differ slightly. This difference, which is typically about 10%, can be attributed to the scattering of subsequent measurement of resonance curves. Moreover, the different deflection sensitivity by tensile and compressive stress shown in Fig. 7.3 c) might be the other speculated origin for the difference in the quality factor of the two read-out systems.

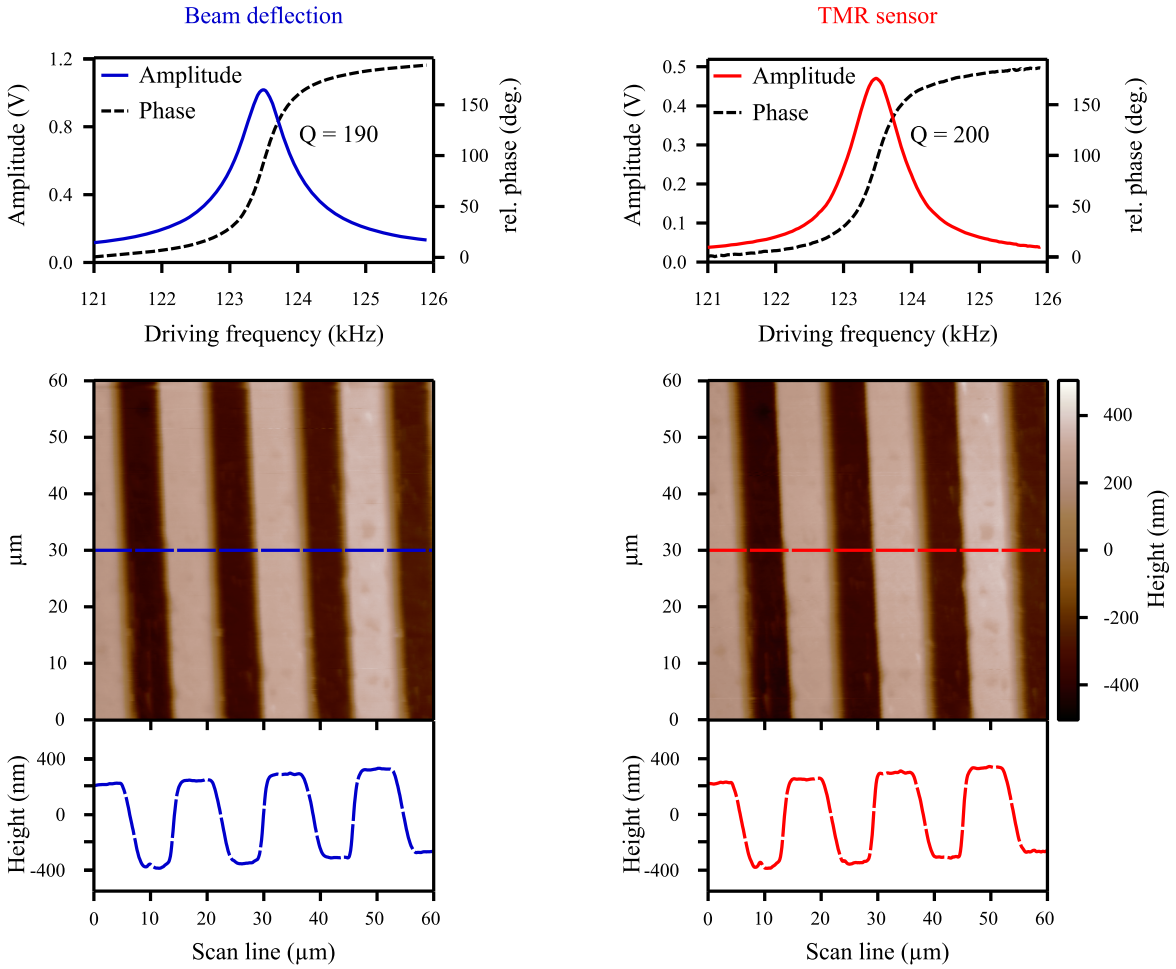

Figure 7.6: *Dynamic imaging of the PMMA grating in the amplitude modulation mode, recorded by the TMR sensor and the optical read-outs*[265]*. The resonance frequency curves measured by both detection systems are shown on top. They exhibit the same resonance frequency and nearly the same quality factors. The difference in the amplitude scales between the two curves is related to different gain factors used for amplification in each detection systems. The topography images measured subsequently at the same position on the sample reveal the same quality as there are no damages like in the contact mode imaging (see Fig. 7.5). From the representative height profiles extracted at the same position, the same data quality and details level can be obtained regarding the height and the width of the grating by the TMR sensor and optical read-outs. Even a small bump in the first trench on the left detected by the beam deflection can also be seen in the TMR sensor height profile.*

The topography images obtained with the feedback on the TMR sensor and the beam deflection are recoded at the same position on the sample while the cantilever is oscillating at its resonance frequency. The damages observed during the contact imaging in Fig. 7.5 are diminished because of imaging in the AM-AFM mode. The topography image recorded by the TMR sensor has the same quality as the image obtained by the optical read-out. As can be seen in the height profile at the bottom of Fig. 7.6, both detection systems reveal the same data quality and details level regrading the height and the width in the grating.

7.4 Minimum Deflection Detection

In addition to the deflection sensitivity, the minimum detectable deflection (MDD), the minimum measurable height step, is the other key parameter for the self-sensing microcantilevers in terms of the sensitivity and the noise level (see sections 2.10.1 and 2.10.2). Noise measurement was not in particular the scope of this work and will be performed in future. Since it is related to several parameters mentioned in section 2.10.2, it requires systematic profound measurements. In order to investigate the MDD of the TMR self-sensing cantilever, Pt tips with averaged $r_t = 30\,\text{nm}$ were integrated to the cantilevers (see Fig. 4.19), resulting in a better lateral resolution.

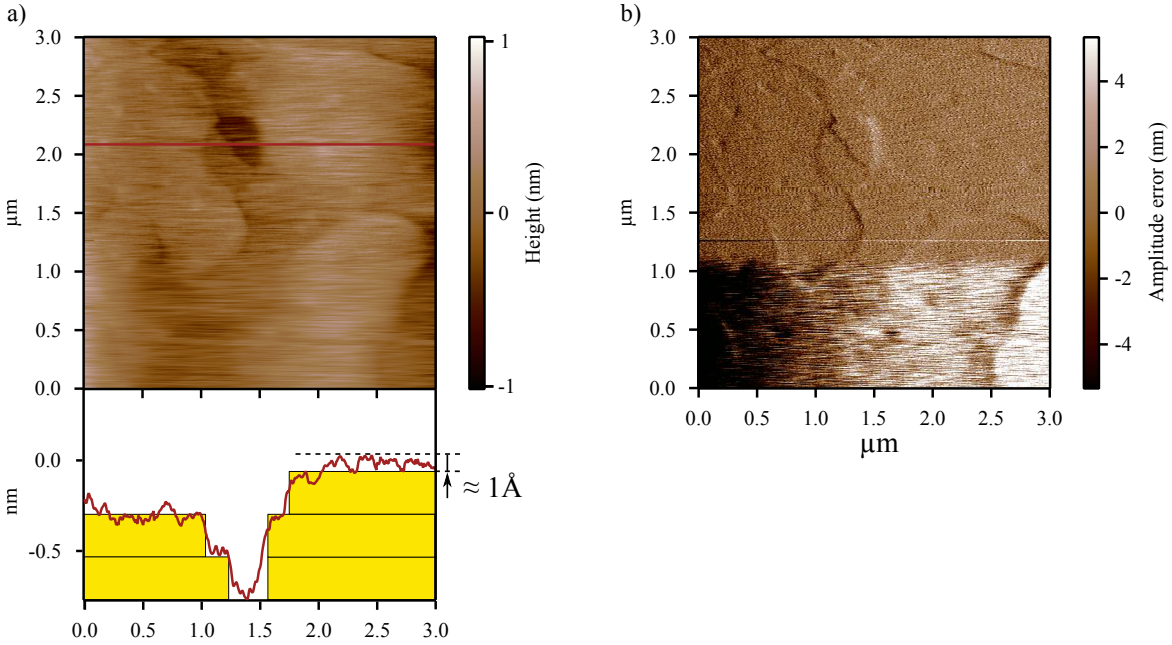

Figure 7.7: ***a)*** *Imaging of atomic step-edges on Au(111) terraces using the AM-AFM mode with the feedback on the TMR sensor[263]. The scanning is carried out as $H_{bias} = 60\,Oe$ applied at $\theta_{H_{bias}} = 105^{\circ}$. The integration of a Pt tip with an average of $r_t = 30\,nm$ improves the lateral resolution. The signal variation of about 1 Å at the step-free part (the dashed line) of the height profile can be useful to estimate possible minimum detectable deflection (MDD). In the middle of the scan area the image becomes blurry, which originates from changes in the geometry of the tip, as shown in Fig. 7.8.* ***b)*** *Amplitude error signal highlights changes of the surface height measured by the difference between the instantaneous amplitude of oscillation and the amplitude set-point.*

Figure 7.7 shows atomic step-edges on Au(111) terraces obtained by the amplitude modulation feedback only on the TMR sensor. Imaging of such steps is a routine measurement by the optical read-out. For scanning the same cantilever as for Fig. 7.3 is used. The bias field is applied at angle $\theta_{H_{bias}} = 105^{\circ}$ with respect to M_{ref} to keep the deflection sensitivity in the maximum level. Consequently, the TMR sensor read-out is able to resolve atomic edges of 2.54 Å, in the range of a monoatomic gold step

of about 2.4 Å[266]. After scanning through half of the scan area, the image becomes blurry, which can be attributed to changes in the tip geometry.

Figure 7.8 shows SEM images of the Pt tip taken before and after the scanning. It is clear that the 500 nm needle and the intermediate base is rubbed away since FIB-deposited Pt is a ductile material.

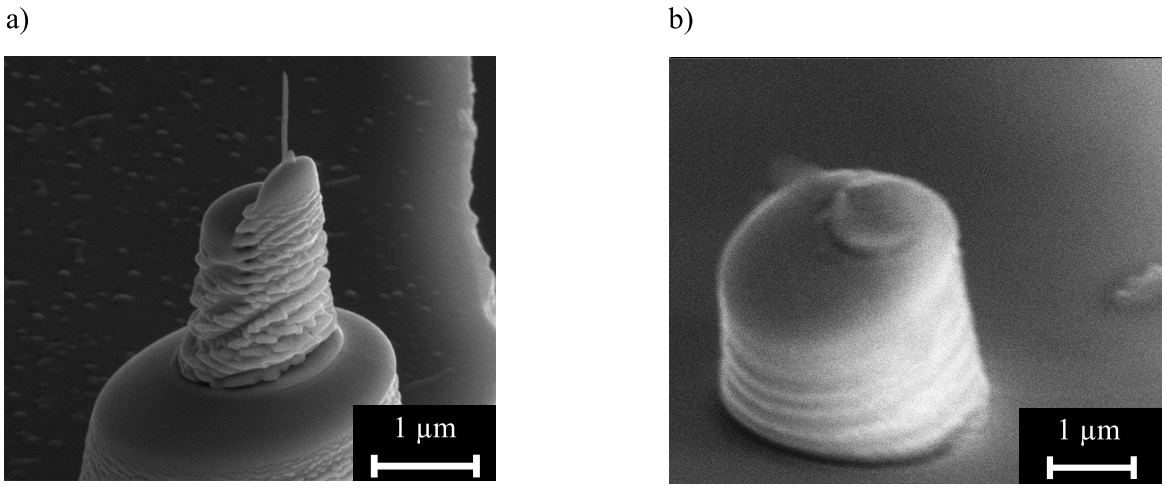

Figure 7.8: *SEM images of the integrated Pt tip after and before scanning the sample. Since the tip is ductile, it is rubbed away during interactions with the sample surface. This change in the geometry leads to the unstable imaging as demonstrated in Fig. 7.7.*

As aforementioned in section 2.10, the amplitude and the frequency can also be monitored as measuring signals in the dynamic mode imaging. In this mode, called the frequency-modulated AFM (FM-AFM), the oscillation amplitude, which is kept small, maintains the tip in either the attractive or repulsive region. However, using small amplitudes in FM-AFM leads to large changes in the oscillating frequency. Imaging in the FM-AFM mode allows to monitor the energy dissipation as the tip interacts with the underlying materials[267]. This provides information in terms of chemical phases which can be used for chemical mapping[268].

In order to study the ability of the TMR self-sensing cantilevers in the FM-AFM mode, self-assembly monolayers of FDTS with 1.3 nm height is used. Using polymer blend lithography the FDTS monolayers were structured to implement disk-shape openings into a SiO_x layer underneath[269]. Sample preparation is explained in detail in a Ph.D. dissertation of Dr. Tobias Meier[260]. Having hydrophilic SiO_x and hydrophobic FDTS on the surface results in a high chemical contrast. On the contrary, exposing the sample to an ambient with humidity around 40% leads to no height contrast in the AM-AFM mode, as can be seen in Fig. 7.9 a). This is related to thin water films formed on the hydrophilic SiO_x layer, which fills out the height difference between the FDTS and the SiO_x layers[270]. Alternatively, topography contrast is observable while scanning inside a liquid[269]. Compared to the height contrast, phase shift signals

are visible originating from different energy dissipation. Consequently, the SiO_x spots appear brighter than the FDTS in the phase signal.

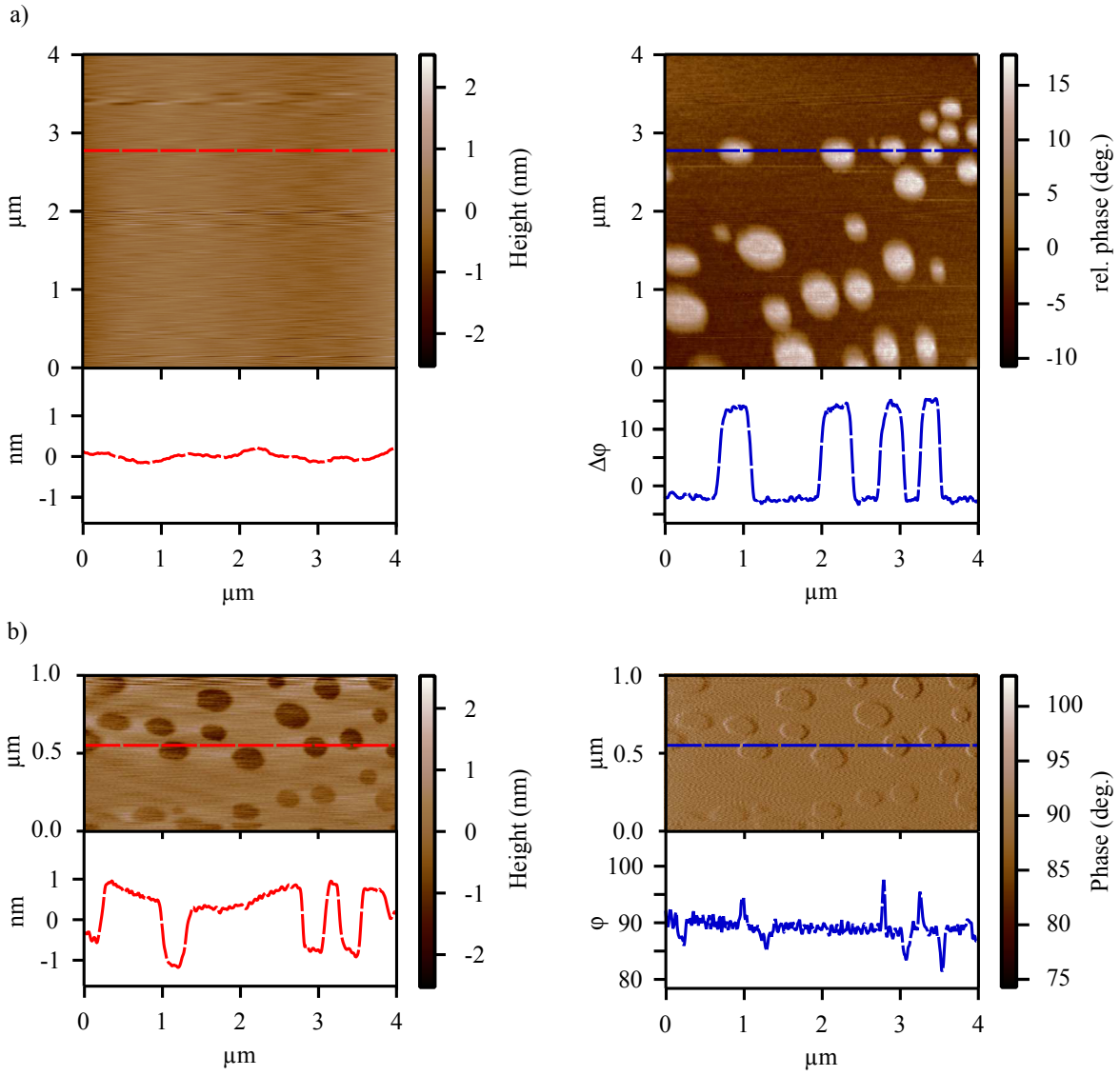

Figure 7.9: *AM-AFM mode and FM-AFM mode imaging of self-assembly monolayers of FDTS with the TMR sensor read-out*[263]. ***a)*** *In the AM-AFM mode, the SiO_x disks structured on the FDTS by polymer blend lithography are not visible in the topography signal, whereas they appear as bright spots in the phase signal image. The hydrophilic and hydrophobic characters by FDTS and SiO_x, respectively, result in formation of thin water films on the SiO_x spots in environments with a humidity of above 40 %. This obscures the height difference between the FDTS and the SiO_x layers. However, the SiO_x spots are visible in the phase signal image due to different energy dissipation between the tip and the underlying materials.* ***b)*** *Phase-locked FM-AFM imaging reveals the topography contrast of the sample as the energy dissipation is the more sensitive signal. On the contrary, since the phase shift is kept constant at 90° for the frequency feedback loop to the driving signal, the phase contrast, present in the AM-AFM mode, vanishes.*

Because of the high phase signal, the same sample, but on another position, is scanned in the FM-AFM mode. Thus, the frequency, at which the cantilever is oscillated, is tracked instead of the amplitude and kept at a constant offset with respect to its resonance frequency by a feedback loop. The frequency tracking therefore also locks the phase signal at a constant value corresponding to the frequency offset. The height of the sample is modulated to maintain this frequency shift constant. As a result, the phase contrast in the AM-AFM mode indicates a high frequency shift, which allows using this shift as a signal for the topography feedback loop. Figure 7.9 b) reveals the height contrast between the FDTS layer and the SiO_x disks. As expected for the FM-AFM mode, the phase shift observed in the AM-AFM mode in Fig. 7.9 a) disappears as it is kept constant by a second feedback loop. Nevertheless, signals regarding transition from the FDTS to the SiO_x regions and vice versa are visible because of changes in the source of the dissipation energy.

7.5 Conclusions

Magnetostrictive TMR sensors with high strain sensitivity and remarkable miniaturization possibilities are successfully integrated onto the AFM cantilevers via an optimized MEMS fabrication flow. The deflection signal can be easily detected as a resistance signal of the magnetostrictive TMR sensor. The FD curves measured using the TMR sensors reveal a non-linear relation to the applied z-displacement. However, during imaging an AFM is typically operated with cantilever deflection below 100 nm and one can assume a roughly linear sensor response for such scales. Self-sensing TMR cantilevers exhibit a deflection sensitivity of $3.9 \times 10^{-6}/\text{Å}$ measured at the beginning of the FD curve. This is better than values obtained by piezoelectric and piezoresistive sensors. These self-sensing cantilevers can be an alternative for replacing the conventional optical read-out as they are successfully used to record typical AFM topography imaging in the contact and dynamic modes.

The deflection sensitivity depends on the bias field direction with respect to M_{ref}, which can be tuned in the dynamic oscillation. The maximum strain sensitivity is observed for $H_{birthdayas} = 60\,\text{Oe}$ at $\theta_{H_{bias}} = 105 - 110\,^{\circ}$. This is in agreement with the calculation on the maximum rate of the resistance change as a function of the angle α using the equation for the angular dependence of the tunnel resistance. In order to improve the lateral resolution, the tips with $r_t = 15 - 30$ nm are grown on the AFM cantilevers. Consequently, the minimum detectable deflection (MDD) as height and phase contrasts are sufficient for imaging atomic-step edges of Au(111) and self-assembled monolayers of FDTS in the AM-AFM and FM-AFM modes.

Chapter 8

Summary and Outlook

Different conditions of Si anisotropic etching in KOH solutions are investigated in order to improve the surface quality of the etched surfaces. Among the techniques studied here, adding Sb_2O_3 to the KOH solution reveals the most effective impact on the surface quality as it reduces the roughness to 8 nm. More importantly, such low roughness remains constant even after Si deep anisotropic etching up to 270 µm, whereas in the other techniques the surface roughness increases for longer etching time. The resulted enhancement in the reflectivity of the etched surface is beneficial for optical MEMS devices. Moreover, thin microstructures such as AFM cantilevers and membranes with very low surface roughness exhibit better mechanical strength. Furthermore, two compensating structures are introduced to develop desired shapes and dimensions of microstructures.

Stress-induced anisotropy effects on hard-axis $R(H)$ loops are investigated for the magnetostrictive TMR sensors with nominal sizes of 100 µm^2, 289 µm^2, 729 µm^2, and 1369 µm^2 in squared, round, elliptical(1:3), and elliptical(1:10) shapes. The external magnetic field and the stress axis are set at $\pi/2$ and $\pi/4$ angle, respectively, toward the induced magnetocrystalline anisotropy. The strain effect on the $R(H)$ loops is the same for all junctions except the elliptical(1:10) junctions. Applying strain alters the magnetization reversal of M_{sen} through M_{ref} in the unstrained state, as approved theoretically by the SW model. A macrospin model supported by the simulations is proposed describing details of the rotation mechanism of M_{sen} in the $R(H)$ loops of junctions exposed to tensile stress. A certain agreement prevails in the experimental results and the representative model. Tensile stress leads to a large resistance increase ΔR at negative fields ($H >$ -3 kA/m), whereas it emerges at positive fields ($H >$ +4 kA/m) for compressive stress. However, a small resistance decrease occurs at positive and negative fields for tensile and compressive strain, respectively. Considering the inverse impact by tensile and compressive stress on the tunnel resistance, a single sensor with a bias field can detect both stresses. This achievement extends application of such sensors to dynamic devices e.g. dynamic mode AFM. Below 0.2×10^{-3} strain, representative tensile and compressive strain loops $R(\varepsilon)$ for a round junction with a diameter of 30 ± 0.2 µm at ± 3.2 kA/m and ± 4 kA/m bias fields reveal the

strain sensitivity dependence on the bias field and again the inverse impact by both stresses on the tunnel resistance. At -3.2 kA/m, the junction exhibits a gauge factor of $GF = 2150 \pm 30$ for tensile strain, whereas for compressive strain a gauge factor of 260 is measured. Conversely, at +4 kA/m, a positive bias field, the junction shows $GF = 1750 \pm 35$ and $GF = 250$ for compressive and tensile strain, respectively. Using energy minimization based on the SW model, rotation of M_{sen} in the tensile and compressive strain loops are successfully simulated. The calculated strain loops exhibit nearly the same trends and gauge factors as the experimentally measured strain loops. In addition, the measured strain loops reveal no indication regarding its dependence on the junctions shapes and sizes used in this study.

The magnetostrictive TMR sensors with high strain sensitivity and remarkable miniaturization possibilities are successfully integrated to the AFM cantilevers via an optimized MEMS fabrication flow. The self-sensing TMR cantilevers with deflection sensitivity of about 3.9×10^{-6}/Å can be an alternative for replacing the conventional optical read-out as they are successfully used to record typical FD curves and AFM topography imaging in the static and dynamic modes. The deflection sensitivity, which can be tuned in dynamic oscillation, depends on the bias field direction with respect to M_{ref}. The maximum strain sensitivity is observed for $H_{bias} = 60\,\mathrm{Oe}$ at $\theta_{H_{bias}}$ =105 °- 110 °. This is in agreement with the calculation on the maximum rate of the resistance change as a function of the angle α using the equation for the angular dependence of the tunnel resistance. In order to improve the lateral resolution, tips with $r_t = 15 - 30$ nm are grown on the AFM cantilevers. Consequently, the minimum detectable deflection (MDD) as height and phase contrasts are achieved by imaging atomic-step edges of Au(111) terraces and self-assembled monolayers of FDTS in the AM-AFM and FM-AFM modes.

Issues still remain regarding the lateral resolution during AFM imaging. Besides temporal solutions such as attachment of Cu spheres and deposition of Pt tips, a step for mass integration of stable tips to the AFM cantilevers should be added to the fabrication process of the TMR self-sensing cantilevers. Accordingly, noise measurements can be reliably performed, which helps to expand understanding of noise origins. As a result, the signal-to-noise ratio can be improved by modification of cantilever conditions, operating parameters, and specifications of TMR sensors.

As short-term planning, a setup for measuring force-distance curves is necessary in order to thoroughly investigate the magnetostrictive TMR sensors on AFM cantilevers in terms of the deflection sensitivity and its angular dependence. This would include FD curve measurements, which can be compared with the results of the four-point bending apparatus. Using the same electronics allows to collate directly TMR sensors response in both measuring tools. Furthermore, such devices are designed for biosensing applications, which can be very helpful to study different parameters of biological systems such as intermolecular forces of deoxyribonucleic acid (DNA) and proteins. Figure 8.1 shows the FD curve-based apparatus. Since no results obtained by this setup is demonstrated in this study, the apparatus is only briefly described here as a future plan.

For the same purpose, samples used for both devices should be prepared from

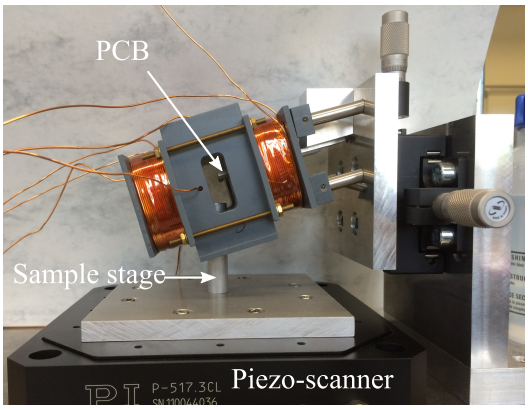

Figure 8.1: *FD curve-based apparatus. A TMR self-sensing cantilever mounted on a PCB can be roughly positioned over a sample using a linear XY-table, M-460A-XY model from Newport Spectra-Physics GmbH. A multi-axis piezo scanner, P-517 from Physik Instrumente, performs approach-retract paths of used sample toward the tip of the TMR self-sensing cantilever. Two pairs of coils serve an external field which is required for a bias field to set the deflection sensitivity at maximum.*

TMR stack deposited on the same wafer. Figure 8.2 a) shows a wafer with junctions successfully fabricated using a new set of masks, which includes three cantilevers for the four-point bending device in addition to AFM cantilevers. As represented in Fig. 8.2 b), these masks also allow implementation of round junctions to AFM microcantilevers. As discussed in chapter 6, the round junctions exhibit high gauge factors of $GF \approx 400$ at zero field. Round junctions integrated to microcantilevers is the first promising achievement to avoid the need of a bias field. This will provide a miniature detection system suitable for strain sensing applications which are limited by the size of read-out systems such as expensive and complex optical read-out systems for AFM imaging in liquid and vacuum environments. A variation of AFM measurements in different environments is in progress to demonstrate capabilities of self-sensing cantilevers with round TMR sensors.

The shape anisotropy of the elliptical junctions is not suitable for replacing the bias field because of its uniaxial character, which might lead to domain formation at low magnetic fields. Another technique, which helps to get rid of required bias field and establishes the highest strain sensitivity, is related to pinning of the magnetization of the sense layer by additional layers on top. Imposing a unidirectional anisotropy at $\alpha = 110°$, the angle with the maximum sensitivity, can substitute energetically the effect of the required bias field. This will not only lead to a simple strain detecting system, but also the maximum strain sensitivity in contrast to the concept of the round TMR junctions at zero field.

Strain-sensitive junctions with few micron and sub-micron sizes are necessary for strain detection in small-sized structures, as the optical read-out suffers from dimension constraint on detectable structures. This extends the possibility of geometries and mechanical properties of cantilevers and MEMS devices, which are desirable for better resolution and higher measurement speeds. Furthermore, this offers usage of more than one TMR sensor, which allows monitoring the strain amount at different

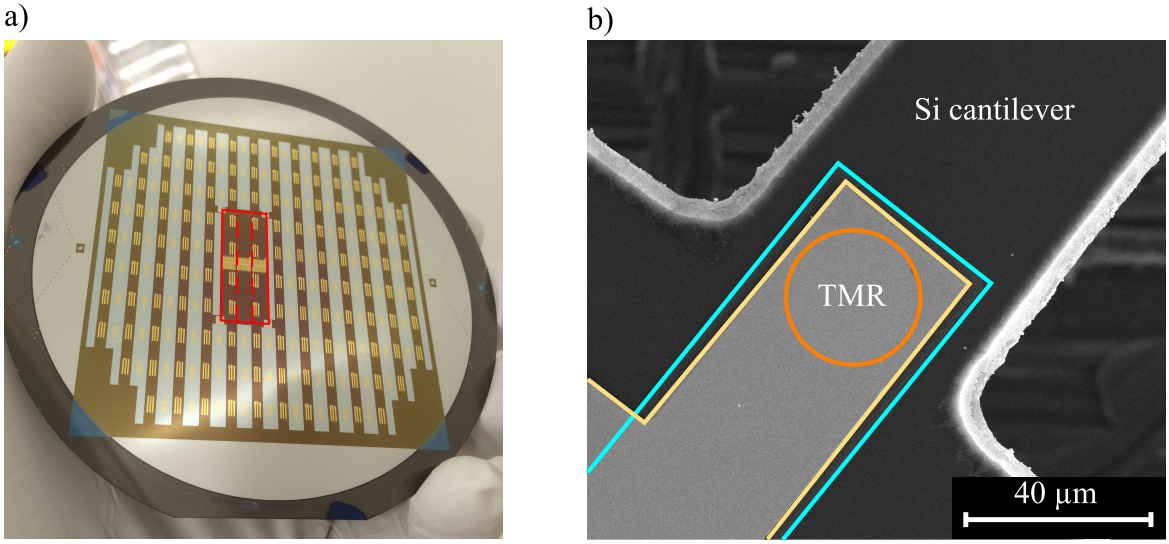

Figure 8.2: a) *A wafer with fabricated TMR junctions on AFM canitlevers and 3 mm × 25 mm-sized cantilevers, marked as three red rectangles, for the four-point bending device.* ***b)*** *A self-sensing AFM cantilever with an integrated round TMR junction.*

locations. Such miniaturization and implementation of multiple sensors will ease simultaneous measurement of lateral bending and torsion of AFM cantilevers as well as multi-frequency techniques in AFM applications.

A new technique is represented to roughly estimate the saturation magnetostriction of the sense layer in patterned MTJs. This allows to characterize different materials as sense layers and influence of layers arrangement of MTJs. Interestingly, the same range of effective saturation magnetostriction values, nearly as in the literature, is measured for the $Co_{40}Fe_{40}B_{20}$ sense layers of junctions with different sizes. Deviation from assumed single-domain behavior can be reduced using larger junctions, which should be further investigated by domain imaging techniques.

Appendix-A

A.1 Etching Profiles by the Modified Bosch Process

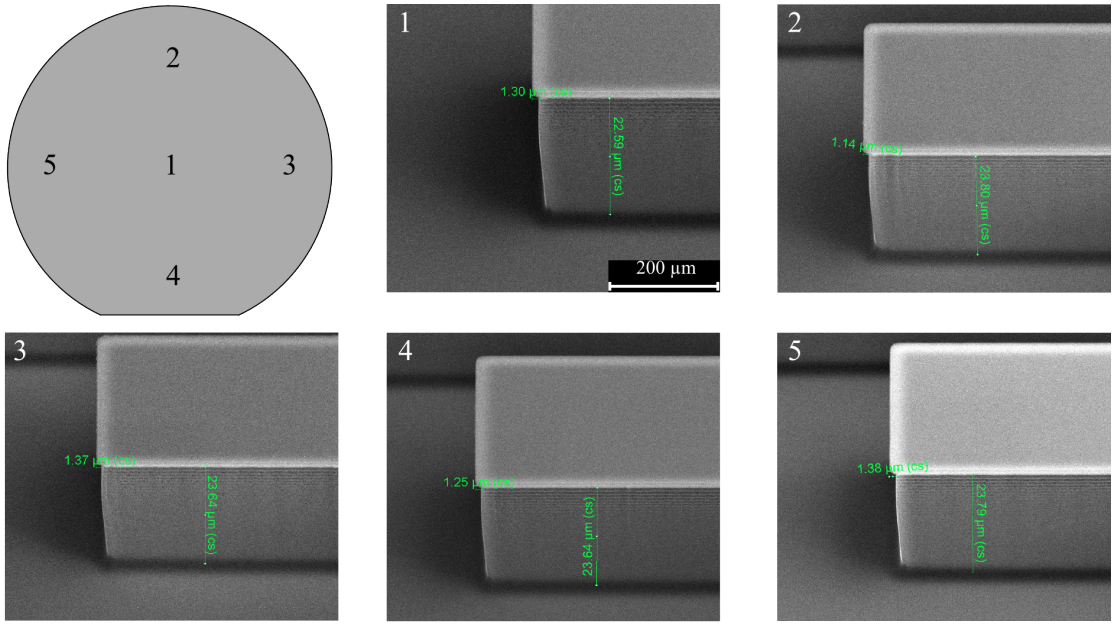

Figure Appendix-A.1: *SEM images of etch profiles after 40 cycles by the optimum process given in Table 3.3 at different locations on a 4″ Si wafer. They show nearly the same etching rates and sidewalls profiles. Here, the etching mask is a 1.5 µm thick SiO_2 film. Underetching is less than 2 µm which is low enough to protect junctions during the cantilevers release.*

A.2 Cantilever Underetching and Uniform Etching Profiles by the Modified Bosch Process

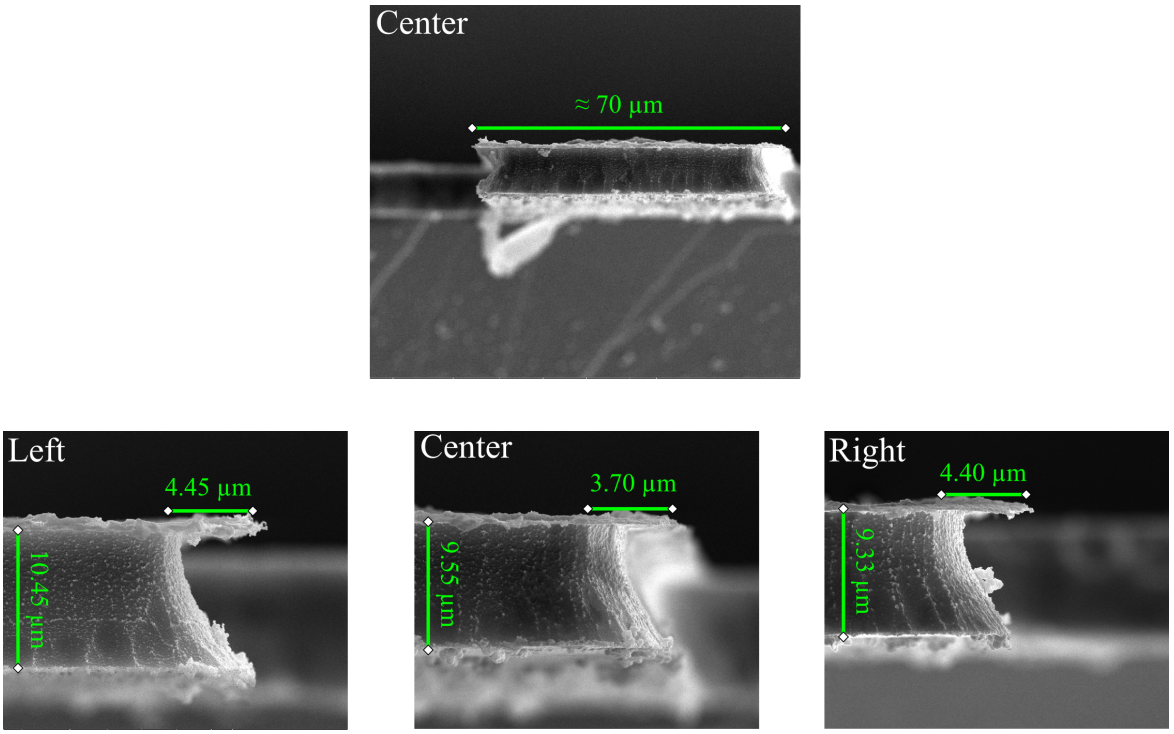

Figure Appendix-A.2: *Front-view SEM images of three cantilevers after the cantilever release during fabrication of the TMR self-sensing cantilevers. The cantilevers are chosen from different locations on the wafer; left, center, and right. The underetching at sidewalls of the cantilevers is less than 5 µm. This value is twice the underetching occurred for structuring of features on the wafer without any membrane or cavity on the back of the wafer, as shown in Fig. Appendix-A.1. Si underetching in the same range over the wafer as well as the same sidewall profiles verifies the uniformity of the RIE process. Moreover, the nearly equal cantilever thickness approves the uniform KOH etching, which overally leads to uniform mechanical properties of the fabricated cantilevers.*

Appendix-B

B.1 Mask Layouts of TMR sensors for Four-point Bending Measurements

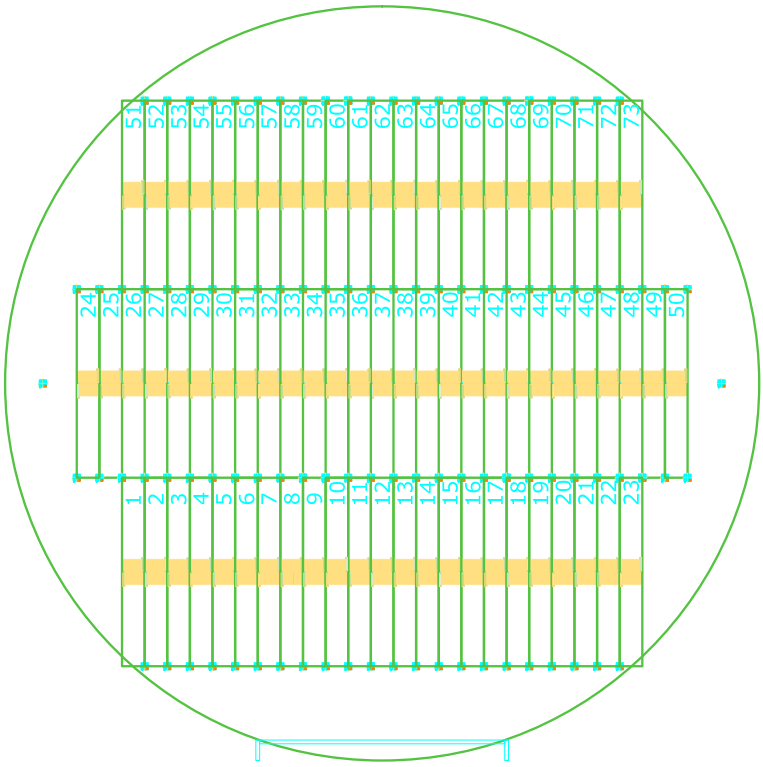

Figure Appendix-B.1: *Mask drawings for fabrication of TMR junctions on 3 mm × 25 mm cantilevers (green outline) for 4-point bending measurements. The fabrication requires three masks: 1) bottom electrode (BE) 2) TMR junctions 3) top electrode (TE). 73 cantilevers can be fabricated from a TMR stack deposited wafer. Mask details are given in Fig. Appendix-B.2.*

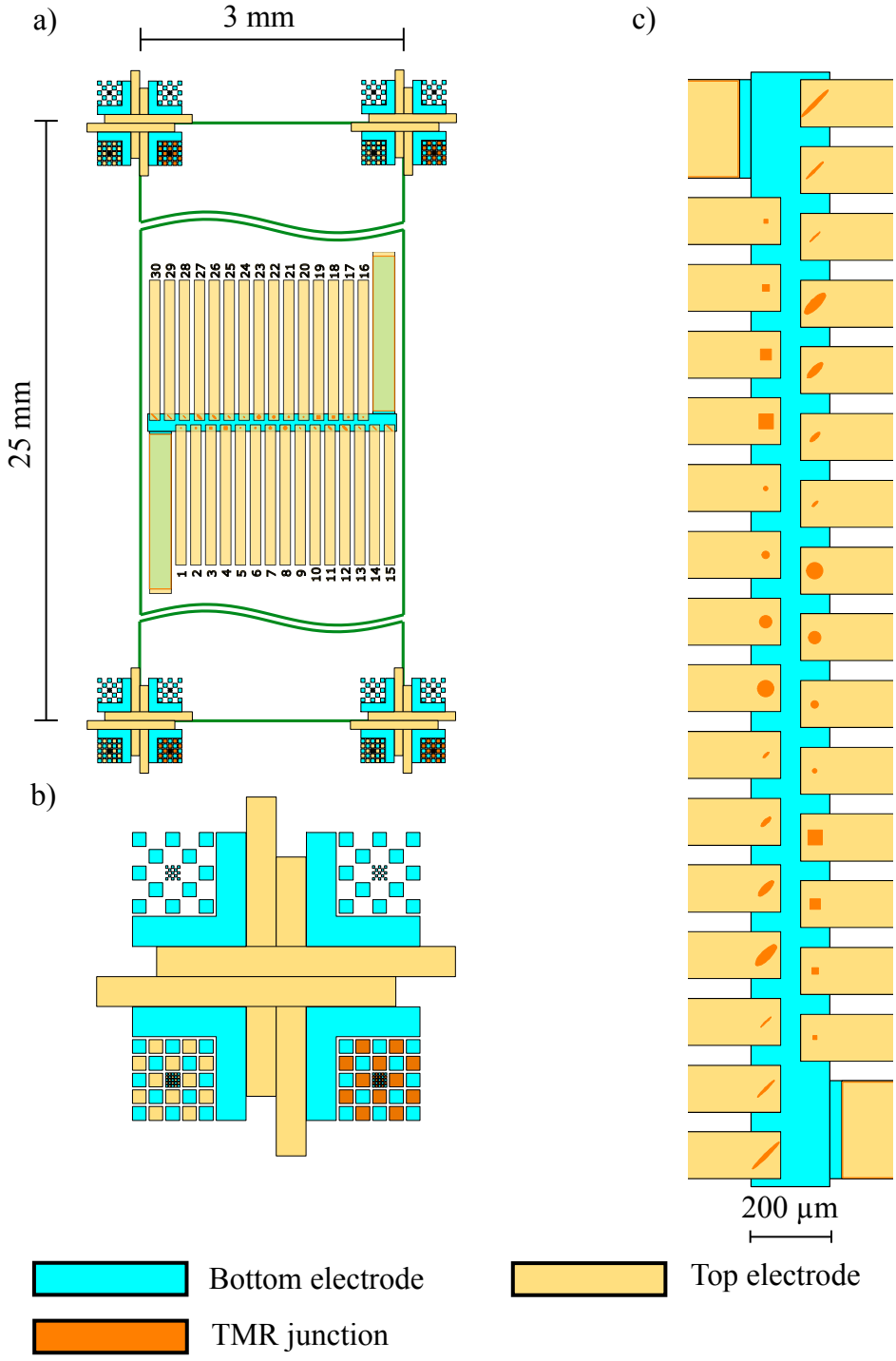

Figure Appendix-B.2: *Mask details of* ***a)*** *a cantilever,* ***b)*** *alignment marks, and* ***c)*** *TMR junctions.*

B.2 Fabrication Recipe of TMR sensors for Four-point Bending Measurements

- ♢ TMR stack deposition at *Bielefeld University*
- ♢ Cleaning in an ultrasonic bath (Aceton, room temperature, 40 kHz, 10 min)
- ♢ Field annealing (360 °C, 1 h, 2 kOe, 1×10^{-6} mbar)
- ♢ A quick TMR measurement on an unpatterned stack to check the annealing performance
- ♢ Cleaning in an ultrasonic bath (Aceton, room temperature, 40 kHz, 10 min)
- ♢ UV-lithography (AZ 6632, mask for bottom electrode (BE))
- ♢ Gettering the IBE chamber by etching Ta (350 mA, 15 min)
- ♢ IBE to define the bottom electodes (BE)s (70 mA, 8 rpm, 1.2×10^{-7} mbar, 15.5 min)
- ♢ Cleaning in an ultrasonic bath (NMP, 60 °C, 400 kHz or 75 °C, 40 kHz, 30 min)
- ♢ UV-lithography (AZ 5214 e, mask for TMR junctions)
- ♢ Gettering the IBE chamber by etching Ta (350 mA, 15 min)
- ♢ IBE to define the TMR junctions (70 mA, 8 rpm, 1.2×10^{-7} mbar, 16 min)
- ♢ SiO_x deposition (150 nm)
- ♢ Lift-off process (NMP, 75 °C, 40 kHz, 30 min)
- ♢ UV-lithography (AZ 5214 e, mask for top electrode)
- ♢ Cr/Au deposition (Cr: 20 nm, Au: 130 nm)
- ♢ Lift-off process (NMP, 75 °C, 40 kHz, 5 min)
- ♢ Dicing the wafer to cantilevers with 3 mm × 25 mm dimension (NMP, 75 °C, 40 kHz, 5 min)

Appendix-C

C.1 Mask Layouts of Self-sensing AFM Microcantilevers

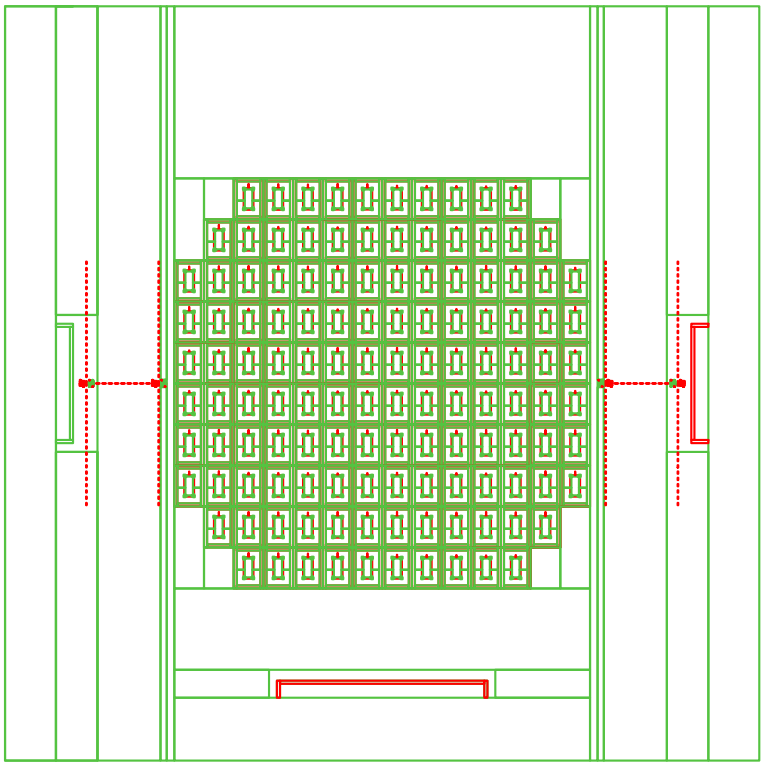

Figure Appendix-C.1: *Mask drawings for fabrication of self-sensing TMR microcantilevers for AFM applications. The fabrication requires five masks: 1) structuring of the backside SiO_2, 2) bottom electrode (BE) 3) TMR junctions, 4) top electrode (TE), 5) release of cantilevers. 128 microcantilevers can be fabricated from a TMR stack deposited wafer. Mask details are given in Fig. Appendix-C.2.*

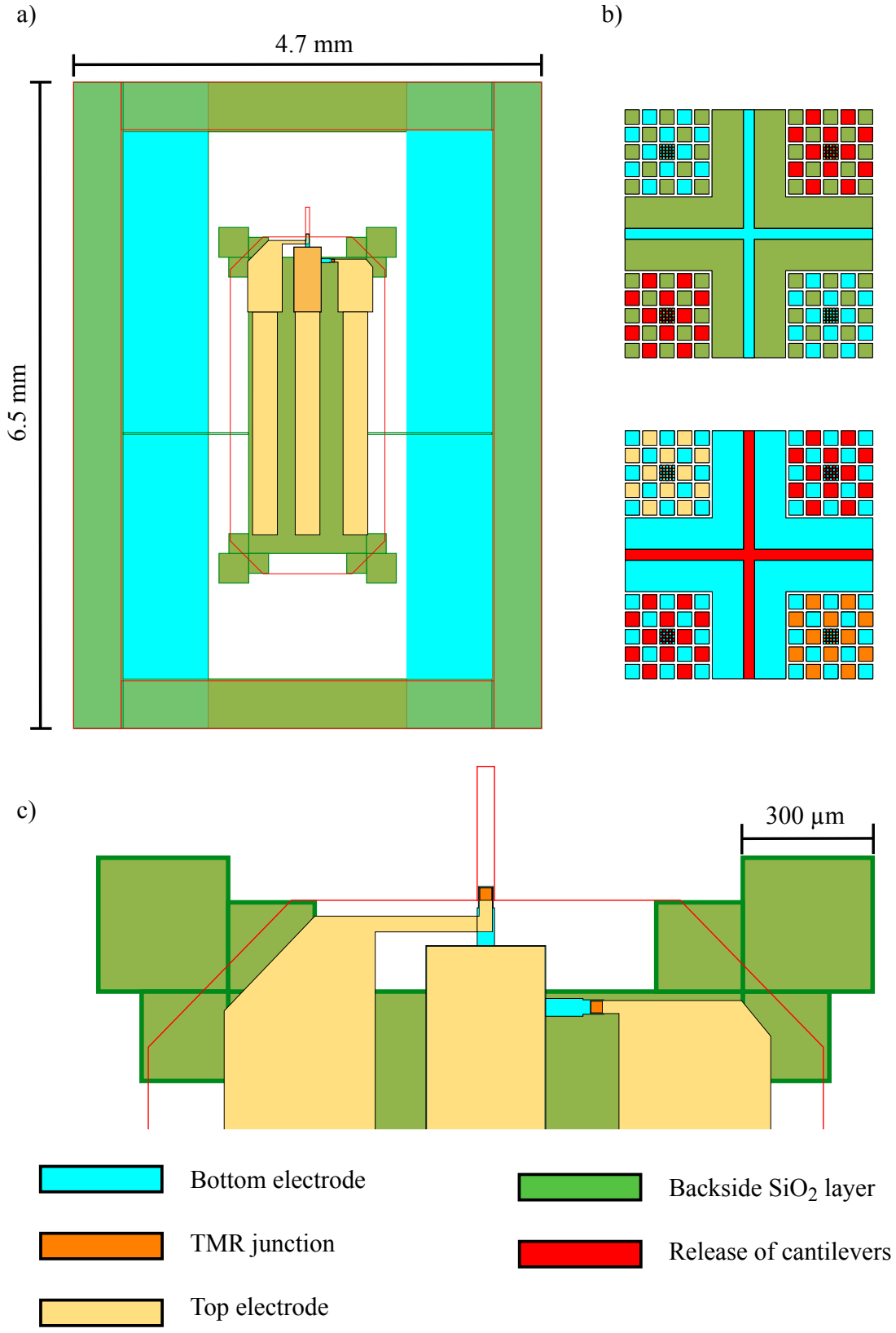

Figure Appendix-C.2: *Mask details of* ***a)*** *a microcantilever unit,* ***b)*** *alignment marks, and* ***c)*** *zoomed-in drawings of TMR junctions on AFM cantilevers.*

C.2 Fabrication Recipe of Self-sensing AFM Microcantilevers

- ♢ Covering the front side of a wafer by a photoresist (AZ 6632, soft bake)
- ♢ UV-lithography on the back side of the wafer (AZ 6632, mask for backside SiO_2 layer)
- ♢ RIE to etch the SiO_2 layer (2 µm) from unprotected areas (CHF_3: 50 sccm ICP power: 800 W, RF power: 120 W, RT, 545 s)
- ♢ Cleaning in an ultrasonic bath (Aceton (NMP), room temperature (75 °C), 40 kHz, 10 min)
- ♢ TMR stack deposition at *Bielefeld University*
- ♢ Cleaning in an ultrasonic bath (Aceton, room temperature, 40 kHz, 10 min)
- ♢ Field annealing (360 °C, 1 h, 2 kOe, 1×10^{-6} mbar)
- ♢ A quick TMR measurement on an unpatterned stack to check the annealing performance
- ♢ Cleaning in an ultrasonic bath (Aceton, room temperature, 40 kHz, 10 min)
- ♢ UV-lithography (AZ 6632, mask for bottom electrode (BE))
- ♢ Gettering the IBE chamber by etching Ta (350 mA, 15 min)
- ♢ IBE to define the bottom electrodes (BE)s (70 mA, 8 rpm, 1.2×10^{-7} mbar, 15.5 min)
- ♢ Cleaning in an ultrasonic bath (NMP, 60 °C, 400 kHz or 75 °C, 40 kHz, 30 min)
- ♢ UV-lithography (AZ 5214 e, mask for TMR junctions)
- ♢ Gettering the IBE chamber by etching Ta (350 mA, 15 min)
- ♢ IBE to define the TMR junctions (70 mA, 8 rpm, 1.2×10^{-7} mbar, 16 min)
- ♢ SiO_x deposition (150 nm)
- ♢ Lift-off process (NMP, 75 °C, 40 kHz, 30 min)
- ♢ UV-lithography (AZ 5214 e, mask for top electrode)
- ♢ Cr/Au deposition (Cr: 20 nm, Au: 130 nm)
- ♢ Lift-off process (NMP, 75 °C, 40 kHz, 5 min)
- ♢ A quick TMR measurement on selective junctions
- ♢ UV-lithography (AZ 6632, 2000 rpm mask for release of cantilevers)

♢ Release of cantilevers (1): RIE to etch the SiO_2 (100 nm) layer from unprotected areas (CHF_3: 50 sccm ICP power: 800 W, RF power: 120 W, RT, 45 s)

♢ Release of cantilevers (2): RIE to etch Si (10-20 µm) from unprotected areas applying a sequence of (1) depassivation: N_2 (200 sccm) and O_2 (50 sccm) ICP power: 700 W, RF power: 14 W, 3 s (2) etching: SF_6 (260 sccm) ICP power: 1000 W, RF power: 15 W, 14 s (3) passivation: CF_4 (50 sccm) ICP power: 700 W, RF power: 9 W, 8 s).

♢ Cr/Au deposition on the back side of the wafer (Cr: 10 nm, Au: 90 nm)

♢ Cleaning the resist on the front side in an ultrasonic bath (NMP, 60 °C, 400 kHz, 1 h)

Appendix-D

D.1 Heating Element

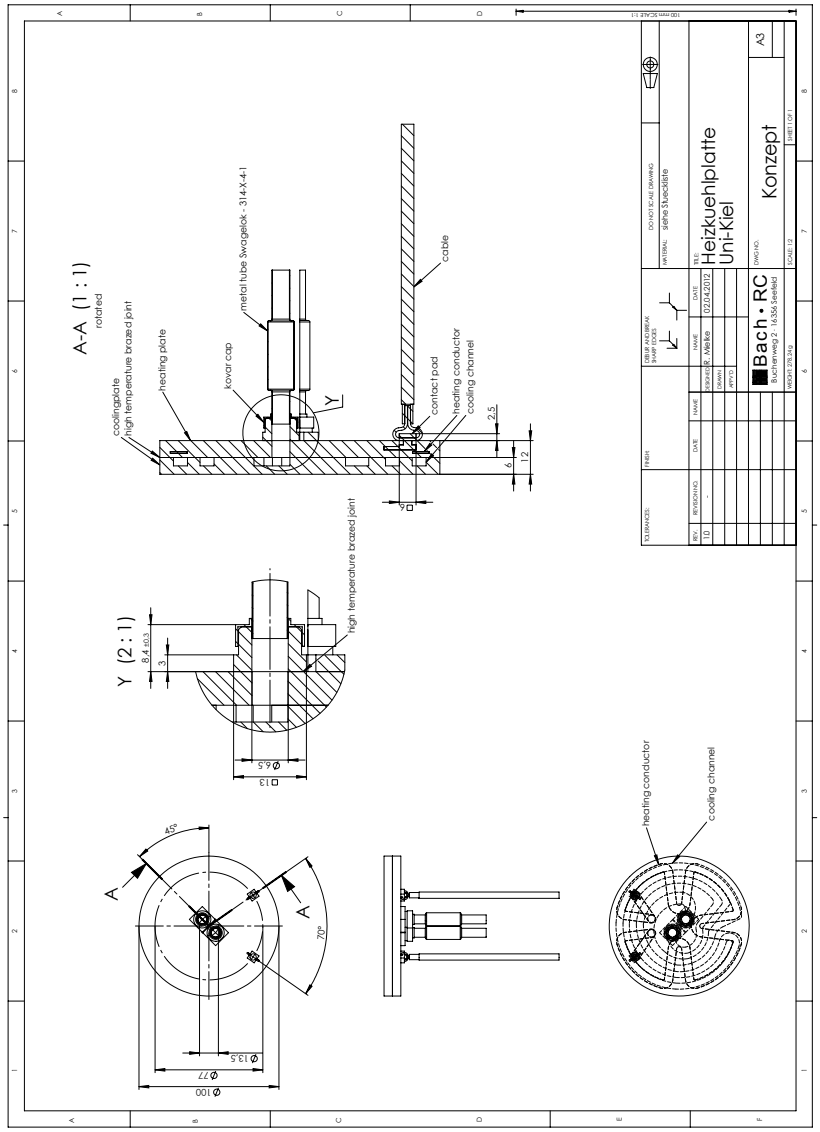

Figure Appendix-D.1: *Drawing of the heating element including the heater and cooling modules*[271]*. Dimensions of the cooling tubes and the electrical wires, and their brazing pads as well as their geometries are specified.*

D.2 ZnSe Viewport

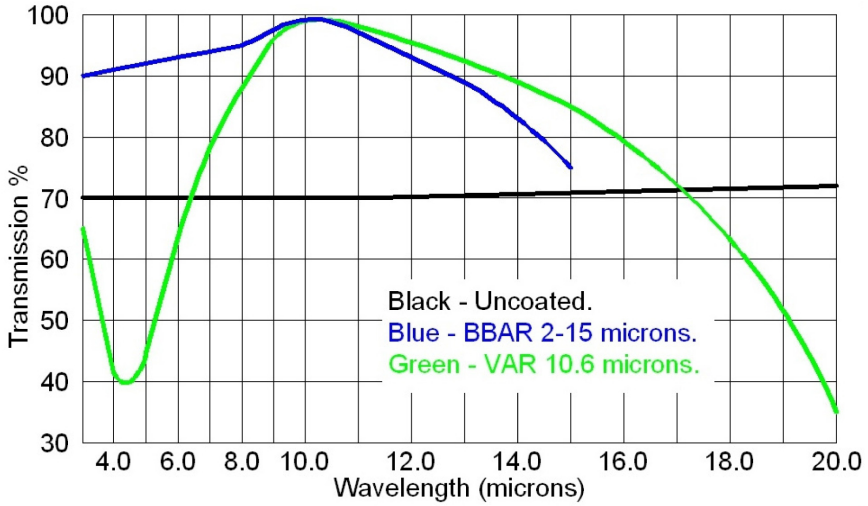

Figure Appendix-D.2: *Transmission spectrum of ZnSe viewport with and without anti-reflective coatings*[272]*. Transmission is more than 95% for the spectral range of approximately 8-11 μm. This range of wavelengths is used for the temperature calibration of the field annealing chamber by the IR camera discussed in section 3.2.*

Appendix-E

E.1 Strain Gauges

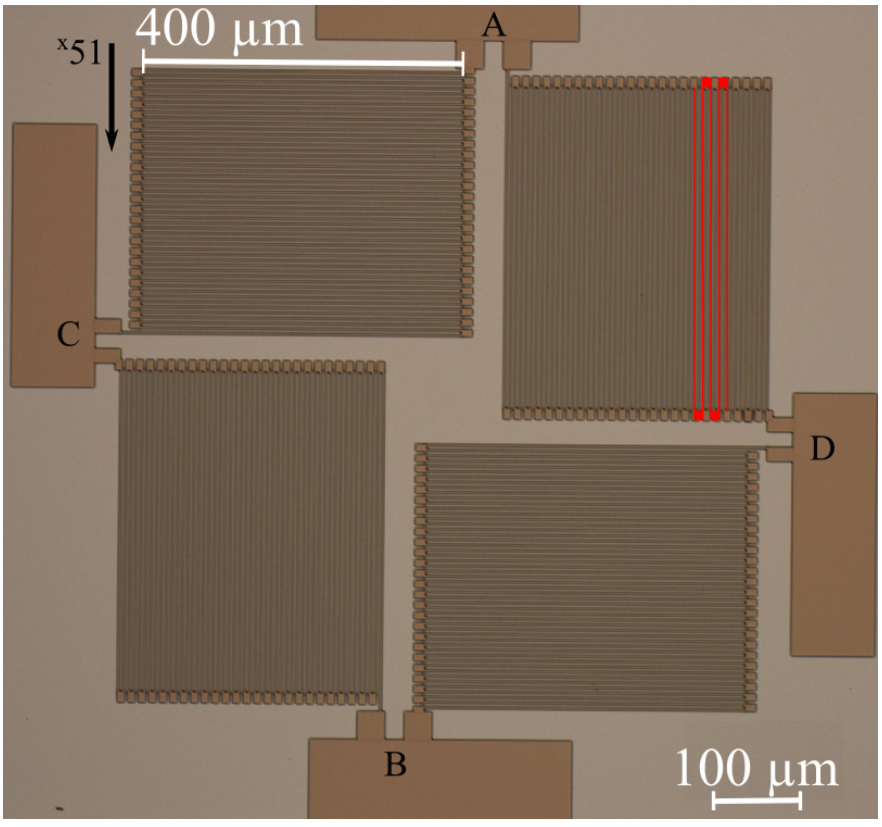

Figure Appendix-E.1: *Strain gauge with a full-bridge configuration. A Cr 10 nm/Pt 250 nm bilayer is patterned by e-beam lithography with a negative resist (AR-N 7520.17, from Allresist GmbH[273]) and a consecutive ion beam etching step. Each unit is a miranda structure, red drawings, of 51 lines with 400 µm length and 2 µm width. These non-magnetic gauges are used to characterize mechanical hysteresis generated by the four-point bending apparatus.*

E.2 Mechanical Hysteresis in the Four-point Bending Apparatus

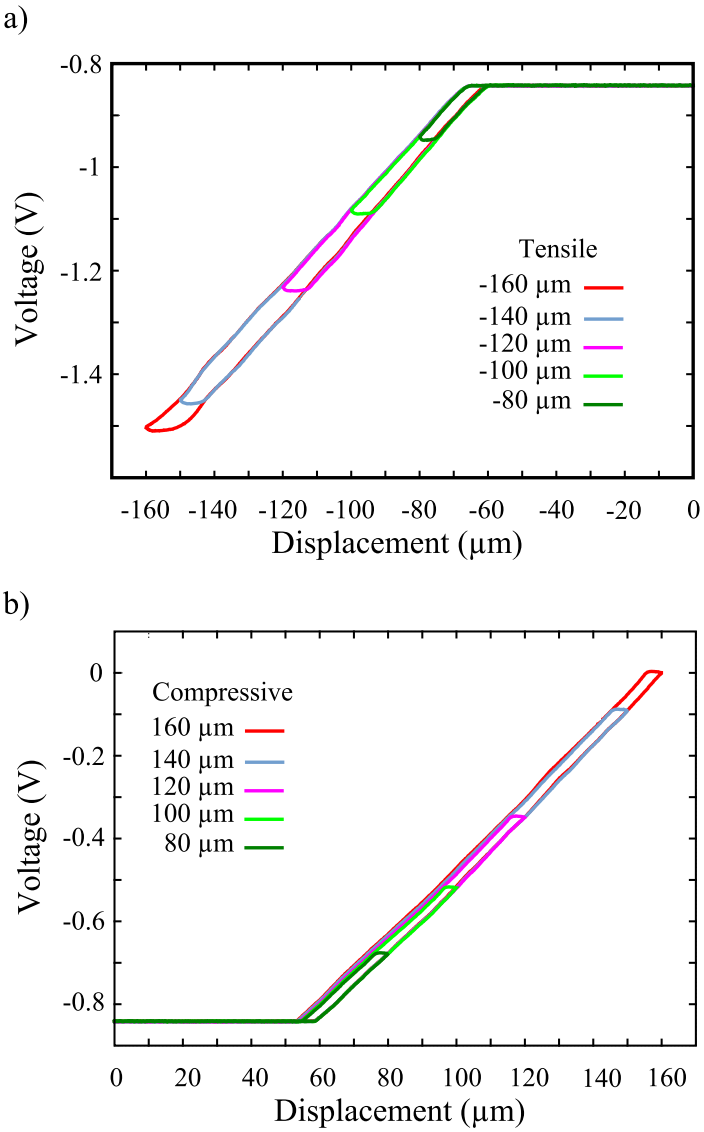

Figure Appendix-E.2: *Tensile and compressive strain loops of the previous strain gauges measured in the four-point bending apparatus described in section 6.1.1. A 5 V input voltage was applied across A-B pads while the strain effect on the resistance, as the output voltage amplified by 40 dB, was monitored at C-D pads. They are linearly strain sensitive and exhibit a gauge factor of* $GF \approx 2.6$*. Offsets between the approach and retract plots reveal mechanical hysteresis of the apparatus.* ***a)*** *For tensile strain different offsets appear at the start, about 6 µm, and at the end of the strain loops. The offset increases at the end of the plot for larger displacements.* ***b)*** *In case of compressive stress, the strain loops show equal offsets of 4 µm at the start and at the end. The offset remains the same for larger displacements and after several loops. The offsets for tensile and compressive stress are subtracted as mechanical hysteresis from the strain loops measured by the TMR sensors in chapter 6.*

Acknowledgments

I am deeply grateful to work in the project of TMR-based atomic force microscopy. The research described in this dissertation would have not been possible without numerous helps of many people. I would like to take this opportunity and thank all my colleagues, friends, and family for making my carrier and personal life easier and more enjoyable.

I would like to express my sincere gratitude to Prof. Dr. -Ing. Eckhard Quandt for giving me the opportunity to join his vibrant group with talented scientists and magnificent labs for MEMS technology. He provides great conditions for growth of intellectual qualities and innovative thinking. I am thankful for his valuable insights during our regular group meetings.

I would also like to express my sincere gratitude to my advisor, Dr. Dirk Meyners, for sharing his research ideas and his non-stop supports throughout all Ph.D. years. Without his dedication and motivation this work could have never advanced to this level today. I admire him for his regular attendance in the lab and interactive discussions. I also appreciate a lot his helps in my personal life.

I would like to thank our project partners, Dr. Karsten Rott and Prof. Dr. Günter Reiss at *Bielefeld University* for providing high quality TMR stacks and Dr. Tobias Meier and Dr. Hendrik Hölscher at *Karlsruhe Institute of Technology* for impeccably conducting the AFM section of the project. Their continuous attempts and contributions are the key point for the progress in this project. I would also like to acknowledge financial supports by the German Science Foundation DFG (ME 3616/1-2, HO 2237/4-1, RE 1052/31-2).

I am very thankful to Dr. Dirk Meyners, Dr. Antonio Malavé, and Dr. Thomas von Hofe for their patient guidance on operation of MEMS-related devices. I am also grateful to our technical staff Dipl.-Ing. Thomas Metzing for his technical assistance on maintenance and construction of lab instruments. I would like to thank M.Sc. Nicole Schneidewind for helping me to develop a modified Bosch process for RIE of Si substrates. I would also like to thank M.Sc. Patrick Hayes for his great contribution to this project during his master thesis. I I would like to sincerely thank all my colleagues in the group of *Inorganic Functional Materials* at *Kiel University*. I learned a lot from them since I joined the group. I specially thank M.Sc. Volker Röbisch who helped me frequently in my carrier and personal life. I would also like to thank my classmates during my master course, specially M.Sc. Laith Kadem, M.Sc. Erdem Yarar,

and Dr. Ahmed Zayed for being always supportive and considerate.

I am very thankful to my dearest friends Dr. Mostafa Enayat and Dr. Mehdi Keshavarz Hedayati, who motivated me in the first place to pursue my education at *Kiel University*. With them I never felt the distance from my family.

Finally, I wish to thank my lovely family for their endless encouragement and selfless supports over the past 22 years of my study.

Publication and Conference

Publication

- A. Tavassolizadeh, P. Hayes, K. Rott, G. Reiss, E. Quandt, and D. Meyners. Highly strain-sensitive magnetostrictive tunnel magnetoresistance junctions. *J. Magn. Magn. Mater.*, 384:308, 2015.
- T. Meier, A. Förste, A. Tavassolizadeh, K. Rott, D. Meyners, R. Gröger, G. Reiss, E. Quandt, T. Schimmel, and H. Hölscher. A scanning probe microscopy for magnetoresistive cantilevers utilizing a nested scanner design for large-area scans. *Beilstein J. Nanotechnol.*, 6:451, 2015.
- A. Tavassolizadeh, T. Meier, K. Rott, G. Reiss, E. Quandt, H. Hölscher, and D. Meyners. Self-sensing atomic force microscopy cantilevers based on tunnel magnetoresistance sensors. *Appl. Phys. Lett.*, 102(15):153104, 2013.

Conference

- A. Tavassolizadeh, T. Meier, K. Rott, G. Reiss, E. Quandt, H. Hölscher, and D. Meyners. Self-sensing atomic force microscopy cantilevers based on tunnel magnetoresistance sensors. *MRS Spring*, San Francisco, 2013.
- A. Tavassolizadeh, T. Meier, K. Rott, G. Reiss, E. Quandt, H. Hölscher, and D. Meyners. Atomic force microscopy using tunnel magnetoresistance sensors integrated with microcantilevers. 1^{st} *Euro Intelligent Materials*, Kiel, 2013.

Bibliography

[1] S. Tadigadapa and K. Mateti. Piezoelectric MEMS sensors: state-of-the-art and perspectives. *Meas. Sci. Technol.*, 20(9):092001, 2009.

[2] A. A. Barlian, W. T. Park, J. R. Mallon, A. J. Rastegar, and B. L. Pruitt. Review: semiconductor piezoresistance for microsystems. *Proc. IEEE*, 97(3):513, 2009.

[3] S. E. Zhu, M. K. Ghatkesar, C. Zhang, and G. C. A. M. Janssen. Graphene based piezoresistive pressure sensor. *Appl. Phys. Lett.*, 102(16):161904, 2013.

[4] Alamusi, N. Hu, H. Fukunaga, S. Atobe, Y. Liu, and J. Li. Piezoresistive strain sensors made from carbon nanotubes based polymer nanocomposites. *Sensors (Basel).*, 11:10691, 2011.

[5] J. Cao, Q. Wang, and H. Dai. Electromechanical properties of metallic, quasimetallic, and semiconducting carbon nanotubes under stretching. *Phys. Rev. Lett.*, 90(15):157601, 2003.

[6] B. Meng, W. Tang, Z. h. Too, X. Zhang, M. Han, W. Liu, and H. Zhang. A transparent single-friction-surface triboelectric generator and self-powered touch sensor. *Energy Environ. Sci.*, 6(11):3235, 2013.

[7] D. J. Lipomi, M. Vosgueritchian, Benjamin C. K. Tee, S. L. Hellstrom, J. A. Lee, C. H. Fox, and Z. Bao. Skin-like pressure and strain sensors based on transparent elastic films of carbon nanotubes. *Nat. Nanotechnol.*, 6(12):788, 2011.

[8] B. C. K. Tee, C. Wang, R. Allen, and Z. Bao. An electrically and mechanically self-healing composite with pressure- and flexion-sensitive properties for electronic skin applications. *Nat. Nanotechnol.*, 7:825, 2012.

[9] T. Yamada, Y. Hayamizu, Y. Yamamoto, Y. Yomogida, A. Izadi-Najafabadi, D. N. Futaba, and K. Hata. A stretchable carbon nanotube strain sensor for human-motion detection. *Nat. Nanotechnol.*, 6(5):296, 2011.

[10] J. Lee, S. Kim, J. Lee, D. Yang, B. C. Park, S. Ryu, and I. Park. A stretchable strain sensor based on a metal nanoparticle thin film for human motion detection. *Nanoscale*, 6(20):11932, 2014.

[11] H. Jaffrès, D. Lacour, F. Nguyen Van Dau, J. Briatico, F. Petroff, and A. Vaurès. Angular dependence of the tunnel magnetoresistance in transition-metal-based junctions. *Phys. Rev. B*, 64(6):064427, 2001.

[12] M. Donahue and D. G. Porteer. OOMMF User's Guide, Version 1.0. *Interagency Rep. No. NISTIR 6376, NIST*, 1999.

[13] M. Tortonese, R. C. Barrett, and C. F. Quate. Atomic resolution with an atomic force microscope using piezoresistive detection. *Appl. Phys. Lett.*, 62(8):834, 1993.

[14] T. Itoh and T. Suga. Scanning force microscope using a piezoelectric microcantilever. *J. Vac. Sci. Technol. B*, 12(3):1581, May 1994.

[15] J. Bay, S. Bouwstra, E. Laegsgaard, and O. Hansen. Micromachined AFM transducer with differential capacitive read-out. *J. Micromech. Microeng.*, 5(2):161, 1995.

[16] G. Meyer and N. M. Amer. Novel optical approach to atomic force microscopy. *Appl. Phys. Lett.*, 53(12):1045, 1988.

[17] K. Karrai and R. D. Grober. Piezo-electric tuning fork tip-sample distance control for near field optical microscopes. *Ultramicroscopy*, 61(1-4):197, 1995.

[18] S. Hembacher, F. J. Giessibl, and J. Mannhart. Evaluation of a force sensor based on a quartz tuning fork for operation at low temperatures and ultrahigh vacuum. *Appl. Phys. Lett.*, 188(3-4):445, 2002.

[19] Y. Seo and W. Jhe. Atomic force microscopy and spectroscopy. *Rep. Prog. Phys.*, 71(1):016101, 2008.

[20] T. Michels, E. Guliyev, M. Klukowski, and I. W. Rangelow. Micromachined self-actuated piezoresistive cantilever for high speed SPM. *Microelectron. Eng.*, 97:265, 2012.

[21] B. P. Brown, L. Picco, M. J. Miles, and C. F. J. Faul. Opportunities in high-speed atomic force microscopy. *Small*, 9(19):3201, 2013.

[22] T. Ando, T. Uchihashi, and T. Fukuma. High-speed atomic force microscopy for nano-visualization of dynamic biomolecular processes. *Prog. Mater. Sci.*, 83(7-9):337, 2008.

[23] S. R. Manalis, S. C. Minne, C. F. Quate, G. G. Yaralioglu, and A. Atalar. Two-dimensional micromechanical bimorph arrays for detection of thermal radiation. *Appl. Phys. Lett.*, 70(24):3311, 1997.

[24] S. A. Miller, K. L. Turner, and N. C. MacDonald. Microelectromechanical scanning probe instruments for array architectures. *Rev. Sci. Instrum.*, 68(11):4155, 1997.

[25] H .P. Lang, R. Berger, F. Battiston, J. P. Ramseyer, E. Meyer, C. Andreoli, J. Brugger, P. Vettiger, M. Despont, T. Mezzacasa, L. Scandella, H. J. Güntherodt, C. Gerber, and J. K. Gimzewski. A chemical sensor based on a micromechanical cantilever array for the identification of gases and vapors. *Appl. Phys. A*, 66(7):S61, 1998.

[26] S. C. Minne, G. Yaralioglu, S. R. Manalis, J. D. Adams, J. Zesch, A. Atalar, and C. F. Quate. Automated parallel high-speed atomic force microscopy. *Appl. Phys. Lett.*, 72(18):2340, 1998.

[27] I. W. Rangelow, Tzv. Ivanov, K Ivanova, B. E. Volland, P. Grabiec, Y. Sarov, A. Persaud, T. Gotszalk, P. Zawierucha, M. Zielony, D. Dontzov, B. Schmidt, M. Zier, N. Nikolov, I. Kostic, W. Engl, T. Sulzbach, J. Mielczarski, S. Kolb, D. P. Latimier, R. Pedreau, V. Djakov, S. E. Huq, K. Edinger, O. Fortagne, A. Almansa, and H. O. Blom. Piezoresistive and self-actuated 128-cantilever arrays for nanotechnology applications. *Microelectron. Eng.*, 84(58):1260, 2007.

[28] E. Eleftheriou. Recent advances in high-throughput scanning probe technology. *Proc. 10th IEEE Int. Conf.*, page 105, 2010.

[29] A. Schneider, R. H. Ibbotson, R. J. Dunn, and E. Huq. Arrays of SU-8 microcantilevers with integrated piezoresistive sensors for parallel AFM applications. *Microelectron. Eng.*, 88(8):2390, 2011.

[30] A. Gaitas and P. French. Piezo-thermal probe array for high throughput applications. *Sens. Actuator A-Phys.*, 186:125, 2012.

[31] J. Fritz, M. K. Baller, H. P. Lang, H. Rothuizen, P. Vettiger, E. Meyer, H. J Güntherodt, Ch. Gerber, and J. K. Gimzewski. Translating biomolecular recognition into nanomechanics. *Science*, 288:316, 2000.

[32] M. Álvarez and J. Tamayo. Optical sequential readout of microcantilever arrays for biological detection. *Sens. Actuators B-Chem.*, 106(2):687, 2005.

[33] B. Rogers, L. Manning, T. Sulchek, and J. D. Adams. Improving tapping mode atomic force microscopy with piezoelectric cantilevers. *Ultramicroscopy*, 100(3-4):267, 2004.

[34] J. D. Adams, L. Manning, B. Rogers, M. Jones, and S. C. Minne. Self-sensing tapping mode atomic force microscopy. *Sens. Actuator A-Phys.*, 121(1):262, 2005.

[35] S. Faegh, N. Jalili, and S. Sridhar. Ultrasensitive piezoelectric-based microcantilever biosensor : theory and experiment. *IEEE/ASME Trans. Mechatronics*, 20(1):308, 2015.

[36] S. Watanabe and T. Fujii. Micro-fabricated piezoelectric cantilever for atomic force microscopy. *Rev. Sci. Instrum.*, 67(11):3898, 1996.

[37] T. Itoh, C. Lee, and T. Suga. Deflection detection and feedback actuation using a self-excited piezoelectric Pb(Zr,Ti)O_3 microcantilever for dynamic scanning force microscopy. *Appl. Phys. Lett.*, 69(14):2036, 1996.

[38] J. C. Doll and B. L. Pruitt. Design of piezoresistive versus piezoelectric contact mode scanning probes. *J. Micromech. Microeng.*, 20(9):095023, 2010.

[39] A. L. Window, editor. *Strain gauge technology.* Springer, New York, 1992.

[40] T. Michels and I. W. Rangelow. Review of scanning probe micromachining and its applications within nanoscience. *Microelectron. Eng.*, 126:191, 2014.

[41] J. Thaysen, A. Boisen, O. Hansen, and S. Bouwstra. Atomic force microscopy probe with piezoresistive read-out and a highly symmetrical Wheatstone bridge arrangement. *Sens. Actuator A-Phys.*, 83(1-3):47, 2000.

[42] X. Yu, J. Thaysen, O. Hansen, and A. Boisen. Optimization of sensitivity and noise in piezoresistive cantilevers. *J. Appl. Phys.*, 92(10):6296, 2002.

[43] J. Lee and W. P. King. Improved all silicon microcantilever heaters with integrated piezoresistive sensing. *J. Microelectromech. Syst*, 17(2):432, 2008.

[44] M. Qazi, N. DeRoller, A. Talukdar, and G. Koley. III-V Nitride based piezoresistive microcantilever for sensing applications. *Appl. Phys. Lett.*, 99(19):193508, 2011.

[45] A. Gaitas, T. Li, and W. Zhu. A probe with ultrathin film deflection sensor for scanning probe microscopy and material characterization. *Sens. Actuator A-Phys.*, 168(2):229, 2011.

[46] L. K. Siong, I. Abdul Azid, O. Sidek, K. Ibrahim, and M. Devarajan. SU-8 piezoresistive microcantilever with high gauge factor. *Micro. Nano. Lett.*, 8(3):123, 2013.

[47] B. L. Pruitt and T. W. Kenny. Piezoresistive cantilevers and measurement system for characterizing low force electrical contacts. *Sens. Actuator A-Phys.*, 104(1):68, 2003.

[48] B. L. Pruitt, W. T. Park, and T. W. Kenny. Measurement system for low force and small displacement contacts. *J. Microelectromech. Syst*, 13(2):220, 2004.

[49] S. C. Seel and C. V. Thompson. Piezoresistive microcantilevers for in situ stress measurements during thin film deposition. *Rev. Sci. Instrum.*, 76(7):075103, 2005.

[50] G. E. Fantner, W. Schumann, R. J. Barbero, A. Deutschinger, V. Todorov, D. S. Gray, A. M. Belcher, I. W. Rangelow, and K. Youcef-Toumi. Use of self-actuating and self-sensing cantilevers for imaging biological samples in fluid. *Nanotechnology*, 20(43):434003, 2009.

[51] B. W. Chui, T. D. Stowe, Y. S. Ju, K. E. Goodson, T. W. Kenny, H. J. Mamin, B. D. Terris, R. P. Ried, and D. Rugar. Low-stiffness silicon cantilevers with integrated heaters and piezoresistive sensors for high-density AFM thermomechanical data storage. *J. Microelectromech. Syst*, 7(1):69, 1998.

[52] M. Lutwyche, C. Andreoli, G. Binnig, J. Brugger, U. Drechsler, W. Häberle, H. Rohrer, H. Rothuizen, P. Vettiger, G. Yaralioglu, and C. Quate. 5x5 2D AFM cantilever arrays a first step towards a Terabit storage device. *Sens. Actuator A-Phys.*, 73(12):89, 1999.

[53] D. R. Sahoo, A. Sebastian, W. Haberle, H. Pozidis, and E. Eleftheriou. Scanning probe microscopy based on magnetoresistive sensing. *Nanotechnology*, 22(14):145501, 2011.

[54] O. Hansen and A. Boisen. Noise in piezoresistive atomic force microscopy. *Nanotechnology*, 10(1):51, 1999.

[55] H. J. Mamin, B. a. Gurney, D. R. Wilhoit, and V. S. Speriosu. High sensitivity spin-valve strain sensor. *Appl. Phys. Lett.*, 72(24):3220, 1998.

[56] H. J. Mamin, R. P. Ried, B. D. Terris, and D. Rugar. High-density data storage based on the atomic force microscope. *Proc. IEEE*, 87(6):7803, 1999.

[57] B. A. Gurney, H. J. Mamin, D. Ruger, and V. S. Speriosu. Atomic force microscope system with cantilever having unbiased spin valve magnetoresistive srain gauge, U.S. patent 5856617, 1999.

[58] M. Nakamura, M. Kimura, K. Sueoka, and K. Mukasa. Scanning magnetoresistance microscopy with a magnetoresistive sensor cantilever. *Appl. Phys. Lett.*, 80(15):2713, 2002.

[59] L. Baril, B. Gurney, D. Wilhoit, and V. Speriosu. Magnetostriction in spin valves. *J. Appl. Phys.*, 85(8):5139, 1999.

[60] R. C. O'Handley and J. R. Chlidress. New spin-valve magnetic field sensors combined with strain sensing and strain compensation. *IEEE Trans. Magn.*, 31(4):2450, 1995.

[61] T. Duenas, A. Sehrbrock, M. Löhndorf, A. Ludwig, J. Wecker, P. Grünberg, and E. Quandt. Micro-sensor coupling magnetostriction and magnetoresistive phenomena. *J. Magn. Magn. Mater.*, 242:1132, 2002.

[62] M. Löhndorf, T. Duenas, M. Tewes, E. Quandt, M. Rührig, and J. Wecker. Highly sensitive strain sensors based on magnetic tunneling junctions. *Appl. Phys. Lett.*, 81(2):313, 2002.

[63] M. Löhndorf, T. A. Duenas, A. Ludwig, M. Rührig, J. Wecker, D. Bürgler, P. Grünberg, and E. Quandt. Strain Sensors Based on Magnetostrictive GMR/TMR Structures. *IEEE Trans. Magn.*, 38(5):2826, 2002.

[64] S. Ikeda, J. Hayakawa, Y. Ashizawa, Y. M. Lee, K. Miura, H. Hasegawa, M. Tsunoda, F. Matsukura, and H. Ohno. Tunnel magnetoresistance of 604% at 300 K by suppression of Ta diffusion in CoFeB/MgO/CoFeB pseudo-spin-valves annealed at high temperature. *Appl. Phys. Lett.*, 93(8):082508, 2008.

[65] D. Meyners, T. von Hofe, M. Vieth, M. Rührig, S. Schmitt, and E. Quandt. Pressure sensor based on magnetic tunnel junctions. *J. Appl. Phys.*, 105(7):07C914, 2009.

[66] C. Albon, A. Weddemann, A. Auge, K. Rott, and A. Huetten. Tunneling magnetoresistance sensors for high resolutive particle detection. *Appl. Phys. Lett.*, 95(2):23101, 2009.

[67] S. Devasia, E. Eleftheriou, and S. O. R. Moheimani. A survey of control issues in nanopositioning. *IEEE Trans. Control Syst. Technol.*, 15:802, 2007.

[68] M. Srinivasa and V Murti. Scanning probe microscopy. *IEEE Control Syst. Mag.*, 1(3):65, 2008.

[69] J. M. D. Coey. *Magnetism and magnetic materials*. Cambridge University Press, New York, 2010.

[70] M. Julliere. Tunneling between ferromagnetic films. *Phys. Lett.*, 54A(3):225, 1975.

[71] P. M. Tedrow and R. Meservey. Magnetic field splitting of the quasiparticle states in superconducting aluminum films. *Phys. Rev. Lett.*, 25:1270, 1970.

[72] R. Meservey and P. M. Tedrow. Spin-polarized electron tunneling. *Phys. Rep.*, 238(4):173, 1994.

[73] M. Ziese and J. M. Thornton, editors. *Spin electronics*. Springer, Berlin, 2001.

[74] R. C. O'Handley. *Modern magnetic materials: principles and applications*. Willey-Interscience, 2000.

[75] E. Y. Tsymbal, O. N. Mryasov, and P. R. Leclair. Spin-dependent tunnelling in magnetic tunnel. *J. Phys. Condens. Matter*, 109:R109, 2003.

[76] S. Yuasa. Giant tunneling magnetoresistance in MgO-based magnetic tunnel junctions. *J. Phys. Soc. Jpn.*, 77(3):031001, 2008.

[77] V. Sapozhnikov, K. Z. Gao, and Y. Chen. Intrinsic asymmetry and angular dependence of the junction resistance for high TMR read sensors. *J. Appl. Phys.*, 105(7):07B722, 2009.

[78] R. Waser. *Nanoelectronics and information technology*. WILEY-VCH, Aachen, third edition, 2012.

[79] M. B. Stearns. Simple explanation of tunneling spin-polarization of Fe, Co, Ni and its alloys. *J. Magn. Magn. Mater.*, 5:167, 1977.

[80] J. C. Slonczewski. Conductance and exchange coupling of two ferromagnets separated by a tunneling barrier. *Phys. Rev. B*, 39(10):6995, 1989.

[81] W. Butler, X.-G. Zhang, T. Schulthess, and J. MacLaren. Spin-dependent tunneling conductance of Fe/MgO/Fe sandwiches. *Phys. Rev. B*, 63(5):054416, 2001.

[82] J. Mathon and A. Umerski. Theory of tunneling magnetoresistance of an epitaxial Fe/MgO/Fe(001) junction.pdf. *Phys. Rev. B*, 63:220403, 2001.

[83] C. Kittel. *Introduction to solid state physics*. Wiley, New York, sixth edition, 1986.

[84] J. S. Moodera, L. R. Kinder, M. W. Terrilyn, and R. Meservey. Large magnetoresistance at room temperature in ferromagnetic thin film tunnel junctions. *Physi. Rev. Lett.*, 74(16):3273, 1995.

[85] D. Wang, C. Nordman, J. M. Daughton, Z. Qian, and J. Fink. 70% TMR at room temperature for SDT sandwich junctions with CoFeB as free and reference layers. *IEEE Trans. Magn.*, 40(4):2269, 2004.

[86] S. S. P. Parkin, C. Kaiser, A. Panchula, P. M. Rice, B. Hughes, M. Samant, and S. H. Yang. Giant tunnelling magnetoresistance at room temperature with MgO (100) tunnel barriers. *Nat. Mater.*, 3(12):862, 2004.

[87] S. Yuasa, T. Nagahama, A. Fukushima, Y. Suzuki, and K. Ando. Giant room-temperature magnetoresistance in single-crystal Fe/MgO/Fe magnetic tunnel junctions. *Nat. Mater.*, 3(12):868, 2004.

[88] D. D. Djayaprawira, K. Tsunekawa, M. Nagai, H. Maehara, S. Yamagata, N. Watanabe, S. Yuasa, Y. Suzuki, and K. Ando. 230% room-temperature magnetoresistance in CoFeB/MgO/CoFeB magnetic tunnel junctions. *Appl. Phys. Lett.*, 86(9):092502, 2005.

[89] S. Yuasa, Y. Suzuki, T. Katayama, and K. Ando. Characterization of growth and crystallization processes in CoFeB/MgO/CoFeB magnetic tunnel junction structure by reflective high-energy electron diffraction. *Appl. Phys. Lett.*, 87(24):242503, 2005.

[90] S. Pinitsoontorn, A. Cerezo, A. K. Petford-Long, D. Mauri, L. Folks, and M. J. Carey. Three-dimensional atom probe investigation of boron distribution in CoFeB/MgO/CoFeB magnetic tunnel junctions. *Appl. Phys. Lett.*, 93(7):071901, 2008.

[91] Y. Lu, B. Lépine, G. Jézéquel, S. Ababou, M. Alnot, J. Lambert, A. Renard, M. Mullet, C. Deranlot, H. Jaffrès, F. Petroff, and J. M. George. Depth analysis of boron diffusion in MgO/CoFeB bilayer by x-ray photoelectron spectroscopy. *J. Appl. Phys.*, 108(4):43703, 2010.

[92] T. Miyajima, T. Ibusuki, S. Umehara, M. Sato, S. Eguchi, M. Tsukada, and Y. Kataoka. Transmission electron microscopy study on the crystallization and boron distribution of CoFeB/MgO/CoFeB magnetic tunnel junctions with various capping layers. *Appl. Phys. Lett.*, 94(12):122501, 2009.

[93] C. Y. You, T. Ohkubo, Y. K. Takahashi, and K. Hono. Boron segregation in crystallized MgO/amorphous-$Co_{40}Fe_{40}B_{20}$ thin films. *J. Appl. Phys.*, 104(3):033517, 2008.

[94] Y. Jang, C. Nam, K. S. Lee, B. K. Cho, Y. J. Cho, K. S. Kim, and K. W. Kim. Variation in the properties of the interface in a CoFeB/MgO/CoFeB tunnel junction during thermal annealing. *Appl. Phys. Lett.*, 91(10):102104, 2007.

[95] J. Y. Bae, W. C. Lim, H. J. Kim, T. D. Lee, K. W. Kim, and T. W. Kim. Compositional change of MgO barrier and interface in CoFeB/MgO/CoFeB tunnel junction after annealing. *J. Appl. Phys.*, 99(8):08T316, 2006.

[96] J. J. Cha, J. C. Read, R. A. Buhrman, and D. A. Muller. Spatially resolved electron energy-loss spectroscopy of electron-beam grown and sputtered CoFeB/MgO/CoFeB magnetic tunnel junctions. *Appl. Phys. Lett.*, 91(6):062516, 2007.

[97] S. S. Mukherjee, D. MacMahon, F. Bai, C. L. Lee, and S. K. Kurinec. Study of boron diffusion in MgO in CoFeB/MgO film stacks using parallel electron energy loss spectroscopy. *Appl. Phys. Lett.*, 94(8):082110, 2009.

[98] J. Schmalhorst, A. Thomas, G. Reiss, X. Kou, and E. Arenholz. Influence of chemical and magnetic interface properties of Co-Fe-B/MgO/Co-Fe-B tunnel junctions on the annealing temperature dependence of the magnetoresistance. *J. Appl. Phys.*, 102(5):053907, 2007.

[99] J. C. Read, P. G. Mather, and R. A.. Buhrman. X-ray photoemission study of CoFeB/MgO thin film bilayers. *Appl. Phys. Lett.*, 90(13):132503, 2007.

[100] T. Takeuchi, K. Tsunekawa, Y. S. Choi, Y. Nagamine, D. D. Djayaprawira, A. Genseki, Y. Hoshi, and Y. Kitamoto. Crystallization of amorphous CoFeB ferromagnetic layers in CoFeB/MgO/CoFeB magnetic tunnel junctions. *Jpn. J. Appl. Phys.*, 46(7L):L623, 2007.

[101] C. Park, Y. H. Wang, D. E. Laughlin, and J. G. Zhu. Effect of adjacent layers on crystallization and magnetoresistance in CoFeB/MgO/CoFeB magnetic tunnel junctions. *IEEE Trans. Magn.*, 42(10):2639, 2006.

[102] J. Hayakawa, S. Ikeda, Y. M. Lee, F. Matsukura, and H. Ohno. Effect of high annealing temperature on giant tunnel magnetoresistance ratio of CoFeB/MgO/CoFeB magnetic tunnel junctions. *Appl. Phys. Lett.*, 89(23):232510, 2006.

[103] J. Hayakawa, S. Ikeda, F. Matsukura, H. Takahashi, and H. Ohno. Dependence of giant tunnel magnetoresistance of sputtered CoFeB/MgO/CoFeB magnetic tunnel junctions on MgO barrier thickness and annealing temperature. *Jpn. J. Appl. Phys.*, 44(16-19):L587, 2005.

[104] W. G. Wang, C. Ni, G. X. Miao, C. Weiland, L. R. Shah, X. Fan, P. Parson, J. Jordan-Sweet, X. M. Kou, Y. P. Zhang, R. Stearrett, E. R. Nowak, R. Opila, J. S. Moodera, and J. Q. Xiao. Understanding tunneling magnetoresistance during thermal annealing in MgO-based junctions with CoFeB electrodes. *Phys. Rev. B*, 81(14):144406, 2010.

[105] D. J. Larson, E. A. Marquis, P. M. Rice, T. J. Prosa, B. P. Geiser, S. H. Yang, and S. S. P. Parkin. Manganese diffusion in annealed magnetic tunnel junctions with MgO tunnel barriers. *Scr. Mater.*, 64(7):673, 2011.

[106] Y. M. Lee, J. Hayakawa, S. Ikeda, F. Matsukura, and H. Ohno. Effect of electrode composition on the tunnel magnetoresistance of pseudo-spin-valve magnetic tunnel junction with a MgO tunnel barrier. *Appl. Phys. Lett.*, 90(21):212507, 2007.

[107] S. Ikeda, J. Hayakawa, Y. M. Lee, F. Matsukura, and H. Ohno. Dependence of tunnel magnetoresistance on ferromagnetic electrode materials in MgO-barrier magnetic tunnel junctions. *J. Magn. Magn. Mater.*, 310:1937, 2007.

[108] Y. M. Lee, J. Hayakawa, S. Ikeda, F. Matsukura, and H. Ohno. Giant tunnel magnetoresistance and high annealing stability in CoFeB/MgO/CoFeB magnetic tunnel junctions with synthetic pinned layer. *Appl. Phys. Lett.*, 89(4):42506, 2006.

[109] P. Wiśniowski, J. M. Almeida, S. Cardoso, N. P. Barradas, and P. P. Freitas. Effect of free layer thickness and shape anisotropy on the transfer curves of MgO magnetic tunnel junctions. *J. Appl. Phys.*, 103(7):07A910, 2008.

[110] P. G. de Gennes. Wetting: statics and dynamics. *Rev. Mod. Phys.*, 57(3):827, 1985.

[111] F. Montaigne, C. Tiusan, and M. Hehn. Angular dependence of tunnel magnetoresistance in magnetic tunnel junctions and specific aspects in spin-filtering devices. *J. Appl. Phys.*, 108(6):063912, 2010.

[112] W. H. Meiklejohn and C. P. Bean. New magnetic anisotropy. *Phys. Rev.*, 105(3):904, 1957.

[113] J. Nogués and I. K. Schuller. Exchange bias. *J. Magn. Magn. Mater.*, 192(2):203, 1999.

[114] J. Camarero, J. Sort, A. Hoffmann, J. M. García-Martín, B. Dieny, R. Miranda, and J. Nogués. Origin of the asymmetric magnetization reversal behavior in exchange-biased systems: competing anisotropies. *Phys. Rev. Lett.*, 95:1, 2005.

[115] X. Zhang, Q. Zhan, G. Dai, Y. Liu, Z. Zuo, H. Yang, B. Chen, and R. W. Li. Effect of mechanical strain on magnetic properties of flexible exchange biased FeGa/IrMn heterostructures. *Appl. Phys. Lett.*, 102(2):022412, 2013.

[116] T. Suzuki and K. Ouchi. Crystal orientation of Mn-Ir antiferromagnetic films for exchange-biased soft-magnetic underlayer in perpendicular recording media. *IEEE Trans. Magn.*, 40(4):2347, 2004.

[117] P. Grünberg, R. Schreiber, Y. Pang, M. B. Brodsky, and H. Sowers. Layered magnetic structures: evidence for antiferromagnetic coupling of Fe layers across Cr interlayers. *Phys. Rev. Lett.*, 57(19):2442, 1986.

[118] S. S. P. Parkin, N. More, and K. P. Roche. Oscillations in exchange coupling and magnetoresistance in metallic superlattice structures: Co/Ru, Co/Cr, and Fe/Cr. *Phys. Rev. Lett.*, 64(19):2304, 1990.

[119] M. N. Baibich, J. M. Broto, A. Fert, F. N. Van Dau, F. Petroff, P. Etienne, G. Creuzet, A. Friederich, and J. Chazelas. Giant magnetoresistance of (001)Fe/(001)Cr magnetic superlattices. *Phys. Rev. Lett.*, 61(21):2472, 1988.

[120] G. Binasch, P. Grünberg, F. Saurenbach, and W. Zinn. Enhanced magnetoresistance in layered magnetic structures with antiferromagnetic interlayer exchange. *Phys. Rev. B*, 39(7):4828, 1989.

[121] S. S. P. Parkin and D. Mauri. Spin-engineering: Direct determination of the Ruderman-Kittel-Kasuya-Yosida far-field range function in ruthenium. *Phys. Rev. B*, 44(6872):7131, 1991.

[122] M. D. Stiles. Interlayer exchange coupling. *J. Magn. Magn. Mater.*, 200(13):322, 1999.

[123] Z. B. Guo, B. Y. Zong, J. J. Qiu, P. Luo, L. H. An, H. Meng, G. C. Han, and H. K. Hui. Tuning exchange coupling by replacing CoFe with amorphous CoFeB in the CoFe/Ru/CoFe synthetic antiferromagnetic structure. *Solid State Commun.*, 150(1-2):45, 2010.

[124] H. A. M. van den Berg, W. Clemens, G. Gieres, G. Rupp, M. Vieth, J. Wecker, and S. Zoll. GMR angle detector with an artificial antiferromagnetic subsystem (AAF). *J. Magn. Magn. Mater.*, 165(1-3):524, 1997.

[125] L. Néel and C. R. Hebd. No Title. *Seances Acad. Sci*, 255:1545, 1962.

[126] J. C. S. Kools, W. Kula, D. Mauri, and T. Lin. Effect of finite magnetic film thickness on Néel coupling in spin valves. *J. Appl. Phys.*, 85(8):4466, 1999.

[127] J. P. Joule. On a new class of magnetic forces. *Ann. Electr. Magn. Chem.*, 8:219, 1842.

[128] B. D. Cullity and C. D. Graham. *Introduction to magnetic materials*. WILEY, New Jersey, second edition, 2009.

[129] E. W. Lee. Magnetostriction and magnetomechanical effects. *Rep. Prog. Phys.*, 18:184, 2002.

[130] E. Villari. Change of magnetization by tension and by electric current. *Ann. Phys.*, 126:87, 1865.

[131] H. Uchida, Y. Matsumura, H. Uchida, and H. Kaneko. Progress in thin films of giant magnetostrictive alloys. *J. Magn. Magn. Mater.*, 239(1-3):540, 2002.

[132] X. Gao, J. Li, J. Zhu, J. Li, and M. Zhang. Effect of B and Cr on mechanical properties and magnetostriction of Iron-Gallium alloy. *Mater. Trans.*, 50:1959, 2009.

[133] A. E. Clark, K. B. Hathaway, M. Wun-Fogle, J. B. Restorff, T. A. Lograsso, V. M. Keppens, G. Petculescu, and R. A. Taylor. Extraordinary magnetoelasticity and lattice softening in bcc Fe-Ga alloys. *J. Appl. Phys.*, 93(10):8621, 2003.

[134] G. A. Lebedev, B. Viala, T. Lafont, D. I. Zakharov, O. Cugat, and J. Delamare. Converse magnetoelectric effect dependence with CoFeB composition in ferromagnetic/piezoelectric composites. *J. Appl. Phys.*, 111(7):07C725, 2012.

[135] M. Ali and R. Watts. Measurement of saturation magnetostriction using novel strained substrate techniques and the control of the magnetic anisotropy. *J. Magn. Magn. Mater.*, 202(1):85, 1999.

[136] M. D. Cooke, L. C. Wang, R. Watts, R. Zuberek, G. Heydon, W. M. Rainforth, and G. A. Gehring. The effect of thermal treatment, composition and substrate on the texture and magnetic properties of FeCo thin films. *J. Phys. D Appl. Phys.*, 33(12):1450, 2000.

[137] D. Hunter, W. Osborn, K. Wang, N. Kazantseva, J. Hattrick-Simpers, R. Suchoski, R. Takahashi, M. L. Young, A. Mehta, L. A. Bendersky, S. E. Lofland, M. Wuttig, and I. Takeuchi. Giant magnetostriction in annealed $Co_{1-x}Fe_x$ thin-films. *Nat. Commun.*, 2:518, 2011.

[138] T. Nakajima, T. Takeuchi, I. Yuito, K. Kato, M. Saito, K. Abe, T. Sasaki, T. Sekiguch, and S. I. Yamaura. Effect of annealing on magnetostrictive properties of Fe-Co alloy thin films. *Mater. Trans.*, 55:556, 2014.

[139] W. Shen, B. D. Schrag, M. J. Carter, and G. Xiao. Quantitative detection of DNA labeled with magnetic nanoparticles using arrays of MgO-based magnetic tunnel junction sensors. *Appl. Phys. Lett.*, 93(3):033903, 2008.

[140] Z. Diao, D. Apalkov, M. Pakala, Y. Ding, Al. Panchula, and Y. Huai. Spin transfer switching and spin polarization in magnetic tunnel junctions with MgO and AlO_x barriers. *Appl. Phys. Lett.*, 87(23):232502, 2005.

[141] S. Yuasa and D. D. Djayaprawira. Giant tunnel magnetoresistance in magnetic tunnel junctions with a crystalline MgO(001) barrier. *J. Phys. D Appl. Phys.*, 40(21):R337, 2007.

[142] H. Kubota, A. Fukushima, K. Yakushiji, T. Nagahama, S. Yuasa, K. Ando, H. Maehara, Y. Nagamine, K. Tsunekawa, D. D. Djayaprawira, N. Watanabe, and Y. Suzuki. Quantitative measurement of voltage dependence of spin-transfer torque in MgO-based magnetic tunnel junctions. *Nat. Phys.*, 4(1):37, 2008.

[143] T. Egami, C. Graham, W. Dmowski, P. Zhou, P. J. Flanders, E. Marinero, H. Notarys, and C. Robinson. Anisotropy and coercivity of amorphous RE-TM films. *IEEE Trans. Magn.*, 23(5):2269, 1987.

[144] L. Néel. Anisotropie magnétique superficielle et surstructures d'orientation. *J. Phys. Radium*, 15(4):225, 1954.

[145] A. T. Hindmarch, A. W. Rushforth, R. P. Campion, C. H. Marrows, and B. L. Gallagher. Origin of in-plane uniaxial magnetic anisotropy in CoFeB amorphous ferromagnetic thin films. *Phys. Rev. B*, 83(21):212404, 2011.

[146] X. Yan, M. Hirscher, T. Egami, and E. E. Marinero. Direct observation of anelastic bond-orientational anisotropy in amorphous $Tb_{26}Fe_{62}Co_{12}$ thin films by x-ray diffraction. *Phys. Rev. B*, 43(11):9300, 1991.

[147] Y. Suzuki, J. Haimovich, and T. Egami. Bond-orientational anisotropy in metallic glasses observed by x-ray diffraction. *Phys. Rev. B*, 35(5):2162, 1987.

[148] G. Suran, H. Ouahmane, M. Rivoire, and J. Sztern. Static and dynamic magnetic properties of $(CoZr)_{100-x}(RE)_x$ amorphous thin films. *J. Appl. Phys.*, 73(10):5721, 1993.

[149] M. González-Guerrero, J. L. Prieto, D. Ciudad, P. Sánchez, and C. Aroca. Engineering the magnetic properties of amorphous $(Fe_{80}Co_{20})_{80}B_{20}$ with multilayers of variable anisotropy direction. *Appl. Phys. Lett.*, 90(16):162501, 2007.

[150] M. Raju, S. Chaudhary, and D. K. Pandya. Effect of interface on magnetic properties of $Co_{20}Fe_{60}B_{20}$ in ion-beam sputtered Si/CoFeB/MgO and Si/MgO/CoFeB bilayers. *J. Magn. Magn. Mater.*, 332:109, 2013.

[151] B. A. Ravan. Multi-band tight-binding calculation of electronic transport in Fe/trans-polyacetylene/Fe tunnel junctions. *Phys. Scr.*, 86(4):45701, 2012.

[152] R. Lavrijsen, P. V. Paluskar, C. T. J. Loermans, P. A. van Kruisbergen, J. T. Kohlhepp, H. J. M. Swagten, B. Koopmans, and E. Snoeck. Magnetism in $Co_{80-x}Fe_xB_{20}$: Effect of crystallization. *J. Appl. Phys.*, 109(9):093905, 2011.

[153] T. Kuschel, J. Hamrle, J. Pištora, K. Saito, S. Bosu, Y. Sakuraba, K. Takanashi, and J. Wollschläger. Magnetic characterization of thin $Co_{50}Fe_{50}$ films by magnetooptic Kerr effect. *J. Phys. D Appl. Phys.*, 45(49):495002, 2012.

[154] H. A. M. van den Berg, W. Clemens, G. Gieres, G. Rupp, M. Vieth, J. Wecker, and S. Zoll. GMR angle detector with an artificial antiferromagnetic subsystem (AAF). *J. Magn. Magn. Mater.*, 165:524, 1997.

[155] M. Löhndorf, S. Dokupil, J. Wecker, M. Rührig, and E. Quandt. Characterization of magnetic tunnel junctions (MTJ) with magnetostrictive free layer materials. *J. Magn. Magn. Mater.*, 272:2023, 2004.

[156] H. Kronmüller and S. Parkin, editors. *Handbook of magnetism and advanced magnetic materials*. Wiley, Chichester, 2007.

[157] N. A. Spaldin. *Magnetic materials*. Cambridge University Press, New York, second edition, 2010.

[158] B. Cappella and G. Dietler. Force-distance curves by atomic force microscopy. *Surf. Sci. Rep.*, 34:1, 1999.

[159] H. C. Hamaker. The London-van der Waals attraction between spherical particles. *Physica*, 4(1058), 1937.

[160] J. E. Jones. On the Determination of Molecular Fields. II. From the Equation of State of a Gas. *Proceedings of the Royal Society of London*, 106:463, 1924.

[161] J. Israelachvili. *Intermolecular and surface forces*. Academic Pr., London, 1991.

[162] E. Meyer, J. H. Hug, and R. Bennewitz. *Scanning probe microscopy*. Springer, Berlin-Heidelberg, 2004.

[163] J. B. Marion. *Classical dynamics of particles and systems*. Academic Pr., New York, 1970.

[164] T. Fukuma and S. P. Jarvis. Development of liquid-environment frequency modulation atomic force microscope with low noise deflection sensor for cantilevers of various dimensions. *Rev. Sci. Instrum.*, 77:043701, 2006.

[165] Y. Hosokawa, T. Ichii, K. Kobayashi, K. Matsushige, and H. Yamada. Small amplitude frequency modulation atomic force microscopy of lead phthalocyanine molecules using cantilever with very high spring constant. *Jpn. J. Appl. Phys.*, 47:6125, 2008.

[166] T. Fukuma. Wideband low-noise optical beam deflection sensor with photothermal excitation for liquid-environment atomic force microscopy. *Rev. Sci. Instrum.*, 80:0237070, 2009.

[167] R. Enning, Ziegler D., A. Nievergelt, R. Friedlos, K. Venkataramani, and A. Stemmer. A high frequency sensor for optical beam deflection atomic force microscopy. *Rev. Sci. Instrum.*, 82:043705, 2011.

[168] F. J. Giessibl. Atomic resolution on Si(111)-(7x7) by noncontact atomic force microscopy with a force sensor based on a quartz tuning fork. *Appl. Phys. Lett.*, 76:1470, 2002.

[169] R. D. Grober, J. Acimovic, J. Schuck, D. Hessman, P. J. Kindlemann, J. Hespanha, S. Morse, K. Karrai, I. Tiemann, and S. Manus. Fundamental limits to force detection using quartz tuning forks. *Rev. Sci. Instrum.*, 71:2776, 2000.

[170] B. W. Hoogenboom, P. L. T. M. Frederix, J. L. Yang, S. Martin, Y. Pellmont, M. Steinacher, S. Zäch, E. Langenbach, H.-J. Heimbeck, A. Engel, and H. J. Hug. A FabryPerot interferometer for micrometer-sized cantilevers. *Appl. Phys. Lett.*, 86:074101, 2005.

[171] H. I. Rasool, P. R. Wilkinson, A. Z. Stieg, and J. K. Gimzewski. A low noise all-fiber interferometer for high resolution frequency modulated atomic force microscopy imaging in liquids. *Rev. Sci. Instrum.*, 81:023703, 2010.

[172] C. Schönenberger and S. F. Alvarado. A differential interferometer for force microscopy. *Rev. Sci. Instrum.*, 60:3131, 1989.

[173] T. R. Albrecht, P. Grutter, D. Horne, and D. Rugar. Frequency modulation detection using high-Q cantilevers for enhanced force microscope sensitivity. *J. Appl. Phys.*, 69(2):668, 1991.

[174] W. Allers, A. Schwarz, U. D. Schwarz, and R. Wiesendanger. Dynamic scanning force microscopy at low temperatures on a van der Waals surface : graphite (0001). *Appl. Surf. Sci.*, 140:247, 1999.

[175] D. S. Senturia. *Microsystem design.* Springer, New York, 2000.

[176] J. B. Johnson. Thermal agitation of electricity in conductors. *Nature*, 119:50, 1927.

[177] H. Nyquist. Thermal agitation of electric charge in conductors. *Phys. Rev.*, 32:110, 1928.

[178] W. Schottky. About spontaneous current instability in different electric conductors. *Ann. Phys. (Paris).*, 57:541, 1918.

[179] E. R. Nowak, M. B. Weissman, and S. S. P. Parkin. Electrical noise in hysteretic ferromagnetinsulatorferromagnet tunnel junctions. *Appl. Phys. Lett.*, 74(4):600, 1999.

[180] K. B. Klaassen, J. C. L. van Peppen, and X. Xing. Noise in magnetic tunnel junction devices. *J. Appl. Phys.*, 93(10):8573, 2003.

[181] P. P. Freitas, R. Ferreira, S. Cardoso, and F. Cardoso. Magnetoresistive sensors. *J. Phys. Condens. Matter*, 19(16):165221, April 2007.

[182] F. N. Hooge. 1/f Noise. *Phys. B*, 83:14, 1976.

[183] F. G. Aliev, R. Guerrero, D. Herranz, R. Villar, F. Greullet, C. Tiusan, and M. Hehn. Very low 1/f noise at room temperature in fully epitaxial Fe/MgO/Fe magnetic tunnel junctions. *Appl. Phys. Lett.*, 91(23):232504, 2007.

[184] J. M. Almeida, P. Wisniowski, and P. P. Freitas. Low-frequency noise in MgO magnetic tunnel junctions: Hooge's parameter dependence on bias voltage. *IEEE Trans. Magn.*, 44(11):2569, 2008.

[185] R. Stearrett, W. G. Wang, L. R. Shah, A. Gokce, J. Q. Xiao, and E. R. Nowak. Evolution of barrier-resistance noise in CoFeB/MgO/CoFeB tunnel junctions during annealing. *J. Appl. Phys.*, 107(6):064502, 2010.

[186] H. Polovy, R. Guerrero, J. Scola, M. Pannetier-Lecoeur, C. Fermon, G. Feng, K. Fahy, S. Cardoso, J. Almeida, and P. P. Freitas. Noise of MgO-based magnetic tunnel junctions. *J. Magn. Magn. Mater.*, 322(9-12):1624, 2010.

[187] S. Ingvarsson, G. Xiao, S. S. Parkin, W. J. Gallagher, G. Grinstein, and R. H. Koch. Low-frequency magnetic noise in micron-scale magnetic tunnel junctions. *Phys. Rev.*, 85(15):3289, 2000.

[188] L. Jiang, E. Nowak, P. Scott, J. Johnson, J. Slaughter, J. Sun, and R. Dave. Low-frequency magnetic and resistance noise in magnetic tunnel junctions. *Phys. Rev. B*, 69(5):054407, 2004.

[189] A. F. Md Nor, T. Daibou, M. Oogane, Y. Ando, and T. Miyazaki. Boron effects on noise in magnetic tunnel junctions. *J. Magn. Magn. Mater.*, 310(2):1917, 2007.

[190] A. Gokce, E. R. Nowak, S. H. Yang, and S. S. P. Parkin. 1f noise in magnetic tunnel junctions with MgO tunnel barriers. *J. Appl. Phys.*, 99(8):08A906, 2006.

[191] Z. Q. Lei, G. J. Li, W. F. Egelhoff, P T Lai, and P. W. T. Pong. Review of noise sources in magnetic tunnel junction sensors. *IEEE Trans. Magn.*, 47(3):602–612, 2011.

[192] J. Scola, H. Polovy, C. Fermon, M. Pannetier-Lecœ ur, G. Feng, K. Fahy, and J. M. D. Coey. Noise in MgO barrier magnetic tunnel junctions with CoFeB electrodes: Influence of annealing temperature. *Appl. Phys. Lett.*, 90(25):252501, 2007.

[193] K. Sato, M. Shikida, T. Yamashiro, M. Tsunekawa, and S. Ito. Roughening of single-crystal silicon surface etched by KOH water solution. *Sens. Actuator A-Phys.*, 73(1-2):122, 1999.

[194] M. Shikida, K. Sato, K. Tokoro, and D. Uchikawa. Differences in anisotropic etching properties of KOH and TMAH solutions. *Sens. Actuator A-Phys.*, 80(2):IEEE Robot and Automat Soc, 2000.

[195] T. Baum and D. J. Schiffrin. AFM study of surface finish improvement by ultrasound in the anisotropic etching of Si in KOH for micromachining applications. *J. Micromech. Microeng.*, 7:338, 1997.

[196] S. A. Campbell, K. Cooper, L. Dixon, R. Earwaker, S. N. Port, and D. J. Schiffrin. Inhibition of pyramid formation in the etching of Si p(100) in aqueous potassium hydroxide-isopropanol. *J. Micromech. Microeng.*, 5:209, 1999.

[197] H. Seidel, L. Csepregi, A. Heuberger, and H. Baumgärtel. Anisotropic etching of crystalline silicon in alkaline solutions. *J. Electrochem. Soc.*, 137(11):3612, 1990.

[198] S. S. Tan, M. L. Reed, H. Han, and R. Boudreau. Mechanisms of etch hillock formation. *J. Microelectromech. Syst*, 5(1):66, 1996.

[199] H. Schröder, E. Obermeier, and A. Steckenborn. Micropyramidal hillocks on KOH etched {100} silicon surfaces: formation, prevention and removal. *J. Micromech. Microeng.*, 9:139, 1999.

[200] A. J. Nijdam, E. Van Veenendaal, H. M. Cuppen, J. Van Suchtelen, M. L. Reed, J. G. E. Gardeniers, W. J. P. Van Enckevort, E. Vlieg, and M. Elwenspoek. Formation and stabilization of pyramidal etch hillocks on silicon 100 in anisotropic etchants: Experiments and Monte Carlo simulation. *J. Appl. Phys.*, 89(2001):4113, 2001.

[201] H. Tanaka, S. Yamashita, Y. Abe, M. Shikida, and K. Sato. Fast etching of silicon with a smooth surface in high temperature ranges near the boiling point of KOH solution. *Sens. Actuator A-Phys.*, 114(2-3):216, 2004.

[202] H. Tanaka, Y. Abe, T. Yoneyama, J. Ishikawa, O. Takenaka, and K. Inoue. Effects of small amount of impurities on etching of silicon. *Sens. Actuator*, 82:270, 2000.

[203] R. Divan, N. Moldovan, and H. Camon. Roughning and smoothing dynamics during KOH silicon etching. *Sens. Actuator A-Phys.*, 74:18, 1999.

[204] M. A. Goálvez and R M Nieminen. Surface morphology during anisotropic wet contact mode of crystalline silicon. *New J. Phys.*, 5:1, 2003.

[205] C. R. Yang, P. Y. Chen, Y. C. Chiou, and R. T. Lee. Effects of mechanical agitation and surfactant additive on silicon anisotropic etching in alkaline KOH solution. *Sens. Actuator A-Phys.*, 119(1):263, 2005.

[206] G. Canavese, S. L. Marasso, M. Quaglio, M. Cocuzza, C. Ricciardi, and C. F. Pirri. Polymeric mask protection for alternative KOH silicon wet etching. *J. Micromech. Microeng.*, 17(7):1387, 2007.

[207] T. A. Kwa and R. F. Wolffenbuttel. Effect of solution contamination on etched silicon surfaces. *J. Micromech. Microeng.*, 5:95, 1999.

[208] C. R. Yang, P. Y. Chen, C. H. Yang, Y. C. Chiou, and R. T. Lee. Effects of various ion-typed surfactants on silicon anisotropic etching properties in KOH and TMAH solutions. *Sens. Actuator A-Phys.*, 119(1):271, 2005.

[209] T. G. Park, J. J. Kim, S. H. Jung, H.J. Song, J. K. Chang, D. C. Han, and S. S. Yang. Fabrication of megasonic-agitated module for improving the characteristics of wet etching. *Jpn. J. Appl. Phys.*, 47(6):5262, 2008.

[210] W. S. Che, C. G. Suk, T. G. Park, J. T. Kim, and J. H. Park. The improvement of wet anisotropic etching with megasonic wave. *Key Eng. Mater.*, 297-300:557, 2005.

[211] W. J. Cho, W. K. Chin, and C. T. Kuo. Effects of alcoholic moderators on anisotropic etching of silicon in aqueous potassium hydroxide solutions. *Sens. Actuator A-Phys.*, 116(2):357, 2004.

[212] C. Mihalcea, A. Holz, A. Kuwahara, J. Tominaga, E. Oesterschulze, and N. Atoda. Improved anisotropic deep etching in KOH-solutions to fabricate highly specular surfaces. *Microelectron. Eng.*, 57-8:781, 2001.

[213] J. Chen, L. T. Liu, Z. J. Li, Z. M. Tan, Q. S. Jiang, H. J. Fang, Y. Xu, and Y. X. Liu. Study of anisotropic etching of (100) Si with ultrasonic agitation. *Sens. Actuator A-Phys.*, 96(2-3):152, 2002.

[214] I. Zubel. Silicon anisotropic etching in alkaline solutions III: On the possibility of spatial structures forming in the course of Si(100) anisotropic etching in KOH and KOH plus IPA solutions. *Sens. Actuator A-Phys.*, 84(1-2):116, 2000.

[215] I. Zubel and M. Kramkowska. The effect of isopropyl alcohol on etching rate and roughness of (100) Si surface etched in KOH and TMAH solutions. *Sens. Actuator A-Phys.*, 93(2):138, 2001.

[216] P. Pal, K. Sato, and S. Chandra. Fabrication techniques of convex corners in a (100)-silicon wafer using bulk micromachining: a review. *J. Micromech. Microeng.*, 17(10):R111, 2007.

[217] W. Fan and D. Zhang. A simple approach to convex corner compensation in anisotropic KOH etching on a (100) silicon wafer. *J. Micromech. Microeng.*, 16(10):1951, 2006.

[218] K. P. Rola and I. Zubel. Modifying of etching anisotropy of silicon substrates by surface active agents. *Cent. Eur. J. Phys.*, 9(2):410, 2011.

[219] Pt deposition technical note, PN 4035 272 21851-A. Technical report, FEI Company.

[220] Results of the new e-beam resist AR-N 7520. *AR news, Allresist GmbH*, (24), 2012.

[221] C. M. Melliar-Smith. Ion etching for pattern delineation. *J. Vac. Sci. Technol.*, 13(5):1008, 1976.

[222] F. Laermer and A. Schilp. Method of anisotropically etching silicon, U. S. patent 5501893, 1996.

[223] R. Nagarajan, K. Prasad, L. Ebin, and B. Narayanan. Development of dual-etch via tapering process for through-silicon interconnection. *Sens. Actuator A-Phys.*, 139(1-2):323, 2007.

[224] R. Abdolvand and F. Ayazi. An advanced reactive ion etching process for very high aspect-ratio sub-micron wide trenches in silicon. *Sens. Actuator A-Phys.*, 144(1):109, 2008.

[225] R. Gesche. RF matching of a reactive ion etching (RIE) plasma reactor. *Frequenz*, 59(3-4):73, 2005.

[226] J. I. Owen. *Growth, etching, and stability of sputtered ZnO:Al for thin-film silicon solar cells*. Forschungszentrum Jülich GmbH Zentralbibliothek, Jülich, 2011.

[227] Ambios Technology, Inc. *XP-2 Stylus profilometer user manual*, 2003.

[228] D. Meyners, J. Puchalla, S. Dokupil, M. Löhndorf, and E. Quandt. Magneto-electrical sensors for mechanical measurements. *ESC Trans.*, 25(3):223, 2007.

[229] M. J. Madou. *Fundamentals of microfabrication and nanotechnoloy*. CRC Press, Boca Raton, third edition, 2012.

[230] A. C. Miller. Redeposition of sputtered species during ion etching of Cu, Ag, and Au. *J. Vac. Sci. Technol.*, 12(5):1086, 1975.

[231] W. C. Young and R.G. Budynas. *Roak's formulas for stress and strain*. McGraw-Hill, New York, sixth edition.

[232] SONOSYS Ultraschallsysteme GmbH. *Manual of megasonic system*, 2007.

[233] J. G. Deak and R. H. Koch. The effect of edge roughness on magnetization reversal in micron-sized permalloy thin films. *J. Magn. Magn. Mater.*, 213(1-2):25, 2000.

[234] Y. J. Lee, J. G. Zhu, M. J. Kao, Y. H. Wang, and M. J. Tsai. SAF exhibits better resistance to roughness edge than single-free layer. *J. Magn. Magn. Mater.*, 310(2 SUPPL. PART 3):2671, 2007.

[235] M. Zhu and R. D. McMichael. Effect of interactions on edge property measurements in magnetic multilayers. *J. Appl. Phys.*, 109(4):043904, 2011.

[236] B. B. Maranville, R. D. McMichael, and D. W. Abraham. Variation of thin film edge magnetic properties with patterning process conditions in $Ni_{80}Fe_{20}$ stripes. *Appl. Phys. Lett.*, 90(23):245, 2007.

[237] S. Pütter, N. Mikuszeit, E. Y. Vedmedenko, and H. P. Oepen. The effect of tilted edges on the shape anisotropy and stray field coupling of uniformly magnetized rectangular elements. *J. Appl. Phys.*, 106(4):043916, 2009.

[238] E. Girgis, S. P. Pogossian, and M. L. Benkhedar. Effects of surface topography on magnetization reversal of magnetic thin films. *J. Nanosci. Nanotechnol.*, 6(4):1135, 2006.

[239] L. S. Uspenskaya, O. A. Tikhomirov, S. I. Bozhko, S. V. Egorov, and A. A. Chugunov. Domain structure and magnetization of the permalloy/niobium bilayers. *J. Appl. Phys.*, 113(16):10, 2013.

[240] Z. Zhang, H. Zhao, Y. Ren, B. Ma, and Q. Y. Jin. Interface roughness effects on the performance of magnetic tunnel junctions. *Thin Solid Films*, 515(7-8):3941, 2007.

[241] B. D. Schrag, A. Anguelouch, G. Xiao, P. Trouilloud, Y. Lu, W. J. Gallagher, and S. S. P. Parkin. Magnetization reversal and interlayer coupling in magnetic tunneling junctions. *J. Appl. Phys.*, 87(9):4682, 2000.

[242] T. von Hofe. Calculation of the strain of a bend bar. *Intern. Sci. Reports, Kiel University, Gr. Inorg. Funct. Mater.*, page 4, 2009.

[243] Newport Corporation. *850G series linear actuator user manual*, Part No. 27481-01, RevA edition, 1999.

[244] P. Hayes. *Investigation of magnetostrictive magnetic tunneling junctions for strain sensing applications.* M.Sc. dissertation, Kiel University, 2013.

[245] J. M. Teixeira, J. Ventura, J. P. Araujo, J. B. Sousa, P. Wisniowski, and P. P. Freitas. Tunneling processes in thin MgO magnetic junctions. *Appl. Phys. Lett.*, 96(26):262506, 2010.

[246] D. Herranz, A. Gomez-Ibarlucea, M. Schäfers, A. Lara, G. Reiss, and F. G. Aliev. Low frequency noise due to magnetic inhomogeneities in submicron FeCoB/MgO/FeCoB magnetic tunnel junctions. *Appl. Phys. Lett.*, 99(6):062511, 2011.

[247] G. V. Swamy, R. K. Rakshit, R. P. Pant, and G. A. Basheed. Origin of in-plane and out-of-plane magnetic anisotropies in as-deposited and annealed CoFeB ferromagnetic thin films. *J. Appl. Phys.*, 117(17):17A312, 2015.

[248] J. M. Teixeira, J. Ventura, M. P. Fernández-García, J. P. Araujo, J. B. Sousa, P. Wisniowski, D. C. Leitao, and P. P. Freitas. Exchange biased CoFeB-MgO tunnel junctions at the onset of perpendicular anisotropy with in-plane/out-of-plane sensing capabilities. *J. Appl. Phys.*, 111(5):053930, 2012.

[249] D. Wang, C. Nordman, Z. Qian, J. Daughton, and J. Myers. Magnetostriction effect of amorphous CoFeB thin films and application in spin-dependent tunnel junctions. *J. Appl. Phys.*, 97(10):10C906, 2005.

[250] Z. Tang, B. Wang, H. Yang, X. Xu, Y. Liu, D. Sun, L. Xia, Q. Zhan, B. Chen, M. Tang, Y. Zhou, J. Wang, and R. W. Li. Magneto-mechanical coupling effect in amorphous $Co_{40}Fe_{40}B_{20}$ films grown on flexible substrates. *Appl. Phys. Lett.*, 105:103504, 2014.

[251] J. M. Barandiarán, J. Gutiérrez, Z. Kaczkowski, and D. De Cos. Influence of annealing temperature on the magnetic and magnetoelastic properties in FeCoB metallic glasses. *J. Non-Cryst. Solids*, 329(1-3):43, 2003.

[252] C. L. Platt, N. K. Minor, and T. J. Klemmer. Magnetic and structural properties of FeCoB thin films. *IEEE Trans. Magn.*, 37(4):2302, 2001.

[253] J. Steiner, R. Schäfer, H. Wieczoreck, J. McCord, and F. Otto. Formation and coarsening of the concertina magnetization pattern in elongated thin-film elements. *Phys. Rev. B*, 85(10):104407, 2012.

[254] D. Meyners, H. Bruckl, and G. Reiss. Influence of boundary roughness on the magnetization reversal in submicron sized magnetic tunnel junctions. *J. Appl. Phys.*, 93(5):2676, 2003.

[255] M. Frankowski, M. Czapkiewicz, W. Skowroski, and T. Stobiecki. Micromagnetic model for studies on Magnetic Tunnel Junction switching dynamics, including local current density. *Phys. B Condens. Matter*, 435:105, 2014.

[256] A. Johnson. *Spin valve systems for angle sensor applications*. Ph.D. dissertation, Technical University of Darmstadt, 2004.

[257] D. Meyners. *Herstellung und charakterisierung von logikarrays mit ultrakleinen magnetischen Tunnelelementen*. Ph.D. dissertation, Bielefeld University, 2006.

[258] J. P. Cascales, D. Herranz, J. L. Sambricio, U. Ebels, J. a. Katine, and F. G. Aliev. Magnetization reversal in sub-100 nm magnetic tunnel junctions with ultrathin MgO barrier biased along the hard axis. *Appl. Phys. Lett.*, 102, 2013.

[259] I. Barsukov, Y. Fu, A. M. Gonçalves, M. Spasova, M. Farle, L. C. Sampaio, R. E. Arias, and I. N Krivorotov. Field-dependent perpendicular magnetic anisotropy in CoFeB thin films. *Appl. Phys. Lett.*, 152403, 2014.

[260] T. Meier. *Magnetoresistive and thermoresistive scanning probe microscopy with applications in micro- and nanotechnology*. Ph.D. dissertation, Karlsruhe Institute of Technology, 2014.

[261] S. Zhang, P. M. Levy, A. C. Marley, and S. S. P. Parkin. Quenching of Magnetoresistance by Hot Electrons in Magnetic Tunnel Junctions. *Phys. Rev. Lett.*, 79(19):3744, 1997.

[262] J. Zhang and R. M. White. Voltage dependence of magnetoresistance in spin dependent tunneling junctions. *J. Appl. Phys.*, 83(11):6512, 1998.

[263] T. Meier, A. Förste, A. Tavassolizadeh, K. Rott, D. Meyners, R. Gröger, G. Reiss, E. Quandt, T. Schimmel, and H. Hölscher. A scanning probe microscope for magnetoresistive cantilevers utilizing a nested scanner design for large-area scans. *Beilstein J. Nanotechnol.*, 6:451, 2015.

[264] G. Binnig, Ch. Gerber, E. Stoll, T. R. Albrecht, and C. F. Quate. Atomic resolution with atomic Force microscope. *Eur. Lett.*, 3(12):1281, 1987.

[265] A. Tavassolizadeh, T. Meier, K. Rott, G. Reiss, E. Quandt, H. Hölscher, and D. Meyners. Self-sensing atomic force microscopy cantilevers based on tunnel magnetoresistance sensors. *Appl. Phys. Lett.*, 102(15):153104, 2013.

[266] J. V. Barth, H. Brune, G. Ertl, and R. J. Behm. Scanning tunneling microscopy observations on the reconstructed Au(111) surface: Atomic structure, long-range superstructure, rotational domains, and surface defects. *Phys. Rev. B*, 42(15):9307, 1990.

[267] F. J. Giessibl. Advances in atomic force microscopy. *Rev. Mod. Phys.*, 75(3):949, 2003.

[268] Y. Sugimoto, T. Namikawa, M. Abe, and S. Morita. Mapping and imaging for rapid atom discrimination: A study of frequency modulation atomic force microscopy. *Appl. Phys. Lett.*, 94(2):245, 2009.

[269] C. Huang, M. Moosmann, J. Jin, T. Heiler, S. Walheim, and T. Schimme. Polymer blend lithography: A versatile method to fabricate nanopatterned self-assembled monolayers. *Beilstein J. Nanotechnol.*, 3(1):620, 2012.

[270] J. Freund, J. Halbritter, and J. K. H. Hörber. How dry are dried samples? Water adsorption measured by STM. *Microsc. Res. Tech.*, 44(5):327, 1999.

[271] BACH Resistor Ceramics GmbH.

[272] Cataloge for anit-reflective coated ZnSe zero length viewports. *published by Torr Sci. Ltd*, 2015.

[273] Negative e-beam resists AR-N 7520 new. Technical report, Allresist GmbH, 2013.